To the Graduate Council:

I am submitting herewith a dissertation written by Jackie Langille entitled "Dome formation during crustal extension: Kinematic and pressure-temperature-time-deformation constraints on extensional exhumation along the southern margin of the Tibetan Plateau." I have examined the final electronic copy of this dissertation for form and content and recommend that it be accepted in partial fulfillment of the requirements for the degree of Doctor of Philosophy with a major in Geological Sciences.

Micah Jessup
Major Professor

We have read this dissertation
and recommend its acceptance:

Robert D. Hatcher, Jr.

Theodore Labotka

John Wilkerson

John Cottle (courtesy member)

Accepted for the Council:

Carolyn R. Hodges
Vice Provost and Dean of the Graduate School

(Original signatures are on file with official student records.)

Dome Formation During Crustal Extension in the Himalaya: Kinematic and Pressure-Temperature-Time-Deformation Constraints on Extensional Exhumation Along the Southern Margin of the Tibetan Plateau

A Dissertation Presented for the
Doctor or Philosophy Degree
The University of Tennessee, Knoxville

Jackie Langille
May 2012

Copyright © 2012 by Jackie Langille
All rights reserved.



Leo Pargil peak (6828 m)

ACKNOWLEDGEMENTS

First and foremost, I must thank my husband Paul whose support and encouragement has been a great strength to me. I cannot express enough how much his sacrifice and support has meant to me. I want to thank my family; specifically my mother, stepfather, and brother who have supported me during my time in graduate school and who have encouraged me the whole way. I also want to thank my friends, including the wonderful new friends that I gained while at the University of Tennessee.

I would like to thank my dissertation advisor, Micah Jessup, for the opportunity that he gave me to continue my academic career, for the funding he provided me to do this research, for the many trips to national and international conferences, and for being a mentor to me. I thank my committee members; Robert D. Hatcher, Jr., Theodore Labotka, and John Wilkerson from the University of Tennessee and John Cottle from the University of California, Santa Barbara; who provided insights and reviews that strengthened this dissertation and my knowledge of this subject. Liz Lee and Paul Langille provided support and assistance during field work over two field seasons. Richard Powlus, Nick Costello, and Ty Conner conducted undergraduate research projects that were incorporated into this dissertation. I also thank Allan Patchen and Larry Taylor for their guidance and support with use of the electron microprobe here at the University of Tennessee. Andrew Kylander-Clark and Gareth Seward provided assistance with the use of the laser ablation inductively coupled plasma mass spectrometer and the scanning electron microscope at the University of California, Santa Barbara.

I would like to thank the sources that provided funds which supported me and this dissertation including the National Science Foundation awarded to Micah Jessup and John Cottle and Sigma Xi, ExxonMobil, the Mayo Educational Foundation, the Geological Society of America, the Knoxville Gem and Mineral Society, and the Department of Earth and Planetary Sciences at the University of Tennessee awarded to Jackie Langille. Without this funding, this research would not have been possible.

ABSTRACT

The Himalaya and Tibetan Plateau were built by a combination of south-directed thrusting, north-directed extension, and generally east-west-directed extension within the Himalaya and Tibetan Plateau all to accommodate convergence between the Indian and Eurasian plates that began in the Eocene. Normal-sense shear zones that accommodate roughly east-west-directed extension across the southern margin of the Himalaya have exhumed young metamorphic domes across the Himalayan front. These metamorphic domes contain high-grade metamorphic rocks bound by normal-sense shear zones. The purpose of this study is to evaluate how these normal-sense shear zones develop and how they exhume metamorphic domes, which remains poorly understood and is critical for understanding the processes that accommodate extensional exhumation in this convergent setting. Two examples of metamorphic domes that were exhumed by east-west-directed normal-sense shear zones in the Himalaya are the Ama Drime Massif, southern Tibet, and the Leo Pargil dome, northwest India-Tibet. The Ama Drime Massif is a 30 km-wide north-south-striking structure that thins toward the north. It is located ~50 km northeast of Mount Everest and is bound by the Nyönno Ri detachment on the eastern flank and the Ama Drime detachment on the western flank. The Leo Pargil dome, ~950 km west of Ama Drime, is a 20 km-wide, northeast-southwest-striking structure composed of high-grade metamorphic rocks and leucogranite. It is bound on the east by the Qusum detachment and on the west by the Leo Pargil shear zone. Field mapping and sample collection were combined with kinematic, microstructural, thermobarometric, and geochronologic methods to constrain the metamorphic conditions, the kinematics of deformation during shearing, the amount of exhumation, and the timing of metamorphism and shear zone initiation. These data demonstrate the exhumation on these normal-sense shear zones in the Himalaya are controlled by an interplay between various processes including a regional kinematic setting that favored extension which led to strain partitioning, fault reactivation, decompression-driven melting, and the development of these deeply-rooted extensional systems.

TABLE OF CONTENTS

INTRODUCTION 1
Purpose of the Study 1
Tectonic Setting 1
Overview of Methods 4
Deformation Temperatures, Kinematic Vorticity, and Strain 4
Pressure-Temperature Estimates 7
U-Th-Pb Geochronology 8
References 10
CHAPTER I: KINEMATIC EVOLUTION OF THE AMA DRIME DETACHMENT: INSIGHTS INTO OROGEN-PARALLEL EXTENSION AND EXHUMATION OF THE AMA DRIME MASSIF, TIBET-NEPAL 13
Abstract 14
Introduction 15
Geologic Setting 16
Regional Geology 16
Geology of the Ama Drime Massif 20
Shear Sense Indicators 23
Results 25
Deformation Temperatures 29
Quartz and Feldspar Microstructures 30
Opening Angle and Quartz [c] Axis Lattice-Preferred Orientations 30
Two-Feldspar Geothermometry 31
Results 33
Vorticity 37
Rigid Grain Technique 38
Quartz Grain Shape Foliation Technique 39
Results 40
Shortening and Extension 42
Discussion 43
Implications for the Ama Drime and Nyönno Ri Detachments 43
Comparison with the North Himalayan Gneiss Domes 46
Exhumation of the Ama Drime Massif 47
Conclusions 49
References 51
Appendix 1.1 60
Appendix 1.2 61
CHAPTER II: TIMING OF METAMORPHISM, MELTING, AND EXHUMATION OF THE LEO PARGIL DOME, NORTHWEST INDIA 64
Abstract 65
Introduction 66
Geologic Setting 69
Regional Geologic Setting 71
Geology of the Leo Pargil Dome 71
Samples 74

Haimanta Group in the Hanging Wall of the Leo Pargil Dome (LP09-10) 74
Leo Pargil Dome (LP09-76, 229, and 162) 75
Leucogranites (LP09-157, 158, 166, and 167) 77
Methodology 77
Pressure-Temperature Estimates 77
Monazite Geochronology 80
Pressure-Temperature Estimates 81
Haimanta Group in the Hanging Wall of the Leo Pargil Dome (LP09-10) 81
Leo Pargil Dome (LP09-76, 229, and 162) 82
In-Situ Monazite Geochronology from Metamorphic Rocks 87
Haimanta Group in the Hanging Wall of the Leo Pargil Dome (LP09-10) 87
Leo Pargil Dome (LP09-76, 229, and 162) 88
Monazite Geochronology from Leucogranites 92
Discussion 93
Monazite Growth in Metamorphic Rocks 93
Barrovian Metamorphism 96
Decompression 97
Tectonic Implications and Processes for Dome Formation 100
Conclusions 103
References 104
Appendix 2.1 112
Appendix 2.2 126
Appendix 2.3 131
CHAPTER III: STRUCTURAL EVOLUTION OF THE LEO PARGIL DOME, NW INDIA: IMPLICATIONS FOR THE TECTONICS OF THE WESTERN HIMALAYA 136
Abstract 137
Introduction 138
Regional Geology 142
Geology of the Leo Pargil Dome 147
Temperatures and Kinematics During Deformation 154
Methodology for Estimating Deformation Temperatures 154
Results 156
Methodology for Estimating Vorticity and Results 157
Thermobarometry 160
Methodology and Results 160
Discussion 163
Evolution of the Leo Pargil Shear Zone 163
Implications for Orogen-Parallel Extension and the Tectonics in the Western Himalaya 166
Conclusions 171
References 172
Appendix 3.1 179
CONCLUSION 180
VITA 181

LIST OF TABLES

Table 1.1. Summary of Shear Sense, Vorticity, and Temperature Data 27
Table 1.2. Rim Compositions of K-Feldspar and Myrmekite 34
Table 2.1. Modal Analysis of LP09-162 79
Table 2.2. Bulk Composition (in wt%) of Sample LP09-162 80
Table 2.3. Compositional Data (in wt%) Used for Thermobarometric Analyses 84
Table 2.4. Pressure-Temperature Estimates for Barrovian Metamorphism 85
Table 3.1. Summary of Kinematic and Deformation Temperature Data 151
Table 3.2. Compositional Data (in wt%) for Near-Garnet-Rim Thermobarometric Analysis ... 162

LIST OF FIGURES

Figure 1. Geologic map of the Himalayan orogen 2
Figure 1.1. Simplified interpretive block diagram of the Everest region 15
Figure 1.2. Geologic map of the Ama Drime Massif 17
Figure 1.3. Field photographs 21
Figure 1.4. Photomicrographs of representative kinematic indicators 24
Figure 1.5. Interpretation of quartz lattice-preferred orientation (LPO) data 25
Figure 1.6. Quartz LPO data in order of increasing structural depth 26
Figure 1.7. Asymmetric myrmekite in sample KA-40 33
Figure 1.8. Deformation temperatures and vorticity estimates 35
Figure 1.9. Estimated deformation temperatures for asymmetric myrmekite 36
Figure 1.10. Examples of Rigid Grain Net (RGN) analysis 39
Figure 1.11. Vorticity analysis from quartz grain shape fabrics 41
Figure 1.12. Simplified geologic cross section through Mount Everest and the Ama Drime Massif 44
Figure 2.1. Location of the Leo Pargil dome 68
Figure 2.2. Field photographs 73
Figure 2.3. Photomicrographs of kinematic indicators 76
Figure 2.4. Images of LP09-162 78
Figure 2.5. Garnet compositions used for pressure-temperature (P-T) estimates 82
Figure 2.6. Pressure-temperature data calculated using THERMOCALC 83
Figure 2.7. Pseudosection of sample LP09-162 87
Figure 2.8. Examples of monazite age domains 88
Figure 2.9. Concordia diagrams of metamorphic in-situ monazite U-Th-Pb analyses 89
Figure 2.10. Probability plots and interpretation of $^{208}Pb/^{232}Th$ ages 90
Figure 2.11. $^{208}Pb/^{232}Th$ ages from leucogranites 93
Figure 2.12. Pressure-temperature-time-deformation (P-T-t-D) path for exhumation of the Leo Pargil dome 98
Figure 2.13. Temperature-time plot for the Leo Pargil dome rocks 99
Figure 3.1. Active faults in the Himalaya 139
Figure 3.2. Geologic map of the southern end of the Leo Pargil dome 144
Figure 3.3. Field photographs from the Leo Pargil dome 148
Figure 3.4. Photomicrographs of samples from the Leo Pargil dome 150
Figure 3.5. Interpretation of quartz lattice-preferred orientation (LPO) data 155
Figure 3.6. Quartz lattice-preferred orientation (LPO) patterns 158
Figure 3.7. Diagram depicting the aspects used in estimation of vorticity (W_m) 159
Figure 3.8. Histograms of quartz grain orientation data and W_m estimates 161
Figure 3.9. Compositional data from garnet 161
Figure 3.10. Pressure-temperature estimate 162
Figure 3.11. Schematic diagrams depicting two models for the evolution of the western Himalaya 168

INTRODUCTION

Purpose of the Study

The main objectives of this study are to: (1) characterize the spatial and temporal patterns of deformation on normal-sense shear zones that bound the Ama Drime Massif in southern Tibet and the Leo Pargil dome in northwest India, (2) characterize the pressure-temperature-time-deformation (P-T-t-d) paths recorded in the rocks within the Leo Pargil dome, and (3) to constrain the processes that resulted in extensional exhumation of these young metamorphic domes along the southern margin of the Tibetan Plateau (Fig. 1). Kinematic, deformation temperature, vorticity, thermobarometry, and geochronology methods were applied to samples from the Ama Drime Massif and Leo Pargil dome. The resulting data from these domes allow evaluation of the processes responsible for exhumation of these domes, including the relationship between the generation of partial melt, tectonic setting, and strain localization with shear zone development and exhumation of these young metamorphic domes.

Tectonic Setting

The Himalayan front at the southern margin of the Tibetan Plateau extends for ~2500 km and has an average elevation of 5000 m (Gansser, 1980). From the Eocene to middle Miocene the Himalayan orogen has accommodated a significant amount of crustal shortening during the north-directed collision of the Eurasian and Indian plates. Since the Miocene, north-directed convergence (at a modern rate of ~35 mm/yr) (Bettinelli et al., 2006) has been accommodated by thrust faults in the foreland while strike-slip and normal faults and graben, such as the Karakoram fault and the Dinggyê graben (Fig. 1), accommodate east-west extension from the orogenic front into the interior of the plateau.

The southern margin of the Tibetan Plateau is composed of three main litho-tectonic units separated by major fault systems. With increasing structural level these units include: the metasedimentary rocks of the Lesser Himalayan sequence, the upper-amphibolite facies metamorphic rocks of the Greater Himalayan sequence (GHS) that contains the anatectic core of

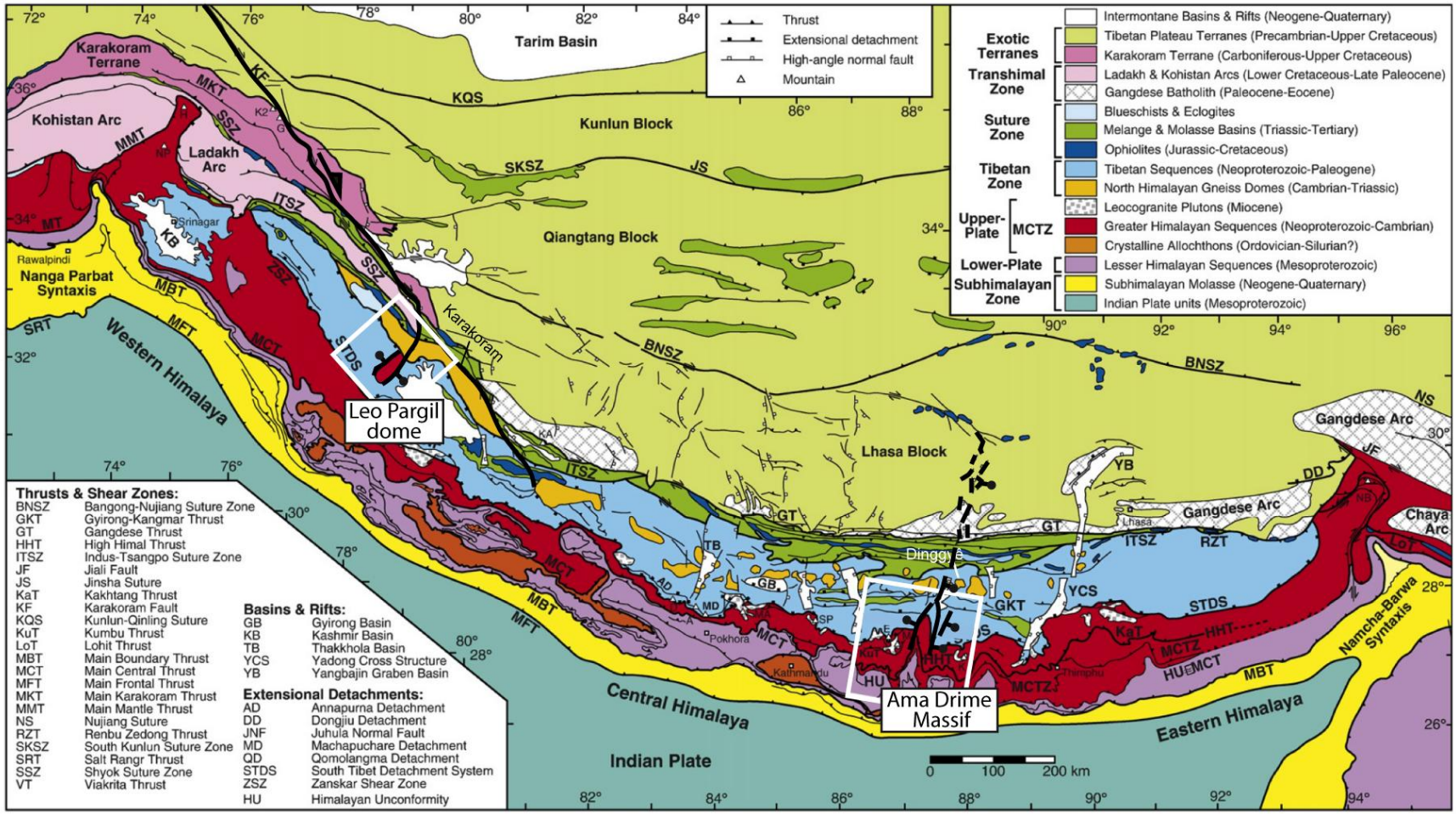

Figure 1. *Geologic map of the Himalayan orogen with locations of the Ama Drime Massif and Leo Pargil dome. After Goscombe et al. (2006).*

the Himalaya, and the low-grade to unmetamorphosed rocks of the Tibetan sedimentary Sequence (TSS) (Fig. 1). The Lesser Himalayan sequence is bound at the base by the Main Boundary thrust and the top by the Main Central thrust zone (MCTZ) (Fig. 1). The MCTZ bounds the bottom of the GHS and the low-angle, normal-displacement South Tibetan detachment system (STDS) bounds the top. The STDS separates the GHS from the overlying TSS (Fig. 1) (e.g., Grasemann et al., 1999; Hodges et al., 2001; Vannay and Grasemann, 2001). The southernmost thrust is the Main Frontal thrust which actively accommodates convergence today. The Main Frontal thrust, Main Boundary thrust, and the MCTZ sole into the Main Himalayan thrust below the Tibetan Plateau (Nelson et al., 1996).

Normal faults and shear zone systems in the central Himalaya (such as those that bound the Ama Drime Massif) developed in the middle Miocene and cut or offset the older STDS (Fig. 1) (e.g., Murphy et al., 2002; Kapp and Guynn, 2004; Murphy and Copeland, 2005; Thiede et al., 2006; Jessup et al., 2008). The Ama Drime Massif is a 30 km-wide north-south-striking antiformal structure located ~50 km northeast of Mount Everest that is bound by the north-south-striking, east-dipping Nyönno Ri detachment on the eastern flank and the north-south-trending, west-dipping Ama Drime detachment (ADD) on the western flank (Fig. 1) (Jessup et al., 2008). To the north, the Nyönno Ri detachment transitions into the Dinggyê graben that extends into the interior of the plateau (Taylor et al., 2003). The ADD is composed of metapelitic rocks, leucogranite, calc-silicate, quartzite, and marble and the Nyönno Ri detachment is composed of metapelitic rocks, leucogranite, and quartzite. The Massif is composed of orthogneiss and paragneiss that contains mafic lenses and is cored by eclogite. The orthogneiss and paragneiss are intruded by leucogranite. The ADD offset the STDS during orogen-parallel extension (Jessup et al., 2008; Langille et al., 2010). Fault scarps on the east side of the Massif suggest that exhumation of the Ama Drime Massif related to extension on the Dinggyê graben into the interior of the plateau continues today.

The Leo Pargil dome in northwest India, ~950 km west of Ama Drime, is located between major fault systems that accommodated north-directed convergence from the Eocene to middle Miocene (such as the MCTZ and STDS) and the Karakoram strike-slip fault system. The dome is bound by normal fault systems that are oriented perpendicular to the orogenic front and accommodate east-west-directed crustal extension. These faults continue north and intersect the

dextral Karakoram fault system (Fig. 1). The dome is a 20 km-wide, northeast-southwest-striking structure composed of high-grade metamorphic rocks and leucogranite (Thiede et al., 2006). These high-grade rocks and leucogranite within the dome are separated from the low-grade TSS and the Haimanta sequence (documented as the base of the TSS) to the west by the west-dipping, normal-displacement Leo Pargil shear zone (LPSZ). Few studies have been conducted on the east side of the dome (e.g., Zhang et al., 2000; Murphy et al., 2009) but suggest that it is bound by an east-dipping detachment that developed during orogen-parallel extension in the late Miocene (Murphy et al., 2009). Previous studies suggest that the onset of ductile exhumation began at a minimum of 16-14 Ma (Thiede et al., 2006). Fault scarps that offset the LPSZ suggest that brittle-faulting that initiated between 6 and 10 Ma (Thiede et al., 2006) continues to exhume the dome today.

Overview of Methods

Field mapping of the Ama Drime Massif was conducted over two field seasons as published by Jessup et al. (2008). This study includes kinematic, deformation temperature, and vorticity analyses conducted on samples collected over these field seasons to constrain the exhumation history of the ADD. Field work at the Leo Pargil dome was conducted over two field seasons in 2009 and 2011 and included geologic mapping and sample collection. Thermobarometry and geochronology methods were applied to samples from the Leo Pargil dome to evaluate the mechanisms responsible for exhumation of this dome. In addition, kinematic, deformation temperature, and vorticity analyses were conducted to constrain the kinematics during exhumation and to evaluate the tectonics in this region of the Himalaya. Details on these methods are included within each chapter.

Deformation Temperatures, Kinematic Vorticity, and Strain

Deformation temperatures can be assessed qualitatively and quantitatively using various methods that utilize deformed quartz or feldspar. These include evaluating (1) the recrystallization textures recorded in quartz and feldspar (Hirth and Tullis, 1992; Fitz Gerald and Stünitz, 1993; Stipp et al., 2002), (2) quartz slip systems determined from quartz lattice preferred

orientation (LPO) patterns (e.g., Mainprice et al., 1986), (3) the opening angle of quartz [c] axis LPO patterns (Law, 1990; Kruhl, 1998; Law et al., 2004), and (4) two-feldspar thermometry of asymmetric strain-induced myrmekite, all of which correspond to certain temperatures. These temperatures are critical to evaluating the depth in the crust where deformation occurred, to interpret exhumation mechanisms that occurred during shearing, and to estimate the amount of displacement that was necessary to exhume the rocks that are now exposed on the surface.

Vorticity analyses were conducted to quantify the relative contribution of pure shear (flattening) and simple shear (shearing with no flattening) during ductile deformation and to characterize the spatial and temporal variability in flow during exhumation. A contribution of pure shear indicates a higher degree of thinning and strain relative to simple shear (Law et al., 2004). Kinematic vorticity (W_k) is a measure of the relative contributions of pure ($W_k = 0$) and simple ($W_k = 1$) shear during steady-state (instantaneous) deformation. In this nonlinear relationship, pure and simple shear components are equal when $W_k = 0.71$ (Tikoff and Fossen, 1995; Law et al., 2004). Spatial and temporal variability of deformation in naturally deformed rocks can be accounted for by using a time-averaged and assumed steady-state deformation history known as the mean kinematic vorticity number (W_m) (e.g., Fossen and Tikoff, 1997, 1998; Jiang, 1998). W_m methods require that deformation progressed during plane strain conditions. Two methods for estimating W_m were applied to thin sections cut perpendicular to the foliation and parallel to the lineation (XZ section); the rigid-grain technique (Passchier, 1987; Wallis et al., 1993; Jessup et al., 2007) and the quartz grain shape foliation technique (Wallis, 1995). The rigid-grain technique involves measuring the aspect ratio (R) of rigid porphyroclasts, such as feldspar, and the acute angle (θ) between the clast long axis and the macroscopic foliation. Grains above a critical aspect ratio (R_c) define a stable orientation and will exhibit a small range in θ, whereas grains below will infinitely rotate and show a larger range of θ. From R_c, vorticity can be calculated as (Passchier, 1987):

$$W_m = (R_c^2 - 1) / (R_c^2 + 1) \quad (1)$$

Plotting the shape factor (B*), where

$$B^* = (M_x^2 - M_n^2) / (M_x^2 + M_n^2) \quad (2)$$

and M_x is the long axis of the grain and M_n is the short axis, versus θ on the rigid-grain net (Jessup et al., 2007) is a graphical approach to calculating W_m. B* and W_m are scaled one-to-one so the rigid-grain net allows real time assessment of the data. W_m estimates derived from this method record the bulk shear.

Quartz oblique fabrics can also be used to estimate vorticity. During deformation, newly recrystallized grains (e.g., quartz) are stretched parallel to the instantaneous stretching axis (ISA) (Wallis, 1995). The maximum angle (θ) between the quartz oblique grain-shape fabric (measured from the thin section) and the flow plane (measured as the perpendicular to the quartz [c] axis patterns) provides an approximate orientation of the ISA. The orientation of the ISA is related to W_m by the equation (Wallis, 1995):

$$W_m = \sin 2\theta \quad (3)$$

The strain ratio (R_{xz}) can be calculated from the geometry of quartz [c] axis LPO patterns and W_m using the following equation (Passchier, 1988; Xypolias, 2009).

$$R_{xz} = \frac{1 - \tan\theta * \tan\beta}{\tan^2\beta + \tan\theta * \tan\beta} \quad (4)$$

where

$$\tan\theta = \cot[2(\beta + \delta)] = \sqrt{1 - W_m^2} / W_m \quad (5)$$

and β is the angle between the flow plane and foliation as measured from the quartz [c] axis fabric and δ is the angle between the quartz oblique fabric and the main foliation. R_{xz} and W_m can be used to calculate the percent shortening and extension by calculating the shortening value (S) using the following equation (Wallis et al., 1993):

$$S = \{0.5(1 - W_m^2)^{0.5}[(R_{xz} + R_{xz}^{-1} + \frac{2(1+W_m^2)}{(1-W_m^2)})^{0.5} + (R_{xz} + R_{xz}^{-1} - 2)^{0.5}]\}^{-1} \quad (6)$$

Pressure-Temperature Estimates

The P-T path recorded in a rock during burial, metamorphism, and exhumation is essential for characterizing the mechanisms associated with the onset of exhumation and the subsequent events leading to exhumation of the rocks. To estimate P-T conditions associated with metamorphism, thermobarometric analyses were performed on samples with suitable assemblages. Petrographic studies were used to evaluate the relationship between phases such as garnet, plagioclase, and biotite, which were used for P-T calculation. Mineral composition analyses were carried out here at the University of Tennessee on the Cameca SX-100 electron microprobe. X-ray maps of Mg, Mn, Ca and Fe were conducted on garnet porphyroblasts to determine zonation. Quantitative compositional line transects were conducted across the garnet porphyroblasts. These data, along with the X-ray maps, were used to interpret the conditions associated with garnet growth. Point analyses were conducted in other phases such as staurolite, biotite, plagioclase, and muscovite to demonstrate the compositional heterogeneities of each phase throughout the sample. P-T estimates at peak temperatures were calculated from the chemical data using the thermobarometric software THERMOCALC 3.33 (Powell and Holland, 1994) using the average P-T mode. Activity coefficients for each phase were calculated using the software AX.

In addition to P-T estimates at peak temperatures, P-T paths can be reconstructed from bulk chemical data for a sample by modeling the mineral assemblages that should exist at certain P-T conditions. The resulting data plotted in P-T space is called a pseudosection. Petrographic observation of the assemblages in equilibrium and the reactions recorded in the sample allow interpretation of the P-T path undergone by the sample. Pseudosections are calculated from the bulk composition of the sample of interest. The Perplex 6.6.6 software package (Connolly, 2009; updated in 2011) for calculation using the Holland and Powell (1998) thermodynamic data file (updated in 2004, hp04ver.dat).

U-Th-Pb Geochronology

U-Th-Pb geochronology was applied to metamorphic rocks and granites from the Leo Pargil dome, the LPSZ, and the immediate hanging wall. Integrating these data with kinematic data and P-T estimates constrain the timing of prograde metamorphism and the onset of exhumation and decompression. U-Th-Pb geochronology analysis uses the radioactive decay of ^{238}U, ^{235}U, and ^{232}Th to ^{206}Pb, ^{207}Pb, and ^{208}Pb, respectively. This method is applied to minerals that contain an abundance of these isotopes, including zircon and monazite. Monazite accepts a large amount of U and Th, it has little tendency for loss of decay products, it has a relatively high closure temperature, and metamorphic monazite commonly grows below the closure temperature; thus it is useful in U-Th-Pb dating and was used for this study. The ratios of these isotopes were used to calculate the age at which the monazite crystallized using the following equations (Jaffey et al., 1971; Dicken, 2005):

$$\left(\frac{^{206}\mathrm{Pb}}{^{238}\mathrm{U}}\right) = e^{\lambda_{238}t} - 1 \quad (7)$$

$$\left(\frac{^{207}\mathrm{Pb}}{^{235}\mathrm{U}}\right) = e^{\lambda_{235}t} - 1 \quad (8)$$

$$\left(\frac{^{208}\mathrm{Pb}}{^{232}\mathrm{Th}}\right) = e^{\lambda_{232}t} - 1 \quad (9)$$

where λ is a decay constant and t is the half-life of decay, assuming a closed system. Potential causes of discordance are the presence of common lead, lead loss during a thermal event, and/or age domain mixing during acquisition of the analyses.

In-situ U-Th-Pb analysis on monazite grains within metamorphic samples used for P-T estimates will provide estimates of the timing of monazite growth during metamorphism. In-situ analysis of monazite is beneficial because it provides a means for relating monazite growth to metamorphic reactions and the growth of phases such as garnet which were used for thermobarometry. For example, the breakdown of garnet releases Y into the system and may be incorporated into monazite rims during monazite growth. The subsequent monazite rim will be

enriched in Y (e.g., Foster et al., 2002). This potentially allows an age to be placed on the P-T estimates. In-situ analysis also enables monazite grains associated with a deformational fabric to be analyzed and can be used to delimit the timing of deformation. In-situ U-Th-Pb analysis was conducted on the laser ablation inductively coupled mass spectrometer (LA-ICPMS) at the University of California, Santa Barbara.

U-Th-Pb analysis of monazite grains in granites collected from the Leo Pargil dome were used to place an age on monazite growth during crystallization of igneous intrusions. U-Th-Pb analysis entailed obtaining monazite mineral separates. Monazite grains from each sample were then mounted in a grain mount. U-Th-Pb ages were calculated from isotopic data also obtained using the LA-ICPMS at the University of California, Santa Barbara.

References

Bettinelli, P., Avouac, J.-P., Flouzat, M., Jouanne, F., Bollinger, L., Willis, P., and Chitrakar, G., 2006, Plate Motion of India and Interseismic Strain in the Nepal Himalaya from GPS and DORIS Measurements: Journal of Geodesy, v. 80, p. 567-589.

Connolly, J., 2009, The geodynamic equation of state: What and how: Geochemistry Geophysics Geosystems, v. 10, 19 p.

Dicken, A., 2005, Radiogenic isotope geology: New York, Cambridge University Press, 492 p.

Fitz Gerald, J., and Stünitz, H., 1993, Deformation of granitoids at low metamorphic grades. I: Reactions and grain size reduction: Tectonophysics, v. 221, p. 269-297.

Fossen, H., and Tikoff, B., 1997, Forward modeling of non-steady state deformations and the 'minimum strain path': Journal of Structural Geology, v. 19, p. 987-996.

Fossen, H., and Tikoff, B., 1998, Forward modeling of non-steady-state deformations and the 'minimum strain path': Reply: Journal of Structural Geology, v. 20, p. 979-981.

Foster, G., Gibson, H., Parrish, R., Horstwood, M., Fraser, J., and Tindle, A., 2002, Textural, chemical and isotopic insights into the nature and behavior of metamorphic monazite: Chemical Geology, v. 191, p. 183-207.

Gansser, A., 1980, The significance of the Himalayan suture zone: Tectonophysics, v. 62, p. 37-52.

Goscombe, B., Gray, D., and Hand, M., 2006, Crustal architecture of the Himalayan metamorphic front in eastern Nepal: Gondwana Research, v. 10, p. 232-255.

Grasemann, B., Fritz, H., and Vannay, J. C., 1999, Quantitative kinematic flow analysis from the Main Central Thrust Zone (NW-Himalaya, India): implications for a decelerating strain path and the extrusion of orogenic wedges: Journal of Structural Geology, v. 21, no. 7, p. 837-853.

Hirth, G., and Tullis, J., 1992, Dislocation creep regimes in quartz aggregates: Journal of Structural Geology, v. 14, no. 2, p. 145-159.

Hodges, K. V., Hurtado, J. M., Jr., and Whipple, K. X., 2001, Southward extrusion of Tibetan crust and its effect on Himalayan tectonics: Tectonics, v. 20, no. 6, p. 799-809.

Holland, T. J. B., and Powell, R., 1998, An internally consistent thermodynamic data set for phases of petrological interest: Journal of Metamorphic Geology, v. 16, p. 309-343.

Jaffey, A., Flynn, K., Glendnin, L., Bentley, C., and Essling, A., 1971, Precision measurement of half-lives and specific activities of ^{235}U and ^{238}U: Physical Review, v. 4, p. 1889-1906.

Jessup, M. J., Law, R. D., and Frassi, C., 2007, The Rigid Grain Net (RGN): An alternative method for estimating mean kinematic vorticity number (W_m): Journal of Structural Geology, v. 29, no. 3, p. 411-421.

Jessup, M. J., Newell, D. L., Cottle, J. M., Berger, A. L., and Spotila, J. A., 2008, Orogen-parallel extension and exhumation enhanced by focused denudation in Arun River gorge, Ama Drime Massif, Tibet-Nepal: Geology, v. 36, p. 587-590.

Jiang, D., 1998, Forward modeling of non-steady-state deformations and the 'minimum strain path': Discussion: Journal of Structural Geology, v. 20, p. 975-977.

Kapp, P., and Guynn, J. H., 2004, Indian punch rifts Tibet: Geology, v. 32, no. 11, p. 993-996.

Kruhl, J. H., 1998, Reply: Prism- and basal-plane parallel subgrain boundaries in quartz: a microstructural geothermometer: Journal of Metamorphic Geology, v. 16, p. 142-146.

Langille, J., Jessup, M., Cottle, J., Newell, D., and Seward, G., 2010, Kinematics of the Ama Drime Detachment: Insights into orogen-parallel extension and exhumation of the Ama Drime Massif, Tibet-Nepal: Journal of Structural Geology, v. 32, p. 900-919.

Law, R. D., 1990, Crystallographic fabrics: a selective review of their applications to research in structural geology: Geological Society [London] Special Publications, v. 54, no. 1, p. 335-352.

Law, R. D., Searle, M. P., and Simpson, R. L., 2004, Strain, deformation temperatures and vorticity of flow at the top of the Greater Himalayan Slab, Everest Massif, Tibet: Journal of the Geological Society, v. 161, p. 305-320.

Mainprice, D., Bouchez, J.-L., Blumenfeld, P., and Tubia, J. M., 1986, Dominant c slip in naturally deformed quartz: Implications for dramatic plastic softening at high temperature: Geology, v. 14, p. 819-822.

Murphy, M. A., and Copeland, P., 2005, Transtensional deformation in the central Himalaya and its role in accommodating growth of the Himalayan Orogen: Tectonics, v. 24, no. 4, p. 19.

Murphy, M. A., Saylor, J., and Ding, L., 2009, Late Miocene topographic inversion in southwest Tibet based on integrated paleoelevation reconstructions in structural history: Earth and Planetary Science Letters, v. 282, p. 1-9.

Murphy, M. A., Yin, A., Kapp, P., Harrison, T. M., Manning, C. E., Ryerson, F. J., Lin, D., and Jinghui, G., 2002, Structural evolution of the Gurla Mandhata detachment system, Southwest Tibet; implications for the eastward extent of the Karakoram fault system: Geological Society of America Bulletin, v. 114, no. 4, p. 428-447.

Nelson, K., Zhao, L., Che, J., Liu, X., Klemperer, Y., et al., 1996, Partially molten middle crust beneath southern Tibet: Synthesis of project INDEPTH results: Science, v. 274, p. 1684-1688.

Passchier, C. W., 1987, Stable positions of rigid objects in non-coaxial flow—a study in vorticity analysis: Journal of Structural Geology, v. 9, p. 679-690.

Passchier, C. W., 1988, The use of Mohr circles to describe non-caxial progressive deformation: Tectonophysics, v. 149, p. 323-338.

Powell, R., and Holland, T., 1994, Optimal geothermometry and geobarometry: American Mineralogist, v. 79, p. 120-133.

Stipp, M., Stunitz, H., Heilbronner, R., and Schmid, S., 2002, Dynamic recrystallization of quartz: correlation between natural and experimental conditions, *in* De Meer, S., Drury, M. R., De Bresser, J. H. P., and Pennock, G. M., eds., Deformation Mechanisms, Rheology and Tectonics: Current Status and Future Perspectives: Geological Society [London] Special Publications, v. 200, p. 171-190.

Taylor, M., Yin, A., Ryerson, F., Kapp, P., and Ding, L., 2002, Conjugate strike-slip faulting along the Bangong-Nujiang suture zone accomodates coeval east-west extension and north-south shortening in the interior of the Tibean Plateau: Tectonics, v. 22, p. 1-25.

Thiede, R. C., Arrowsmith, J. R., Bookhagen, B., McWilliams, M., Sobel, E. R., and Strecker, M. R., 2006, Dome formation and extension in the Tethyan Himalaya, Leo Pargil, northwest India: Geological Society of America Bulletin, v. 118, no. 5-6, p. 635-650.

Tikoff, B., and Fossen, H., 1995, The limitations of three-dimensional kinematic vorticity analysis: Journal of Structural Geology, v. 17, p. 1771-1784.

Vannay, J. C., and Grasemann, B., 2001, Himalayan inverted metamorphism and syn-convergence extension as a consequence of a general shear extrusion: Geological Magazine, v. 138, no. 3, p. 253-276.
Wallis, S.R., 1995, Vorticity analysis and recognition of ductile extension in the Sanbagawa belt, SW Japan: Journal of Structural Geology, v. 17, p. 1077-1093.
Wallis, S. R., Platt, J. P., and Knott, S. D., 1993, Recognition of syn-convergence extension in accretionary wedges with examples from the Calabrian Arc and the Eastern Alps: American Journal of Science, v. 293, p. 463-495.
Xypolias, P., 2009, Some new aspects of kinematic vorticity analysis in naturally deformed quartzites: Journal of Structural Geology, v. 31, p. 3-10.
Zhang, J., Ding, L., Zhong, D., and Yong, Z., 2000, Orogen-parallel extension in Himalaya: Is it the indicator of collapse or the product in process of compressive uplift?: Chinese Science Bulletin, v. 45, p. 114-120.

CHAPTER I:
KINEMATIC EVOLUTION OF THE AMA DRIME DETACHMENT: INSIGHTS INTO OROGEN-PARALLEL EXTENSION AND EXHUMATION OF THE AMA DRIME MASSIF, TIBET-NEPAL

A version of this chapter was originally published by Jackie Langille, Micah Jessup, John Cottle, Dennis Newell, and Gareth Seward:

Langille, J., Jessup, M., Cottle, J., Newell, D., and Seward, G., 2010, Kinematic evolution of the Ama Drime detachment: Insights into orogen-parallel extension and exhumation of the Ama Drime Massif, Tibet-Nepal: Journal of Structural Geology, v. 32, p. 900-919.

My major contributions to this paper include: (1) conducting the kinematic and deformation temperature analyses that are included in the manuscript, (2) writing the manuscript, (3) creating most of the illustrations, and (4) submitting and revising the manuscript.

Abstract

The Ama Drime Massif is a north-south trending antiformal structure located on the southern margin of the Tibetan Plateau that is bound by the Ama Drime and Nyönno Ri detachments on the western and eastern sides, respectively. Detailed kinematic and vorticity analyses were combined with deformation temperature estimates on rocks from the Ama Drime detachment to document spatial and temporal patterns of deformation. Deformation temperatures estimated from quartz and feldspar microstructures, quartz [c] axis fabrics, and two-feldspar geothermometry of asymmetric strain-induced myrmekite range between ~400 and 650 ° C. Micro- and macro-kinematic indicators suggest west-directed displacement dominated over this temperature range. Mean kinematic vorticity estimates record early pure shear dominated flow (49-66% pure shear) overprinted by later simple shear (1-57% pure shear), high-strain (36-50% shortening and 57-99% down-dip extension) dominated flow during the later increments of ductile deformation. Exhumation of the Massif was accommodated by at least ~21-42 km of displacement on the Ama Drime detachment. Samples from the Nyönno Ri detachment were exhumed from similar depths. This study suggests that exhumation on the Nyönno Ri detachment during initiation of orogen-parallel extension (11-13 Ma) resulted in a west-dipping structural weakness in the footwall that reactivated as the Ama Drime detachment.

Introduction

Continental collision between the Indian and Asian plates from the Eocene to Holocene resulted in profound crustal shortening and thickening that produced the Himalaya and Tibetan Plateau. Previous studies (e.g., Hodges et al., 1992, 2001; Grujic et al., 1996, 2002; Vannay and Grasemann, 1998; Grasemann et al., 1999; Grujic, 2006) have largely focused on the southward propagation or extrusion of the Greater Himalayan Series (GHS) from the Eocene to middle Miocene during continental convergence (Fig. 1.1). Southward flow was accommodated by coeval movement on the South Tibetan detachment system (STDS) on top of the GHS and the Main Central thrust zone (MCTZ) at the bottom (Fig. 1.1) (Nelson et al., 1996; Searle et al., 2006).

After the middle Miocene, a transition from south-directed mid-crustal flow to orogen-parallel extension occurred in the Himalaya that resulted in the formation of north-south striking normal faults, graben, and domes that often offset or reactivate the STDS and/or the MCTZ (Fig. 1.2) (Murphy et al., 2002; Kapp and Guynn, 2004; Murphy and Copeland, 2005; Thiede et al.,

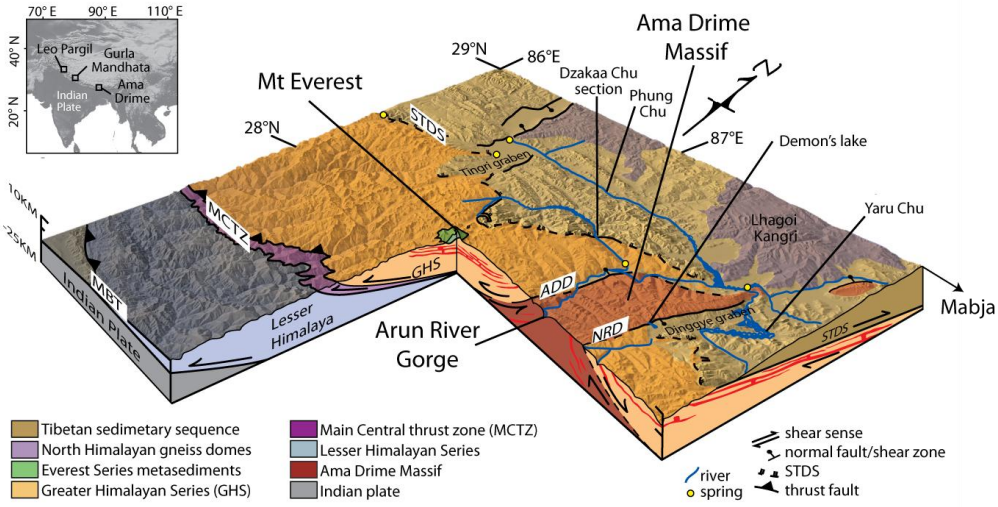

Figure 1.1. *Simplified interpretive block diagram of the Everest region. STDS, South Tibetan detachment system; MBT, Main Boundary thrust; MHT, Main Himalayan thrust; ADD, Ama Drime detachment; NRD, Nyönno Ri detachment. After Jessup et al. (2008a) and Searle et al. (2006).*

2005, 2006; Jessup et al., 2008a; Jessup and Cottle, 2010). Structural, geochronologic, and thermochronometric data from the Leo Pargil dome, the Gurla Mandhata core complex, and the Ama Drime Massif (ADM) demonstrate that faults and shear zones that accommodated crustal shortening (i.e. the STDS and MCTZ) between the Eocene and early Miocene are now inactive and are therefore no longer capable of accommodating south-directed mid-crustal flow (Cottle et al., 2007; Murphy, 2007).

The ADM is a ~30 km-wide north-south striking antiformal structure that narrows towards the north and is located ~50 km northeast of Mount Everest. It is bound by the north-south striking Nyönno Ri detachment (NRD) on the eastern flank and the north-south trending Ama Drime detachment (ADD) on the western flank (Figs. 1.1 and 1.2) (Jessup et al., 2008a). To the north, the NRD transitions into the Xainza-Dinggyê graben that offsets the STDS (Burchfiel et al., 1992; Zhang and Guo, 2007) and is kinematically linked to east-west extension in the interior of the plateau (Taylor et al., 2003). Structural, petrologic, and geochronologic data indicate that the antiformal structure of the ADM is the result of evolving mid-crustal flow along the southern margin of the Tibetan Plateau (Jessup et al., 2008a; Cottle et al., 2009a). This study presents new kinematic, microstructural, and vorticity data from three transects across the ADD on the western flank of the ADM along with one transect from the NRD on the eastern flank. These data provide new constraints on the role of strain partitioning and shear zone development associated with orogen-parallel extension in a convergent setting. These new data are integrated with existing data to propose a model for the evolution of the ADM.

Geologic Setting

Regional Geology

The geology in the Mount Everest region, southwest of the ADM can be grouped into three main fault-bounded litho-tectonic units. In order of increasing structural position these include (from south to north); the Lesser Himalayan series (LHS), the GHS, and the Tibetan Sedimentary series (TSS). These units are separated by three north dipping fault systems; the Main Boundary thrust (MBT), the MCTZ, and the STDS (Fig. 1.1). The MCTZ and the MBT are inferred, based

Figure 1.2. *(a) Geologic map of the Ama Drime Massif (Jessup et al., 2008c) and Mount Everest (Jessup et al., 2008b) including structural data and sample locations. Modified after Jessup et al. (2008a,b). Aside from the Nyönno Ri detachment (NRD), data from the eastern side is after Burchfiel et al. (1992). Structural data at the nose of the Massif, the NRD, and the Sangkar Fault after Kali et al. (2010). Everest data and map from Jessup et al. (2008b), Hubbard (1989), Murphy and Harrison (1999) and, Searle et al. (2003). Nyönno Ri Boundary after Kali et al. (2010). ADD, Ama Drime detachment. (b) Location map of the Yo Ri 1 and Yo Ri 2 transect samples. (c) Location map of the Sharka transect samples. (d) Location map of the Pung Chu transect samples. (e) Location map of Demon's Lake and Dzong Tso transect samples. Arial imagery in (b) through (e) from Google. (f) Geologic cross section through the Ama Drime Massif. Cross section location shown in (a). Not the same scale as the map. Modified from Jessup et al. (2008a).*

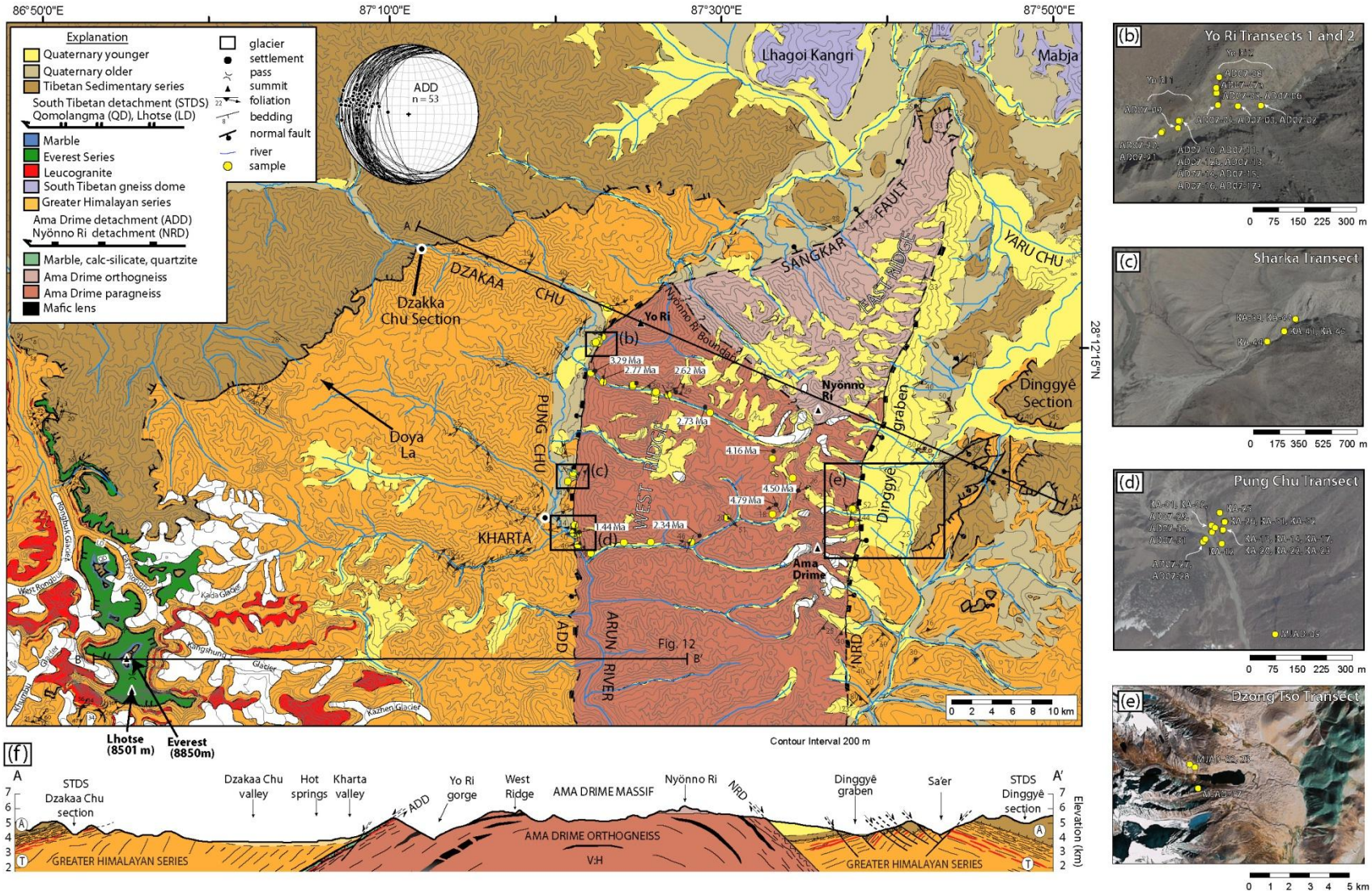
86°50'0"E
87°10'0"E
87°30'0"E
87°50'0"E
28°12'15"N
Explanation
Quaternary younger
Quaternary older
Tibetan Sedimentary series
South Tibetan detachment (STDS)
Qomolangma (QD), Lhotse (LD)
Marble
Everest Series
Leucogranite
South Tibetan gneiss dome
Greater Himalayan series
Ama Drime detachment (ADD)
Nyönno Ri detachment (NRD)
Marble, calc-silicate, quartzite
Ama Drime orthogneiss
Ama Drime paragneiss
Mafic lens
glacier
settlement
pass
summit
foliation
bedding
normal fault
river
sample
ADD
n = 53
Lhagoi Kangri
Mabja
DZAKAA CHU
Dzakka Chu Section
Doya La
PUNG CHU
Yo Ri
Nyönno Ri Boundary
SANGKAR FAULT
EAST RIDGE
YARU CHU
Nyönno Ri
Dinggyê graben
Dinggyê Section
WEST RIDGE
KHARTA
Ama Drime
ADD
ARUN RIVER
NRD
Fig. 12
B'
3.29 Ma
2.77 Ma
2.62 Ma
2.73 Ma
4.16 Ma
4.50 Ma
4.79 Ma
1.44 Ma
2.34 Ma
(b)
(c)
(d)
(e)
Lhotse (8501 m)
Everest (8850m)
0 2 4 6 8 10 km
Contour Interval 200 m
(f)
A
A'
STDS Dzakaa Chu section
Dzakaa Chu valley
Hot springs
Kharta valley
ADD
Yo Ri gorge
West Ridge
AMA DRIME MASSIF
Nyönno Ri
NRD
Dinggyê graben
Sa'er
STDS Dinggyê section
AMA DRIME ORTHOGNEISS
V:H
GREATER HIMALAYAN SERIES
GREATER HIMALAYAN SERIES
Elevation (km)
(b)
Yo Ri Transects 1 and 2
0 75 150 225 300 m
(c)
Sharka Transect
0 175 350 525 700 m
(d)
Pung Chu Transect
0 75 150 225 300 m
(e)
Dzong Tso Transect
0 1 2 3 4 5 km

on geophysical data, to sole into the Main Himalayan thrust (MHT) to the north beneath the Tibetan Plateau (Nelson et al., 1996; Searle et al., 2006). Below the MHT (35-75 km) the lower crust is composed of Archean Indian shield granulite facies rocks (Searle et al., 2006).

The 20 km-thick LHS, bound between the MBT below and the MCTZ above, consists of Paleo- to Mesoproterozoic metamorphosed clastic sediments and gneiss (Brookfield, 1993; Pognante and Benna, 1993; Goscombe et al., 2006). The Neoproterozoic to Cambrian GHS is bound at the base by the MCTZ and at the top by the STDS. The upper GHS is separated from the lower GHS by the High Himalayan thrust (HHT) (Goscombe et al., 2006). The lower GHS is bound between the HHT and the base of the MCTZ. The upper GHS structurally overlies metapelitic schists and the Ulleri and Num orthogneisses in the lower GHS (within the MCTZ) (Searle et al., 2008). In contrast, others (e.g., Goscombe et al., 2006) place the Ulleri orthogneiss in the LHS. The GHS is composed of a ~28 km-thick section of metapelitic rocks, augen gneiss, calc-silicates, and marble that was metamorphosed to amphibolites facies and intruded by Miocene sills and dikes (Hodges, 2000; Searle et al., 2003; Viscupic et al., 2005).

South of Mount Everest, in the Dudh Kosi drainage, the maximum age for movement along the MCTZ is constrained by $^{40}Ar/^{39}Ar$ hornblende and $^{208}Pb/^{232}Th$ monazite geochronology and indicates that amphibolite-facies metamorphism of hanging wall rocks occurred at 22 ± 1 Ma (Hubbard and Harrison, 1989) and potentially as early as 24-29 Ma (Catlos et al., 2002). The GHS in the Everest region experienced an early kyanite-grade event (550-560° C and 0.8-1.0 GPa) at 38.9 ± 0.9 Ma that is a record of crustal thickening (Cottle et al., 2009b). Kyanite-grade metamorphism was overprinted by a high-temperature low-moderate-pressure sillimanite-grade event (650-750° C and 0.4-0.7 GPa) associated with decompression melting and granite emplacement between 28.0 and 22.6 Ma (Pognante and Benna, 1993; Simpson et al., 2000; Viskupic et al., 2005; Jessup et al., 2008b; Cottle et al., 2009b). $^{40}Ar/^{39}Ar$ biotite ages from the GHS are <14 Ma, suggesting that metamorphism in the interior portion of the GHS had ceased by this time (Viskupic et al., 2005).

Timing constraints on the STDS in the Mount Everest region suggest that the system was active from 20 Ma until 18-13 Ma (Hodges et al., 1992; Murphy and Harrison, 1999; Searle et al., 2003; Cottle et al., 2011). In the Dzakaa Chu section of the STDS (Figs. 1.1 and 1.2), U-Th-Pb geochronology conducted on a leucogranite dike that crosscuts the mylonitic fabric within the

lower part of the STDS suggests that fabric development in this section of the shear zone occurred at <20 Ma (Cottle et al., 2007). In the Dinggyê graben, the ductile portion of the footwall rocks ~100 m below the STDS brittle detachment were active until ~15-16 Ma (Leloup et al., 2010).

The structurally highest unit, the TSS, consists of Proterozoic to Jurassic pre-, syn-, and post-rift sedimentary rocks, a Jurassic to Cretaceous passive continental margin sedimentary sequence, and an upper Cretaceous to Eocene syn-collisional sedimentary sequence (Gansser, 1964; Le Fort, 1975; Gaetani and Garzanti, 1991; Brookfield, 1993; Liu and Einsele, 1994; Garzanti, 1999). Middle Miocene to Holocene north-south-striking normal faults cut these older structures forming a series of graben that are characteristic of the southern Tibetan Plateau (e.g., Armijo et al., 1986; Wu et al., 1998; Stockli et al., 2002; Taylor et al., 2003; Dewane et al., 2006; Hager et al., 2006; Zhang and Guo, 2007).

Geology of the Ama Drime Massif

The Ama Drime Massif (ADM) is a north-trending antiformal structure that is composed of the Ama Drime orthogneiss to the south and the Ama Drime paragneiss to the north (Fig. 1.2) (Kali et al., 2010) that are separated by the relatively unexplored Nyönno Ri Boundary (Fig. 1.2) (Kali et al., 2010). The western flank of the ADM is defined by the ~100-300 m-thick, west-dipping ADD that is composed of schist, leucogranite, calc-silicate, quartzite, and marble that records solid-state fabric development (Jessup et al., 2008a). The shear zone separates migmatitic orthogneiss of the GHS in the hanging wall from the granulite facies (750° C and 0.7-0.8 GPa), migmatitic Ama Drime orthogneiss in the footwall (Fig. 1.3a, b, and c) (Jessup et al., 2008a; Cottle et al., 2009a). The shear zone rocks record polyphase folding of a pervasive foliation that is interpreted to record earlier deformation associated with movement on this contact (Jessup et al., 2008a). Rocks within the shear zone preserve a well-developed S-C fabric with a down-dip stretching lineation and are locally folded. Layers of ultra-mylonite are parallel to the main mylonitic fabric (Fig. 1.3d). These ductile features are offset by at least one brittle detachment (Fig. 1.3e) filled with fault gouge. Veins of pseudotachylite truncate the mylonitic fabric at high angles and contain fragments of the host rock (Fig. 1.3f). $^{40}Ar/^{39}Ar$ biotite ages

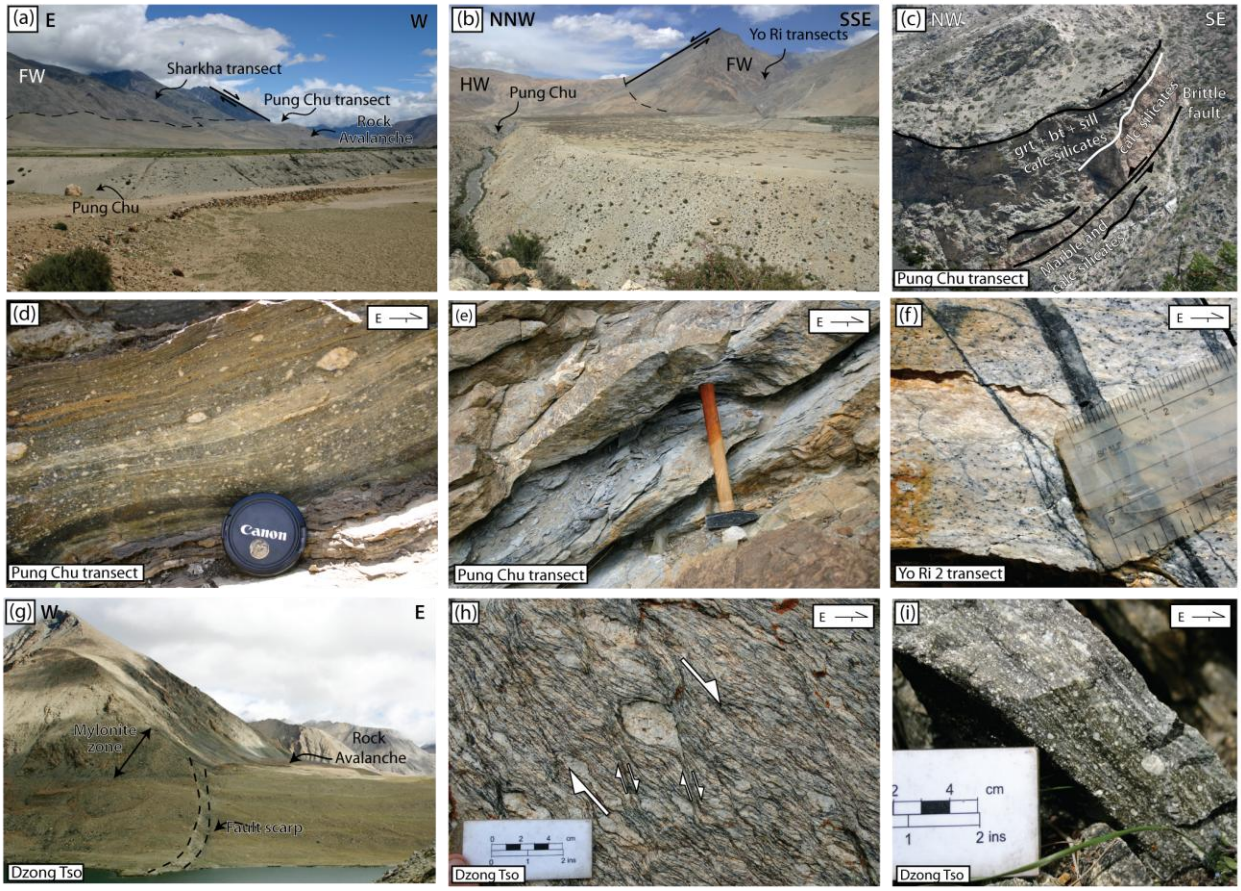

Figure 1.3. *Field photographs. (a) View of the Pung Chu and Sharka transects looking south. FW, footwall. (b) View of the Yo Ri transects looking northeast. (c) Exposure of the ADD shear zone exposed in the Pung Chu transect. Black lines represent the shear zone boundary and brittle faults. White lines represent lithologic contacts. (d) Example of a mylonitic calc-silicate exposed within the Pung Chu transect that records top-to-the-west sense of shear. (e) Brittle fault filled with fault gouge exposed within the Pung Chu transect. (f) Pseudotachylite within leucogranite near the Yo Ri 2 transect. (g) View of a fault scarp offsetting Quaternary deposits, looking north from Dzong Tso (Demon's Lake) on the eastern flank of the ADM. (h) Augen gneiss on the eastern limb of the ADM exposed north of Demon's Lake. Asymmetric tails indicate top-to-the-east sense of shear. (i) Mylonite containing feldspar porphyroclasts exposed along the NRD.*

from the mylonitic footwall suggest that the ADD was active between 10-6 Ma (Kali et al., 2010). Toward the north, the ADD transitions into the Sangkar fault (~12 Ma $^{40}Ar/^{39}Ar$ muscovite age) and eventually to the nose of the ADM (the hinge of the antiform) where faults have a minimum displacement (Fig. 1.2) (Kali et al., 2010).

The south-central portion of the ADM is composed of Ama Drime orthogneiss that is variably migmatized (12.8 ± 0.2 Ma) and dominated by melt-present deformation features (Cottle et al., 2009a; Kali et al., 2010). Protolith ages for the Ama Drime orthogneiss (1799 ± 9 Ma) may correlate to the Ulleri orthogneiss that is interpreted to be at the base of GHS, below the HHT in the hanging wall of the MCTZ (Cottle et al., 2009a; Searle et al., 2008), or in the underlying LHS (e.g., Goscombe et al., 2006). Mafic lenses cored by granulitized eclogite are surrounded by orthogneiss that experienced muscovite dehydration melting (Lombardo et al., 1998; Lombardo and Rolfo, 2000; Groppo et al., 2007; Guillot et al., 2008) and anatexis at <13.2 ± 1.4 Ma (Cottle et al., 2009a). Melt-filled fractures that break a boudinaged mafic lens were emplaced at 11.6 ± 0.4 Ma and record top-to-the-west shearing during the initial stages of orogen-parallel extension (Jessup et al., 2008a; Cottle et al., 2009a). Other mafic layers are cross-cut by pegmatite dikes (9.8 ± 1.2 Ma) on the eastern side of the interior portion of the ADM (Kali et al., 2010). Exhumation rates of 2.2 ± 0.2 mm/yr from 0.7-0.8 GPa between ~13-2 Ma (Cottle et al., 2009a) were accommodated by the development of the ADD and NRD during orogen-parallel extension. (U-Th)/He apatite ages from the central portion of the ADM define an exhumation rate of ~1 mm/yr between 1.4 and 4.2 Ma that records continued exhumation with movement on the ADD and NRD (Jessup et al., 2008a; Kali et al., 2010).

The NRD is composed of a system of shear zones and faults that occur within the Ama Drime orthogneiss and paragneiss and defines the eastern limb of the ADM (Jessup et al., 2008a). Hanging wall rocks have been removed by normal faulting in the Dinggyê graben. 1-km-tall triangular facets extend above Dzong Tso where moraine deposits are offset by a fault scarp with ~5 m of throw and an apparent normal displacement (Jessup et al., 2008a) (Fig. 1.3g). A decrease in the height of the triangular facets toward the north is interpreted as evidence for decrease in displacement along the NRD towards the north (Kali et al., 2010).

Footwall rocks record a steepening of the main foliation 25-45° towards the shear zone where they preserve a mylonite zone with a pervasive S-C fabric and down-dip stretching lineation that records top-to-the-east sense of shear (Burchfiel et al., 1992; Jessup et al., 2008a). Near Dzong Tso (Demon's Lake), footwall rocks are well-exposed and contain a ~100-300-m-thick mylonite zone that strikes north-south, dips ~45° east, and preserves a down-dip stretching lineation (Fig. 1.3g) (Jessup et al., 2008a). Migmatitic orthogneiss exposed at deeper structural

positions record melt-present high temperature fabric development. At structurally shallower positions, feldspar grains begin to act as semi-rigid bodies suggesting deformation at moderate temperatures (Fig. 1.3h). Rigid feldspar porphyroclasts suspended in a fine-grained matrix of aligned recrystallized quartz and phyllosilicates mark narrow zones of mylonite and ultramylonite that are subparallel to the main shear zone fabric (Fig. 1.3i). An undeformed leucogranite dike (11 ± 0.4 Ma) that crosscuts the NRD footwall mylonites provides a minimum age for fabric development (Kali et al., 2010). $^{40}Ar/^{39}Ar$ muscovite and biotite ages of 10-13 Ma indicate the onset of east-west extension and exhumation after the cessation of movement on the STDS in this region (Zhang and Guo, 2007; Leloup et al., 2010; Kali et al., 2010; Jessup and Cottle, 2010).

Shear Sense Indicators

Oriented samples were collected from three transects across the ADD and one from the NRD. Along the ADD, from north to south these transects include the Yo Ri (1 and 2), the Sharkha, and the Pung Chu transects (Fig. 1.2). The Dzong Tso transect crosses the NRD on the eastern limb of the range (Fig. 1.2e). Samples were cut parallel to the lineation and perpendicular to the foliation (XZ section). C- and C'-type shear bands (Fig. 1.4a), mica fish (Fig. 1.4a), σ-and δ-type asymmetric tails on porphyroclasts (Fig. 1.4b and c), oblique quartz grain shape foliation (Fig. 1.4d), shear folds, and offset porphyroclasts (Fig. 1.4e) were used to determine the spatial distribution of shear sense in samples collected from three transects across the ADD and one across the NRD.

Electron backscatter diffraction (EBSD) analysis was used to generate quartz lattice-preferred orientation (LPO) diagrams, from which the asymmetry of the [c] and <a> axes patterns with respect to the foliation and lineation was also used to determine shear sense (Fig. 1.5a) (e.g., Lister and Hobbs, 1980; Law, 1990). Diffraction patterns were collected using an FEI Quanta 400 FEG scanning electron microscope coupled with a HKL Nordlys 2 EBSD camera at the University of California, Santa Barbara. CHANNEL 5 HKL software was used to index the

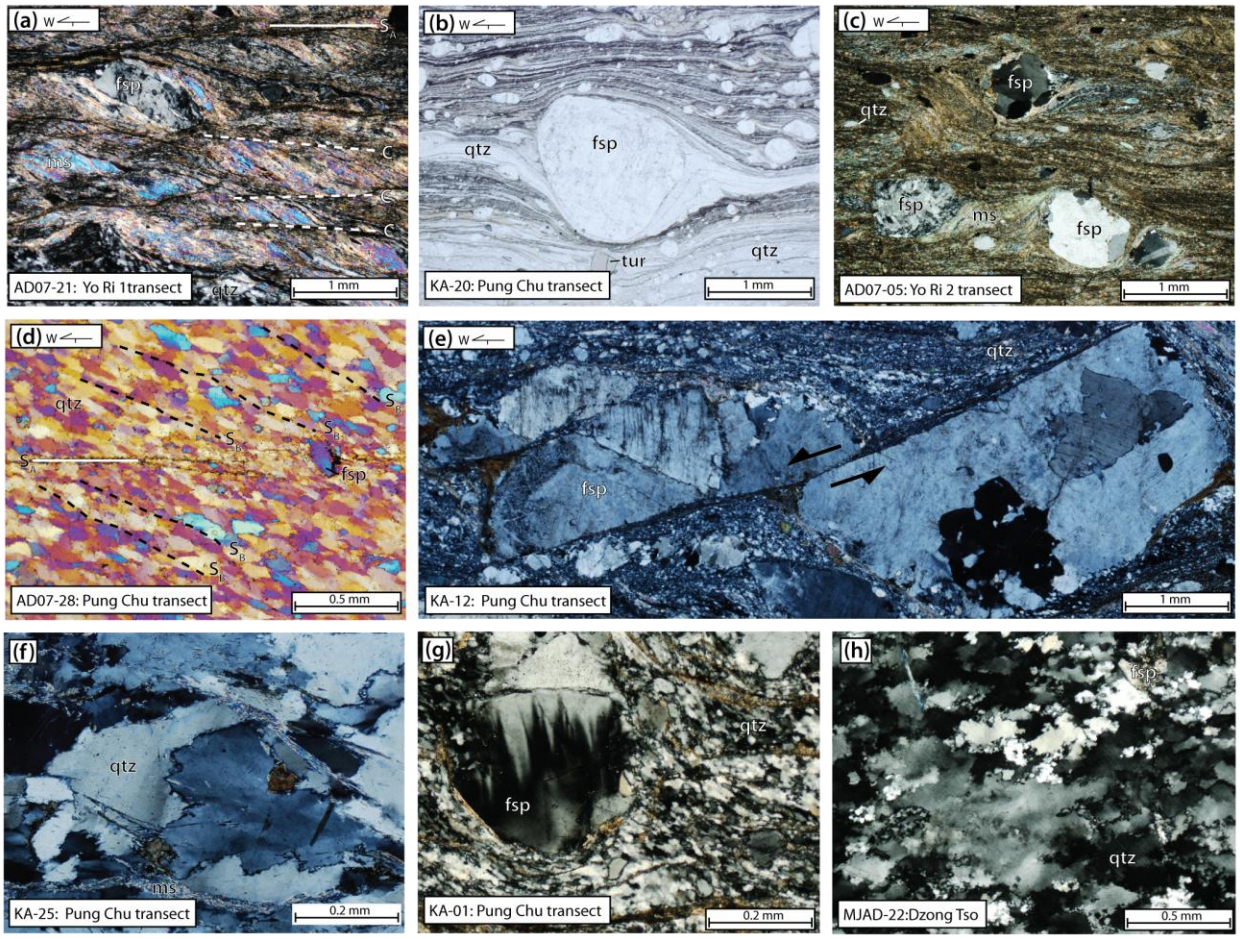

Figure 1.4. *Photomicrographs of representative kinematic indicators from the ADD transects, (a) through (e), and quartz and feldspar deformation textures, (f) through (h). (a) Mica fish that record top-to-the-west sense of shear; cross polars. S_A, main foliation; C, C-type shear bands; fsp, feldspar; ms, muscovite. (b) δ-type strain shadow on a feldspar porphyroclast indicating top-to-the-west sense of shear; plane light. qtz, quartz; tur, tourmaline. (c) σ-type strain shadows on feldspar porphyroclasts indicating top-to-the-west sense of shear, cross polars. (d) Quartz grain shape foliation (S_B) indicating top-to-the-west sense of shear; cross polars with gypsum plate inserted. (e) Offset feldspar porphyroclast suggesting top-to-the-west sense of shear; cross polars. (f) Quartz exhibiting bulging (BLG) recrystallization at quartz grain boundaries indicating deformation temperatures of 280-400° C overprinting a higher temperature fabric, cross polars. (g) Quartz exhibiting sub-grain rotation (SGR) recrystallization indicating deformation temperatures between 400-500° C. Flame perthite in a rigid feldspar porphyroclast also indicates deformation temperatures between 400-500° C; cross polars. (h) Quartz exhibiting grain-boundary migration (GBM) recrystallization indicating deformation temperatures of 500-650° C; cross polars.*

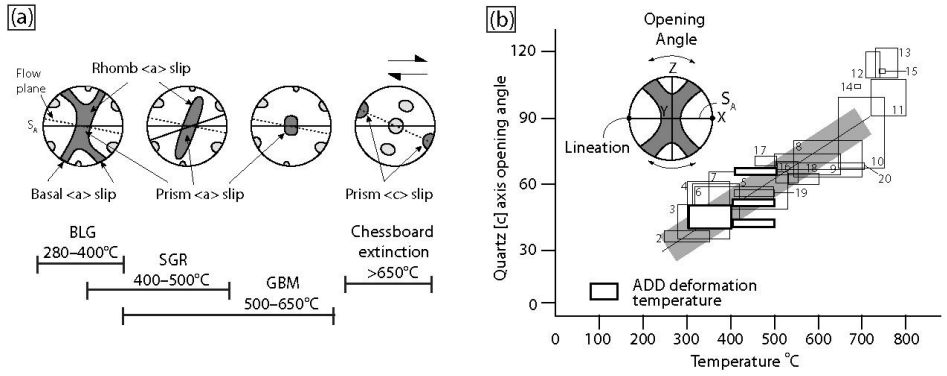

Figure 1.5. *Interpretation of quartz lattice-preferred orientation (LPO) data. (a) Simplified stereonets showing the dependence of quartz LPOs and inferred slip systems on increasing temperature during noncoaxial deformation and plane strain (see text). [c] axes are shown in dark grey and <a> axes in light grey. Modified from Passchier and Trouw (2005). (b) Relationship between [c] axis opening angle and temperature. Grey line is the best fit line with ± 50° C error. X, Y, and Z strain axes are shown. Boxes 1-15: from Kruhl (1998); 16: Law et al. (1992); 17: Nyman et al. (1995); 18: Okudaira et al. (1995); 19-20: Langille et al. (2010). Data from this study are shown. Modified from Law et al. (2004).*

quartz diffraction patterns that were obtained using a Hough resolution of 80, detecting 7-8 bands with standard divergence, and a quartz structure file containing 60 reflectors.

Results

The Pung Chu transect is the southernmost transect across the ADD and contains marble, schist, calc-silicate, leucogranite, and quartzite (Fig. 1.2d). δ- and σ-type asymmetric tails on feldspar (Fig. 1.4b) and diopside porphyroclasts, mica fish, oblique quartz grain shape foliation (Fig. 1.4d), C- and C'-type shear bands, offset porphyroclasts (Fig. 1.4e), and quartz LPO patterns (Fig. 1.6a) preserved in samples from this transect (Figs. 1.2b and 1.4a) consistently record top-to-the-west shear sense (Table 1.1). Samples AD07-27 and MJAD-05 are exceptions to this trend and exhibit σ-type strain shadows, C'-type shear bands, mica fish, and quartz [c] and <a> axis LPO patterns which indicate top-to-the-east sense of shear (Fig. 1.6a; Table 1.1). MJAD-05 was collected ~1 km from the remainder of the Pung Chu samples in an ultra-mylonite zone that dips steeply to the east (355°, 72°E), contains a down dip stretching lineation, and records top-to-the-east displacement. This is the only steeply dipping mylonite zone that was

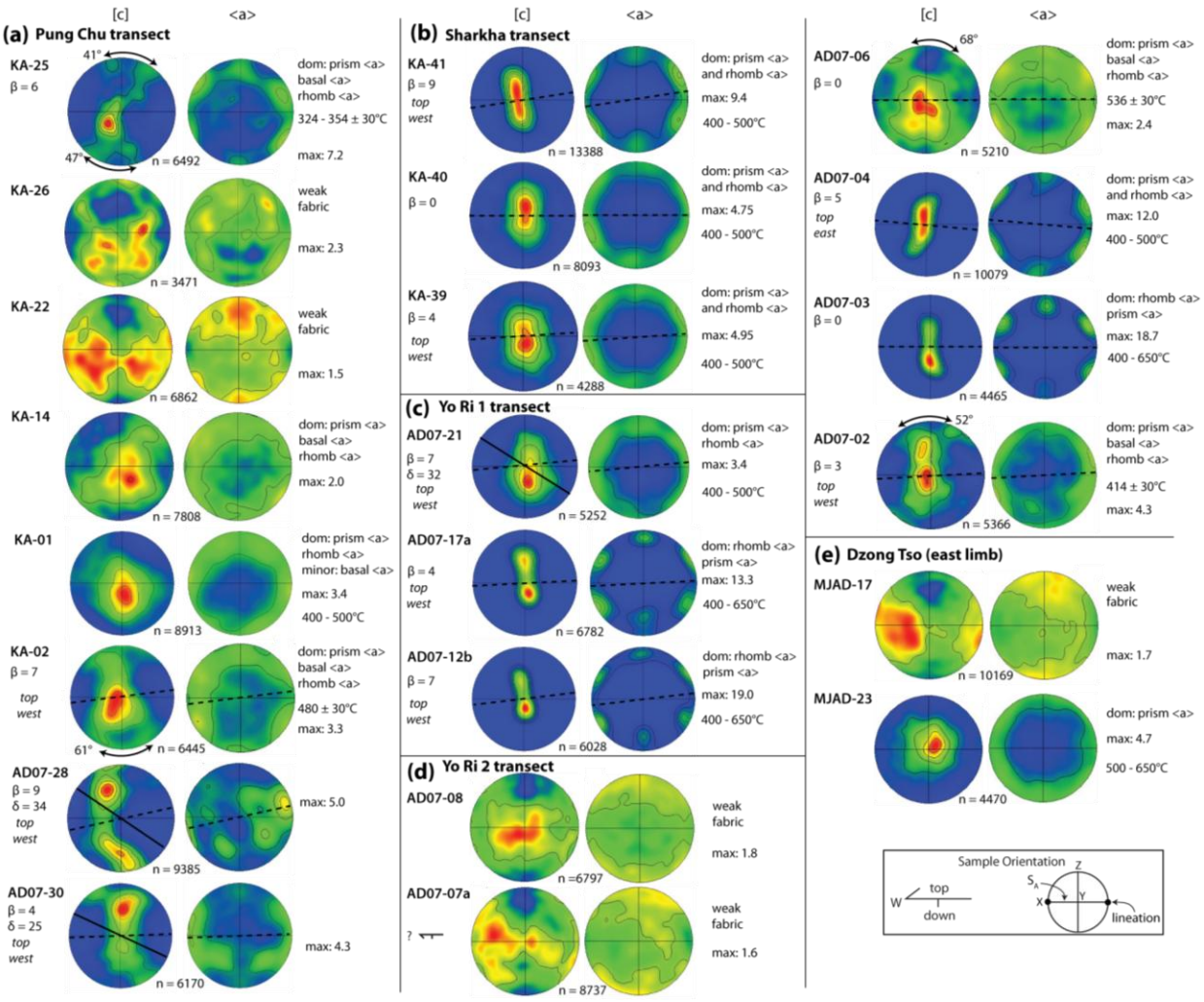

Figure 1.6. *Quartz LPO data in order of increasing structural depth for the (a) Pung Chu, (b) Sharka, (c) Yo Ri 1, (d) Yo Ri 2, and (e) Dzong Tso transects. Upper hemisphere [c] and <a> axis stereonet plots shown. Opening angle and corresponding deformation temperature, quartz texture derived deformation temperature, flow plane (dashed line), quartz grain shape foliation (S_B, solid line), angle between foliation (S_A) and flow plane (β), angle between S_A and S_B (δ), shear sense, quartz slip systems, and number (n) of quartz grains measured noted. All plots oriented as indicated in the sample orientation box. Data are point-per grain; contouring based on mean uniform density (m.u.d.) with maximum (max) values indicated.*

Table 1.1. Summary of Shear Sense, Vorticity, and Temperature Data.

Sample	Rock type	Shear sense	W_m RGN	W_m GSF	R_{xz}	Deformation temperature (° C)	Temperature Indicator[d]
Pung Chu Transect							
KA-25[a]	qtz	t-E[c]	—	—	—	324 ± 30, 354 ± 30, 280–400	o.a., s.s.
KA-31	mbl	—	—	—	—	400–500	—
KA-26[a]	sch	t-W[c]	—	—	—	400–500	—
KA-32	c.s.	—	—	—	—	400–500	—
KA-17	mbl	t-W[c]	0.60–0.65	—	—	400–500	—
KA-20	qtz	—	0.56–0.57	—	—	400–500	—
KA-22[a]	c.s.	t-W[c]	0.57–0.63	—	—	400–500	—
KA-23	mbl	t-W[c]	0.54–0.62	—	—	400–500	—
KA-14[a]	c.s.	t-W[c]	0.52–0.58	—	—	400–500	—
KA-13	c.s.	t-W[c]	0.56–0.59	—	—	400–500	—
KA-01[a]	qtz	t-W[c]	0.69–0.72	—	—	400–500	s.s.
KA-02[a]	qtz	t-W[b], t-W[c]	0.52–0.55	—	—	480 ± 30, 400–500	o.a., s.s.
KA-12	qtz	t-W[c]	0.53–0.61	—	—	400–500	—
AD07-28[a]	qtz	t-W[b], t-W[c]	0.57–0.59	0.93–0.99	10.6–24	400–500	—
AD07-29a	c.s.	—	—	—	—	400–500	—
AD07-29b	c.s.	t-W[c]	—	—	—	400–500	—
AD07-30[a]	qtz	t-W[b], t-W[c]	0.54–0.61	0.62–0.84	6.4–19.2	400–500	—
AD07-31	qtz	t-W[c]	—	—	—	400–500	—
AD07-27	c.s.	t-E[c]	—	—	—	400–500	—
MJAD-05	c.s.	t-E[c]	—	—	—	400–500	—
Sharka Transect							
KA-44	c.s.	t-W[c]	0.50–0.58	—	—	400–500	—
KA-41[a]	c.s.	t-W[b], t-W[c]	0.55–0.59	—	—	400–500	—
KA-43	qtz	—	—	—	—	400–500	—
KA-39[a]	leuc	t-W[b], t-W[c]	—	—	—	400–500	—
KA-40[a]	c.s.	t-W[c]	0.57–0.61	—	—	369–435, 400–500	f.g.

Table 1.1. Continued.

Sample	Rock type	Shear sense	W_m RGN	W_m GSF	R_{xz}	Deformation temperature (° C)	Temperature Indicator[d]
Yo Ri 1Transect							
AD07-20	qtz	t-W[c]	—	—	—	400–500	—
AD07-21[a]	qtz	t-W[b], t-W[c]	0.57–0.64	0.74–0.98	6.7–24	400–500	s.s.
AD07-17a[a]	qtz	t-W[b], t-W[c]	—	—	—	400–650	s.s.
AD07-16	qv	—	—	—	—	400–500	—
AD07-15	qv	t-E[c]	—	—	—	400–500	—
AD07-14	qv	t-W[c]	—	—	—	400–500	—
AD07-13	qv	t-W[c]	—	—	—	400–500	—
AD07-12b[a]	qv	t-W[b], t-W[c]	—	—	—	400–650	s.s.
AD07-10	qv	t-W[c]	—	—	—	400–500	—
AD07-11	qv	t-W[c]	0.52–0.55	—	—	500–650	—
AD07-09	qv	t-W[c]	—	—	—	400–500	—
Yo Ri 2 Transect							
AD07-08[a]	qtz	t-W[c]	0.53–0.60	—	—	500–650	s.s.
AD07-07a	c.s.	—	0.61–0.65	—	—	400–500	—
AD07-05	c.s.	t-W[c]	0.57–0.63	—	—	500–650	—
AD07-06[a]	leuc	t-W[c]	—	—	—	537 ± 30, 400–500	o.a., s.s.
AD07-04[a]	qtz	t-E[b], t-E[c]	—	—	—	400–500	s.s.
AD07-03[a]	qtz	t-W[c]	—	—	—	400–650	s.s.
AD07-02[a]	gns	t-W[b], t-W[c]	—	—	—	414 ± 30, 400–500	o.a., s.s.
Dzong Tso Transect (east limb)							
MJAD-17[a]	c.s.	t-E[c]	—	—	—	400–500	—
MJAD-22	qtz	t-E[c]	—	—	—	500–650	—
MJAD-23[a]	qtz	t-E[c]	—	—	—	500–650	s.s.

Note: See Appendix 1.1 for sample locations. qtz, quartzite; qv, quartz vein; mbl, marble; c.s., calc-silicate; sch, schist; leuc, leucogranites; gns, gneiss; t-E, top-to-the-east; t-W, top-to-the-west. Samples are in order of increasing structural depth per transect.

[a]Sample analyzed with EBSD

[b]Shear sense determined from EBSD-generated quartz LPO data

[c]Shear sense determined from microstructural geometries

[d]All samples utilized quartz and feldspar textures. o.a., opening angle; s.s., quartz LPO slip systems; f.g., feldspar geothermometry.

documented in the more internal portion of the range.

Samples along the Sharkha transect are composed of calc-silicate, quartzite, and deformed leucogranite that contain σ-type asymmetric tails on feldspar porphyroclasts and mica fish that record top-to-the-west sense of shear (Table 1.1). Quartz [c] and <a> LPO axes patterns from samples KA-39 and KA-41 (Fig. 1.6b) also confirm top-to-the-west sense of shear (Table 1.1). σ-type strain shadows on feldspar porphyroclasts and mica fish (Fig. 1.4a) within quartzite and vein quartz along the Yo Ri 1 transect (Fig. 1.2b and 1.3b) record top-to-the-west sense of shear; the exception being AD07-15, which contains σ-type strain shadows on feldspar porphyroclasts and mica fish that indicate top-to-the-east sense of shear (Table 1.1). Quartz [c] and <a> axis LPO patterns from samples AD07-21, AD07-17a, and AD07-12b consistently define top-to-the-west sense of shear (Fig. 1.6c; Table 1.1).

In the Yo Ri 2 transect (Figs. 1.2b and 1.3b), σ-type strain shadows on feldspar and diopside porphyroclasts (Fig. 1.4c), mica fish, C'-type shear bands, and drag folds within quartzite, calc-silicate, gneiss, and deformed leucogranite record top-to-the-west sense of shear. One exception is AD07-04, which has a poorly developed grain shape foliation, mica fish, and a quartz [c] and <a> axis LPO indicating top-to-the-east sense of shear (Fig. 1.6d; Table 1.1). Quartz [c] and <a> axis LPO patterns from sample AD07-02 suggest top-to-the-west sense of shear (Fig. 1.6d; Table 1.1).Within the NRD near Dzong Tso (Fig. 1.2e), σ-type tails on feldspar porphyroclasts, mica fish, quartz grain shape foliation, and drag folds within three samples, two quartzite and one calc-silicate, indicates top-to-the-east sense of shear (Table 1.1).

Deformation Temperatures

Deformation temperatures during the development of the kinematic indicators and quartz LPO fabrics mentioned above were estimated using: (1) recrystallized quartz and feldspar deformation microstructures (e.g., Jessell, 1987; Hirth and Tullis, 1992; Fitz Gerald and Stünitz, 1993; Lloyd and Freeman, 1994; Hirth et al., 2001; Stipp et al., 2002a, b), (2) the opening angle of quartz [c] axis LPOs (Kruhl, 1998; Law et al., 2004), (3) quartz slip systems (e.g., Mainprice et al., 1986; Tullis and Yund, 1992), and (4) two-feldspar geothermometry (Stormer, 1975;

Whitney and Stormer, 1977; Simpson and Wintsch, 1989).

Quartz and Feldspar Microstructures

Quartz exhibits bulging recrystallization (BLG) at temperatures of 280-400° C (Stipp et al., 2002a, b) (Fig. 1.4f), sub-grain rotation recrystallization (SGR) at temperatures of 400-500° C (Stipp et al., 2002a, b) (Fig. 1.4g), and grain boundary migration recrystallization (GBM) (Fig. 1.4h) at temperatures >500° C (Stipp et al., 2002a, b). At deformation temperatures where quartz experiences BLG recrystallization, feldspar deforms by brittle fracturing. At temperatures where quartz experiences SGR recrystallization, feldspar deforms by internal microfracturing with minor dislocation glide (Pryer, 1993). Flame perthite is also common in albite porphyroclasts at these temperatures (Fig. 1.4g) (Pryer, 1993). At quartz GBM recrystallization conditions, feldspar deforms by microfracturing. However, dislocation glide and BLG recrystallization can occur in feldspar at higher temperatures (Tullis and Yund, 1991).

Opening Angle and Quartz [c] Axis Lattice-Preferred Orientations

The opening angle is defined as the angle between the girdles measured in the plane perpendicular to foliation and parallel to lineation (XZ section) (Fig. 1.5b) (Kruhl, 1998). Experimental studies (e.g., Tullis et al., 1973; Lister et al., 1978; Lister and Hobbs, 1980; Lister and Dornsiepen, 1982; Wenk et al., 1989) indicate that the opening angle of quartz [c] axis LPOs increases with increasing deformation temperature (Fig. 1.5b). The opening angle can be used to calculate the deformation temperature with an error of ± 50° C based on the standard deviation of the data from 280 to >650° C (Kruhl, 1998). The relationship between the opening angle and temperature changes at temperatures of >650° C, when quartz begins to deform by prism [c] slip. The standard deviation of the data below 650° C suggests an error ± 30° C for data between 280 and 650° C. Other factors such as strain rate also play a role in the development of the opening angle (Tullis et al., 1973). Our deformation temperatures derived from quartz and feldspar recrystallization textures are plotted against the opening angle for samples KA-25, KA-02, AD07-06, and AD07-02 (Fig. 1.5b). In addition, deformation temperatures estimated from quartz and feldspar recrystallization textures from the Mabja Dome (Fig. 1.2) (Langille et al., 2010) are

also plotted against opening angle (boxes 19-20, Fig. 1.5b). These data provide an independent confirmation of the relationship between increasing opening angle and deformation temperature between ~300-700° C (Fig. 1.5b).

Temperatures defining the transition from prism <a> slip to prism [c] slip, expressed as a maxima in the Y direction and maxima parallel to lineation (Fig. 1.5a), respectively, in quartz are well constrained (e.g., Kruhl, 1998). However, the transitions from mixed basal <a>, rhomb <a>, and prism <a> (type-I and II girdles) to dominantly rhomb <a> and prism <a> to purely prism <a> slip (Y axis maxima) are poorly constrained. To place temperature ranges on these quartz slip systems, quartz LPO opening angles (Fig. 1.6) along with the corresponding deformation temperatures estimated from quartz recrystallization textures from this study and from Langille et al. (2010) on samples from Mabja dome (Fig. 1.2) were compiled to constrain deformation temperatures expected for the quartz LPO patterns shown in Figure 1.5a. With the exception of samples AD07-17a, AD07-12b, and AD07-03 from this study, samples that exhibit dominantly basal <a>, rhomb <a>, and prism <a> slip (Figs. 1.5a and 1.6) have quartz BLG recrystallization suggesting deformation temperatures of ~280-400° C. Opening angle derived temperatures from these samples fall within this temperature range. Samples which exhibit dominantly rhomb <a> and prism <a> slip along with minor basal <a> slip (Figs. 1.5a and 1.6) display quartz microstructures suggesting SGR recrystallization and opening angles indicating deformation temperatures of ~400-500° C. Samples that exhibit dominantly prism <a> slip with minor rhomb <a> and basal <a> slip (Figs. 1.5a and 1.6) have quartz suggesting GBM recrystallization and opening angles that indicate deformation temperatures of ~500-650° C. While temperatures of >650° C are not recorded in this study, other studies (i.e. Lister and Dornsiepen, 1982; Mainprice et al., 1986) show that at these temperatures quartz begins to show chessboard extinction and quartz LPOs exhibit prism [c] slip (Fig. 1.5a).

Two-Feldspar Geothermometry

Simpson and Wintsch (1989) suggest that myrmekite replaces K-feldspar porphyroclasts in areas of high-strain. During deformation the replacement occurs adjacent to foliation surfaces (C-surfaces) facing the maximum shortening direction (S-surfaces) (Fig. 1.7a and b). They

suggest that two-feldspar geothermometry of strain induced myrmekite replacement in K-feldspar porphyroclasts can estimate deformation temperatures associated with an incremental shortening direction.

Sample KA-40 (Sharkha transect) contains an asymmetric K-feldspar grain with blades of albite that contain a network of vermicular quartz that extends into the interior of the grain (Fig. 1.7a). After initial identification, a second polished thin section was made using the same billet for microprobe analysis. The myrmekite is distributed asymmetrically on the K-feldspar grain and extends ~90° from the S-surfaces. S-C fabric and mica fish confirm top-to-the-west shear sense (Fig. 1.7a). This strain-induced myrmekite provides a rare opportunity to quantify deformation temperatures directly associated with the development of shear sense indicators that record top-to-the-west sense of shear in the ADD.

Minimum and maximum temperatures of replacement are based on the analytical expressions of Whitney and Stormer (1977) where deformation temperature can be calculated using the equation:

$$T(K) = \frac{\{7973.1 - 16910.6X_{ab,AF} + 9901.9\,X_{ab,AF}^2 + (0.11 - 0.22X_{ab,AF} + 0.11\,X_{ab,AF}^2)P\}}{\left\{-1.9872\ln\left(\frac{X_{ab,AF}}{\alpha_{ab,PL}}\right) + 6.48 - 21.58\,X_{ab,AF} + 23.72\,X_{ab,AF}^2 - 8.62\,X_{ab,AF}^3\right\}} \quad (1)$$

where $X_{ab,AF}$ is the molar fraction of albite in the K-feldspar porphyroclast, $\alpha_{ab,PL}$ is the activity coefficient of albite in the myrmekite, and P (bars) is an assumed pressure. This equation is modified from the original feldspar geothermometer presented by Stormer (1975).
Compositional maps were made of portions of the myrmekite blades (Fig. 1.7c and d). In addition, orientation maps of portions of the myrmekite blades were created using EBSD at the University of California, Santa Barbara to test for the development of a crystal lattice and suggest that the myrmekite contains a lattice independent of the K-feldspar. Microprobe analyses were carried out on a Cameca SX-100 electron microprobe at the University of Tennessee. Na, K, and Si compositional maps of the entire grain as well as smaller areas were created to define mineral zoning and justify the locations for quantitative point analyses (Fig. 1.7b). Mapping was done at 15 keV, 20 nA, and a dwell time of 0.1 seconds. Mineral composition analyses along six transects (Fig. 1.7e; Table 1.2) within the K-feldspar porphyroclast containing strain-induced

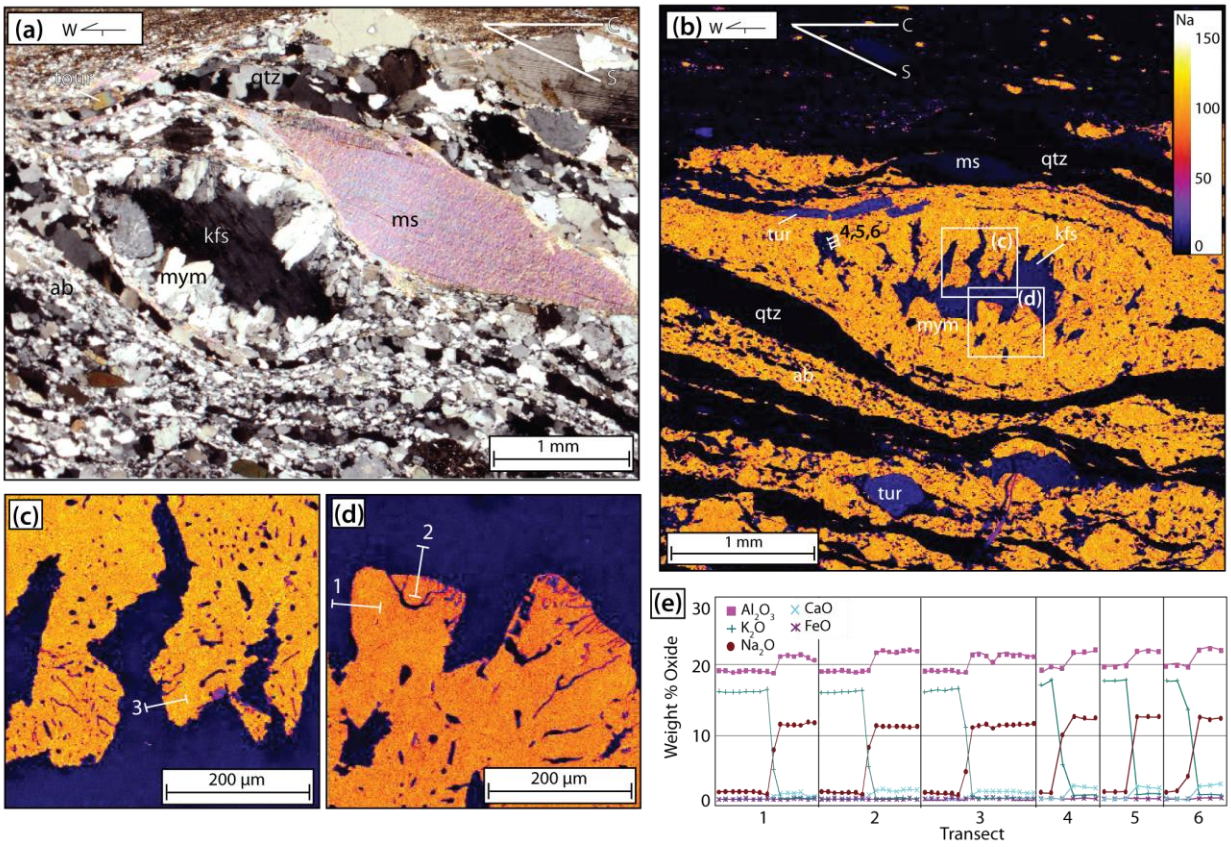

Figure 1.7. *(a) Asymmetric myrmekite in sample KA-40 from the Sharka transect. kfs, potassium feldspar; mym, myrmekite; ab, albite; ms, muscovite; tur, tourmaline; cross polars. (b) Sodium compositional map of the asymmetric myrmekite cut deeper to create a second thin section of the same clast. Locations of composition transects included: 1-3 in boxes c and d and 4-6 in (b). (c) and (d) are detailed sodium compositional maps of myrmekite lobes outlined in (b). Composition scale is the same as that in (b). (e) Compositional data for the six transects*.

myrmekite were conducted at 15 keV, 10 nA, and a 5 µm spot size. Activity coefficients (with an error of ± 3% propagated from the microprobe data) were calculated from electron microprobe data using the program AX (Holland and Powell, 2000) (Table 1.2).

Results

Samples at the top of the shear zone along the Pung Chu transect contain quartz that records BLG recrystallization (Fig. 1.4f) that overprints a higher temperature fabric. SGR recrystallization (Fig. 1.4g) within the shear zone rocks suggest an increase in deformation

Table 1.2. Rim Compositions of K-Feldspar and Myrmekite.

Transect	1	2	3	4	5	6
K-feldspar						
$X_{ab,AF}$	0.05	0.06	0.04	0.05	0.05	0.06
$X_{an,AF}$	0	0	0	0	0	0
$X_{or,AF}$	0.95	0.94	0.96	0.95	0.95	0.94
Total %	100	100	100	100	100	100
Myrmekite						
$X_{ab,PF}$	0.93	0.89	0.92	0.95	0.95	0.94
$X_{an,PF}$	0.06	0.1	0.04	0.04	0.04	0.05
$X_{or,PF}$	0.01	0.01	0.04	0.01	0.01	0.01
Total %	100	100	100	100	100	100
$\alpha_{ab,\ PF}$	0.92	0.89	0.92	0.95	0.95	0.94

Note: Refer to Fig. 1.7 for transect locations. X_{ab}, molar fraction of albite; X_{an}, molar fraction of anorthite; X_{or}, molar fraction of orthoclase; AF, alkali feldspar; PF, plagioclase; $\alpha_{ab,\ PF}$, activity coefficient of albite in myrmekite.

temperature from ~280-400° C at the top of the shear zone to ~400-500° C structurally deeper within the shear zone (Fig. 1.8a, Table 1.1). Feldspar porphyroclasts within samples from this transect all deform by brittle fracturing. Flame perthite is present within some albite porphyroclasts (Fig. 1.4g) indicating deformation temperatures of 400-500° C. The quartz [c] axis opening angle indicates deformation temperatures of 324 ± 50° C and 354 ± 50° C (KA-25) at the top of the shear zone and 480 ± 50° C (KA-01) structurally deeper in the shear zone (Fig. 1.6), which confirms estimates based on quartz and feldspar microstructures (Fig. 1.8a, Table 1.1). Quartz [c] and <a> axis LPO patterns from this transect record a range from multiple slip systems to those that are dominated by prism <a> slip suggesting deformation temperatures of 280-500° C (Fig. 1.6).

Within samples from the Sharkha transect, quartz experienced SGR recrystallization and feldspar porphyroclasts that deform by brittle fracture indicating deformation temperatures of 400-500° C (Fig. 1.8b, Table 1.1). Quartz [c] and <a> axis LPO patterns indicate mixed slip dominated by rhomb <a> and prism <a> slip suggesting deformation temperatures of 400-500° C (Fig. 1.6). Assuming 0.5 GPa, two-feldspar geothermometry of the strain induced myrmekite within sample KA-40 indicates that top-to-the-west shear occurred at deformation temperatures of 369-435° C, from calculations on six compositional transects (Fig. 1.9). Calculations were

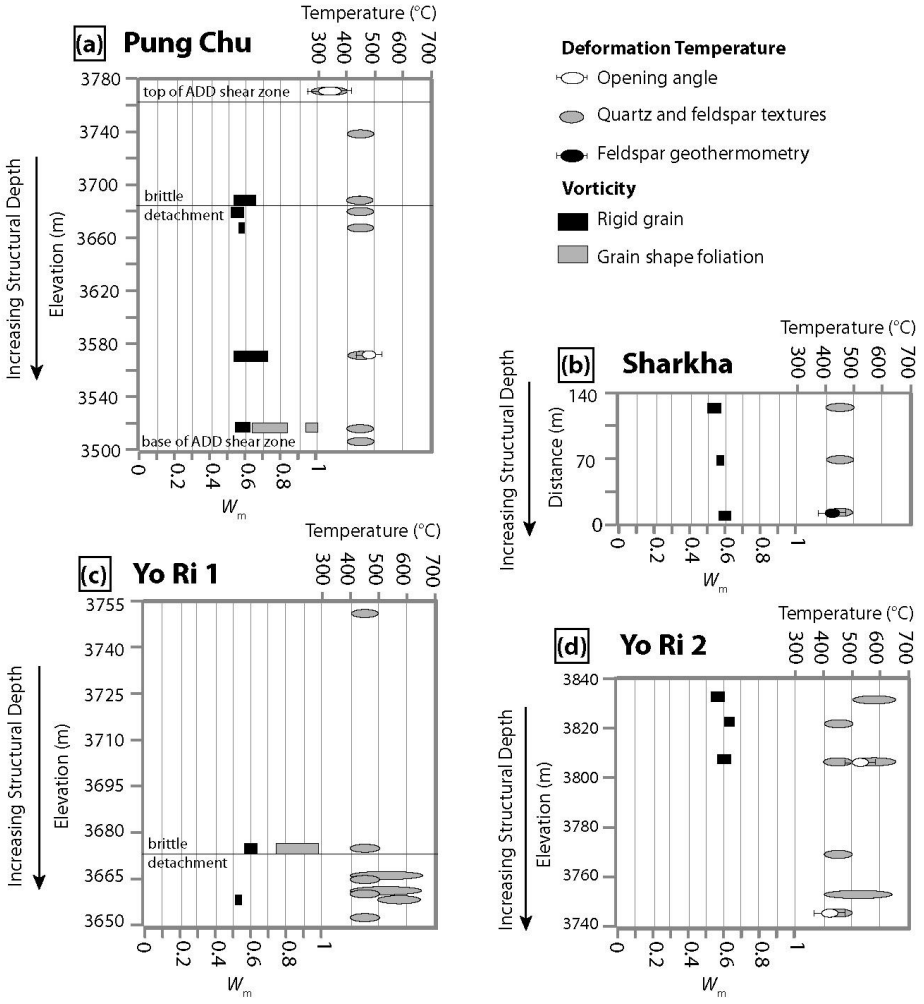

Figure 1.8. *Deformation temperatures and vorticity estimates for samples from the (a) Pung Chu transect, (b) Sharka transect, (c) Yo Ri 1, and (d)Yo Ri 2 transects. Multiple samples at or near the same structural depth represented as a single rectangle and/or ellipse. Vorticity and deformation temperature methods discussed in text.*

also made assuming a pressure of 0.8 GPa and demonstrate that the calculation is relatively insensitive to changes in assumed pressure and resulted in <40° C difference. These data were compared to temperatures derived using the Nekvasil and Burnham (1987) two-feldspar geothermometer with the program SOLVCALC (Wen and Nekvasil, 1994), which yielded temperatures within <25° C of estimates derived from the Whitney and Stormer (1977) method (Fig. 1.9). Other studies (i.e. Vernon, 1991; Hippert and Valarelli, 1998) dispute the formation of strain-induced myrmekite suggesting that there is no microstructural evidence for myrmekite

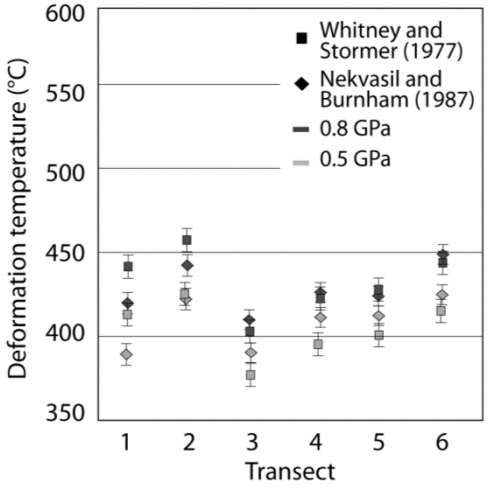

Figure 1.9. *Estimated deformation temperatures for all six transects through the asymmetric myrmekite. Refer to Figure 1.7 for transect locations.*

replacement of K-feldspar. However, our study shows that myrmekite often protrudes into the K-feldspar at ~90° to the S-surfaces (Fig. 1.7a). Our estimate for deformation temperature derived from both the Whitney and Stormer (1977) and Nekvasil and Burnham (1987) models also agree with independent deformation temperatures derived from quartz and feldspar microstructures and quartz slip systems inferred from the LPO (Fig. 1.8b, Table 1.1).

Quartz experienced SGR to GBM recrystallization within samples from the Yo Ri 1 transect indicating deformation temperatures ranging from 400-650° C (Fig. 1.8c, Table 1.1). Sample AD07-12b contains sillimanite cored muscovite fish and GBM recrystallization overprinted by lower temperature SGR recrystallization. Sample AD07-17a also has GBM recrystallization overprinted by lower temperature SGR recrystallization. Feldspar porphyroclasts within this transect deform mainly by brittle fracturing with minor bulging recrystallization at grain boundaries indicating temperatures of 400-650° C (Fig. 1.8c, Table 1.1). Quartz [c] and <a> axis LPO patterns indicate slip dominated by rhomb <a> and prism <a> slip indicating deformation temperatures of 400-500° C (Fig. 1.6).

Quartz experienced SGR to GBM recrystallization within samples from the Yo Ri 2 transect indicating deformation temperatures that range from 400° C to 650° C (Fig. 1.8d, Table 1.1). Feldspar porphyroclasts within this transect deform mainly by brittle fracturing with smaller clasts deforming plastically indicating deformation temperatures of 400-650° C. Sample AD07-03 contains GBM recrystallization overprinted by SGR recrystallization. The quartz [c] axis opening angle from sample AD07-06 indicates deformation temperatures of 536 ± 50° C and the angle from sample AD07-02 indicates temperatures of 414 ± 50° C, both similar to those based on quartz and feldspar textures (Figs. 1.6 and 1.8d, Table 1.1). Quartz [c] and <a> axis LPO patterns from this transect exhibit mixed <a> slip dominated by prism <a> slip indicating deformation temperatures ranging between 400-650° C (Fig. 1.6).

Quartz experienced SGR and GBM recrystallization within the three samples from the NRD on the eastern limb indicating deformation temperatures that range from 400−650° C (Fig. 1.8, Table 1.1). Feldspar porphyroclasts from these samples deform mainly by brittle fracturing with minor BLG recrystallization also indicating temperatures between 400-650° C (Tullis and Yund, 1991) (Table 1.1). Quartz [c] and <a> axis LPO patterns from MJAD-23 suggest dominantly prism <a> slip indicating deformation temperatures between 500-650° C (Fig. 1.6e). These deformation temperatures overlap with those from deformed rocks along the ADD.

Vorticity

Vorticity analyses were conducted to quantify the relative contribution of pure and simple shear during ductile deformation and to characterize the spatial and temporal variability in flow during exhumation along the ADD. Characterizing the proportions of pure and simple shear is important because a significant contribution of pure shear indicates significant thinning and extension, and an increase in strain and extrusion rates relative to simple shear (Law et al., 2004). Kinematic vorticity number (W_k) is a measure of the relative contributions of pure ($W_k = 0$) and simple ($W_k = 1$) shear during steady-state (instantaneous) deformation. In this nonlinear relationship pure and simple shear components are equal when $W_k = 0.71$ (Tikoff and Fossen, 1995; Law et al., 2004). The potential for spatial and temporal variability of vorticity in naturally deformed rocks (e.g., Fossen and Tikoff, 1997, 1998; Jiang, 1998) can be accounted for by using a time-averaged and assumed steady-state deformation history known as the mean kinematic vorticity number (W_m). W_m methods require that deformation progressed during plane strain conditions.

To estimate W_m, two methods were applied to thin sections cut perpendicular to the foliation and parallel to the lineation (XZ section); the rigid-grain technique (Passchier, 1987; Wallis et al., 1993; Jessup et al., 2007) and the quartz grain shape foliation technique (Wallis, 1995). Measurements were made directly from photomicrographs of the entire thin section taken using a high definition Nikon DS-Fi1 camera. Aspect ratio and angle data was collected on-screen using the semi-axis and angle measurement tools of the Nikon Imaging System-Elements 2.3 imaging software (Laboratory Imaging, 2007) (Fig. 1.10a) and saved allowing for later

reference to measured grains. Grain quality was evaluated both from the photomicrographs and on the microscope. This method allows for efficient and more accurate measurement compared to standard optical measurement techniques.

Rigid Grain Technique

The rigid-grain technique (Wallis et al., 1993) was applied to 19 samples and involves measuring the aspect ratio (R) of a rigid porphyroclast such as feldspar and the acute angle (θ) between the clast long axis and the macroscopic foliation (Fig. 1.10a). Grains above a critical aspect ratio (R_c) define a stable orientation and will exhibit a small range in θ, whereas grains below infinitely rotate and will show a larger range of θ. From R_c, vorticity can be calculated as (Passchier, 1987):

$$W_m = (R_c^2 - 1) / (R_c^2 + 1) \quad (2)$$

Plotting the shape factor (B*), where

$$B^* = (M_x^2 - M_n^2) / (M_x^2 + M_n^2) \quad (3)$$

and M_x = long axis and M_n = short axis of a clast, versus θ on the Rigid Grain Net (RGN) is a graphical approach to calculating W_m (Fig. 1.10b) (Jessup et al., 2007). Similar to R_c, the critical shape factor B^*_c separates grains that reached a stable orientation versus those that rotated freely. W_m can be determined directly from B* because B* and W_m are scaled one to one.

The following criteria must be met to apply the rigid-grain technique; (1) the porphyroclasts must predate the dominant deformation fabric, (2) the porphyroclasts are internally undeformed, (3) there is no mechanical interaction between adjacent clasts or the matrix, and (4) the porphyroclasts occur within a homogeneously deformed matrix (Jessup et al., 2007). Uncertainties in vorticity values estimated using this technique can arise if (1) recrystallization-induced changes in the aspect ratio (R) during or after deformation, (2) high

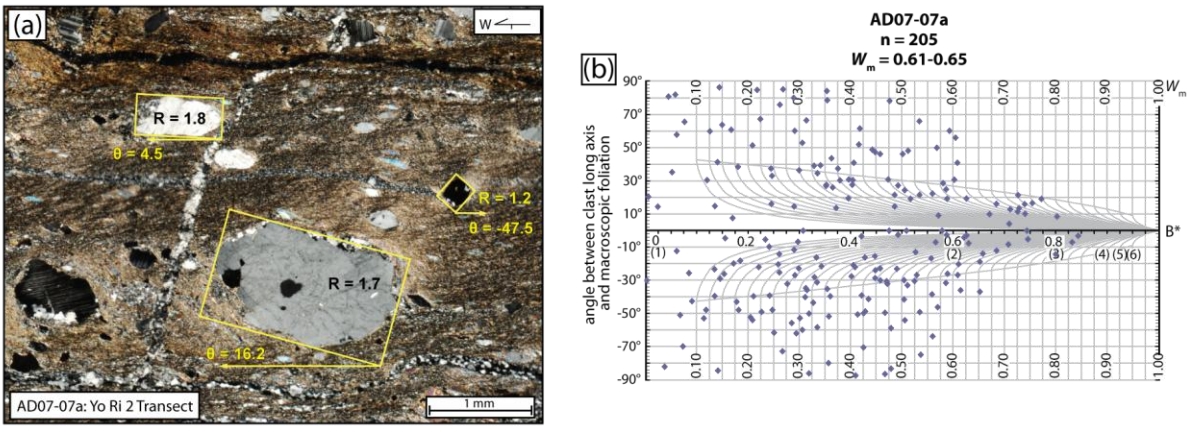

Figure 1.10. *Example Rigid Grain Net (RGN) analysis. (a) Grain axis and angle measurement. (b) RGN of feldspar porphyroclasts corresponding to the sample in (a). n = number of grains measured. B* is the shape factor (refer to text) and the numbers in parenthesis are aspect ratios.*

aspect ratio rigid grains in low-strain rocks have not rotated into their stable orientations, (3) rigid grains with high-aspect ratios are fractured, or (4) the sectional radii of the porphyroclast in the thin section misrepresents the actual radii (Jessup et al., 2007; Iacopini et al., 2008). To limit potential inaccuracies, grains measured showed little to no sign of plastic deformation, mechanical interaction with other grains, recrystallization, or fracturing.

Quartz grain Shape Foliation Technique

During deformation, newly recrystallized grains (e.g., quartz) are stretched parallel to the instantaneous stretching axis (ISA) (Wallis, 1995). The maximum angle (θ) between the oblique grain shape fabric and the flow plane provides an approximate orientation of the ISA (Wallis, 1995). The flow plane is defined as the perpendicular to the [c] axis girdle of the quartz LPO where β is the angle between the flow plane and the main foliation (S_A) (Law et al., 1990; Wallis, 1995). The orientation of the ISA is related to W_m by the equation (e.g., when θ = 45, W_m = 1; Wallis, 1995):

$$W_m = \sin 2\theta = \sin [2(\delta+\beta)] \quad (4)$$

where δ is the angle between the quartz oblique grain shape fabric (S_B) and S_A (Fig. 12A).

The long axis of the quartz grains from four samples were measured from the high-resolution mosaic image of the thin section and the flow plane was measured from the quartz LPO patterns (Fig. 1.6). To accurately define the ISA, θ was measured on ~100 quartz grains per sample (Fig. 1.11b). Application of the grain shape foliation technique requires a well-developed quartz LPO and oblique grain shape fabric to accurately define both the flow plane and the ISA, and thus θ (Wallis, 1995; Xypolias and Koukouvelas, 2001; Xypolias, 2009). Histograms were used to define the range in θ used for the W_m estimate. The range in θ used for the W_m estimate was defined as where the frequency of θ on the histogram reaches its highest value to where it declines to a maximum measured angle (grey area in Figure 1.11b).

Uncertainties in vorticity values estimated using this technique can be attributed to; (1) heterogeneity of matrix material, (2) the presence of porphyroclasts, and (3) folding—which may all deflect or influence the orientation of the quartz fabric. To limit possible inaccuracies, measurements were made from quartz fabrics that were unaffected by these interferences.

Results

From the Pung Chu transect, W_m estimates using the rigid-grain technique on feldspar porphyroclasts range between 0.52 and 0.72 (49-65% pure shear) (n=11) (Table 1.1, see Appendix 1.2 for additional Rigid Grain Nets). Our vorticity estimates assume plane strain deformation which is supported by the development of quartz [c] axis single girdles, type-I cross-girdles, and prism <a> slip patterns in the Y-direction (refer to Figs. 1.5 and 1.6) which indicate plane strain (Lister and Hobbs, 1980). Two exceptions include samples AD07-28 and AD07-30 which have <a> axis patterns subparallel to the lineation suggesting flattening (Fig. 1.6) (Lister and Hobbs, 1980; Barth et al., 2010). However, Tikoff and Fossen (1995) note that the percentage of pure shear measured in 2D on rocks that record a small proportion of non-plane strain is only overestimated by <0.05, which is minor compared to standard errors associated with W_m measurement. In addition, these samples yield W_m estimates consistent with the other samples in this study suggesting that these measurements are reliable (Fig. 1.8, Table 1.1). W_m estimates using the quartz grain shape foliation technique range from 0.62 to 0.99 (1-57% pure shear) (n = 2) within samples from the Pung Chu transect, suggesting dominantly simple shear to sub-equal amounts of pure and simple shear (Fig. 1.8a, Table 1.1).

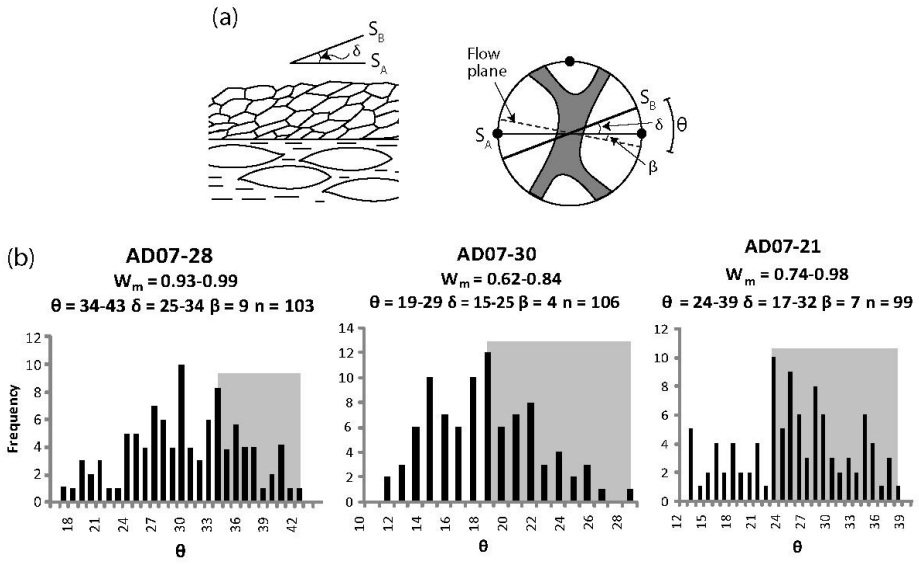

Figure 1.11. *Vorticity analysis from quartz grain shape fabrics. (a) Schematic diagram demonstrating the relationship between the main foliation (S_A), the quartz fabric (S_B), the flow plane, and the quartz [c] axis LPO. (b) Frequency diagrams used for vorticity (W_m) estimates using the quartz grain shape foliation technique. θ = the angle between S_B and the flow plane. n = number of analyses. Shaded regions represent the range in θ used for W_m estimates.*

W_m estimates using the rigid-grain technique on rigid feldspar porphyroclasts were applied to three samples from the Sharkha transect and yield estimates that range from 0.50 to 0.61 (58-66% pure shear) (Fig. 1.8b, Table 1.1), similar to those in the Pung Chu transect. The rigid-grain technique was applied to feldspar in two samples from the Yo Ri 1 transect and yielded values of 0.52-0.64 (55-64% pure shear) suggesting a dominant pure shear component. These estimates are similar to those from the other transects. The quartz grain shape foliation technique was applied to AD07-21 from the Yo Ri 1 transect and yielded values of 0.74-0.98 (1-44% pure shear), suggesting a large simple shear component (Fig. 1.8c, Table 1.1). The rigid-grain technique was applied to feldspar in three samples from the Yo Ri 2 transect and yielded W_m estimates ranging from 0.53 to 0.65 (54-64% pure shear) suggesting a large pure shear component (Fig. 1.8d; Table 1.1).

Shortening and Extension

The strain ratio (R_{xz}) can be calculated from the following equation which utilizes the angular relationships between the quartz oblique grain shape fabrics and quartz [c] axis fabrics (Passchier, 1988; Xypolias, 2009):

$$R_{xz} = \frac{1-\tan\theta*\tan\beta}{\tan^2\beta+\tan\theta*\tan\beta} \quad (5)$$

where

$$\tan\theta = \cot[2(\beta+\delta)] = \sqrt{1-W_m^2}\,/\,W_m \quad (6)$$

and β is the angle between the flow plane and S_A as measured from the quartz [c] axis fabric and δ is the angle between the quartz oblique fabric (S_B) and the main foliation (S_A) (Fig. 1.11a). This equation was applied to three samples from the ADD and yields R_{xz} values of 6.4-24 (Table 1.1).

Using our W_m (0.74-0.98 from the quartz grain shape fabric technique) and R_{xz} estimates (6.7-24) from sample AD07-21(our only W_m estimate with evidence for plane strain deformation), percent shortening and extension was estimated by calculating the shortening value (S) using the following equation (Wallis et al., 1993):

$$S = \{0.5(1-W_m^2)^{0.5}[(R_{xz}+R_{xz}^{-1}+\frac{2(1+W_m^2)}{(1-W_m^2)})^{0.5}+(R_{xz}+R_{xz}^{-1}-2)^{0.5}]\}^{-1} \quad (7)$$

Our data show that this sample experienced 36-50% shortening and 57-99% down-dip extension at the time that our vorticity estimates were recorded in the deformed quartz at temperatures of 400-500° C (deformation temperature estimate for sample AD07-21).

Discussion

Implications for the Ama Drime and Nyönno Ri Detachments

The ADM records anatectic melting in the core of the range during the onset of orogen-parallel extension (Cottle et al., 2009a). Exhumation (2.2 ± 0.2 mm/yr) was accommodated by two shear zones (ADD and NRD) that currently dip in opposite direction away from the core of the range (Cottle et al., 2009a). Shear zone nucleation occurred at high-temperatures as a distributed shear zone that was progressively overprinted by deformation mechanisms that were active at decreasing temperature and varying strain rates (Fig. 1.12). Pseudotachylite records high strain events that punctuated the exhumation history. Qualitative evidence for this range in deformation conditions that occurred at high temperature and presumably an earlier portion of the history is taken from footwall rocks whereas brittle detachments that occur within the section record the final stages of exhumation. Mylonitic samples from the ADD and NRD provide an opportunity to quantify the kinematic evolution of solid-state fabric development that link early and late stages of this exhumation history.

Mean kinematic vorticity estimates from rocks within the ADD range between 0.50-0.72 (49-66% pure shear) using the rigid-grain technique and 0.62-0.99 (1-57% pure shear) using the oblique quartz grain shape foliation technique (n = 3). Vorticity estimates derived from quartz fabrics record a higher component of simple shear than estimates derived from rigid porphyroclasts. Assuming quartz is more sensitive to late stage changes in deformation than the rigid porphyroclasts, W_m estimates derived from the quartz fabrics can be interpreted as recording the last increment of deformation (Wallis, 1995; Xypolias, 2009). This interpretation was suggested for Rongbuk valley where quartz fabrics yield higher W_m estimates than those obtained using rigid porphyroclasts (Law et al., 2004). Johnson et al. (2009a and b) propose that increased mica content results in decoupling between the porphyroclast and matrix interface, which can potentially overestimate the pure shear component when rigid porphyroclasts are used for W_m estimates. W_m estimates are consistent between samples that contain a range in composition and mica content (i.e. marble, quartzite, leucogranite, etc.) suggesting that decoupling was either minimal or if present, the decoupling resulted in an error that was

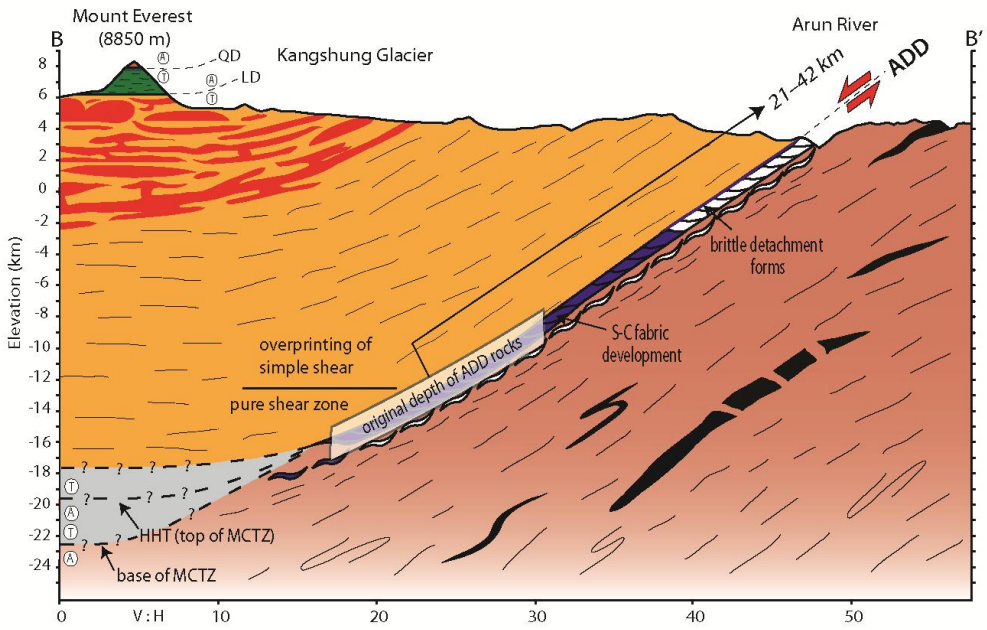

Figure 1.12. *Simplified geologic cross section through Mount Everest and the Ama Drime Massif with a schematic diagram overlay that depicts the kinematic evolution of the Ama Drime detachment (ADD) assuming a geothermal gradient of 25-35° C/km. Refer to Figure 1.2 for cross section location and legend. Blue on the shear zone demonstrates active systems present as the rocks were exhumed and narrowed into the ~300 m-thick shear zone. Shear zone thickness not to scale. Other possible depths for the deepest position of the ADD are dashed. QD, Qomalangma detachment; LD, Lhotse detachment; HHT, High Himalayan thrust.*

independent of mica content. In addition to vorticity estimates, the asymmetry or lack of asymmetry of quartz LPO patterns (Fig. 1.6) suggests that some samples record noncoaxial deformation (e.g., KA-25 and AD07-04) while others suggest coaxial deformation (e.g., AD07-12b, AD07-17a, AD07-03). As mentioned earlier, samples AD07-17a, AD07-12b, and AD07-03 contain quartz GBM recrystallization overprinted by SGR recrystallization suggesting that earlier pure shear dominated flow may be associated with GBM (coaxial quartz LPO patterns and rigid-grain technique vorticity estimates) at higher temperatures and was overprinted by noncoaxial flow (quartz grain shape foliation vorticity estimates) at lower temperatures.

The rigid grain technique (49-66% pure shear) records an early part of the exhumation history when deformation transitioned from high-temperature distributed shear to mylonite development (Fig. 1.12). This was followed by W_m estimates from quartz fabrics (1-57% pure

shear) that record a later part of the exhumation history as these rocks were exhumed (Fig. 1.12). These data indicate a spatial and temporal variation in deformation that progressed from dominantly pure shear to dominantly simple shear deformation during exhumation between ~400-650° C. These data indicate that the rocks exposed within the ADD experienced 36-50% shortening and 57-99% down-dip extension at the time that the vorticity estimates were recorded in the deformed quartz. This suggests a substantial amount of crustal thinning and strain during the later increments of deformation. Previous estimates yielded 10-30% shortening and 10-40% down-dip extension within the GHS near the STDS in the Mabja Dome and the Everest region (Law et al., 2004; Langille et al., 2010). This implies that the rocks exposed within the ADD experienced a significantly larger amount of shortening and extension than the GHS in the footwall of the STDS.

Deformation temperatures derived from asymmetric quartz [c] axis LPO opening angles and two-feldspar thermometry of asymmetric myrmekite that are directly related to top-to-the-west shear (369-587° C) were used to estimate the amount of top-to-the-west displacement on the ADD. Assuming a geothermal gradient of ~25-35° C/km, deformation temperature estimates suggest that the rocks exposed within the ADD shear zone were exhumed from a minimum depth of 11-21 km (Fig. 1.12). Projecting this depth below the current surface expression of the ADD using a constant dip of ~30° for the ADD (based on structural data from Jessup et al., 2008a; Fig. 3) yields a minimum of ~21-42 km of down-dip displacement (Fig. 1.12), similar to other estimates of ~30 km (Kali et al, 2010). Uncertainties are associated with the poorly constrained geothermal gradient. Estimates of deformation temperatures (400−650° C) experienced by rocks exposed within the NRD (Fig. 1.6, Table 1.1) indicate that it exhumed footwall rocks from similar depths as the ADD. The Gurla Mandhata core complex, ~650 km west of the ADM, is another feature that was exhumed during orogen-parallel extension. The core complex is bound on the west by the Gurla Mandhata-Humla extensional fault system that records 35-66 km of top-to-the-west displacement during extension after 15 Ma (Murphy et al., 2002, 2007), similar to the displacement estimate for the ADD.

Comparison with the North Himalayan Gneiss Domes

Although the ADM is located just south of two of the North Himalayan gneiss domes, the Lhagoi Kangri and Mabja domes (Figs. 1.1 and 1.2a), data from this study suggests that these are very different types of migmatite-cored domes. North Himalayan gneiss domes expose middle crustal rocks belonging to an originally ~35-km-thick mid-crustal channel composed of the GHS (e.g., Burg and Chen, 1984; Chen et al., 1990; Lee et al., 2000, 2002, 2004, 2006; Zhang et al., 2004; Aoya et al., 2005, 2006; Quigley et al., 2006, 2008; Lee and Whitehouse, 2007). W_m studies of the GHS (Grasemann et al., 1999; Law et al., 2004; Carosi et al., 2006, 2007; Jessup et al., 2006; Larson and Godin, 2009) suggest that the low-viscosity mid-channel deformed by general shear with an increasing component of pure shear towards the center. Langille et al. (2010) demonstrated that mid-crustal rocks exposed within the Mabja dome preserve mixed top-to-the-north and top-to-the-south shear at the top of the channel and top-to-the-south shear at the bottom, an increasing pure shear component with structural depth, and increasing deformation temperatures towards the middle of the dome, patterns consistent with those predicted for the deformed mid-crustal channel. Lee et al. (2006) and Lee and Whitehouse (2007) suggest that these deformational patterns were developed between ~16 and 35 Ma, and correlate closely to ages estimated for metamorphism and anatexis of the GHS (Burg et al., 1984; Pognante and Benna, 1993; Simpson et al., 2000; Viskupic et al., 2005; Cottle et al., 2009b). Data from the Mabja and the Kangmar domes (Lee et al., 2000) suggest that the rocks exposed within the North Himalayan gneiss domes originated from within the mid-crustal channel and were later brought to the surface through thrust faulting along the Gyirong-Kangmar thrust fault during the middle Miocene (Burg and Chen, 1984; Burg et al., 1987; Lee et al., 2000).

Structural and geochronologic data (i.e. Liu et al., 2007; Zhang and Gao, 2007; Jessup et al., 2008a; Cottle et al., 2009a; this study) suggest that the kinematic, metamorphic, and exhumation history of the ADM differs from that of the North Himalayan gneiss domes. In contrast to the rocks exposed within Mabja Dome that record a spatial transition from dominantly simple shear to dominantly pure shear deformation with increasing structural depth across the dome, the rocks exposed within the ADD record a temporal transition with an early phase of movement that was dominated by pure shear deformation that is overprinted by predominantly simple shear deformation during the later stages of the exhumation history on the

shear zone (Fig. 1.12). In addition, the rocks exposed within the ADD were deformed at temperatures ranging between ~400-650° C and are exposed within a ~300-m-thick shear zone. In contrast, the rocks exposed within the Mabja Dome record deformation temperatures increasing from ~450° C to >700° C and are exposed within a 13-km-thick zone. Kinematic indicators within the ADD and NRD indicate opposite sense of shear on either side of the ADM that record orogen-parallel extension. Mabja is dominated by top-to-the-north shear sense that transitions to top-to-the-south shear sense with increasing structural depth related to south-directed flow. $^{40}Ar/^{39}Ar$ ages for muscovite and biotite from the NRD (Zhang and Guo, 2007) and U-Th-Pb ages from the ADM (Liu et al., 2007; Cottle et al., 2009a) suggest that east-west extension initiated at ~13 Ma, which post-dates south-directed flow recorded in the North Himalayan gneiss domes by ~3 Ma. Based on these characteristics, the structural and kinematic evolution of the ADM is more closely related to metamorphic domes developed during orogen-parallel extension, such as the Gurla Mandhata core complex (Murphy et al., 2002) and Leo Pargil dome (Thiede et al., 2006), rather than the North Himalayan gneiss domes.

Exhumation of the Ama Drime Massif

Borghi et al. (2003) projected the MCTZ along the western side of the ADM while others (Lombardo and Rolfo, 2000; Groppo et al., 2007; Liu et al, 2007) projected the MCTZ around the ADM. Several possibilities exist for the structural positions juxtaposed by the ADD. Lombardo and Rolfo (2000) interpret the ADM orthogneiss to correspond to the Num orthogneiss (lower GHS) whereas the grt + bt + sil gneiss in the hanging wall of the ADD is equivalent to the Barun Gneiss (upper GHS) of the Sedua-Makalu section. Based on this, they propose that the Kharta section is structurally lower relative to the MCTZ exposed in the Sedua-Makalu section (HHT of Goscombe et al., 2006). The protolith age for the Ama Drime orthogneiss is equivalent to Proterozoic gneisses in the foreland (e.g., Ulleri orthogneiss) (Goscombe et al., 2006; Searle et al., 2008; Cottle et al., 2009a).

The map relationships between the ADD, the HHT (top of the MCTZ), and STDS are depicted on a cross section from the center of the ADM to the Khumbu glacier (Fig. 1.12). The ADD was projected ~10 km further south than the southernmost mapped contacts into the border

region between Tibet and Nepal to construct a cross section that is perpendicular to the ADD and that passes through a known location of the Qomolangma detachment (QD). This southern projection of the ADD is balanced by structural data from the footwall and hanging wall of the NRD from Burchfiel et al. (1992) that indicates that it extends to at least this position on the southern portion of the eastern side of the ADM (Fig. 1.2). The QD exposed on the summit of Mount Everest dips northeast and juxtaposes TSS in the hanging wall with the Yellow band in the uppermost section of the Everest Series schist and calc-silicate in the footwall (Burchfiel et al., 1992; Searle et al., 2003; Jessup et al., 2006; Jessup et al., 2008b). The base of the Everest Series is defined by the northeast-dipping Lhotse detachment (LD) (Searle, 1999). Using the structural distance between the QD and the top of the MCTZ (HHT), the GHS between the STDS and the MCTZ is estimated to be ~28 km thick below the QD on the summit of Mount Everest (Searle et al., 2006).

Using an average dip of 30°, the ADD can be projected from the surface to deeper structural positions, through a minimum depth of ~11-21 km from the estimated deformation temperatures, where it presumably shallows out beneath the summit of Mount Everest. Based on these data, the ADD might sole into the HHT or a deeper structural position such as the base of the MCTZ or some other (lithologic, stratigraphic, or structural) boundary that is not exposed in the foreland (Fig. 1.12). Assuming that the orientation for this contact was originally north dipping then it was potentially rotated to its current orientation and reactivated as the ADD to accommodate exhumation of the ADM.

This study suggests that prior to the onset of orogen-parallel extension, the crustal profile of the Everest area included a 28 km-thick section of GHS. The section was juxtaposed with the TSS at the top by top-to-the-north displacement on the STDS and granulite facies rocks at the bottom by top-to-the-south displacement on the MCTZ (Searle et al., 2006). Rocks that are currently exposed in the central section of the ADM (750° C and 0.7-0.8 GPa) were located at an unknown structural position between the upper GHS and the LHS. Here they experienced muscovite dehydration melting (11-13 Ma) in a kinematic setting that was dominated by orogen-parallel extension.

Exhumation of footwall rocks of the NRD by 10-13 Ma was kinematically linked to extension in the interior of the Tibetan Plateau (Zhang and Guo, 2007; Kali et al., 2010).

$^{40}Ar/^{39}Ar$ muscovite and biotite ages suggest that exhumation on the NRD (10-13 Ma) began prior to the ADD (6-10 Ma). One possible interpretation is that back-rotation of the NRD footwall toward the west during initial exhumation of the ADM resulted in a west-dipping lithologic or structural boundary. This weakness was reactivated during top-to-the-west shearing that produced at least 21-42 km of displacement along the portion between the Yo Ri and Pung Chu gorges. Deformed leucogranite dikes and undeformed dikes in the NRD that crosscut the main shear zone fabric indicate that ductile movement on the NRD ended by ~11 Ma (Kali et al., 2010). Thus, the ADD outlasted the ductile history of the NRD (Kali et al., 2010). Displacement on the NRD and ADD decreases toward the north where it is minimal at the north-plunging nose (Kali et al., 2010). Not only does this indicate that the southernmost transects record the deepest record of the fault in the study area, but also that the Ama Drime orthogneiss exposed between these represents the deepest structural position of the Massif.

Conclusions

New detailed microstructural and kinematic analyses, estimates of deformation temperatures, and vorticity analyses conducted on rocks from the western limb of the Ama Drime Massif suggests that these rocks record top-to-the-west shear sense between ~400-650° C. Mean kinematic vorticity estimates from within this temperature interval record an earlier pure shear dominated flow (49-66% pure shear, rigid grain technique) overprinted by a later simple shear (1-57% pure shear, quartz fabrics) dominated flow. These data suggest that the rocks exposed within the ADD experienced 36-50% shortening and 57-99% down-dip extension during the later increments of deformation. Deformation temperatures recorded during top-to-the-west shear are combined with an assumed dip for the detachment of 30° to create a minimum estimate of 21-42 km of displacement for the Ama Drime detachment. Data from the eastern limb of the Ama Drime Massif indicate that the Nyönno Ri detachment may have experienced a similar magnitude of displacement during exhumation of the Ama Drime Massif. Exhumation of the Massif began during the initiation of orogen-parallel extension in the Dinggyê graben. Back-rotation of the footwall block resulted in a west-dipping footwall block. During back-rotation, a

weakness in the footwall block was reactivated to accommodate top-to-the-west shear along the ADD during orogen-parallel extension.

References

Aoya, M., Wallis, S.R., Terada, K., Lee, J., Kawakami, T., Wang, Y., and Heizler, M., 2005, North-south extension in the Tibetan crust triggered by granite emplacement: Geology, v. 33, p. 853-856.

Aoya, M., Wallis, S.R., Kawakami, T., Lee, J., Wang, Y., and Maeda, H., 2006, The Malashan gneiss dome in south Tibet: comparative study with the Kangmar dome with special reference to kinematics of deformation and origin of associated granites, *in* Law, R.D., Searle, M.P., and Godin, L., eds., Channel flow, ductile extrusion and exhumation in continental collision zones: Geological Society [London] Special Publication, v. 268, p. 471-495.

Armijo, R., Tapponnier, P., Mercier, J., and Han, T., 1986, Quaternary extension in southern Tibet: Field observations and tectonic implications: Journal of Geophysical Research, v. 91, p. 13803-13872.

Barth, N.C., Hacker, B.R., Seward, G.G.E., Walsh, E.O., Young, D., and Johnston, S., 2010, Strain Within the ultrahigh-pressure Western Gneiss region of Norway recorded by quartz CPOs: Geological Society [London] Special Publication, v. 335, p. 663-685.

Borghi, A., Castelli, D., Lombardo, B., and Visoná, D., 2003, Thermal and baric evolution of garnet granulites from the Kharta region of S Tibet, E Himalaya: European Journal of Mineralogy, v. 15, p. 401-418.

Brookfield, M.E., 1993, The Himalayan passive margin from Precambrian to Cretaceous: Sedimentary Geology, v. 84, p. 1-35.

Burchfiel, B.C., Chen, Z., Hodges, K.V., Yiping, L., Royden, L.H., Deng, C., and Xu, J., 1992, The South Tibetan detachment system, Himalayan orogen: extension contemporaneous with and parallel to shortening in a collisional mountain belt: Geological Society of America Special Paper 269, 41 p.

Burg, J.P., and Chen, J.M., 1984, Tectonics and structural zonation of southern Tibet, China: Nature, v. 311, p. 219-223.

Burg, J.P., Leyreloup, A., Girardeau, J., and Chen, G.M., 1987, Structure and metamorphism of a tectonically thickened continental crust: The Yalu Tsangpo suture zone (Tibet): Royal Society of London Philosophical Transactions, v. 321, p. 67-86.

Carosi, R., Montomoli, C., Rubatto, D., and Visoná, D., 2006, Normal-sense shear zones in the core of the Higher Himalayan Crystallines (Bhutan Himalaya); evidence for extrusion?, *in* Law, R.D., Searle, M.P., and Godin, L., eds., Channel flow, ductile extrusion and exhumation in continental collision zones: Geological Society [London] Special Publication, v. 268, p. 425-444.

Carosi, R., Montomoli, C., and Visoná, D., 2007, A structural transect in the Lower Dolpo: Insights on the tectonic evolution of Western Nepal: Journal of Asian Earth Sciences, v. 29, p. 407-442

Catlos, E.J., Harrison, T.M., Manning, C.E., Grove, S.M., Hubbard, M.S., and Upreti, B.N., 2002, Records of the evolution of the Himalayan orogen from in-situ Th-Pb ion microprobe dating of monazite: eastern Nepal and western Garhwal: Journal of Asian Earth Science, v. 20, p. 459-479.

Chen, Z., Liu, Y., Hodges, K. V., Burchfiel, B. C., Royden, L. H., and Deng, C. 1990, The Kangmar Dome; a metamorphic core complex in southern Xizang (Tibet): Science, v. 250, p. 1552−1556.

Cottle, J.M., Jessup, M.J., Newell, M.J., Searle, M.P., Law, R.D., and Horstwood, M., 2007, Structural insights into the early stages of exhumation along an orogen-scale detachment: the South Tibetan Detachment system, Dzakaa Chu section, eastern Himalaya: Journal of Structural Geology, v. 29, p. 1781-1797.

Cottle, J.M., Jessup, M.J., Newell, D.L., Horstwood, S.A., Noble, S.R., Parrish, R.R., Waters, D.J., and Searle, M.P., 2009, Geochronology of granulitized eclogite from the Ama Drime Massif: implications for the tectonic evolution of the South Tibetan Himalaya: Tectonics, v. 28, p. 1-25.

Cottle, J.M., Searle, M.P., Horstwood, M.S.A., and Waters, D.J. 2009b, Timing of mid-crustal metamorphism, melting and deformation in the Mount Everest region of southern Tibet revealed by U(-Th)-Pb geochronology: Journal of Geology, v. 117, p. 643-664.

Cottle, J.M., Waters, D.J., Riley, D., Beyssac, O., and Jessup, M.J., 2011, Metamorphic history of the South Tibetan Detachment System, Mt. Everest region, revealed by RSCM thermometry and phase equilibria modeling: Journal of Metamorphic Geology, v. 29, p. 561-582.

Dewane, T.J., Stockli, D.F., Hager, C., Taylor, M., Ding, L., and Lee, J., 2006. Timing of Cenozoic E-W extension in Tangra Yum Co rift, central Tibet: Journal of Asian Earth Sciences, v. 26, p. 133.

Fitz Gerald, J.D., and Stünitz, H., 1993, Deformation of granitoids at low metamorphic grades. I: Reactions and grain size reduction: Tectonophysics, v. 221, p. 269-297.

Fossen, H., and Tikoff, B., 1997, Forward modeling of non-steady-state deformations and the 'minimum strain path': Journal of Structural Geology, v. 19, p. 987-996.

Fossen, H., and Tikoff, B., 1998, Forward modeling of non-steady-state deformations and the 'minimum strain path': Reply: Journal of Structural Geology, v. 20, p. 979-981.

Gaetani, M., and Garzanti, E., 1991, Multicyclic history of the northern India continental margin (northwestern Himalaya): American Association of Petroleum of Geologists Bulletin, v. 75, p. 1427-1446.

Gansser, A., 1964, Geology of the Himalayas: Wiley-Interscience, London.

Garzanti, E., 1999, Stratigraphy and sedimentary history of the Nepal Tethys Himalaya passive margin: Journal of Asian Earth Sciences, v. 17, p. 805-827.

Goscombe, B., Gray, D., and Hand, M., 2006, Crustal architecture of the Himalayan meamotphic front in eastern Nepal: Gondwana Research, v. 10, p. 232-255.

Grasemann, B., Fritz, H., and Vannay, J.-C., 1999, Quantitative kinematic flow analysis from the Main Central Thrust Zone (NW-Himalaya, India): implications for a decelerating strain path and the extrusion of orogenic wedges: Journal of Structural Geology, v. 21, p. 837-853.

Groppo, C., Lombardo, B., Rolfo, F., and Pertusanti, P., 2007, Clockwise exhumation path of granulitized eclogites from the Ama Drime range (Eastern Himalayas), Journal of Metamorphic Geology, v. 25, p. 51-75.

Grujic, D., 2006, Channel flow and continental collision tectonics; an overview, *in* Law, R.D., Searle, M.P., and Godin, L., eds., Channel flow, ductile extrusion and exhumation in

continental collision zones: Geological Society [London] Special Publication, v. 268, p. 25-37.
Grujic, D., Hollister, L.S., and Parrish, R.R., 2002, Himalayan metamorphic sequence as an orogenic channel: insight from Bhutan: Earth and Planetary Letters, v. 198, p. 177-191.
Grujic, D., Martin, C., Davidson, C., Hollister, L.S., Kuendig, R., Pavlis, T.L., and Schmid, S.M., 1996, Ductile extrusion of the Higher Himalayan Crystalline in Bhutan; evidence from quartz microfabrics: Tectonophysics, v. 260, p. 21-43.
Guillot, S., Mahéo, G., deSigoyer, J., Hattori, K.H., and Pêcher, A., 2008, Tethyan and Indian subduction viewed from the Himalayan high- to ultrahigh-pressure metamorphic rocks: Tectonophysics, v. 451, p. 225-241.
Hager, C., Stockli, D.F., Dewane, T.J., and Ding, L., 2006, Episodic Mio-Pliocene rifting in south-central Tibet. Thermochronometric constraints from the Xainza rift: Eos (Transactions, American Geophysical Union), v. 87, T34C-02.
Hippert, J. F., and Valarelli, J.V., 1998, Myrmekite: constraints on the available models and a new hypothesis for its formation: European Journal of Mineralogy, v. 10, p. 317-331.
Hirth, G., Teyssier, C., and Dunlap, J., 2001, An evaluation of quartzite flow laws based on comparisons between experimentally and naturally deformed rocks: International Journal of Earth Sciences, v. 90, p. 77-87.
Hirth, G., and Tullis, J., 1992, Dislocation creep regimes in quartz aggregates: Journal of Structural Geology, v. 14, p. 145-159.
Hodges, K.V., 2000, Tectonics of the Himalaya and southern Tibet from two perspectives: Geological Society of America Bulletin, v. 112, p. 324-350.
Hodges, K.V., Hurtado, J.M., and Whipple, K.X., 2001, Southward extrusion of Tibetan crust and its effect on Himalayan tectonics: Tectonics, v. 20, p. 799-809.
Hodges, K.V., Parrish, R., Housh, T., Lux, D., Burchfiel, B., Royden, L., and Chen, Z., 1992, Simultaneous Miocene extension and shortening in the Himalayan orogen: Science, v. 258, p. 1466-1470.
Holland, T.J., and Powell, R., 2000, AX: A program to calculate activities of mineral end members from chemical analyses (usually determined by electron microprobe).
Hubbard, M.S., and Harrison, T.M., 1989, $^{40}Ar/^{39}Ar$ age constrains on deformation and metamorphism in the Main Central Thrust Zone and Tibetan slab, eastern Nepal Himalaya: Tectonics, v. 8, p. 865-880.
Iacopini, D., Carosi, R., Montomoli, C., and Passchier, C.W., 2008, Strain analysis and vorticity of flow in the Northern Sardinian Variscan Belt: recognition of a partitioned oblique deformation event: Tectonophysics, v. 446, p. 77-96.
Jessell, M.W., 1987, Grain-boundary migration microstructures in a naturally deformed quartzite: Journal of Structural Geology, v. 9, p. 1007-1014.
Jessup, M., and Cottle, J., Progression from south-directed extrusion to orogen-parallel extension in the southern margin of the Tibetan Plateau, Mount Everest Region, Tibet: The Journal of Geology, v. 118, p. 467-486.
Jessup, M., Cottle, J.M., Newell, D., Berger, A., and Spotila, J., 2008c. Exhumation of the Trans-Himalayan Ama Drime Massif: Implications for Orogen-Parallel Mid-Crustal Flow and Exhumation on the Southern Margin of the Tibetan Plateau: Joint meeting of the Geological Society of America.

Jessup, M.J., Cottle, J.M., Searle, M.P., Law, R.D., Newell, D.L., Tracy, R.J., and Waters, D.J., 2008b, P-T-t-D paths of Everest Series schist, Nepal: Journal of Metamorphic Geology, v. 26, p. 717-739.

Jessup, M.J., Law, R.D., and Frassi, C., 2007, The rigid grain net (RGN): an alternative method for estimating mean kinematic vorticity number (W_m): Journal of Structural Geology, v. 29, p. 411-421.

Jessup, M.J., Law, R.D., Searle, M.P., and Hubbard, M.S., 2006, Structural evolution and vorticity of flow during extrusion and exhumation of the Greater Himalayan Slab, Mount Everest Massif, Tibet/Nepal: Implications for orogen-scale flow partitioning, *in* Law, R.D., Searle, M.P., and Godin, L., eds., Channel flow, ductile extrusion and exhumation in continental collision zones: Geological Society [London] Special Publication, v. 268, p. 379-413.

Jessup, M., Newell, D.L., Cottle, J.M., Berger, A., and Spotila, J., 2008a, Orogen-parallel extension and exhumation enhanced by denudation in the trans-Himalayan Arun River gorge, Ama Drime Massif, Tibet-Nepal: Geology, v. 36, p. 587-590.

Jiang, D., 1998, Forward modeling of non-steady-state deformations and the 'minimum strain path': Discussion: Journal of Structural Geology, v. 20, p. 975-977.

Johnson, S., Lenferink, H., Price, N., Marsh, J., Koons, P., West, D., and Beane, R., 2009a, Clast-based kinematic vorticity gauges: The effect of slip at matrix/clast interfaces: Journal of Strucural Geology, v. 31, p. 1322-1339.

Johnson, S., Lenferink, H., Marsh, J., Price, N., Koons, P., and West, D., 2009b, Kinematic vorticity analysis and evolving strength of mylonitic shear zones: New data and numerical results: Geology, v. 37, p. 1075-1078.

Kali, E., Leloup, P.H., Arnaud, N., Mahéo, G., Liu, D., Boutonnet, E., VanderWoerd, J., Xiaohan, L., Liu-Zeng, J., and Haibing, L., 2010, Exhumation history of the deepest central Himalayan rocks (Ama Drime range): key P-T-D-t constraints on orogenic models: Tectonics, v. 29, p. 1-31.

Kapp, P., and Guynn, J., 2004, Indian punch rifts Tibet: Geology, v. 32, p. 993-996.

Kruhl, J.H., 1998, Reply: Prism- and basal-plane parallel subgrain boundaries in quartz: a Microstructural geothermometer: Journal of Metamorphic Petrology, v. 16, p. 142-146.

Langille, J., Lee, J., Hacker, B., and Seward, G., 2010, Middle crustal ductile deformation patterns in southern Tibet: insights from vorticity studies in Mabja Dome: Journal of Structural Geology, v. 32, p. 70-85.

Larson, K.P., and Godin, L., 2009, Kinematics of the Greater Himalayan series, Dhaulagiri Himal: implications for the structural framework of central Nepal: Journal of the Geological Society [London], v. 166, p. 25-43.

Law, R.D., 1990, Crystallographic fabrics: a selective review of their applications to research in structural geology, *in* Knipe, R.J., Rutter, E.H., eds., Deformation mechanisms, rheology and tectonics: Geological Society [London] Special Publication, v. 54, p. 335-352.

Law, R.D., Morgan, S.S., Casey, M., Sylvester, C.M., and Nyman, M., 1992, The Papoose Flat pluton of eastern California: a re-assessment of its emplacement history in the light of new microstructural and crystallographic fabric observations: Transactions of the Royal Society of Edinburgh: Earth Sciences, v. 83, p. 361-375.

Law, R.D., Searle, M.P., and Simpson, R.L., 2004, Strain, deformation temperatures and vorticity of flow at the top of the Greater Himalayan Slab, Everest Massif, Tibet: Journal of the Geological Society [London], v. 161, p. 305-320.

Lee, J., Dinklage, W.S., Hacker, B.R., Wang, Y., Gans, P.B., Calvert, A., Wan, J., Chen, W., Blythe, A., and McClelland, W., 2000, Evolution of the Kangmar Dome, southern Tibet: structural, petrologic, and thermochronologic constraints: Tectonics, v. 19, p. 872-896.

Lee, J., Dinklage, W.S., Wang, Y., and Wan, J., 2002, Geology of the Kangmar Dome, southern Tibet with explanatory notes: Geological Society of America Map and Chart Series MCH090, 1:50,000 scale, 8 p.

Lee, J., Hacker, B., and Wang, Y, 2004, Evolution of North Himalayan gneiss domes: structural and metamorphic studies in Mabja Dome, southern Tibet: Journal of Structural Geology, v. 26, p. 2297-2316.

Lee, J., McClelland, W., Wang, Y., Blythe, A., and McWilliams, M., 2006, Oligocene-Miocene middle crustal flow in the southern Tibet: geochronology of Mabja Dome, *in* Law, R.D., Searle, M.P., and Godin, L., eds., Channel flow, ductile extrusion and exhumation in continental collision zones: Geological Society [London] Special Publication, v. 268, p. 445-469.

Lee, J., and Whitehouse, M.J., 2007, Onset of mid-crustal extensional flow in southern Tibet: Evidence from U/Pb zircon ages: Geology, v. 35, p. 45-48.

Le Fort, P., 1975, Himalayas; the collided range; present knowledge of the continental arc: American Journal of Science, v. 275-A, p. 1-44.

Leloup, P., Mahéo, G., Kali, E., Boutonnet, E., Liu, D., Xiahan, L., and Haibing, L., 2010, The South Tibetan detachment shear zone in the Dinggye area: Time constraints on extrusion models of the Himalayas: Earth and Planetary Science Letters, v. 292, p. 1-16.

Lister, G.S., and Dornsiepen, U.F., 1982, Fabric transitions in the Saxony granulite terrain: Journal of Structural Geology, v. 4, p. 81-93.

Lister, G.S., and Hobbs, B.E., 1980, The simulation of fabric development during plastic deformation and its application to quartzite: the influence of deformation history: Journal of Structural Geology, v. 2, p. 355-370.

Lister, G.S., Paterson, M.S., and Hobbs, B.E., 1978, The simulation of fabric development in plastic deformation and its application to quartzite; the model: Tectonophysics, v. 45, p. 107-158.

Liu, G., and Einsele, G., 1994, Sedimentary history of the Tethyan basin in the Tibetan Himalayas: Geologische Rundschau, v. 82, p. 32-61.

Liu, Y., Siebel, W., Massonne, H., and Xiao, X., 2007, Geochronological and petrological constraints for tectonic evolution of the central Greater Himalayan series in the Kharta area, southern Tibet: Journal of Geology, v. 115, p. 215-242.

Lloyd, G.E., and Freeman, B., 1994, Dynamic recrystallization of quartz under greenschist conditions: Journal of Structural Geology, v. 16, p. 867-881.

Lombardo, B., and Rolfo, F., 2000, Two contrasting eclogite types in the Himalayas: implications for the Himalayan orogeny: Journal of Geodynamics, v. 30, p. 37-60.

Lombardo, B., Pertusati, P., Rolfo, F., and Visonà, D., 1998, First report of eclogites from the E Himalaya: implications for the Himalayan orogeny: Memorie di Scienze Geogiche dell'Università di Padova, v. 50, p. 67-68.

Mainprice, D., Bouchez, J.L., Blumenfeld, P., and Tubia, J.M., 1986, Dominant c slip in naturally deformed quartz; implications for dramatic plastic softening at high temperature: Geology, v. 14, p. 819-822.
Murphy, M.A., 2007, Isotopic characteristics of the Gurla Mandhata metamorphic core complex:implications for the architecture of the Himalayan orogen: Geology, v. 35, p. 983-986.
Murphy, M.A., and Copeland, P., 2005, Trantensional deformation in the central Himalaya and its role in accommodating growth of the Himalayan orogen: Tectonics, v. 24, p. 1-19.
Murphy, M. A., and Harrison, T. M., 1999, Relationship between leucogranites and the Qomolangma Detachment in the Rongbuk Valley, South Tibet: Geology, v. 27, p. 831-834.
Murphy, M.A., Yin, A., Kapp, P., Harrison, T.M., and Manning, C.E., 2002, Structural evolution of the Gurla Mandhata detachment system, southwest Tibet: implications for the eastward extent of the Karakoram fault system: Geological Society of America Bulletin, v. 114, p. 428-447.
Nekvasil, H., and Burnham, C. W., 1987, The calculated individual effects of pressure and water content on phase equilibiria in the granite system, *in* Mysen, B. O., ed., Magmatic processes: Physicochemical principles: Geochemical Society, University Park, Pennsyvania, 500 p.
Nelson, K.D., Zhao, W., Brown, L.D., Kuo, J., Jinkai, C., Liu, X., Klemperer, S., Makovsky, Y., Meissner, R., Mechie, J., Kind, R., Wenzel, F., Ni, J., Nabelek, J., Leshou, C., Tan, H., Wei, W., Jones, A., Booker, J., Unsworth, M., Kidd, W., Hauck, M., Alsdorf, D., Ross, A., Cogan, M., Wu, C., Sandvol, E., and Edwards, M., 1996, Partially molten middle crust beneath southern Tibet: synthesis of project INDEPTH results: Science, v. 274, p. 1684-1688.
Nyman, M.W., Law, R.D., and Morgan, S.S., 1995, Conditions of contact metamorphism, Papoose Flat Pluton, eastern California, USA: implications for cooling and strain histories: Journal of Metamorphic Geology, v. 13, p. 627-643.
Okudaira, T., Takesbita, T., Hara, I., and Ando, J., 1995, A new estimate of the conditions for transition from basal <a> to prism [c] slip in naturally deformed quartz: Tectonophysics, v. 250, p. 31-46.
Passchier, C.W., 1987, Stable positions of rigid objects in non-coaxial flow: a study in vorticity analysis: Journal of Structural Geology, v. 9, p. 679-690.
Passchier, C.W., 1988, The use of Mohr circles to describe non-coaxial progressive deformation: Tectonophysics, v. 149, p. 323-338.
Passchier, C.W., and Trouw, R.A.J., 2005, Microtectonics: Springer Berlin Heidelberg, New York.
Pognante, U., and Benna, P., 1993, Metamorphic zonation, migmatization and leucogranites along the Everest transect of eastern Nepal and Tibet: record of an exhumation history: Geological Society Special Publications, v. 74, p. 323-340.
Pryer, L.L., 1993, Microstructures in feldspars from a major crustal thrust zone: the Grenville Front, Ontario, Canada: Journal of Structural Geology, v. 15, p. 21-36.
Quigley, M., Liangjun, Y., Gregory, C., Corvino, A., Sandiford, M., Wilson, C.J.L., and Xiaohan, L., 2008, U/Pb SHRIMP zircon geochronology and T-t-d history of the Kampa

Dome, southern Tibet; implications for tectonic evolution of the North Himalayan gneiss domes: Tectonophysics, v. 446, p. 97-113.
Quigley, M., Liangjun, Y., Xiaohan, L., Wilson, C.J.L., Sandiford, M., and Phillips, D., 2006, $^{40}Ar/^{39}Ar$ thermochronology of the Kampa Dome, southern Tibet; implications for tectonics evolution of the North Himalayan gneiss domes: Tectonophysics, v. 421, p. 269-297.
Simpson, R.L., Parrish, R.R., Searle, M.P., and Waters, D.J., 2000, Two episodes of monazite crystallization during metamorphism and crustal melting in the Everest region of the Nepalese Himalaya: Geology, v. 28, p. 403-406.
Simpson, C., and Wintsch, R.P., 1989, Evidence for deformation-induced K-feldspar replacement by myrmekite: Journal of Metamorphic Geology, v. 7, p. 261-275.
Searle, M., 1999, Extensional and compressional faults in the Everest-Lhotse Massif, Khumbu Himalaya, Nepal: Journal of the Geological Society, v. 156, p. 227-240.
Searle, M., Law, R., and Jessup, M., 2006, Crustal structure, restoration and evolution of the Greater Himalaya in Nepal-South Tibet: implications for channel flow and ductile extrusion of the middle crust, *in* Law, R.D., Searle, M.P., Godin, L., eds., Channel flow, ductile extrusion and exhumation in continental collision zones: Geological Society [London] Special Publication, v. 268, p. 355-378.
Searle, M., Law, R., Godin, L., Larson, K., Streule, M., Cottle, J., and Jessup, M., 2008, Defining the Himalayan Central Thrust in Nepal: Journal of the Geological Society [London], v. 165, p. 523-534.
Searle, M.P., Simpson, R.L., Law, R.D., Parrish, R.R., and Waters, D.J., 2003, The structural geometry, metamorphic and magmatic evolution of the Everest Massif, High Himalaya of Nepal-South Tibet: Journal of the Geological Society [London], v. 160, p. 345-366.
Stipp, M., Stünitz, H., Heilbronner, R., and Schmid, S.M., 2002a, The eastern Tonale fault zone: a 'natural laboratory' for crystal plastic deformation of quartz over a temperature range from 250 to 700 ° C: Journal of Structural Geology, v. 24, p. 1861-1884.
Stipp, M., Stünitz, H., Heilbronner, R., and Schmid, S.M., 2002b, Dynamic recrystallization of quartz: correlation between natural and experimental conditions, *in* De Meer, S., Drury, M.R., De Bresser, J.H.P., and Pennock, G.M., eds., Deformation mechanisms, rheology and tectonics: Current status and future perspectives: Geological Society [London] Special Publications, v. 200, p. 171-190.
Stockli, D.F., Taylor, M., Yin, A., Harrison, T.M., D'Andrea, J., Lin, D., and Kapp, P., 2002, Late Miocene-Pliocene inception of E-W extension in Tibet as evidenced by apatite (U-Th)/He data: Geological Society of America Abstracts with Programs, v. 34, p. 411.
Stormer, J.C., 1975, Practical two-feldspar geothermometer: American Mineralogist, v. 60, p. 667-674.
Taylor, M., Yin, A., Ryerson, F., Kapp, P., and Ding, L., 2003, Conjugate strike-slip faulting along the Bangong-Nujiang suture zone accommodates coeval east-west extension and north-south shortening in the interior of the Tibetan Plateau: Tectonics, v. 22, p. 1-16.
Theide, R.C., Arrowsmith, J.R., and Bookhagen, B., 2005, From tectonically to erosionally controlled development of the Himalayan orogen: Geology, v. 33, p. 689-692.
Theide, R.C., Arrowsmith, J.R., Bookhagen, B., McWilliams, M., Sobel, R., and Strecker, M., 2006, Dome formation and extension in the Tethyan Himalaya, Leo Pargil, northwest India: Geological Society of America Bulletin, v. 118, p. 635-650.

Tikoff, B., and Fossen, H., 1995, The limitations of three-dimensional kinematic vorticity analysis: Journal of Structural Geology, v. 17, p. 1771-1784.
Tullis, J., Christie, J.M., and Griggs, D.T., 1973, Microstructures and preferred orientations of experimentally deformed quartzites: Geological Society of America Bulletin, v. 84, p. 297-314.
Tullis, J., and Yund, R., 1991, Diffusion creep in feldspar aggregates: experimental evidence: Journal of Structural Geology, v. 13, p. 987-1000.
Tullis, J., and Yund, R., 1992, The brittle-ductile transition in feldspar aggregates; an experimental study, *in* Evans, B., and Wong, T.F., eds., Fault mechanics and transport properties in rocks: Academic Press, New York, p. 89-118.
Vannay, J.-C., and Grasemann, B., 1998, Inverted metamorphism in the High Himalaya of Himachal Pradesh (NW India): Phase equilibria versus thermobarometry: Schweizerische Mineralogische und Petrographische Mitteilungen, v. 78, p. 107-132.
Vernon, R.H., 1991, Questions about myrmekite in deformed rocks: Journal of Structural Geology, v. 13, p. 979-985.
Viskupic, K., Hodges, K.V., and Bowring, S.A., 2005, Timescales of melt generation and the thermal evolution of the Himalayan metamorphic core, Everest region, eastern Nepal: Contributions of Mineralogy and Petrology, v. 149, p. 1-21.
Wallis, S.R., 1995, Vorticity analysis and recognition of ductile extension in the Sanbagawa belt, SW Japan: Journal of Structural Geology, v. 17, p. 1077-1093.
Wallis, S.R., Platt, J.P., and Knott, S.D., 1993, Recognition of syn-convergence extension in accretionary wedges with examples from the Calabrian Arc and the Eastern Alps: American Journal of Science, v. 293, p. 463-495.
Wen, S., and Nekvasil, H., 1994, SOLVCALC: An interactive graphics program package for calculating the ternary feldspar solvus and for two-feldspar geothermometry: Computers and Geosciences, v. 20, p. 1025-1040.
Wenk, H.R., Canova, G., Molinari, A., and Kocks, U.F., 1989, Viscoplastic modeling of texture development in quartzite: Journal of Geophysical Research, v. 94, p. 17895-17906.
Whitney, J.A., and Stormer, J.C., 1977, The distribution of $NaAlSi_3O_8$ between coexisting microcline and plagioclase and its effect on geothermometric calculations: American Mineralogist, v. 62, p. 687-691.
Wu, C., Nelson, K.D., Wortman, G., Samson, S.D., Yue, Y., Li, J., Kidd, W.S.F., and Edwards, M.A., 1998, Yadong cross structure and South Tibetan Detachment in the east central Himalaya (89°-90°E): Tectonics, v. 17, p. 28-45.
Xypolias, P., 2009, Some new aspects of kinematic vorticity analysis in naturally deformed quartzites: Journal of Structural Geology, v. 31, p. 3-10.
Xypolias, P., and Koukouvelas, I. K., 2001, Kinematic vorticity and strain patterns associated with ductile extrusion in the Chelmos shear zone (External Hellenides, Greece): Tectonophysics, v. 338, p. 59-77.
Zhang, J., and Guo, L., 2007, Structure and geochronology of the southern Xainza-Dinggyê rift and its relationship to the South Tibetan detachment system: Journal of Asian Earth Sciences, v. 29, p. 722-736.

Zhang, H., Harris, N., Parrish, R., Kelley, S., Zhang, L., Rogers, N., Argles, T., and King, J., 2004, Causes and consequences of protracted melting of the mid-crust exposed in the North Himalayan antiform: Earth and Planetary Science Letters, v. 228, p. 195-212.

Appendix 1.1

Appendix 1.1. Sample Locations.

Sample	Latitude	Longitude	Sample	Latitude	Longitude
KA-25	28.0961°	87.3668°	KA-40	28.1480°	87.3713°
KA-31	28.0951°	87.3669°	AD07-20	28.2654°	87.3919°
KA-26	28.0951°	87.3669°	AD07-21	28.2654°	87.3919°
KA-32	28.0951°	87.3669°	AD07-17	28.2655°	87.3924°
KA-17	28.0946°	87.3667°	AD07-16	28.2655°	87.3924°
KA-20	28.0946°	87.3667°	AD07-15	28.2655°	87.3924°
KA-22	28.0946°	87.3667°	AD07-14	28.2655°	87.3924°
KA-23	28.0946°	87.3667°	AD07-13	28.2655°	87.3924°
KA-14	28.0946°	87.3667°	AD07-12	28.2655°	87.3924°
KA-13	28.0946°	87.3667°	AD07-10	28.2655°	87.3924°
KA-01	28.0954°	87.3657°	AD07-11	28.2655°	87.3924°
KA-02	28.0952°	87.3659°	AD07-09	28.2655°	87.3924°
KA-12	28.0944°	87.3664°	AD07-08	28.2639°	87.3961°
AD07-28	28.0947°	87.3652°	AD07-07	28.2665°	87.3937°
AD07-29	28.0950°	87.3655°	AD07-05	28.2665°	87.3937°
AD07-30	28.0950°	87.3655°	AD07-06	28.2665°	87.3937°
AD07-31	28.0950°	87.3655°	AD07-04	28.2662°	87.3939°
AD07-27	28.0945°	28.0945°	AD07-03	28.2662°	87.3946°
MJAD-05	28.0872°	87.3707°	AD07-02	28.2662°	87.3954°
KA-44	28.1470°	87.3699°	MJAD-17	28.1109°	87.6471°
KA-41	28.1473°	87.3703°	MJAD-22	28.1193°	87.6442°
KA-43	28.1473°	87.3703°	MJAD-23	28.1193°	87.6442°
KA-39	28.1480°	87.3713°			

Appendix 1.2

Additional Rigid Grain Nets

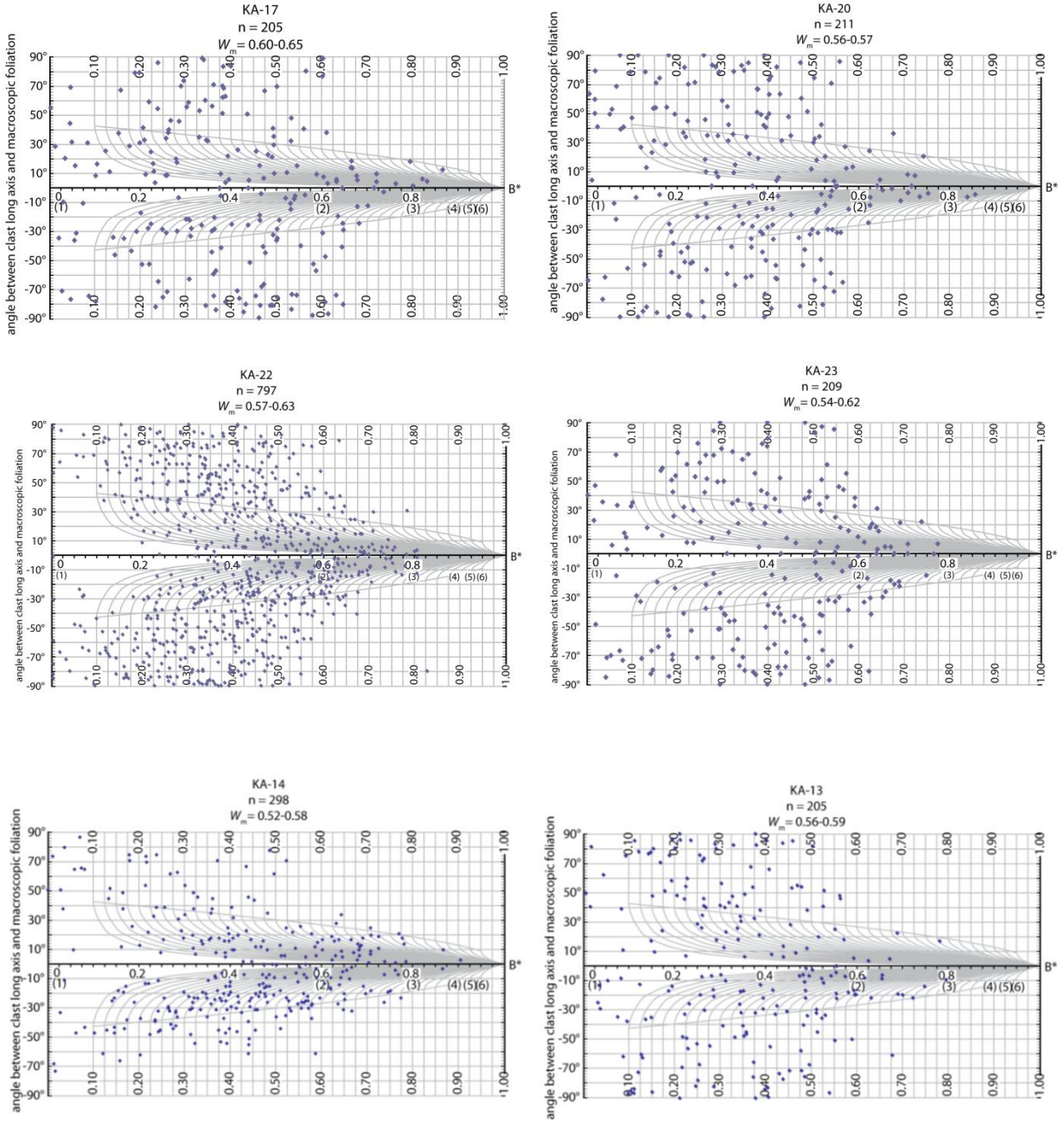

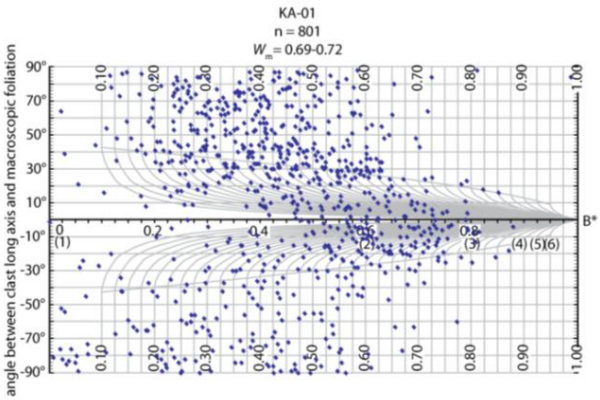
KA-01
n = 801
W_m = 0.69-0.72
angle between clast long axis and macroscopic foliation
B*

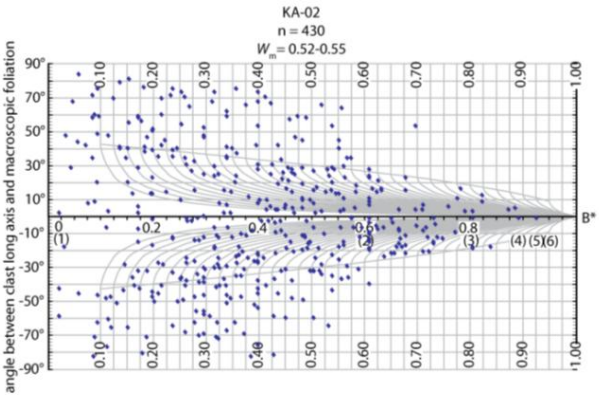
KA-02
n = 430
W_m = 0.52-0.55
angle between clast long axis and macroscopic foliation
B*

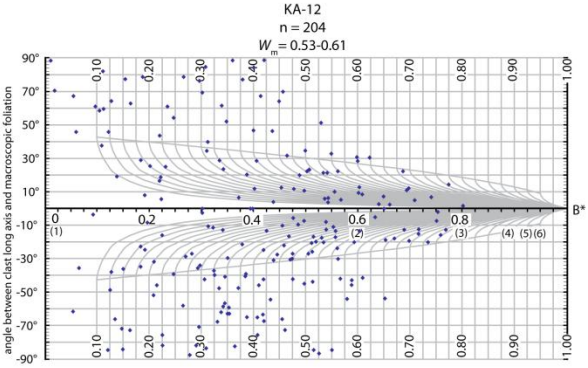
KA-12
n = 204
W_m = 0.53-0.61
angle between clast long axis and macroscopic foliation
B*

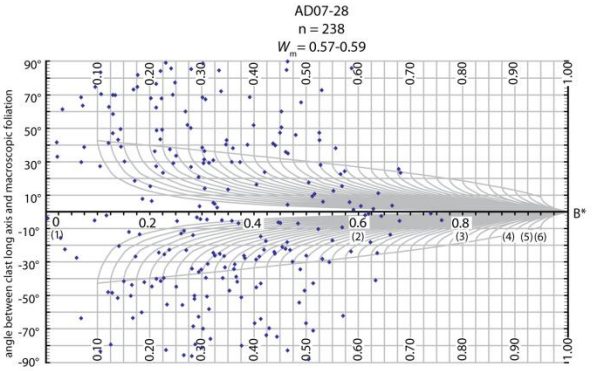
AD07-28
n = 238
W_m = 0.57-0.59
angle between clast long axis and macroscopic foliation
B*

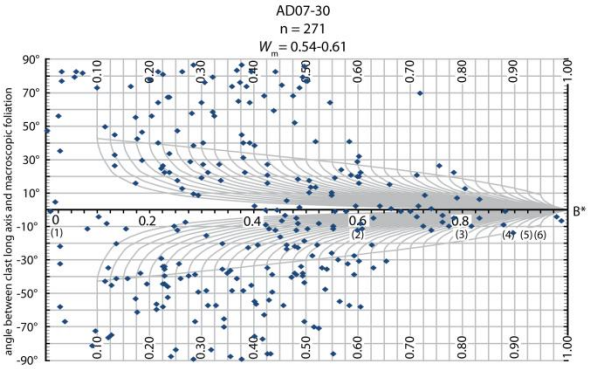
AD07-30
n = 271
W_m = 0.54-0.61
angle between clast long axis and macroscopic foliation
B*

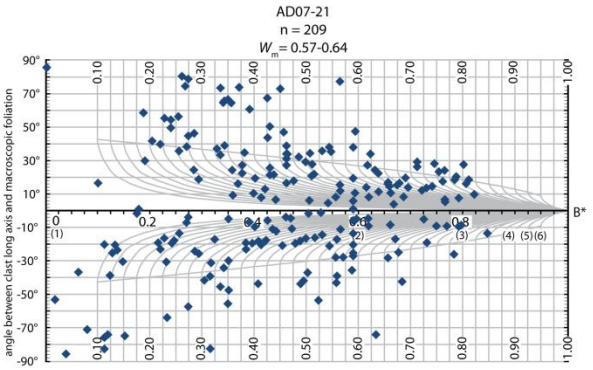
AD07-21
n = 209
W_m = 0.57-0.64
angle between clast long axis and macroscopic foliation
B*

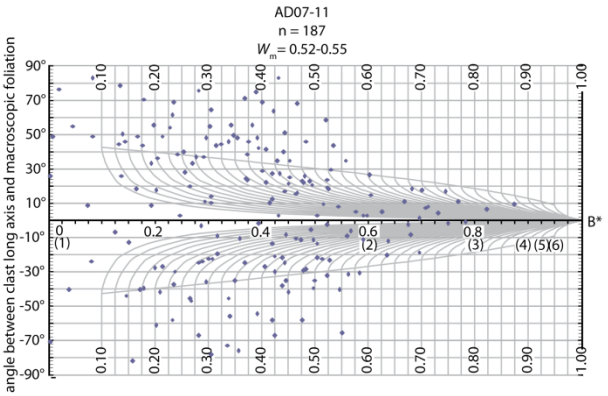
AD07-11
n = 187
W_m = 0.52-0.55
angle between clast long axis and macroscopic foliation
B*
(1)
(2)
(3)
(4) (5)(6)

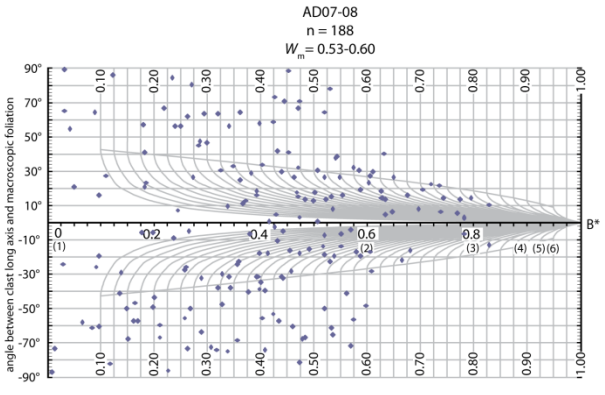
AD07-08
n = 188
W_m = 0.53-0.60
angle between clast long axis and macroscopic foliation
B*
(1)
(2)
(3)
(4) (5)(6)

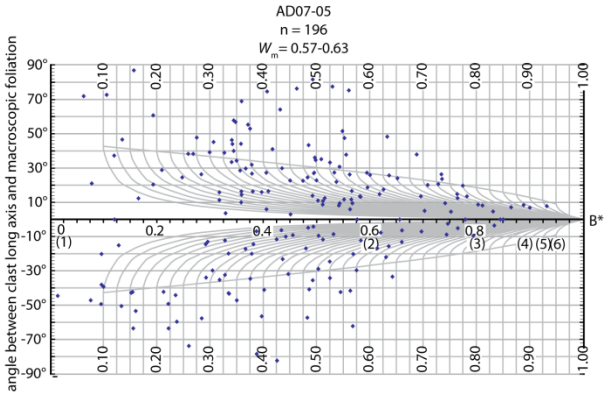
AD07-05
n = 196
W_m = 0.57-0.63
angle between clast long axis and macroscopic foliation
B*
(1)
(2)
(3)
(4) (5)(6)

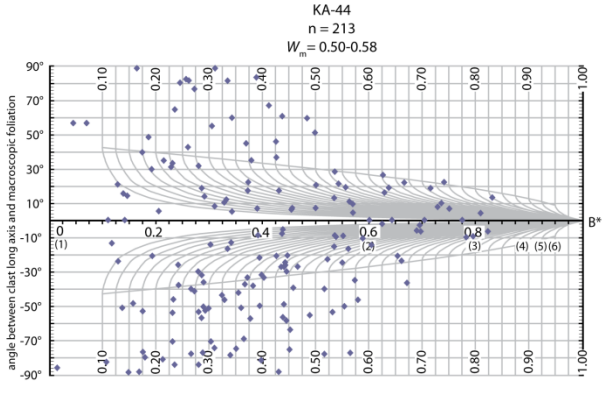
KA-44
n = 213
W_m = 0.50-0.58
angle between clast long axis and macroscopic foliation
B*
(1)
(2)
(3)
(4) (5)(6)

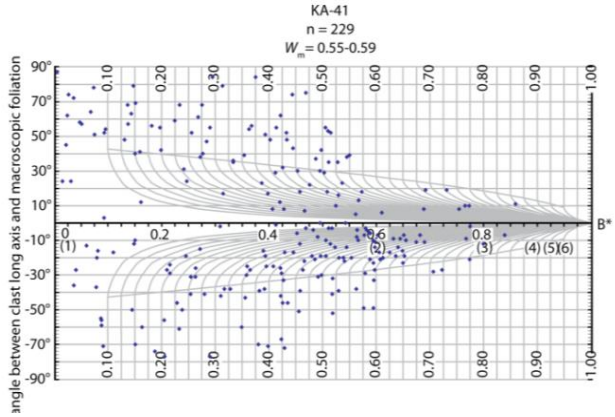
KA-41
n = 229
W_m = 0.55-0.59
angle between clast long axis and macroscopic foliation
B*
(1)
(2)
(3)
(4) (5)(6)

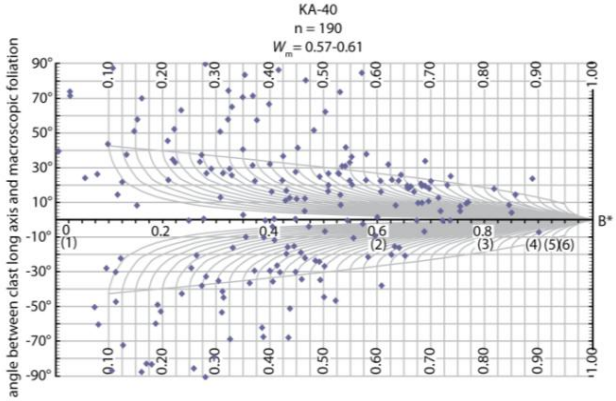
KA-40
n = 190
W_m = 0.57-0.61
angle between clast long axis and macroscopic foliation
B*
(1)
(2)
(3)
(4) (5)(6)

CHAPTER II:
TIMING OF METAMORPHISM, MELTING, AND EXHUMATION OF THE LEO PARGIL DOME, NORTHWEST INDIA

A version of this chapter was originally submitted for publication by Jackie Langille, Micah Jessup, John Cottle, Graham Lederer, and Talat Ahmad:

Langille, J., Jessup, M., Cottle, J., Lederer, G., and Ahmad, T., in review, Timing of metamorphism, melting, and exhumation of the Leo Pargil dome, northwest India: Journal of Metamorphic Geology.

My major contributions to this paper include: (1) conducting the field mapping and sample collection, (2) conducting the metamorphic monazite geochronology and thermobarometry analyses that are included in the manuscript, (3) writing the manuscript, (4) creating the illustrations, and (5) submitting and revising the manuscript.

Abstract

The Leo Pargil dome, northwest India, is a 30 km-wide, northeast trending structure that is cored by gneiss and mantled by amphibolite-facies metamorphic rocks that are intruded by a leucogranite injection complex. Oppositely dipping, normal-sense shear zones that accommodated orogen-parallel extension within a convergent orogen bound the dome. The broadly distributed Leo Pargil shear zone defines the west flank of the dome and separates the dome from the metasedimentary and sedimentary rocks in the hanging wall to the west and south. Thermobarometry and in-situ monazite U-Th-Pb monazite geochronology were conducted on metamorphic rocks from within the dome and in the hanging wall. These data were combined with U-Th-Pb monazite geochronology of leucogranites from the injection complex to evaluate the relationship between metamorphism, crustal melting, and the onset of exhumation. Rocks within the dome and in the hanging wall contain garnet, kyanite, and staurolite porphyroblasts that record prograde Barrovian metamorphism during crustal thickening that reached ~530-630° C and ~7-8 kbar, ending by ~30 Ma. Cordierite and sillimanite overgrowths on Barrovian assemblages within the dome record top-down-to-the-west shearing and near-isothermal decompression of the footwall rocks to ~4 kbar by 23 Ma during an exhumation rate of 1.3 mm/yr. Monazite growth accompanied Barrovian metamorphism and decompression. The leucogranite injection complex within the dome initiated at 23 Ma and continued to 18 Ma. These data show that orogen-parallel extension in this part of the Himalaya occurred earlier than previously documented (16 Ma). Contemporaneous onset of near-isothermal decompression, top-

down-to-the-west shearing, and injection of the leucogranite injection complex suggests that early crustal melting may have created a weakened crust immediately proceeded by localization of strain that promoted shear zone development. Exhumation along the shear zone initiated decompression by 23 Ma in a kinematic setting that favored orogen-parallel extension potentially related to the Karakoram fault to the north, during a time of north-directed extension on the South Tibetan detachment system to the south.

Introduction

Metamorphic domes cored by migmatites and granites are exhumed as a result of various processes during orogenesis. These processes include but are not limited to crustal melting and strain localization in a melt-weakened mid-crust during extension (e.g., Teyssier and Whitney, 2002; Kruckenberg et al., 2008) or oblique extension (e.g., D'Lemos et al., 1992; Whitney et al., 2007; McFadden et al., 2010), doming of mid-crustal rocks triggered by underthrusting (Lee et al., 2000, 2004; Beaumont et al., 2001, 2004), and buoyancy-driven flow of melt-weakened mid-crustal rocks into areas of extension (e.g., Beaumont et al., 2001; Teyssier and Whitney, 2002). Models for exhumation of gneiss domes in the Himalaya have involved south-directed mid-crustal flow (e.g., Lee et al., 2000, 2004; Beaumont et al., 2001, 2004), orogen-parallel extension (e.g., Jessup et al., 2008), and rapid exhumation at the syntaxes (Zeitler et al., 2001). These domes provide an opportunity to investigate the processes of mid-crustal deformation, metamorphism, and melting that drive exhumation and also yield insights into the evolution of mid-crustal flow within a transitional zone between crustal shortening in the foreland and extension in the Tibetan plateau (e.g., Jessup and Cottle, 2010).

The North Himalayan gneiss domes (e.g., Mabja, Malashan, Lhagoi Kangri, and Kangmar domes) in south-central Tibet (e.g., Aoya et al., 2006; Chen et al., 1990; Lee et al., 2000, 2004; Quigley et al., 2006; Larson et al., 2010), located between the South Tibetan detachment system (STDS) and the Indus-Yarlung suture zone, contain deformed mid-crustal rocks of the Greater Himalayan sequence (GHS). One interpretation is that they were exhumed and domed during underthrusting (Lee et al., 2000, 2004). In this model, doming followed middle Miocene mid-crustal anatexis and flow of the GHS as a low-viscosity channel (Burg and Chen, 1984;

Ratschbacher et al., 1994; Wu et al., 1998; Lee et al., 2000, 2004; Lee and Whitehouse, 2007; Larson et al., 2010) between the north-directed STDS above and the south-directed Main Central thrust zone (MCTZ) below. Another interpretation is that the North Himalayan gneiss domes were formed during southward extrusion of the GHS by doming of the ductile mid-crustal channel within the GHS in the hinterland of the orogen (e.g., Grujic et al., 2002; Beaumont et al., 2004; Hodges, 2006; Jamieson et al., 2006).

In contrast to the North Himalayan gneiss domes, the Gurla Mandhata core complex (Murphy et al., 2002; Murphy, 2007) and the Ama Drime Massif (Jessup et al., 2008; Cottle et al., 2009a; Kali et al., 2010) on the southern margin of the Tibetan Plateau were exhumed during orogen-parallel extension since the middle to late Miocene. The Ama Drime Massif in the central Himalaya was exhumed along normal faults and shear zones that reactivated and/or offset the STDS and the MCTZ and post-dates southward extrusion of the GHS (Jessup et al., 2008; Jessup and Cottle, 2010; Langille et al., 2010). The normal faults that bound the Ama Drime Massif extend into the Tibetan Plateau where they are associated with conjugate sets of strike slip faults in the interior of the plateau (Taylor et al., 2003; Kali et al., 2010). The Gurla Mandhata core complex in the western Himalaya is bound by normal faults that accommodate a portion of the orogen-parallel extension in the western Himalaya. In contrast to the Ama Drime Massif, exhumation of the Gurla Mandhata core complex occurred in a zone of transtension associated with strike slip faulting on the Karakoram fault system (Murphy et al., 2000, 2002; Murphy and Burgess, 2006; Murphy, 2007).

The Leo Pargil dome (LPD), located west of the Gurla Mandhata (Fig. 2.1a), is another example of a dome that was potentially exhumed by extension related to strike-slip faults in the Himalaya. Previous investigations of the LPD in northwest India and western Tibet (Fig. 2.1) have suggested alternative interpretations of the dome, either as a North Himalayan gneiss dome (Leech, 2008; Chambers et al., 2009) or as a dome that was exhumed during orogen-parallel extension associated with the Karakoram fault system (Thiede et al., 2006; Hintersberger et al., 2010, 2011), in an analogous manner to the Gurla Mandhata core complex. Others describe the dome as being exhumed during extension of a pull-apart basin associated with the Karakoram fault system (Ni and Barazangi, 1985).

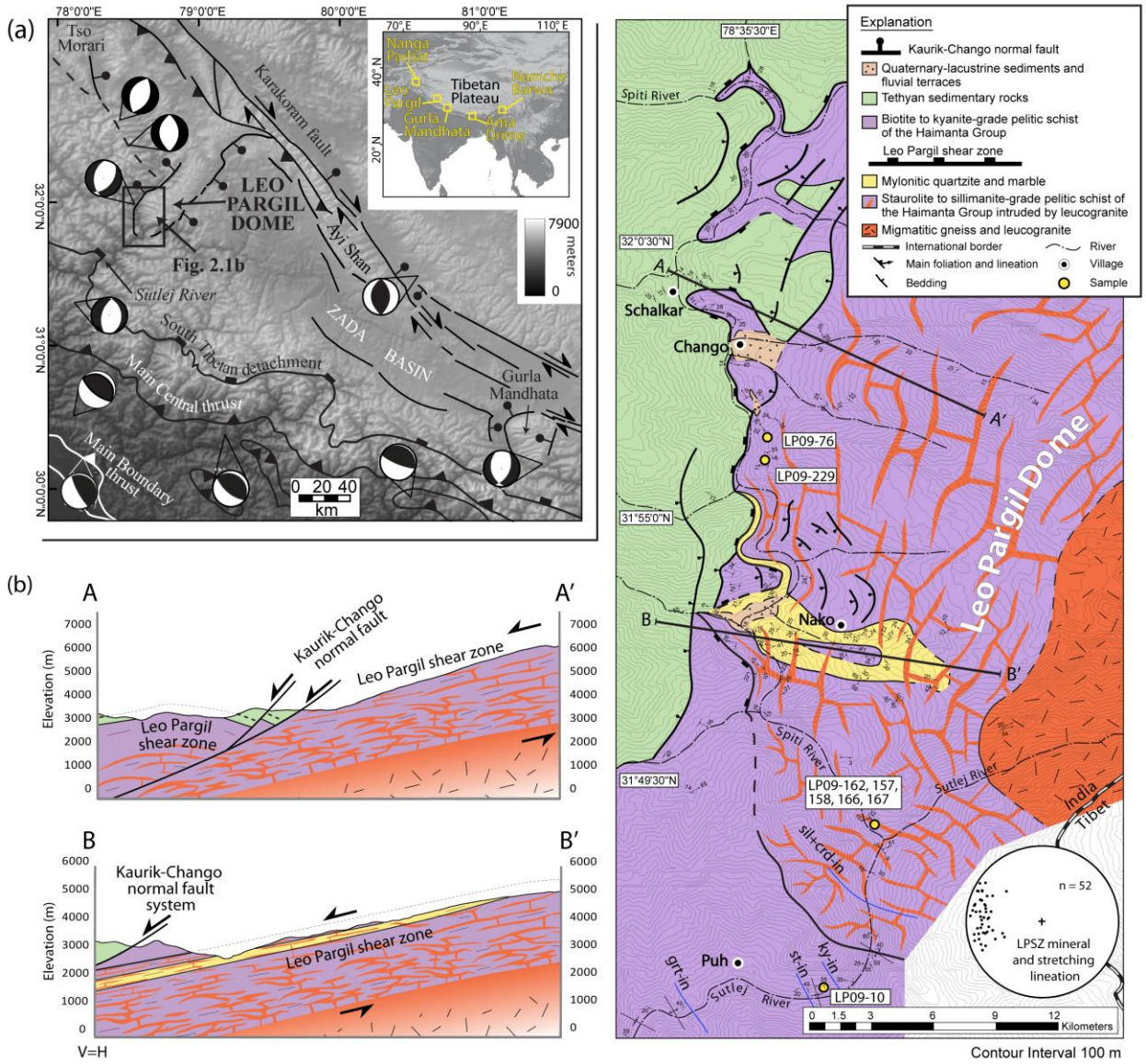

Figure 2.1. *(a) Location of the Leo Pargil dome with focal mechanism solutions for select earthquakes. Modified after Thiede et al. (2006). (b) Geologic map and cross-sections through the Leo Pargil dome. Structural data for the Leo Pargil shear zone (LPSZ) plotted on an equal-area stereonet. Kaurik-Chango normal fault and previous mapping from Thiede et al. (2006). The LPSZ on cross-section A-A' modified from Thiede et al. (2006). Metamorphic isograds are from this study and Chambers et al. (2009). grt, garnet; st, staurolite; ky, kyanite; sil, sillimanite; crd, cordierite.*

The LPD is a 30 km-wide, northeast striking, elongate domal structure composed of amphibolite-facies metamorphic rocks that are cored by migmatites and leucogranites. The

metamorphic rocks in the dome are intruded by multiple generations of leucogranite dikes and sills. The west side of the LPD is defined by the northeast-trending Leo Pargil shear zone (LPSZ) that accommodated exhumation of the high-grade core during orogen-parallel extension (Thiede et al., 2006) that is potentially kinematically linked to the right-lateral Karakoram fault system to the north (Ni and Barazangi, 1985; Murphy et al., 2009; Saylor et al., 2010).

Previous studies have focused on the regional structure and exhumation history of the LPD at temperatures of <350° C (Thiede et al., 2006), the timing of leucogranite injection (Leech, 2008), and the neotectonic history during extension (Hintersberger et al., 2010, 2011). However, major gaps remain in the pressure-temperature-time-deformation (P-T-t-D) paths recorded in the metamorphic rocks exposed within the LPD, and immediately around the LPD. This paper contributes P-T and age constraints from metamorphic rocks and ages from leucogranites to constrain the P-T-t-D path at temperatures of >350° C. These provide a valuable test of the relationship between metamorphism, crustal melting, and the transition from melt-present to solid-state fabric development associated with exhumation of the LPD. These data demonstrate that a complex relationship between early anatexis, strain-localization into melt-weakened crust, decompression-induced melting, and a kinematic setting that favored orogen-parallel extension in the western Himalaya contributed to exhumation of the LPD. These data suggests that orogen-parallel extension in this part of the Himalaya occurred ~7 m.y. earlier than previously documented (e.g., Thiede et al., 2006).

Geologic Setting

Continental collision between the Indian and Eurasian plates since the Eocene resulted in crustal shortening and thickening in the Himalaya (e.g., Searle et al., 1987; Najman et al., 2010). The arc-parallel MCTZ and the STDS accommodated exhumation of the anatectic core of the Himalaya (the GHS) until the middle Miocene (e.g., Grujic et al., 1996, 2002; Grasemann et al., 1999; Vannay and Grasemann, 2001; Vannay et al., 2004; Searle et al., 2006) and as young as ~11 Ma in the eastern Himalaya (Kellett et al., 2009).

After the middle Miocene, movement on the STDS was overprinted by orogen-parallel extension resulting in the development of extensional shear zones and normal faults in southern Tibet (e.g., Ama Drime detachment, Dinggyê graben, Tingri graben, Thakkola graben) that dissect the southern margin of the Tibetan Plateau (e.g., Kapp and Guynn, 2004; Jessup et al., 2008; Jessup and Cottle, 2010; Lee et al., 2011). These normal faults and graben are kinematically linked to strike-slip faults in the interior of the plateau (e.g., Armijo et al., 1986; Taylor et al., 2003; Kapp and Guynn, 2004; Jessup and Cottle, 2010). In the western Himalaya, the Gurla Mandhata detachment records middle Miocene orogen-parallel extension that is kinematically linked to graben formation and strike-slip fault displacement on the Karakoram fault system (e.g., Murphy et al., 2002). Active orogen-parallel extension is >3cm/year across the southern margin of the Himalaya and Tibetan Plateau measured from Global Positioning System geodetic velocity studies (Styron et al., 2011).

The LPD in northwest India is defined on the southwest flank by the normal-sense LPSZ and brittle faults interpreted to accommodate orogen-parallel extension (Fig. 1) (Ni and Barazangi, 1985; Zhang et al., 2000; Thiede et al., 2006; Hintersberger et al., 2010). Amphibolite-facies rocks within the dome are separated from low- to moderate-grade metasedimentary rocks to the west by the LPSZ (Thiede et al., 2006). At the southern end of the dome, the shear zone is a west- to southwest-dipping zone that accommodated normal-displacement during dominantly top-down-to-the-west shearing. The Kaurik-Chango brittle normal fault on the west side of the dome offsets the LPSZ (Singh et al., 1975; Molnar and Chen, 1983; Thiede et al., 2006; Hintersberger et al., 2010). The dome extends northeast to the Ayi Shan that is bound by the Karakoram fault system (Valli et al., 2007; Sanchez et al., 2010) (Fig. 1). The northeast-striking, southeast-dipping Qusum detachment fault (Zhang et al., 2000) separates the southeastern margin of the dome from the Zada basin (Murphy et al., 2009; Saylor et al., 2010).

Regional Geologic Setting

In the southern Sutlej valley, the Main Boundary thrust (MBT) and Munsiari thrust are present in the footwall of the MCTZ (e.g., Vannay and Grasemann, 2001). To the north, the GHS is exposed between the MCTZ and the Sangla detachment (local equivalent to the STDS) (e.g., Vannay and Grasemann, 2001). The base of the Tethyan Sedimentary sequence (TSS) above the Sangla detachment in the northern Sutlej valley is comprised of the Lower Proterozoic to Cambrian metasediments of the Haimanta Group (e.g., Frank et al., 1995; Vannay and Grasemann, 2001; Weismayr and Grasemann, 2002; Chambers et al., 2009) that is intruded at the base by the 488 Ma Akpa (also termed 'Kinnaur Kailas') granite (e.g., Miller et al., 2001).

North from the Akpa granite, metamorphic grade decreases up-section in the north-dipping Haimanta Group from the kyanite-isograd (~650° C, 6-7 kbar) exposed structurally above the Akpa granite to the biotite-isograd approximately 6 km up-section (Chambers et al., 2009). The Haimanta Group transitions to south-dipping at the southern end of the LPD (Fig. 2.1b). Chambers et al. (2009) demonstrated that prograde metamorphism in the Haimanta Group in the Sutlej valley began at >34 Ma with peak burial at 30 Ma and garnet growth ending by 28 Ma. The Haimanta Group contains original sedimentary bedding (seen at the uppermost structural positions as upright ripples and cross beds) that is deformed by recumbent folds. The Upper Haimanta Group is separated from the overlying Ordovician to Jurassic sedimentary rocks of the TSS associated with the former Indian passive margin (e.g., Shian, Pin, and Muth Formations) by an unconformity (Wiesmayr and Grasemann, 2002).

Geology of the Leo Pargil Dome

The southwest flank of the LPD is composed of amphibolite-facies schist that is intruded by several generations of deformed and undeformed leucogranite dikes and sills (e.g., Thiede et al., 2006). From the village of Puh towards the LPD, metamorphic grade increases in the Haimanta Group from the biotite isograd, through the garnet and staurolite-isograds, to the kyanite-isograd adjacent to the dome (Fig. 2.1b). Here, a complex system of leucogranite dikes and sills begins

within the Haimanta Group that are generally undeformed (Fig. 2.2a and b). This system is referred to as the leucogranite injection complex. The dome in the Sutlej valley is defined by the first appearance of the injection complex within Haimanta Group. Rocks within the dome also contain deformed leucogranite that is cross cut by the injection complex thus they appear to predate the injection complex (Fig. 2.2c). In the Spiti valley, the dome is defined as the metamorphic rocks that record top-down-to-the-west shearing associated with the LPSZ. Pelitic host rock (Haimanta Group) near the margins of the dome that is intruded by the injection complex lacks evidence for in-situ partial melting. These rocks transition into gneiss in the core of the dome where leucosome development that was derived from segregated partial melting of the pelitic rocks is preserved (Fig. 2.2c and d). Here, leucogranites discordantly encompass blocks of migmatitic host rock that experienced in-situ partial melting (Fig. 2.2d). Based on the structure, it is presumed that the migmatite rocks in core correlates to the GHS but more data is necessary to evaluate this.

Rocks within the dome are sheared by the top-down-to-the-west LPSZ on the southwest flank of the dome (Fig. 2.1) (Thiede et al., 2006). The uppermost structural level of the LPSZ on the southwest flank of the dome near the village of Chango (Fig. 2.1b, cross section A-A') is marked by a steep metamorphic gradient between the upper Haimanta Group at the base of the TSS (within the LPSZ) and the weakly to unmetamorphosed sedimentary rocks (TSS) in the hanging wall (Thiede et al., 2006). Here, the Kaurik-Chango normal fault system offsets the broadly distributed LPSZ and juxtaposes the structurally higher LPSZ rocks in the hanging wall of the Kaurik-Chango normal fault with structurally deeper LPSZ rocks in the footwall (Thiede et al., 2006). The rocks in the footwall of the Kaurik-Chango normal fault system are composed of sheared schist (biotite ± garnet ± staurolite ± kyanite ± sillimanite) and leucogranites (Fig. 2.2e).

To the south, near the villages of Nako and Leo (Fig. 2.1b, cross section B-B'), the LPSZ within the Haimanta Group is composed of schist (biotite ± garnet ± staurolite ± kyanite ± sillimanite) and leucogranite with a several-hundred-meter-thick unit composed of sheared quartzite, marble, and leucogranite (Figs. 2.1b and 2.2f). The quartzite and marble unit contains a strong west-directed stretching lineation that is defined by elongate quartz grains (average 21°→275°). Macroscopic shear sense indicators, viewed on surfaces that are perpendicular to the

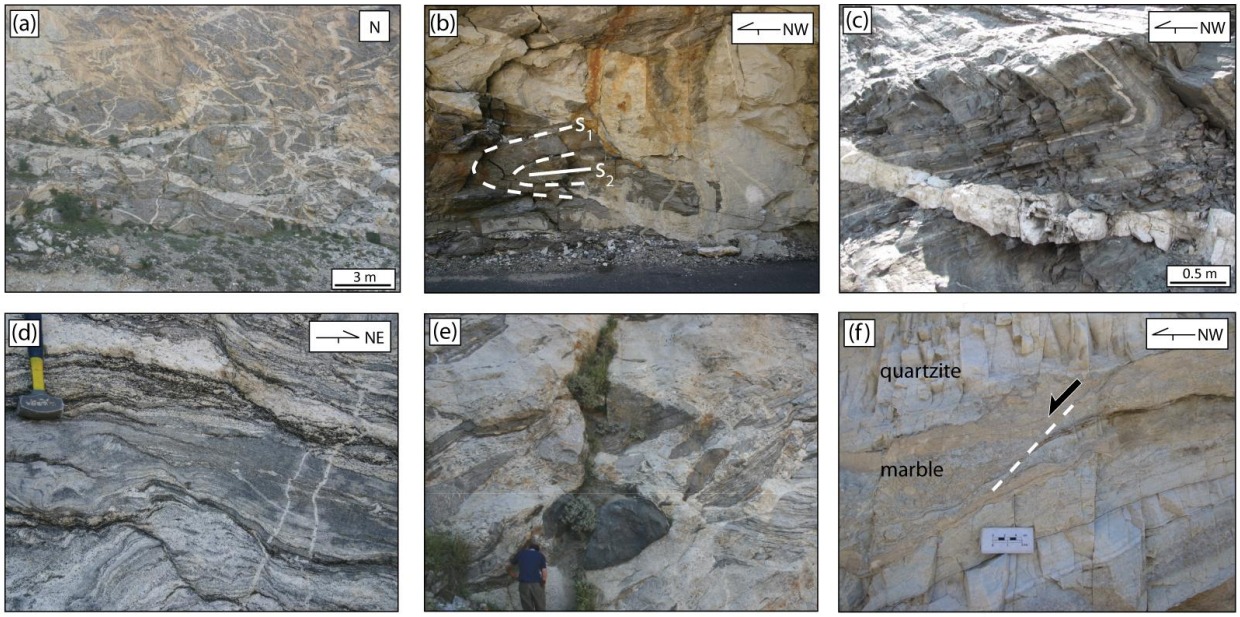

Figure 2.2. *Field photographs. (a) Leucogranite injection complex viewed toward the west, just south of the confluence of the Spiti and Sutlej Rivers. See Figure 2.1b. (b) Folded biotite schist within the Leo Pargil dome that is intruded by the leucogranite injection complex. (c) Migmatitic biotite gneiss exposed in the core of the dome. (d) Melt-present migmatite with mafic pods in the core of the dome. (e) Biotite schist within the LPSZ intruded by pre-kinematic and post-kinematic leucogranite. (f) Mylonitic quartzite and marble within the LPSZ with shear bands indicating top-down-to-the-west shear sense.*

foliation and parallel to the stretching lineation, such as shear bands, record top-down-to-the-west shear sense (Fig. 2.2f). Preliminary investigations of quartz microstructures from the rocks exposed in the shear zone suggest top-down-to-the-west shear sense.

White mica and biotite $^{40}Ar/^{39}Ar$ and apatite fission track ages (Thiede et al., 2006; Hintersberger et al., 2010) of samples from within the dome suggest that ductile deformation through ~350° C occurred at ~16 Ma and exhumation continued along the brittle, high-angle Kaurik-Chango normal fault began at ~10 Ma. Saylor et al. (2010) document growth structures within lacustrine sediments filling the Zada basin to the east of the LPD, suggesting exhumation continued along the southeast flank of the dome between 9 and 1 Ma.

The northeast-striking, southeast-dipping Qusum detachment fault (050°, 30°SE) on the east side of the LPD (Zhang et al., 2000) separates the eastern flank of the dome from the Zada basin in the hanging wall (Murphy et al., 2009; Saylor et al., 2010). A switch from top-down-to-

the-west shear sense on the southwest flank of the dome to top-down-to-the-east shear sense in the migmatite core of the dome is observed (Figs. 2.1b and 2.2c) recorded by shear bands and tails on porphyroblasts. The central section of the dome exposed in the footwall of the Qusum detachment fault is composed of a leucogranite body that transitions into gneiss and biotite schist toward structurally shallower positions on the southeastern flank of the dome (Zhang et al., 2000). The gneiss and biotite schist are intruded by leucogranite that is folded and boudinaged and records top-down-to-the-southeast displacement. Muscovite K-Ar data from the deformed leucogranite suggests that this shear zone was active at ~16 Ma (Zhang et al., 2000).

Samples

From >200 samples, pelitic schist and leucogranite samples that best represent the P-T-t-D history of these rocks were chosen for thermobarometric and geochronologic analyses. A pelitic sample from the Haimanta Group (LP09-10) in the hanging wall of the dome records Barrovian metamorphism and was selected for thermobarometric and geochronological analyses to constrain the P-T-t-D history recorded in rocks of the hanging wall. Two pelitic samples (LP09-76, LP09-229) from the LPD between the villages of Nako and Chango were selected because they contain Barrovian porphyroblasts that are overprinted by top-down-to-the-west shearing. These samples were used to constrain the P-T-t-D history associated with Barrovian metamorphism followed by shearing on the LPSZ. One pelitic sample (LP09-162) and four leucogranite samples (LP09-157, LP09-158, LP09-166, and LP09-167) were selected from just north of the confluence of the Spiti and Sutlej Rivers within the LPD (Fig. 2.1b). Here, the host rock contains Barrovian porphyroblasts that are overprinted by cordierite and sillimanite associated with top-down-to-the-west shearing and is intruded by multiple generations of leucogranite. This outcrop is representative of Barrovian metamorphism followed by decompression, top-down-to-the-west shearing, and leucogranite intrusion within the LPD.

Haimanta Group in the Hanging Wall of the Leo Pargil Dome (LP09-10)

LP09-10 (31.7522°, 78.6196°) is pelitic schist with subhedral staurolite and garnet porphyroblasts that was collected within the staurolite-grade rocks of the Haimanta Group in the

hanging wall of the LPD (Fig. 2.1). Subhedral garnet porphyroblasts preserve a relict fabric (S_1) and are in a foliated matrix (S_3) (185°, 18° E and 15°→060°) of biotite and muscovite interlayered with quartz and albite (Fig. 2.3a). S_2 is defined by biotite and muscovite that occurs at an angle to the S_3 fabric. Ilmenite, apatite, and rare monazite and zircon occur throughout the matrix. Few xenotime grains are present. Garnet porphyroblasts contain ilmenite, apatite, quartz, biotite, and albite inclusions. Staurolite contains quartz, ilmenite, apatite, and rare monazite inclusions. Chlorite occurs throughout the sample as a retrograde replacement of biotite. Quartz exhibits undulose extinction and sub-grains.

Leo Pargil Dome (LP09-76, 229, and 162)

Sample LP09-76 (31.9462°, 78.6023°) was collected from the LPSZ that is exposed between the villages of Nako and Chango (Fig. 2.1). It is pelitic schist that contains subhedral garnet and staurolite porphyroblasts in a foliated matrix (Fig. 2.3b) (305°, 35° SW and 6°→300°) defined by biotite, muscovite, and chlorite interlayered with anhedral quartz and albite. Ilmenite, apatite, zircon, and monazite occur throughout the matrix. Kyanite is present but is rare. Garnet occurs as both subhedral and nodular grains. Garnet contains quartz, apatite, albite, ilmenite, and biotite inclusions. Small (<10 μm), rare zircon and monazite are also present as inclusions in the garnet. Xenotime is rare in the matrix. Staurolite contains quartz, apatite, albite, and rare xenotime inclusions. C'-type shear-bands record top-down-to-the-northwest shear sense (Fig. 2.3b). Porphyroblasts are mantled by asymmetric strain shadows (quartz, biotite, muscovite, and albite) that record top-down-to-the-northwest shear sense. Chlorite occurs throughout the sample as a retrograde replacement of biotite. Quartz exhibits undulose extinction, subgrains, and lobate grain boundaries.

Sample LP09-229 (31.9349°, 78.6027°) was collected from the LPSZ, within the shear zone just south of sample LP09-76 (Fig. 2.1). This sample is pelitic schist with subhedral staurolite and nodular garnet porphyroblasts in a foliated and lineated matrix (324°, 37° SW and 20°→273°) defined by biotite and muscovite that also contains anhedral quartz, and albite. Ilmenite, apatite, zircon, monazite, and tourmaline occur throughout the matrix. There is no xenotime. Garnet and staurolite contain quartz, ilmenite, and rare monazite and apatite inclusions that define a curved relict fabric (S_1) that the porphyroblasts overgrew (Fig. 2.3c). C'-type shear-

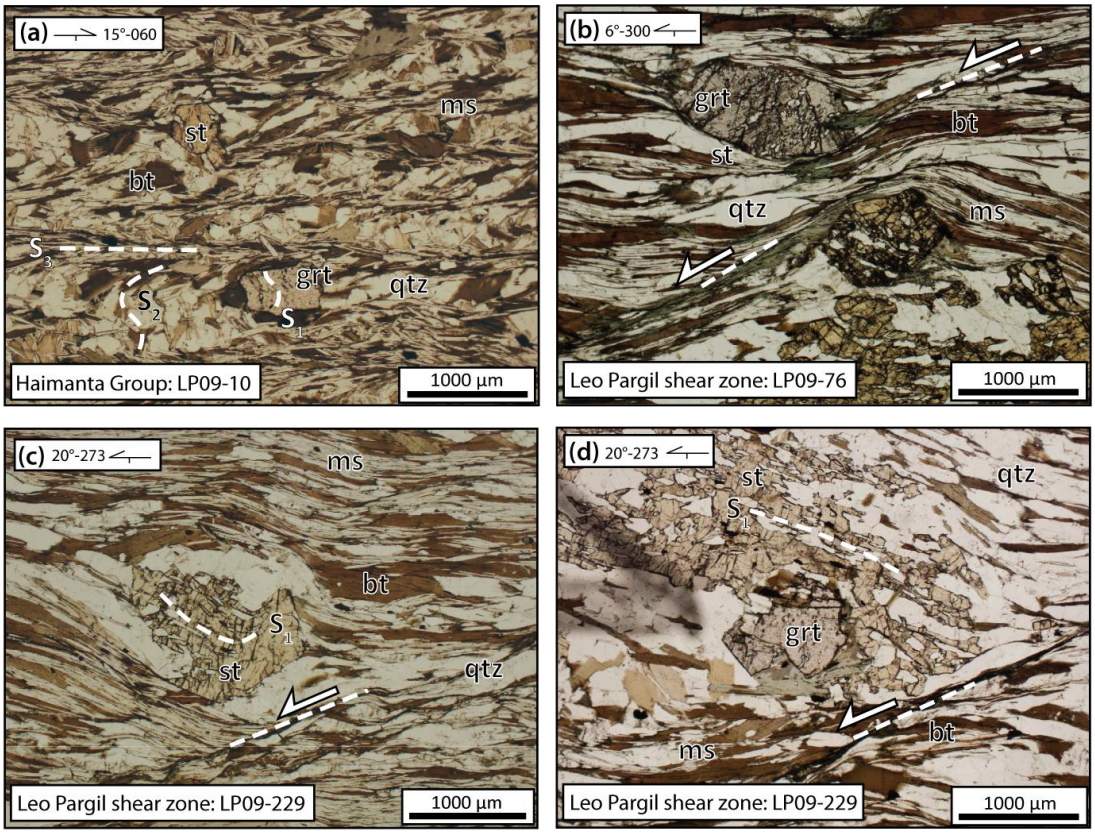

Figure 2.3. *Photomicrographs of kinematic indicators. (a) Garnet and staurolite associated with Barrovian metamorphism in the Haimanta Group (hanging wall of the LPSZ) with inclusions recording an early fabric (S_1) overprinted by S_2 and S_3. qtz, quartz; bt, biotite; ms, muscovite. (b) Shear bands in a sample from the LPSZ that suggests dominantly top-down-to-the-northwest shear. (c) Staurolite porphyroblast recording an early fabric (S_1) overprinted by the LPSZ fabric that suggests top-down-to-the-west shear. (d) Garnet partially included in a staurolite porphyroblast bound by a shear band recording top-down-to-the-west shear sense.*

bands record top-down-to-the-west shear sense (Fig. 2.3c and d). Asymmetric strain shadows composed of quartz, biotite, muscovite, and plagioclase mantle porphyroblasts and record dominantly top-down-to-the-west shear sense (Fig. 2.3c and d). Subhedral to anhedral staurolite and garnet porphyroblasts indicate partial resorption. Some garnet is partially included in staurolite (Fig. 2.3d). Chlorite occurs as a retrograde replacement of biotite. Quartz exhibits undulose extinction, subgrains, and lobate grain boundaries.

LP09-162 (31.8069°, 78.6332°) is a pelitic schist that was collected just north of the confluence of the Spiti and Sutlej rivers (Figs. 2.1 and 2.2b). It contains subhedral staurolite and

kyanite porphyroblasts in a foliated matrix (319°, 32° SW and 31°→255°) that is defined by biotite, albite, and cordierite. Minor amounts of muscovite, chlorite and quartz are present (<2% of the sample). Shear bands and strain shadows on porphyroblasts record top-down-to-the-west shear sense (Fig. 2.4a). Rutile and tourmaline are abundant in the matrix. ~20-50 μm zircon and monazite are common within the matrix. Xenotime is absent. Kyanite and staurolite porphyroblasts contain biotite and monazite inclusions and are surrounded by cordierite rims (Fig. 2.4b and c). Kyanite occurs as inclusions in staurolite (Fig. 2.4b) and as intergrowths with staurolite. The porphyroblasts are boudinaged and the opening between the fragments is filled with fibrolitic sillimanite, cordierite, rutile, and tourmaline (Fig. 2.4c). Cordierite and sillimanite also occur in strain shadows of kyanite and staurolite porphyroblasts (Fig. 2.4c). These strain shadows suggest top-down-to-the-west shear sense during cordierite and sillimanite growth.

Leucogranites (LP09-157, 158, 166, and 167)

Samples LP09-157, 158, 166, and 167 (31.8069°, 78.6332°) are leucogranites collected from the same outcrop as LP09-162 (Figs. 2.1 and 2.2b). LP09-158 is an undeformed, course grained (3-10 mm) tourmaline-bearing leucogranite that cuts host rock and then cut by LP09-157 and LP09-167. LP09-157 and LP09-167 are undeformed, medium grained (quartz and feldspar <3 mm) leucogranites that are both from the second generation of melt. Two samples were collected from this generation to evaluate the homogeneity of the age throughout this generation of leucogranite. LP09-166 was collected from a third generation of leucogranite that cuts LP09-157 and LP09-167 and is undeformed. It is coarse grained (quartz and feldspar < 1.5 cm) and occurs as 5-10 cm-wide dikes.

Methodology

Pressure-Temperature Estimates

Mineral composition analyses for thermobarometric estimates were obtained on a Cameca SX-100 electron microprobe at the University of Tennessee. A PGT Si (Li) detector energy-dispersive spectrometer was used along with electron back-scatter imaging (BSE) for qualitative

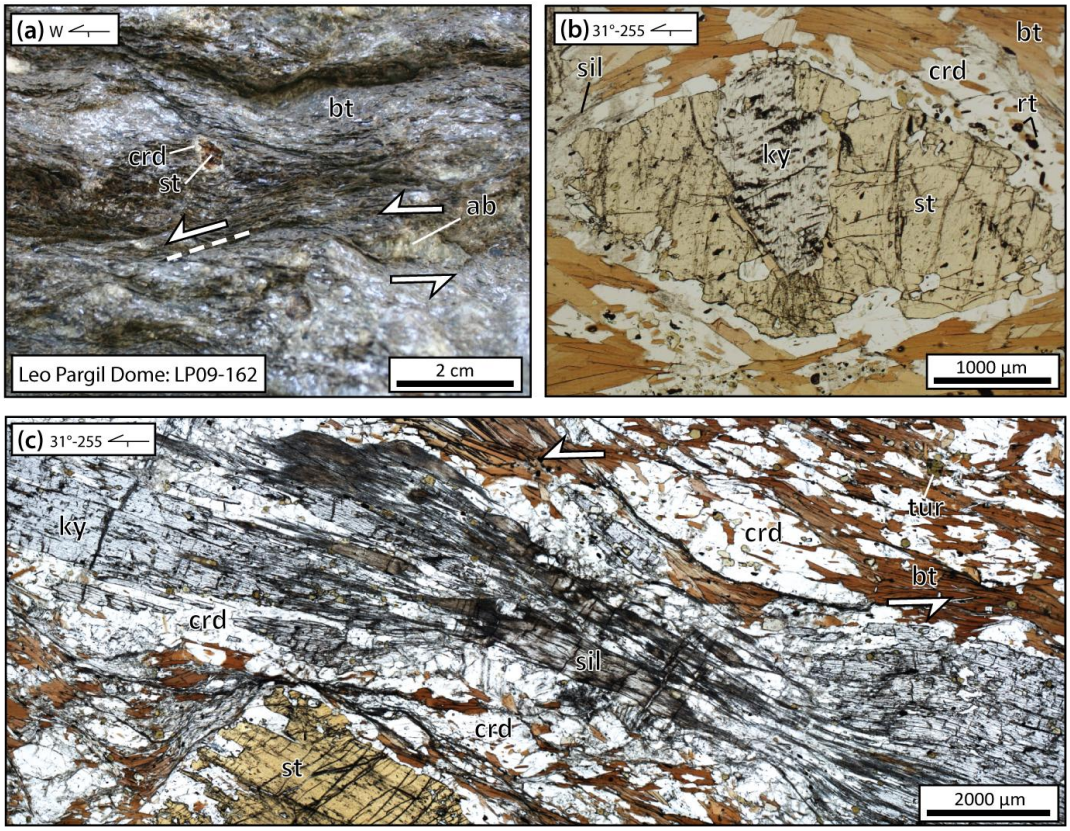

Figure 2.4. *Images of LP09-162. (a) Field photo from the outcrop (Figure 2.2b) where sample LP09-162 was collected. Staurolite porphyroblast contains a cordierite rim. Shear bands and strain shadow on albite (ab) documents top-down-to-the-west shear sense. (b) Kyanite inclusion in staurolite. A cordierite rim is present on the staurolite and contains rutile (rt) and sillimanite. (c) Cordierite overgrowths on staurolite and kyanite. Kyanite is boudinaged and filled in by sillimanite and cordierite. tur, tourmaline.*

identification of phases during real time analysis. X-ray maps using wavelength-dispersive spectrometery of Mg, Mn, and Ca along with quantitative line transects were conducted across garnet porphyroblasts at 15 kV, 30 nA, 30 ms, and a 6 µm spot size to characterize compositional zonation. Point analyses at 15 kV, 20 nA, and a spot size of 1µm were conducted on phases to be used for P-T estimates such as staurolite, biotite, plagioclase, and muscovite to assess compositional heterogeneities of each phase throughout the sample. Plagioclase was analyzed at 10 kV. Natural and synthetic compounds were used for standards and were checked prior to and following the analyses. Elemental abundances <300 ppm are considered below the detection limit for all elements except for Y which is ~400 ppm.

P-T estimates at peak temperatures were calculated from the chemical data using THERMOCALC v. 3.33 in the average P-T mode (Powell and Holland, 1998). Calculations were made using the updated Holland and Powell (1998) data set (tc-ds55.txt). Activity coefficients for each phase were calculated using the AX software.

A pseudosection for a sample collected from the LPD (LP09-162) was calculated from the bulk composition obtained by combining compositional data collected from the electron microprobe with point counts across the entire thin section of the sample to quantify the proportions of the phases present (Table 2.1 and 2.2). Fe^{3+} was not measured, but its composition is assumed to be minor due to the absence of magnetite. Phases in this sample contained little to no compositional zonation so the average composition of each phase was used along with the mode to calculate the bulk composition.. The P-T pseudosection was calculated with the Perplex 6.6.6 software package (Connolly, 2009; updated in 2011) using the Holland and Powell (1998) thermodynamic data file (updated in 2004, hp04ver.dat). The hp04ver.dat data file predicts a slight shift in the aluminum silicate triple point. The NCKFMASH system is generally considered as a representative system for metapelites. However, MnO and TiO_2 are also important (White et al., 2000, 2001) so the MnNCKFMASTH system was used for the calculation. Gridded minimization was used with no saturated components or phases. The CORK equation of state for H_2O was used (Holland and Powell, 1998). Holland and Powell solid solution models were used for chlorite, biotite, garnet, and staurolite (Holland et al., 1998; Holland and Powell, 1998; Powell and Holland, 1999). The Fuhrman and Lindsley (1988) feldspar solution model was used. To produce rutile in the calculation, Ti-end members of biotite (mtbi, ftbi, and tbi) and ilmenite (oilm) were excluded.

Table 2.1. Modal Analysis of LP09-162.

Mineral	Count	Percent (%)
albite	86	9.5
cordierite	148	16.4
biotite	438	48.5
staurolite	85	9.4
muscovite	1	0.1
rutile	4	0.4
tourmaline	23	2.5
kyanite	77	8.5
sillimanite	24	2.7
quartz	13	1.4
chlorite	4	0.4
Total	903	100%

Table 2.2. Bulk Composition (in wt.%) of Sample LP09-162.

	SiO_2	TiO_2	Al_2O_3	FeO	MnO	MgO	CaO	Na_2O	K_2O	H_20	Total
LP09-162	41.46	1.36	30.17	8.54	0.05	8.62	0.18	1.38	4.12	2.23	98.12

Monazite Geochronology

Monazite grains in the four metamorphic rock samples used for thermobarometry (LP09-10, LP09-76, LP09-229, and LP09-162) were located using the methodology of Williams and Jercinovic (2002). Ce X-ray maps overlain on Al or Mg X-ray maps for reference were conducted for the full thin section and used to locate all monazite grains. Maps were collected using stage scan mapping at 20 keV, 35 μm steps, beam defocused to 35 μm, 150 nA, and 20 ms count time/pixel on the Cameca SX-100 electron microprobe at the University of Tennessee. These maps allow all monazite grains larger than ~10 μm in the sample to be located and placed in a metamorphic and textural context. From the monazite grains located, ~20 grains per sample were selected as candidates for analysis. X-ray maps of Y, Th, Pb, and U were obtained for each of these grains at 25 kV, 40 nA, 90 ms, and a spot size of 0.255 μm. The compositional maps were used to interpret potential age domains and the relationship of monazite growth domains with the fabric and metamorphic reactions. Based on these criteria, locations for laser-ablation inductively coupled plasma-mass spectrometry (LA-ICPMS) analyses were determined from the compositional maps (Appendix 2.1). Th zonation was generally patchy and too small for analysis while Y and U exhibit discrete compositional domains (Appendix 2.1), so locations for LA-ICPMS analyses were chosen to obtain analyses that were each completely (or as close to as possible) within each Y and/or U compositional domain.

Igneous monazite grains were separated from the four leucogranite samples using standard crushing and separation techniques at the University of California, Santa Barbara (UCSB). Monazite grains were mounted in epoxy and polished. They were then evaluated from BSE images taken by the FEI Quanta scanning electron microscope (SEM) at UCSB to determine the grains suitable for U-Th-Pb analysis.

U-Th-Pb ages were obtained using an AttoM single-collector LA-ICPMS (metamorphic monazite) or a Nu Plasma multi-collector ICPMS (igneous monazite) attached to a 193nm ArF laser ablation system (Photon Machines). Metamorphic monazite was analyzed for 30 s at 4-5 Hz and 2.6 J/cm^2 with a spot size of 10 μm, 20 μm, or a line of 10x20 μm. Monazite grains from the

leucogranites were analyzed for 30 s at 3 Hz and 4.8 J/cm^2 using a 7.2 μm spot. Analytical protocol is similar to that described by Cottle et al. (2009b, c) with the modification that the collector arrangement on the Nu Plasma at UCSB allows for simultaneous determination of ^{232}Th and ^{238}U on high-mass side Faraday cups equipped with 10^{11} ohm resistors and ^{208}Pb, ^{207}Pb, ^{206}Pb and ^{204}Pb on four low-mass side ETP discrete dynode secondary electron multipliers.

An in-house primary reference monazite (512 ± 0.2 Ma) was employed to monitor and correct for mass bias as well as Pb/U and Pb/Th fractionation. Three secondary reference monazites were used to monitor data accuracy: the moacyr monazite (474 Ma, Seydoux-Guillaume et al., 2002), manangotry (554 Ma, Paquette et al., 1994), and FC1 (55.6 Ma, Horstwood et al., 2003). These reference monazite grains were analyzed concurrently (once every 5-7 unknowns) with the unknown monazites and were mass bias- and fractionation corrected on the basis of measured isotopic ratios of the primary reference material.

Data reduction, including corrections for baseline, instrumental drift, mass bias and age calculations were carried out using in-house software. All uncertainties are quoted at the 95% confidence or 2σ level and include contributions from the external reproducibility of the primary reference material for the ^{206}Pb/^{238}U and ^{206}Pb/^{232}Th ratios.

Concordia diagrams were constructed using Isoplot 2.4 (Ludwig, 2000). ^{208}Pb/^{232}Th ages are insensitive to the effects of disequilibrium in the ^{238}U decay chain and excess ^{206}Pb that can occur in monazite grains (e.g., Schärer, 1984). Furthermore, Th concentrations in monazite are high resulting in high levels of ^{208}Pb (Harrison et al., 1995) so ^{208}Pb/^{232}Th ages are used throughout this study.

Pressure-Temperature Estimates

Haimanta Group in the Hanging Wall of the Leo Pargil Dome (LP09-10)

Garnets in sample LP09-10 exhibit a decrease in X_{spess} from core to near rim with a thin (~5μm) inflection at the rim (Fig. 2.5a) suggesting prograde growth followed by late stage retrograde net transfer at the rim (Kohn and Spear, 2000). Biotite, muscovite, and plagioclase near and away from the garnet exhibit little compositional variation. Staurolite also exhibits minor compositional variation. The near-rim composition of the garnet along with averaged data

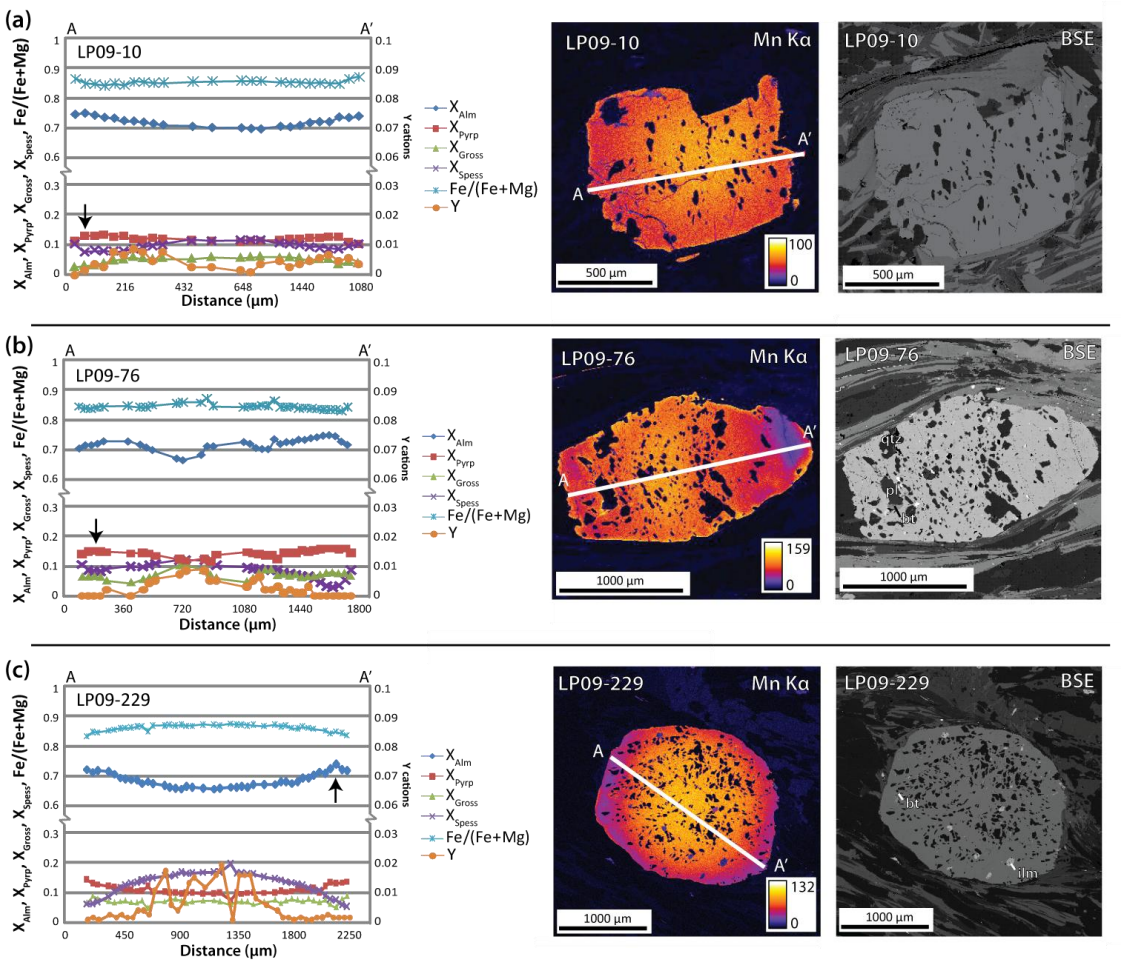

Figure 2.5. *Garnet compositions used to estimate pressure-temperature (P-T) estimates. Arrows indicate the data point used for P-T estimates. pl, plagioclase.*

from biotite near the garnets and muscovite, plagioclase, and staurolite data from throughout the sample were used to calculate metamorphic conditions (Table 2.3). These data yield 597 ± 84° C and 7.2± 1.3 kbar for staurolite grade rocks (Fig. 2.6; Table 2.4).

Leo Pargil Dome (LP09-76, 229, and 162)

Compositional X-ray maps (Fig. 2.5b) of a garnet in sample LP09-76 show that garnet in this sample exhibits a slight decrease in X_{Spess} from core to near rim with a thin (~5-20 μm) inflection at the rim that records late stage retrograde net transfer (Kohn and Spear, 2000). The core of the garnet in Figure 2.5b contains quartz and albite inclusions that partially define a

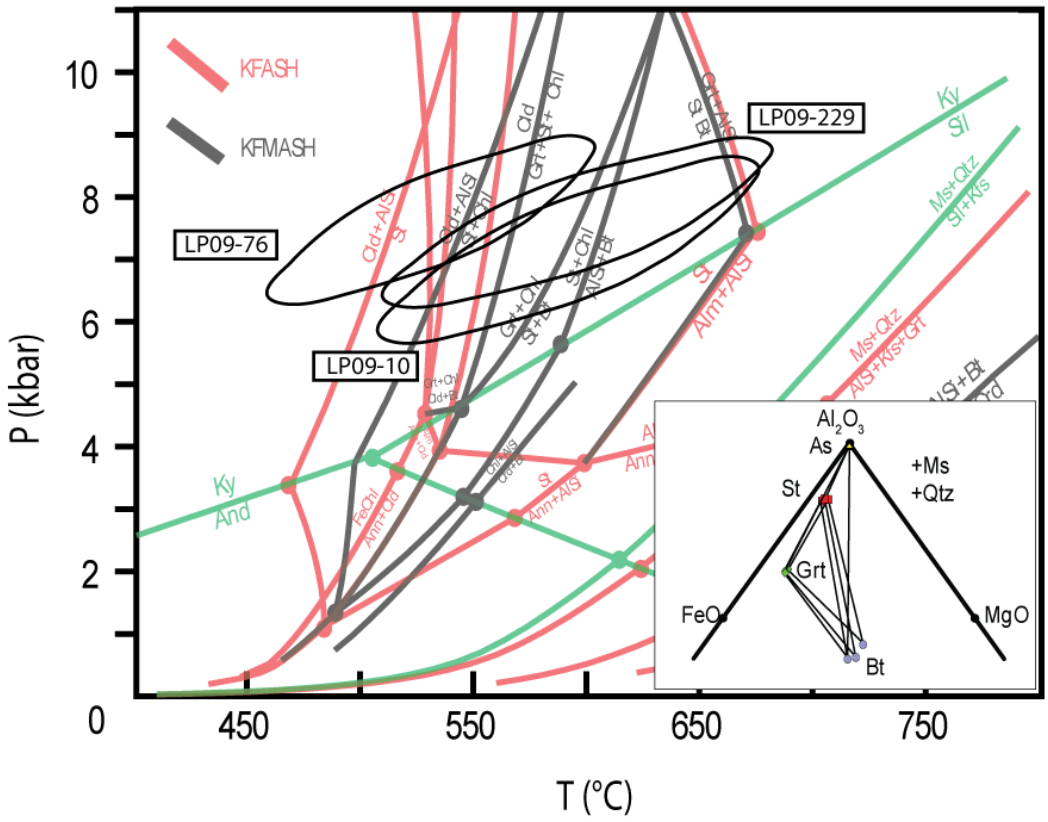

Figure 2.6. *Pressure-temperature data calculated using THERMOCALC overlain on petrogenetic grid from Holland and Powell (1998). AFM diagram inset shows compositions of phases from samples LP09-229, LP09-76, and LP09-10 projected from muscovite. Data shown in Table 2.4. As, aluminum silicate.*

sigmoidal inclusion pattern that can be interpreted as an overgrowth of a crenulation or as syntectonic rotation and growth. Larger quartz and albite inclusions in the garnet bound the core. The truncation of compositional zoning at the top and bottom of the garnet indicates partial removal of garnet has occurred in sites of higher strain. Because biotite located near garnet porphyroblasts and albite and muscovite at various distances from the garnet contained little compositional variation, data from these phases were averaged for thermobarometric calculations. Staurolite contained little compositional variation and was also averaged for thermobarometric calculations. Combinations of these phases along with the near rim composition of the garnet were used to calculate the P-T at peak metamorphic temperatures (Fig.

Table 2.3. Compositional Data (in wt. %) Used for Thermobarometric Analyses.

	Garnet near rim	Biotite	Plagioclase	Muscovite	Staurolite
LP09-10		(16)	(26)	(24)	(11)
SiO_2	37.18	35.65	64.39	45.85	27.33
TiO_2	0.01	1.49	0	0.37	0.64
Al_2O_3	21.10	19.05	22.38	35.66	53.06
FeO	34.19	18.31	0.13	1.69	13.95
MnO	3.66	0.10	0	0.01	0.28
MgO	3.45	11.22	0	0.52	1.82
CaO	1.35	0.02	3.19	0.01	0.00
Na_2O	0.02	0.35	9.62	1.78	0.02
K_2O	0	8.94	0.07	8.17	0.00
∑	100.96	99.08	99.78	98.53	99.25
Si	2.97	5.39	2.84	6.13	3.83
Ti	0.00	0.17	0	0.04	0.07
Al	1.99	3.39	1.16	5.62	8.77
Fe	2.29	2.31	0.01	0.19	1.64
Mn	0.25	0.01	0	0.00	0.03
Mg	0.41	2.53	0	0.10	0.38
Ca	0.12	0.00	0.15	0.00	0.00
Na	0.00	0.10	0.82	0.46	0.01
K	0	1.72	0.00	1.39	0.00
∑	8.03	19.68	5.00	17.95	16.72
LP09-76		(12)	(22)	(15)	(9)
SiO_2	37.30	35.19	62.84	45.88	27.45
TiO_2	0.02	1.65	0	0.54	0.64
Al_2O_3	21.16	19.10	23.24	35.43	53.74
FeO	32.73	19.17	0.05	1.39	14.20
MnO	3.57	0.15	0	0.02	0.37
MgO	3.62	10.97	0	0.65	1.61
CaO	2.16	0.00	4.38	0.01	0.00
Na_2O	0.02	0.31	9.36	1.48	0.01
K_2O	0	8.73	0.09	8.70	0.01
∑	100.58	99.20	99.96	98.59	98.03
Si	2.98	5.34	2.78	6.14	3.81
Ti	0.00	0.19	0	0.05	0.07
Al	1.99	3.42	1.21	5.59	8.80
Fe	2.19	2.43	0.00	0.16	1.65
Mn	0.24	0.02	0	0.00	0.04
Mg	0.43	2.48	0	0.13	0.33
Ca	0.18	0.00	0.21	0.00	0.00
Na	0.00	0.09	0.80	0.38	0.00
K	0	1.69	0.01	1.49	0.00
∑	8.02	19.66	5.01	17.94	16.72

Table 2.3. Continued.

	Garnet near rim	Biotite	Plagioclase	Muscovite	Staurolite
LP09-229		(11)	(30)	(10)	(14)
SiO_2	36.97	35.70	64.70	46.69	27.41
TiO_2	0.00	1.60	0	0.44	0.57
Al_2O_3	21.27	19.57	22.64	35.69	53.70
FeO	33.13	17.43	0.08	1.57	13.92
MnO	3.51	0.13	0	0.02	0.33
MgO	3.41	11.38	0	0.52	2.02
CaO	2.27	0.03	3.38	0.02	0.00
Na_2O	0.00	0.36	9.75	1.51	0.00
K_2O	0	8.32	0.08	7.95	0.00
∑	100.56	98.49	100.32	98.44	100.13
Si	2.96	5.39	2.83	6.19	3.81
Ti	0.00	0.18	0	0.04	0.06
Al	2.01	3.48	1.17	5.58	8.79
Fe	2.22	2.20	0.00	0.17	1.62
Mn	0.24	0.02	0	0.00	0.04
Mg	0.41	2.56	0	0.10	0.42
Ca	0.19	0.00	0.16	0.00	0.00
Na	0.00	0.11	0.83	0.39	0.00
K	0	1.60	0.00	1.35	0.00
∑	8.03	19.54	5.00	17.84	16.74

Note: Numbers in parenthesis represent the number of data points averaged. Analyses of 0 indicate that the composition was not analyzed.

Table 2.4. Pressure-Temperature Estimates for Barrovian Metamorphism.

Sample	THERMOCALC							Peak depth (km)[b]
	T (° C)	P (kbar)	Assemblage	Removed	Cor.	Fit	No. rxn.	
LP09-10	597±84	7.2±1.3	grt+st+bt+ms+pl+qtz	fcel, mst	0.66	0.75	5	27
LP09-76	592±83	7.5±1.3	grt+st+bt+ms+pl+qtz+ky	fcel, mst, cel	0.72	0.66	4	28
LP09-229	529±72	7.6±1.3	grt+st+bt+ms+pl+qtz	mst	0.72	0.93	4	28
LP09-162[a]	630±30	6.6±0.8	—	—	—	—	—	25

Note: THERMOCALC results calculated using the average PT mode. Assemblage, used for THERMOCALC estimate; Cor., correlation coefficient; no. rxn., number of reactions used for THERMOCALC calculation.

[a]Calculated from pseudosection modeling. These conditions were followed by a drop to 592±32° C and 4.4±0.7 kbar during decompression.

[b]Calculated assuming a lithostatic pressure gradient of 3.7 km/kbar.

2.5b; Table 2.3). These data yielded a P-T estimate of 592 ± 83° C and 7.5 ± 1.3 kbar (Fig. 2.6; Table 2.4).

Compositional X-ray maps (Fig. 2.5c) of garnets in sample LP09-229 record prograde zonation defined by a decrease in X_{Spess} from core to near rim (Kohn and Spear, 2000). A thin resorption rind (~5 μm) at the garnet rim defined by a minor increase in X_{Spess} is attributed to late stage retrograde metamorphism. The Y concentration decreases from the core to the rim. The near rim composition at the X_{Spess} trough (Kohn and Spear, 2000) combined with averaged data from biotite near the garnet, muscovite, plagioclase, and staurolite (Table 2.3) was used for thermobarometry and yielded a P-T estimate of 529 ± 72° C and 7.6± 1.3 kbar (Fig. 2.6; Table 2.4).

A pseudosection was calculated for sample LP09-162 to model that P-T path for the growth of staurolite, kyanite, cordierite, and sillimanite that are present in this sample (Table 2.1 and 2.2; Fig. 2.7). Kyanite is included in and intergrown with staurolite suggesting an early stage of porphyroblast growth included kyanite growth that was followed by a second stage of porphyroblast growth that included synchronous staurolite and kyanite growth during Barrovian metamorphism. Kyanite and staurolite are stable together in the assemblage at peak temperatures of 630 ± 30° C and 6.6 ± 0.8 kbar, shown in white in Figure 2.7. The pseudosection shows garnet growth along with staurolite and kyanite at peak temperatures (Fig. 2.7). It is assumed that all the garnet reacted out and is no longer preserved in this sample. Staurolite and kyanite are overgrown by cordierite, rutile, and sillimanite along with biotite and albite in the matrix that record near-isothermal decompression to 592±32° C and 4.4 ± 0.7 kbar (shown in white in Figure 2.7). Cordierite and sillimanite occur within the strain shadows of staurolite and kyanite suggesting that near-isothermal decompression occurred during top-down-to-the-west shearing following cessation of staurolite and kyanite growth.

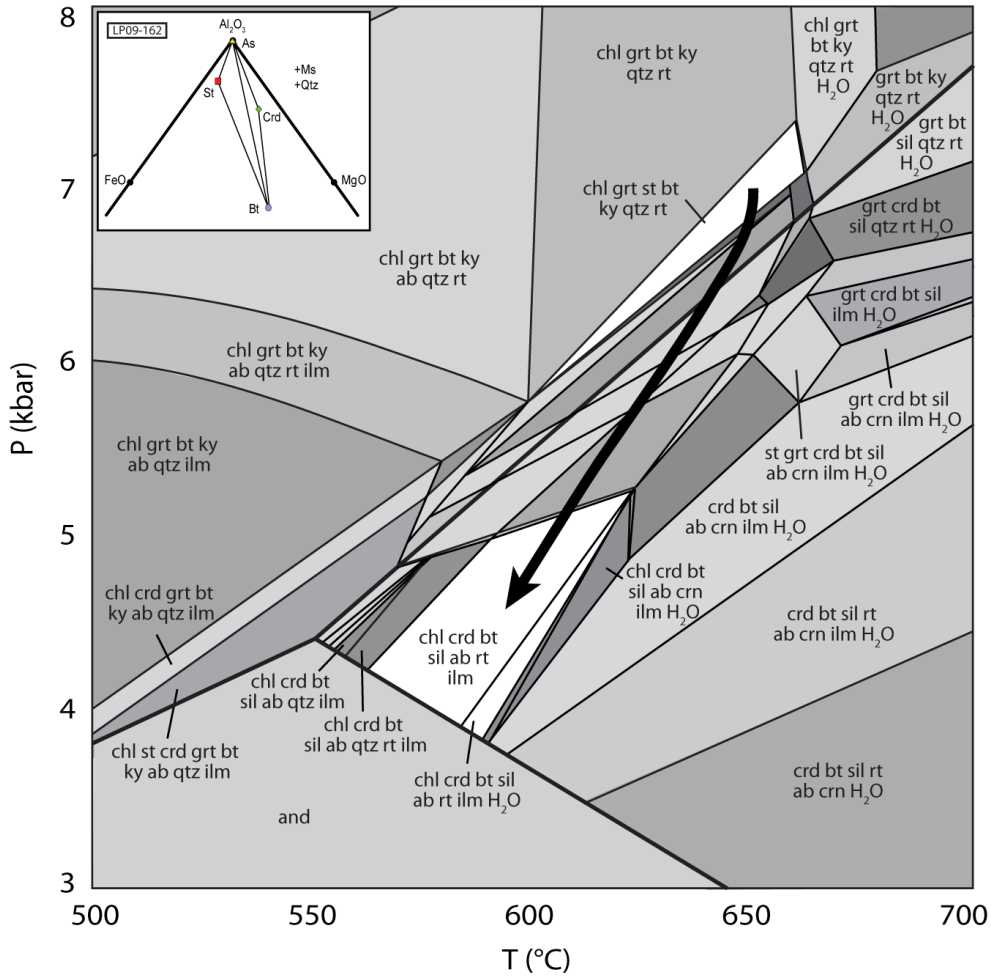

Figure 2.7. *Pseudosection for sample LP09-162. White represents the interpreted assemblages recorded in this sample. The P-T path is noted by the arrow. The aluminum-silicate triple point in bold. For simplification, fields containing andalusite (and) were not plotted. chl, chlorite; ilm, ilmenite; crn, corundum. Inset shows the assemblages in this sample projected from muscovite.*

In-Situ Monazite Geochronology from Metamorphic Rocks

Haimanta Group in the Hanging Wall of the Leo Pargil Dome (LP09-10)

Monazite grains in the matrix of sample LP09-10 contain patchy Th zonation (Appendix 2.1). Y zonation defines three domains: low-Y cores (not seen in Fig. 2.8a, see Appendix 2.1), relatively high-Y mantles, and high-U rims that contain variable amounts of Y (Fig. 2.8a, Appendix 2.1). Monazite grains of sufficient size for analysis were not found as inclusions in the porphyroblasts. Low-Y cores yield ages from 33.5 ± 3.6 to 32.3 ± 2.6 Ma (n=7), high-Y mantles

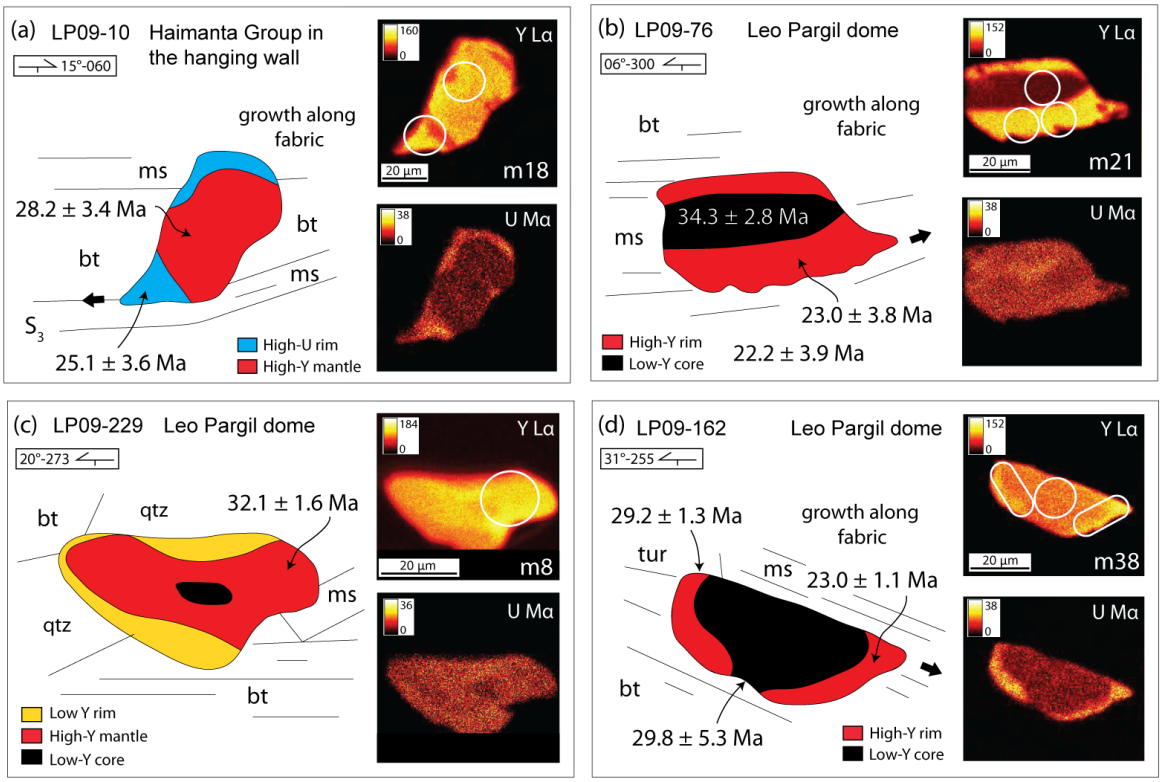

Figure 2.8. *Examples of monazite age domains interpreted from Y and U compositional maps from the four samples used for in-situ monazite U-Th-Pb analysis. (a), (b), and (d) contain rims that grew along the matrix fabric. White circles and ellipses on compositional maps correspond to analysis location. S_3 in (a) corresponds to that in Figure 2.3a.*

yield ages from 31.9 ± 2.8 to 23.6 ± 3.0 Ma (n=13), and two analyses from the high-U rims yield ages of 24.8 ± 3.5 Ma and 25.1 ± 3.6 Ma (Figs. 2.8a and 2.9a; Appendix 2.2). One of the analyses on the high-U rims is on a rim that grew along the matrix fabric (Fig. 2.8a), implying that the fabric (S_3, Fig. 2.3a) was present at 25.1 ± 3.6 Ma.

Leo Pargil Dome (LP09-76, 229, and 162)

Matrix monazite grains in sample LP09-76 contain patchy Th zonation (Appendix 2.1). Y zonation defines low-Y cores and relatively high-Y rims (Fig. 2.8b; Appendix 2.1). No monazite grains of sufficient size were found as inclusions within the garnet and staurolite porphyroblasts.

Monazite exhibits minor U zonation (Fig. 2.8b; Appendix 2.1). Some of the high-Y rims grew along the matrix fabric so the data have been divided into the following: low-Y cores, high-

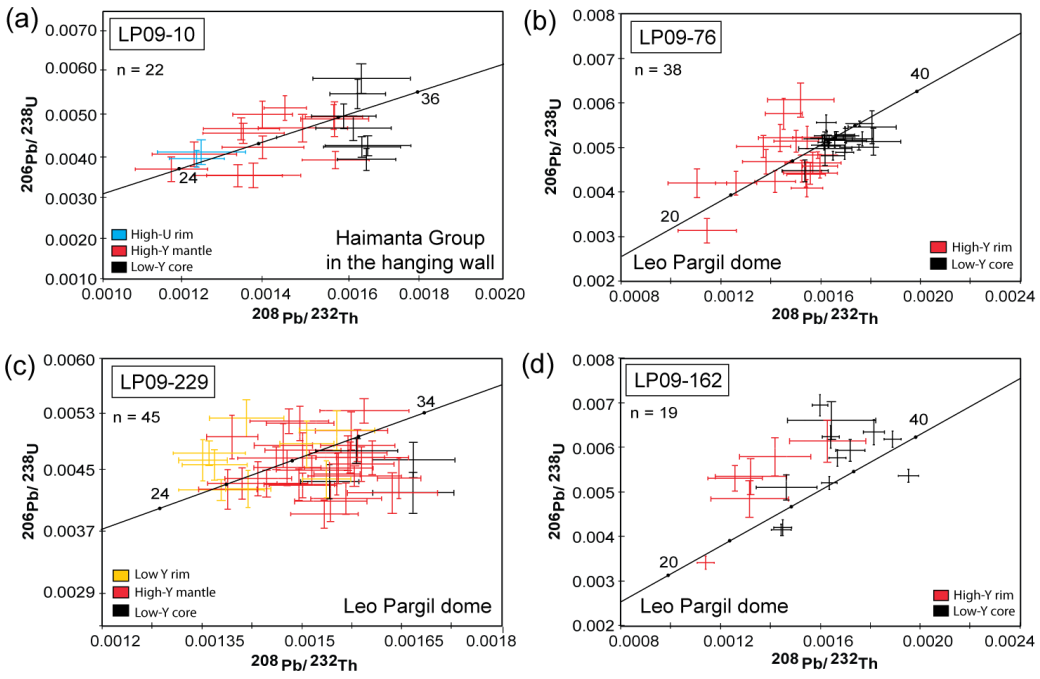

Figure 2.9. *Concordia diagrams of metamorphic in-situ monazite U-Th-Pb analyses. Colors correspond to those used in Figure 2.8.*

Y rims, and high-Y rims that grew along the matrix fabric (Figs. 2.8b, 2.9b, and 2.10b). Low-Y cores of the monazite grains in this sample yield ages from 36.5 ± 3.6 to 32.0 ± 2.6 Ma (n=20) and high-Y rims yield ages from 32.8 ± 3.4 to 27.7 ± 3.7 Ma (n=16) (Fig. 2.10b; Appendix 2.1 and 2.2). Two ages from the high-Y rims that grew along the matrix fabric have ages of 23.0 ± 3.8 Ma and 22.2 ± 3.9 Ma (Fig. 2.10b; Appendix 2.2).

Monazite grains present in the matrix and as inclusions in staurolite porphyroblasts in sample LP09-229 were analyzed. These monazite grains contain patchy Th zonation (Appendix 2.1). Y zonation defines low-Y cores, relatively high-Y mantles, and relatively low-Y rims in both matrix grains (Fig. 2.8c; Appendix 2.1) and inclusions. The boundary between the low-Y cores and the high-Y mantles is generally gradational. U exhibits minor zonation (Fig. 2.8c). In some monazite grains, the low-Y rims correlate with a high-U rim. However, the U zonation sometimes mimics the patchy Th zonation. Analyses on matrix monazite grains yields ages of 33.6 ± 2.0 to 30.8 ± 1.7 Ma (n=3) for low-Y cores, 33.0 ± 2.2 to 28.5 ± 1.8 Ma for high-Y

Figure 2.10. *Probability plots and interpretation of $^{208}Pb/^{232}Th$ ages from metamorphic monazite in four samples. The data are grouped according to the compositional domains in the monazite from which the analysis were taken. Due to small sample size in some of these domains, the probability plot is used only to demonstrate ages with their associated errors. Monazite grains were included in staurolite grains in LP09-229 and in staurolite and kyanite in LP09-162. See text for discussion on the timing of porphyroblast growth. Colors correspond to those used in Figures 2.8 and 2.9.*

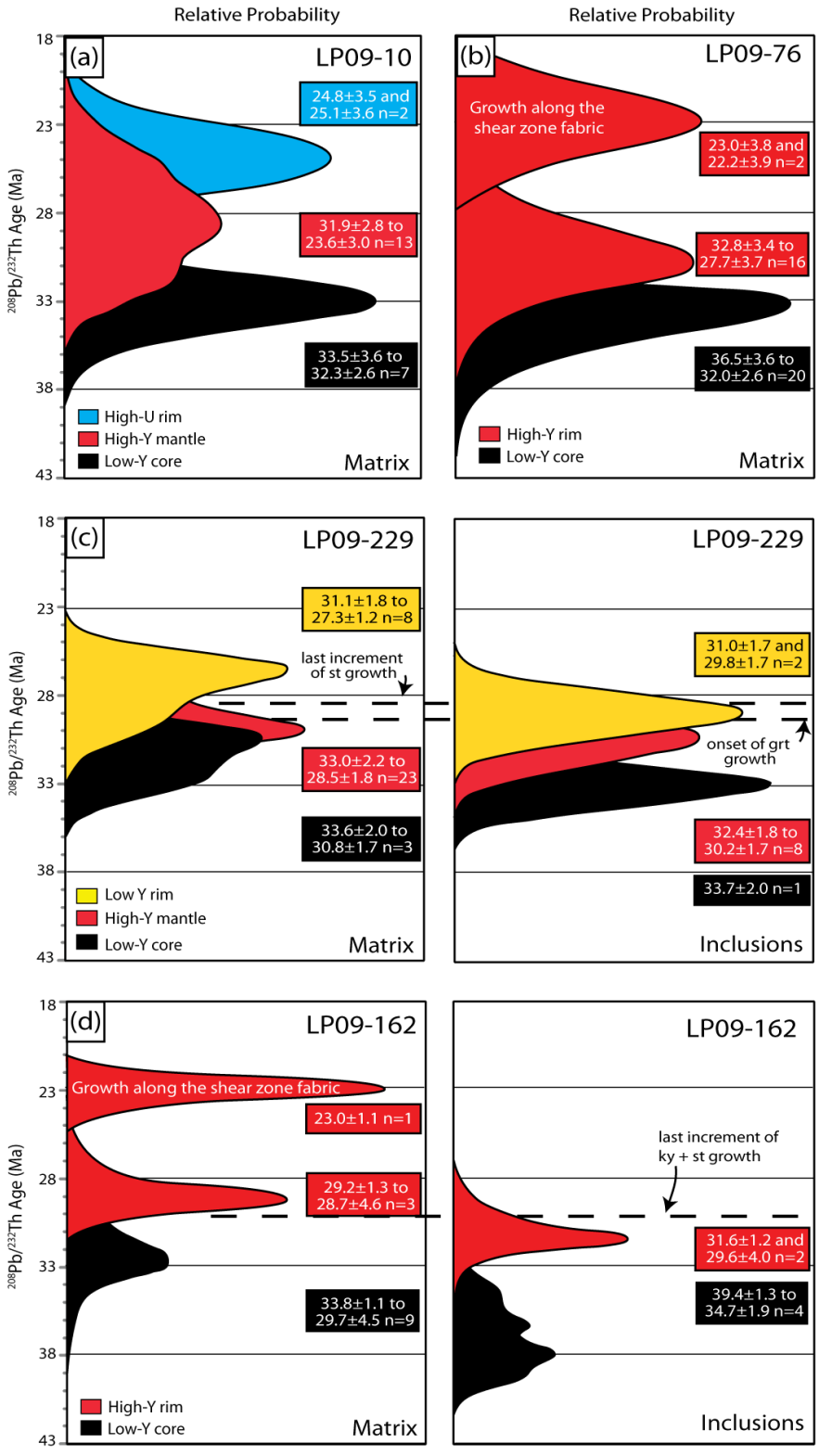
Relative Probability
Relative Probability
(a)
LP09-10
24.8±3.5 and 25.1±3.6 n=2
31.9±2.8 to 23.6±3.0 n=13
33.5±3.6 to 32.3±2.6 n=7
High-U rim
High-Y mantle
Low-Y core
Matrix
(b)
LP09-76
Growth along the shear zone fabric
23.0±3.8 and 22.2±3.9 n=2
32.8±3.4 to 27.7±3.7 n=16
36.5±3.6 to 32.0±2.6 n=20
High-Y rim
Low-Y core
Matrix
(c)
LP09-229
31.1±1.8 to 27.3±1.2 n=8
last increment of st growth
33.0±2.2 to 28.5±1.8 n=23
33.6±2.0 to 30.8±1.7 n=3
Low Y rim
High-Y mantle
Low-Y core
Matrix
LP09-229
31.0±1.7 and 29.8±1.7 n=2
onset of grt growth
32.4±1.8 to 30.2±1.7 n=8
33.7±2.0 n=1
Inclusions
(d)
LP09-162
Growth along the shear zone fabric
23.0±1.1 n=1
29.2±1.3 to 28.7±4.6 n=3
33.8±1.1 to 29.7±4.5 n=9
High-Y rim
Low-Y core
Matrix
LP09-162
last increment of ky + st growth
31.6±1.2 and 29.6±4.0 n=2
39.4±1.3 to 34.7±1.9 n=4
Inclusions
208Pb/232Th Age (Ma)
18
23
28
33
38
43

mantles (n=23), and 31.1 ± 1.8 to 27.3 ± 1.2 Ma (n=8) for the low-Y rims (Figs. 2.8c and 2.9c). Monazite inclusions in staurolite yield ages of 33.7 ± 2.0 Ma for low-Y cores (n=1), 32.4 ± 1.8 to 30.2 ± 1.7 Ma for high-Y mantles (n=8), and two ages from low-Y rims of 31.0 ± 1.7 and 29.8 ± 1.7 Ma (Figs. 2.8c and 2.9c; Appendix 2.2). Monazite grains included in staurolite and kyanite along with monazite in the matrix in sample LP09-162 (used for pseudosection calculation) generally exhibit patchy Th zonation (Appendix 2.1). Y zonation defines low-Y cores and thin (~5-10 μm) relatively high-Y rims (Fig. 2.8d; Appendix 2.1). U zonation mimics the Y zonation. Some of the high-Y rims grew along the top-down-to-the-west matrix fabric (Fig. 2.8d). The age data have been separated into three groups: low-Y cores, high-Y rims, and high-Y rims that grew along the fabric. Monazite compositions from this sample dominantly plot above the concordia (Fig. 2.9d), suggesting excess ^{206}Pb. The excess may be from accumulation of ^{206}Pb during ^{238}U disequilibrium (e.g., Schärer, 1984) but ^{208}Pb/^{232}Th ages do not use ^{206}Pb so these ages are unaffected. Analyses on matrix monazite grains yield ages of 33.8 ± 1.1 Ma to 29.7 ± 4.5 Ma for the low-Y cores (n=9), 29.2 ± 1.3 to 28.7 ± 4.6 Ma for the high-Y rims (n=3), and one age of 23.0 ± 1.1 Ma from a high-Y rim that grew along the matrix fabric (Figs. 2.7d, 2.8d, and 2.9d; Appendix 2.1 and 2.2). Analyses on monazite inclusions in staurolite and kyanite yield ages of 39.4 ± 1.3 to 34.7 ± 1.9 Ma for the low-Y cores (n=4) and two ages from the high-Y rims, 31.6 ± 1.2 Ma and 29.6 ± 4.0 Ma (Figs. 2.8d and 2.9d; Appendix 2.1 and 2.2).

Monazite Geochronology from Leucogranites

Monazites in sample LP09-158, from the first generation of leucogranite, yielded ages ranging from 22.4 ± 0.4 Ma to 19.4 ± 0.3 Ma (n=33) (Fig. 2.11; Appendix 2.3). Samples LP09-167 and LP09-157, both from the second generation of leucogranite, yielded ages ranging from 24.7 ± 0.2 Ma to 18.4 ± 0.2 (n=69) and 23.1 ± 0.3 Ma to 18.8 ± 0.2 (n=48), respectively (Fig. 2.11; Appendix 2.3). LP09-166 from the third and youngest generation of leucogranite yields ages ranging from 19.5 ± 0.2 Ma to 18.1 ± 0.2 (n=38) (Fig. 2.11; Appendix 2.3).

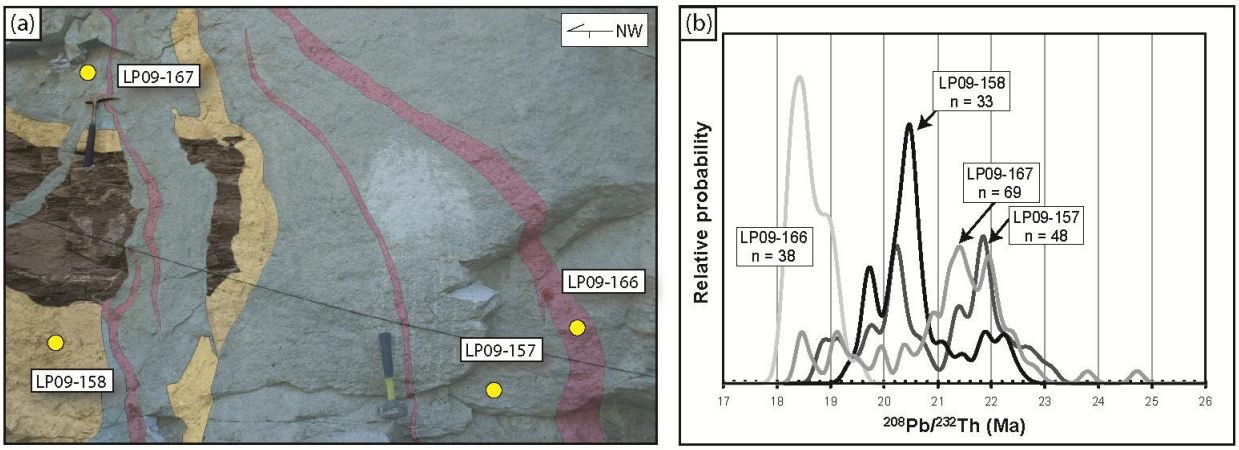

Figure 2.11. *$^{208}Pb/^{232}Th$ ages from leucogranites. (a) Photo of three generations of leucogranite within the injection complex in the Leo Pargil dome and the four leucogranite samples collected. Refer to Figure 2.2b. (b) Relative probability plots for the four leucogranite samples.*

Discussion

Monazite Growth in Metamorphic Rocks

Although U, Th, and Y in metamorphic monazite can relate to age domains in metamorphic monazite, they commonly exhibit complex zonation patterns that may not relate to age zoning alone, but also to reactions and processes that occurred in the rock during metamorphism (e.g., DeWolf et al., 1993; Montel, 1993; Hawkins and Bowring, 1997; Williams et al., 1999; Foster et al., 2000; Williams and Jercinovic, 2002; Spear and Pyle, 2010). Metamorphic monazite from this study exhibits patchy Th compositional zonation, discrete Y compositional zones, and U zonation that generally mimics the Y zonation but sometimes also mimics the patchy Th zonation (Appendix 2.1) suggesting that these domains reflect processes other than age alone..

Y zonation in monazite is sensitive to garnet and xenotime growth or breakdown. Modeling of monazite growth by Spear and Pyle (2010) demonstrates that at intermediate pressures, Y zonation is controlled by xenotime in the absence of garnet and by garnet in the absence of xenotime. In rocks with minimal xenotime, garnet entrains most of the bulk Y within a rock during or after its growth. Low-Y domains can grow on monazite grains during and after garnet growth as the Y is partitioned into the garnet (e.g., Pyle and Spear, 1999; Foster et al., 2000,

2002; Pyle et al., 2001; Cottle et al., 2009b). Likewise, high-Y domains can grow on monazite grains after the breakdown of garnet as the bulk Y is released from the garnet (e.g., Pyle and Spear, 1999; Foster et al., 2000, 2002; Pyle et al., 2001; Cottle et al., 2009b). This allows the monazite composition and ages for the compositional domains, specifically the Y compositional zonation, to be related to garnet growth and P-T estimates (e.g., Foster et al., 2004), notwithstanding complications regarding concomitant xenotime growth and dissolution. Compositional zonation in monazite can also be controlled by dissolution monazite and later reprecipitation of this material onto rims of existing monazite grains (Seydoux-Guillaume et al., 2002).

Metamorphic monazite grains in samples from the LPD (LP09-76, LP09-229, and LP09-162) and the Haimanta Group (LP09-10) in the hanging wall of the dome record an episode of semi-continuous growth from ~40 Ma to 25 Ma (Fig. 2.10) and a second episode of growth at ~23 Ma (LP09-76 and LP09-162) with the grains growing along the shear zone fabric (Fig. 2.10b and d). These samples from within the dome and the Haimanta Group in the hanging wall record a change from low-Y growth (cores) to high-Y growth (rims or mantles) at ~33-32 Ma (Fig. 2.10). High-Y growth continued through ~28 Ma and again at ~23 Ma in rocks within the dome, with the exception of LP09-229 which has monazite grains that contain low-Y rims following the growth of the high-Y domain. Due to the absence of xenotime anywhere in this sample, the change to low-Y rim growth in LP09-229 grains is likely related to the onset of garnet growth where the Y begins being partitioned into the garnet rather than the monazite at ~31 Ma. This implies that the Y incorporated into the high-Y domains that began at ~33 Ma was either sourced from an earlier garnet breakdown reaction, from the breakdown of xenotime, or from fluid driven dissolution of the low-Y monazite cores and subsequent reprecipitation into the high-Y monazite domains (Seydoux-Guillaume et al., 2002).

Metamorphic monazite is produced through a variety of reactions at different metamorphic conditions (e.g., Kingsbury et al., 1993; Spear and Pyle, 2002, 2010; Kohn and Malloy, 2004). For example, it can form as a replacement of allanite at staurolite-grade conditions (~600° C) (Spear and Pyle, 2002), at garnet-grade conditions (~550° C) from REE rich clay in the parent rock (Kingsbury et al., 1993), at low-grade (<400 ºC) conditions as a breakdown product of allanite (Spear and Pyle, 2002), and from the breakdown of muscovite, chlorite, and garnet at the

staurolite-isograd in metapelitic rocks (Kohn and Malloy, 2004). Chambers et al. (2009) suggested that the breakdown of muscovite and chlorite at the garnet-isograd produced the P and LREE's necessary for monazite growth in the Haimanta Group in the hanging wall of the LPD.

This study suggests that the first episode of monazite growth in these samples (~40-25 Ma) occurred during prograde Barrovian metamorphism and that the second episode (~23 Ma) occurred concurrent with the initial stages of decompression and exhumation of the LPD following the end of prograde Barrovian metamorphism (see discussion in the following section). Ages for Barrovian metamorphism overlap with those from Chambers et al. (2009), who suggested that the Haimanta Group to the south of the field area records garnet growth beginning at >34 Ma, peak burial at 30 Ma at 610-620° C and 7-8 kbar, and the end of garnet growth at 28 Ma.

Garnet porphyroblasts in the LPD samples contain few monazite inclusions, while staurolite and kyanite contain more abundant monazite inclusions. Garnet porphyroblasts in sample LP09-229 are included in staurolite suggesting that garnet growth predates staurolite growth (Fig. 2.3d). This implies that monazite growth began prior to garnet growth (>31 Ma) at or near the garnet-isograd (involving the garnet-isograd reaction) and the monazite was later incorporated into the garnet during growth, beginning soon before 31 Ma. More monazite grew following garnet growth involving the staurolite-isograd reaction, and was incorporated in staurolite porphyroblasts when they were growing. Monazite grains within the matrix that were not incorporated into the staurolite and kyanite in samples from within the dome continued to grow until ~28 Ma during Barrovian metamorphism, after the growth of staurolite and kyanite had ceased. This demonstrates that monazite grains in these samples grew as a result of multiple reactions associated with prograde Barrovian metamorphism.

A second episode of monazite growth occurred at ~23 Ma during retrograde metamorphism associated with decompression and top-down-to-the-west shearing, after ~5 Ma of no growth following the end of Barrovian metamorphism. Decompression is associated with the breakdown of staurolite and kyanite and the growth of cordierite and sillimanite (Fig. 2.7). Mahan et al. (2006) documented monazite growth during decompression in samples from the Legs Lake shear zone system in the western Canadian Shield. They suggest that major silicate phases such as garnet can be the source of P needed for monazite growth. The breakdown of chlorite and garnet

has also been reported to source P and LREE's for monazite (Kohn and Malloy, 2004; Chambers et al., 2009). This study suggests that retrograde monazite in sample LP09-162 may have formed by reactions that included the breakdown of garnet, kyanite, chlorite, and staurolite, based on the observed assemblages in this sample (Fig. 2.7).

Barrovian Metamorphism

P-T constraints from this study indicate that the rocks exposed within the LPD and the LPSZ experienced peak temperatures during metamorphic conditions of 530-630° C and ~7-8 kbar during Barrovian metamorphism (Table 2.4). Barrovian metamorphism is attributed to crustal thickening following the initial collision (~50 Ma; Searle et al., 1987; Najman et al., 2010) of the Indian and Eurasian plates. Monazite growth initiated at ~40 Ma during prograde metamorphism and continued until ~25 Ma. In sample LP09-229, low-Y rims on monazite inclusions in staurolite range from 31.0 ± 1.7 Ma to 29.8 ± 1.7 Ma and low-Y rims on monazite grains in the matrix range from 31.1 ± 1.8 to 27.3 ± 1.2 Ma (Fig. 2.10c). This suggests that low-Y rims were growing on matrix monazites at ~31 Ma and some of the monazites were later included in staurolite grains. This was followed by the cessation of staurolite growth soon after ~30 Ma, after which low-Y rims continued to grow on the monazite grains within the matrix until ~27 Ma. The transition from the growth of high-Y mantles (~33-29 Ma) to low-Y rims (~31-27 Ma) on the monazite grains could reflect the onset of xenotime and/or garnet growth as Y began to be partitioned into these phases rather than the monazite (e.g., Pyle and Spear, 1999; Foster et al., 2000, 2002; Pyle et al., 2001). However, since there is no evidence for xenotime in sample LP09-229, it is interpreted the Y zonation is related to garnet growth. This suggests that garnet growth potentially began by ~31 Ma in this sample (Fig. 2.10c), overlapping with estimates from Chambers et al. (2009). Garnet is sometimes partially included in staurolite grains (Fig. 2.3d). There is no evidence for garnet overgrowths on staurolite, suggesting that staurolite growth began after garnet growth had ceased. These data indicate that the transition from garnet growth to staurolite growth occurred at ~31-30 Ma.

High-Y rims on monazite inclusions in staurolite and kyanite in sample LP09-162 are ~31 Ma and high-Y rims on monazite grains in the matrix are younger, ~29 Ma (Fig. 2.10d). This suggests that staurolite and kyanite were growing at and before ~31 Ma and incorporating

monazite grains with high-Y rims. Porphyroblast growth ceased soon after and high-Y rims continued to grow on matrix monazite at ~29 Ma. This bracket for staurolite and kyanite growth overlaps with the data from sample LP09-229.

Decompression

Cordierite and sillimanite occur in rocks from within the dome in top-down-to-the-west strain shadows and as overgrowths on staurolite and kyanite porphyroblasts that grew during Barrovian metamorphism at >30 Ma. The cordierite and sillimanite record near-isothermal decompression to ~4 kbar during top-down-to-the-west shearing (Figs. 2.7 and 2.12). LP09-76 contains a monazite with a rim that grew along the matrix fabric (22.2 ± 3.9 Ma and 23.0 ± 3.8 Ma; Fig. 2.8b), placing a minimum age for the top-down-to-the-west fabric at ~23 Ma. The 23.0 ± 1.1 Ma age for the high-Y rim that grew along the matrix fabric in sample LP09-162 (Fig. 2.8d) suggests that the fabric associated with decompression, which contains sillimanite and cordierite in the matrix and in strain shadows on staurolite and kyanite, was present by this time. These consistent data from two different portions of the LPSZ separated by 15 km demonstrate that top-down-to-the-west shearing and decompression associated with the cordierite + sillimanite occurred at >23 Ma. The cordierite + sillimanite assemblage is attributed to decompression (e.g., Brown and Earl, 1983; Norlander et al., 2002) during exhumation of the dome and temperature influx from leucogranite intrusion, maintaining near-isothermal conditions during the initial stages of exhumation.

Peak pressure estimates of 6.6 kbar (LP09-162) suggest that the rocks within the dome were at a depth of ~25 km (assuming a lithostatic pressure gradient of 3.7 km/kbar) during Barrovian metamorphism and staurolite and kyanite growth, with kyanite and staurolite growth ending soon after 30 Ma. Lower pressures (4.5 kbar; depth of ~17 km) overprinted early Barrovian metamorphism during decompression by 23 Ma (Table 2.4). Using the P-T conditions of the host rocks between 29 Ma (end of Barrovian in this sample) and 23 Ma (minimum for onset of exhumation) and a lithostatic pressure gradient of 3.7 km/kbar yields a minimum exhumation rate of 1.3 mm/yr between 29 and 23 Ma (Fig. 2.13). This exhumation rate underestimates the true exhumation rate because the age for decompression is a minimum since the age is from a monazite rim that grew along the shear zone fabric, suggesting that the fabric

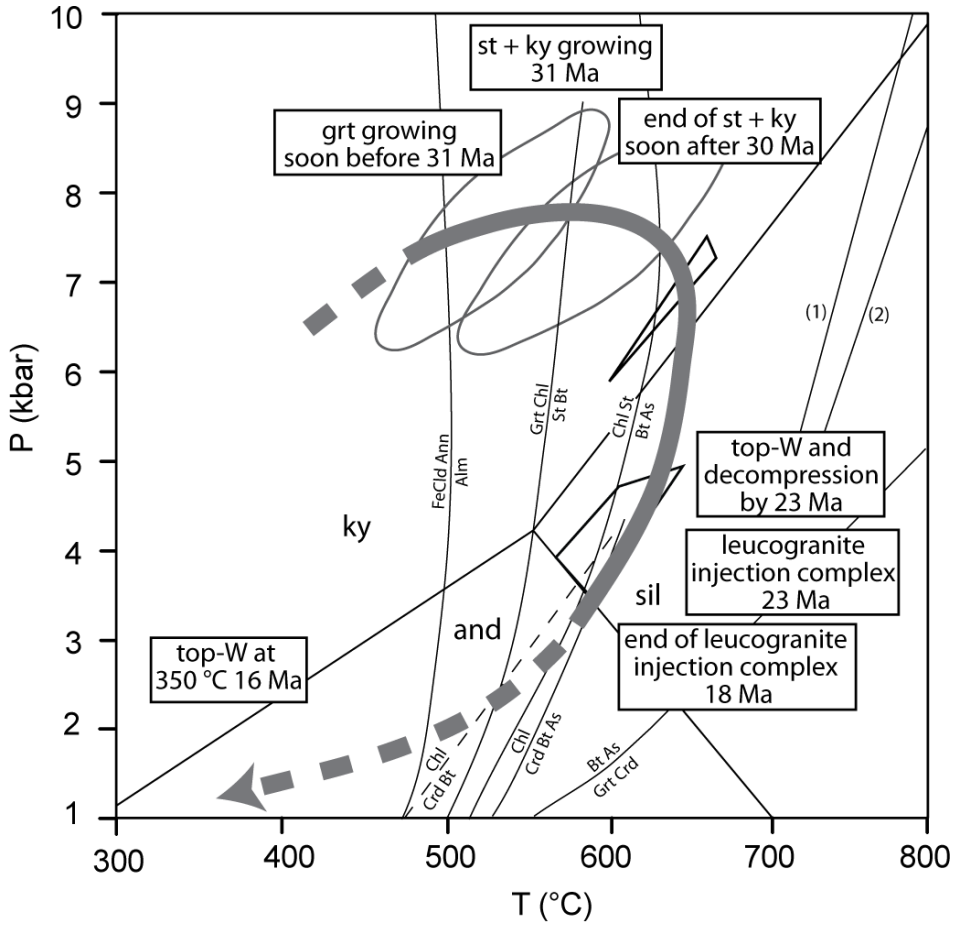

Figure 2.12. *Pressure-temperature-time-deformation (P-T-t-D) path for exhumation of the Leo Pargil dome, dashed where inferred. Continued ductile exhumation at 16 Ma during top-down-to-the-west shearing on the LPSZ after Thiede et al. (2006). Grey ellipses represent P-T estimates from the LPSZ and white polygons are from Figure 2.7. (1) and (2) are wet melting curves for two real pelites of differing compositions from Nepal (Patino-Douce and Harris, 1998). Examples of isograd and cordierite reactions from Spear (1995).*

was there prior to growth of the rim. The exhumation rate is estimated from data for a sample collected near the confluence of the Spiti and Sutlej Rivers at the southernmost end of the dome. White mica $^{40}Ar/^{39}Ar$ ages record continued exhumation through ~350° C at ~16 Ma (Thiede et al., 2006), following the onset of shear zone development (Figs. 2.11 and 2.12). Apatite fission track ages suggest that exhumation into positions in the crust that were dominated by brittle deformation continued to exhume the LPD along the Kaurik-Chango normal fault at 10 Ma (Thiede et al., 2006; Hintersberger et al., 2010, 2011).

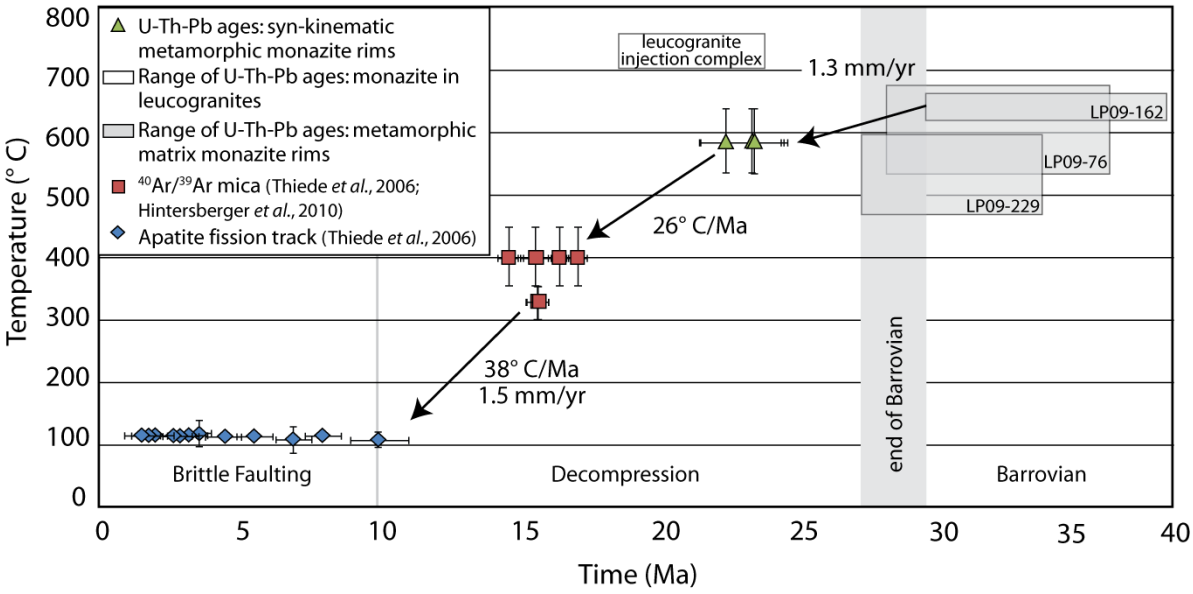

Figure 2.13. *Temperature-time plot for the Leo Pargil dome rocks. Metamorphic monazite ages are plotted against peak temperatures calculated for these samples, with the exception of syn-kinematic monazite. Temperatures for syn-kinematic monazite ages are from temperatures during decompression calculated from sample LP09-162 (see Figure 2.7). Syn-kinematic monazite ages are the minimum age for top-down-to-the-west to shearing and decompression. All other age data is plotted against closure temperature. See text for discussion about exhumation rates from 29 to 23 Ma. Cooling rates are calculated from a best fit line between syn-kinematic monazite and mica data and between the mica and apatite data. Corresponding exhumation rates following cessation of leucogranite intrusion are calculated from the cooling rate assuming a geothermal gradient of 25° C/km.*

A compilation of monazite U-Th-Pb ages from metamorphic rocks and leucogranites presented in this investigation, $^{40}Ar/^{39}Ar$ mica ages (Thiede et al., 2006; Hintersberger et al., 2010), and apatite fission track ages (Thiede et al., 2006) show an increase in cooling rate of 26° C/Ma between 23-16 Ma and 38° C/Ma (1.5 mm/yr) between 16-10 Ma, after which exhumation transitioned to brittle faults (Fig. 2.13) (Thiede et al., 2006; Hintersberger et al., 2010). The temperature during decompression was controlled in part by a temperature influx during leucogranite intrusion until 18 Ma when leucogranite intrusion ceased. The transition from ductile exhumation to brittle faults is defined by a large decrease in the cooling rate beginning at ~10 Ma (Thiede et al., 2006).

Tectonic Implications and Processes for Dome Formation

The northward termination of the LPSZ and the Qusum detachment fault bounding the LPD with the Karakoram fault system suggests that extension along the flanks of the LPD is potentially kinematically linked to right-lateral slip on the Karakoram fault system. The onset age of the Karakoram fault system and its total amount of displacement is widely debated, but ages vary from ~13-15 Ma (e.g., Phillips et al., 2004; Searle et al. 2007) to >25 to 21 Ma (e.g., Lacassin et al., 2004; Valli et al., 2007). The older ages overlap with the age for the onset of orogen-parallel extension and exhumation of the LPD (>23 Ma), suggesting that there may be an early dextral movement on the Karakoram fault system that when combined with a weakened crust could have produced the kinematic setting that led to the development of the LPSZ and exhumation of the LPD. In contrast, younger ages for initiation of the Karakoram suggests that early (~23 Ma) exhumation of the LPD was decoupled from dextral displacement on the Karakoram fault.

Hintersberger et al. (2010) suggests that the Karakoram fault accommodates a minimal amount of modern displacement, implying that east-west extension in this part of the Himalaya cannot all be transferred from the Karakoram fault. In this model, the Karakoram fault only accommodates a portion of the east-west displacement from within the Tibetan Plateau and the remainder of the deformation is transferred south, to a system of north-south trending brittle normal faults, including the brittle faults on the southwest flank of the LPD (Hintersberger et al., 2010). Other studies suggest a large amount of total displacement (up to 120 km) has occurred along the Karakoram fault (Valli et al., 2007). This data suggests that orogen-parallel extension in this portion of the Himalaya began at >23 Ma, much earlier than previously recorded (minimum 16 Ma, Thiede et al., 2006) implying that at this time a tectonic regime existed that promoted orogen-parallel extension, whether it be transferred from the Karakoram fault or from the Tibetan Plateau.

The Tso Morari dome (Fig. 2.1a) contains ultrahigh-pressure rocks that record eclogitic conditions at ~55 Ma that were exhumed by ~29 Ma (de Sigoyer et al., 2004). Portions of the Tso Morari dome were later overprinted by dextral shear associated with the Karakoram fault system suggesting that here the Karakoram fault is <29 Ma. If the LPD is kinematically linked to movement on the Karakoram fault, new ages from this investigation for the initiation of top-

down-to-the-west shearing on the southwest flank of the LPD along with existing data from the Tso Morari Dome potentially bracket the timing of initiation of the Karakoram fault system along this portion of the fault to between <29 and 23 Ma. However, further details about the kinematic evolution of the LPSZ and the potential links with the Karakoram fault must be evaluated before these links can be established.

The onset of orogen-parallel extension and decompression by 23 Ma coincided with intrusion of the injection complex from 23 to 18 Ma suggesting a relationship exists between the onset of extension and crustal melting. Melt in thickened crust can result in and potentially enhance lateral or buoyant vertical crustal flow that will promote the development of extensional shear zones (e.g., Royden, 1996; Rey et al., 2001; Teyssier and Whitney, 2002). In contrast, melting could develop in response to crustal extension by decompression-driven melting (e.g., Hodges, 1998; Whitney et al., 2003).

Aspects of this investigation that are most relevant to testing models for dome formation are the P-T conditions for Barrovian metamorphism, the timing and duration of leucogranite injection, and timing of the onset of isothermal decompression and deformation on the LPSZ. U-Th-Pb ages from the leucogranite injection complex suggest that leucogranite intrusion occurred from 23-18 Ma in the southern portion of the dome (Figs. 2.10b and 2.12). U-Pb ages of zircons from LPD leucogranites from Leech (2008) range from 28-19 Ma. The host rocks within the dome contain sillimanite + cordierite overgrowths and strain shadows on assemblages that grew during Barrovian metamorphism at >30 Ma (e.g., staurolite and kyanite). Cordierite + sillimanite record the onset of near-isothermal decompression to 4.3 kbar and top-down-to-the-west shearing by 23 Ma (Figs. 2.6 and 2.12). These data can test the probability of several possible models to describe the exhumation of the LPD.

Model 1: One model for exhumation of the dome invokes a mid-crust with partial melting (28-18 Ma) that developed during south-directed extrusion of the GHS between the MCTZ and STDS (Vannay and Grasemann, 2001). In this model, near-isothermal decompression that is recorded in rocks currently exposed in the dome was created by ductile movement on the STDS. The Kaurik-Chango normal fault system, potentially related to movement on the Karakoram fault, exhumed mid-crustal rocks that record melting and leucogranite injection that predate exhumation of the dome. This model predicts that all of the exhumation was accommodated on

the brittle Kaurik-Chango normal fault and therefore no ductile top-down-to-the-west shear zone develops.

Model 2: An alternative model builds on the previous model where all of the P-T-t-D history of the dome formed during early ductile south-directed extrusion between the STDS and MCTZ. However, instead of attributing all of the exhumation to a brittle normal fault, the LPSZ represents the sheared contact between the Haimanta Group and underlying GHS that was rotated and reactivated during top-down-to-the-west shear (Thiede et al., 2006). In this model, the ductile top-down-to-the-west LPSZ exhumes rocks that record a P-T-t-D history that predate exhumation of the dome by movement on the LPSZ.

Model 3: Initial melt generation and leucogranite emplacement began at ~28 Ma (Leech, 2008) and continued to 18 Ma as a protracted event that created a weakened crust by generating a hot ductile mid-crust (e.g., Hollister and Crawford, 1986; Beaumont et al., 2004). The initiation of extension on the broadly distributed LPSZ triggered decompression melting, ascent and intrusion of accumulated melt into the injection complex at 23 Ma. In this model, the decompression path recorded in rocks within the dome accompanied exhumation of the dome.

Model 1 predicts exhumation of the LPD on only the brittle Kaurik-Chango normal fault system. This model does not account for the presence of a broadly distributed LPSZ that records top-down-to-the-west deformation. Data from this investigation demonstrates that west-directed ductile extension resulted in the development of cordierite + sillimanite assemblages during decompression (>23 Ma) that was immediately followed by intrusion and crystallization of decompression-driven melts (23-18 Ma). This implies that melting and decompression recorded in the LPD are linked to movement on the LPSZ that accommodated exhumation, in contrast to Model 2. Predictions of Model 3 best explains the evolution of the LPD, where early partial melting weakened the mid-crust and east-west-directed exhumation that was trigged by some kinematic driver such as movement on the Karakoram fault lead to decompression melting.

Previous studies suggested that ductile exhumation of the LPD began at a minimum of 16 Ma (Thiede et al., 2006). Our data implies that orogen-parallel extension in this part of the Himalaya occurred ~7 Ma earlier (Thiede et al., 2006), potentially during a time of active exhumation along the STDS recorded to the south in Sutlej valley (e.g., Inger and Harris, 1993; Hodges, 2000; Harris and Massey, 1994; Vannay et al., 2004). Mitsuishi et al. (2012) document

east-west extension on the Kung Co rift (19 Ma) concurrently with north-south extension along the STDS in southern Tibet, suggesting that east-west extension in this portion of the Tibetan Plateau also potentially occurred during a time of active exhumation of the GHS.

Competing models for melt-present flow and subsequent exhumation of gneiss domes in different kinematic settings (e.g., Teyssier and Whitney, 2002; Beaumont et al., 2004; Lee et al., 2000, 2004) (including crustal melting and buoyancy driven flow, crustal extension, transpression, or thrusting) demonstrate the complexities of gneiss dome formation. Data from the LPD suggest that multiple mechanisms worked to exhume this dome including an interplay between a kinematic setting that favored orogen-parallel extension, protracted anatexis, strain partitioning, and decompression. These processes may pertain to models for gneiss dome formation in other settings where crustal melting and strain partitioning occur.

Conclusions

P-T-t-D constraints on the timing of metamorphism, melting, and onset of exhumation of the LPD indicate that the rocks within the dome experienced prograde Barrovian metamorphism associated with the growth of staurolite and kyanite at conditions of 530-630° C and ~7-8 kbar prior to 30 Ma. This was followed by top-down-to-the-west shearing and near-isothermal decompression of the LPD rocks to ~4 kbar by 23 Ma and emplacement of the leucogranite injection complex from 23 to 18 Ma. Competing models for the feedback between melt-present flow and subsequent exhumation of domes in different kinematic settings (e.g., Teyssier and Whitney, 2002; Beaumont et al., 2004; Lee et al., 2000, 2004) demonstrate the complexities of dome exhumation. Gneiss domes in orogenic settings can be exhumed through multiple processes including but not limited to crustal melting and buoyancy driven flow, crustal extension, transpression, or thrusting. Data from this investigation suggests that multiple processes worked to exhume the LPD. The processes that exhumed this dome were controlled by a relationship between a kinematic setting that favored orogen-parallel extension, protracted anatexis, strain partitioning, and decompression. Melt-weakening of the crust and strain localization promoted shear zone development, decompression of the footwall rocks by 23 Ma, and decompression melting in the core during exhumation of the dome from 23 to 18 Ma.

References

Aoya, M., Adam, J., Wallis, S., Kawakami, T., Lee, J., Wang, Y., and Maeda, H., 2006, The Malashan in south Tibet; comparative study with the Kangmar dome with special reference to kinematics of deformation and origin of associated granites, *in* Law, R.D., Searle, M.P., and Godin, L., eds., Channel flow, ductile extrusion and exhumation in continental collision zones: Geological Society [London] Special Publication, v. 268, p. 471-495.

Armijo, R., Tapponnier, P., Mercier, J., and Tong-Lin, H., 1986, Quaternary extension in southern Tibet: Field observations and tectonic implications: Journal of Geophysical Research, v. 91, p. 803-813.

Beaumont, C., Jamieson, R., Nguyen, M., and Lee, B., 2001, Himalayan tectonics explained by extrusion of a low-viscosity crustal channel coupled to focused surface denudation: Nature, v. 414, p. 738-742.

Beaumont, C., Jamieson, B., Nguyen, M., and Medvedev, S., 2004, Crustal channel flows: 1. Numerical models with applications to the tectonics of the Himalayan-Tibetan orogen: Journal of Geophysical Research, v. 109, p. 1-29.

Brown, M., and Earl, M., 1983, Cordierite-bearing schists and gneisses from Timor, eastern Indonesia: P-T conditions of metamorphism and tectonic implications: Journal of Metamorphic Geology, v. 1, p. 183-203.

Burg, J., and Chen, J., 1984, Tectonics and structural zonation of southern Tibet, China: Nature, v. 311, p. 219-223.

Chambers, J. A., Caddick, M., Argles, T. W., Horstwood, M. S. A., Sherlock, S., Harris, N. B. W., Parrish, R. R., and Ahmad, T., 2009, Empirical constraints on extrusion mechanisms from the upper margin of an exhumed high-grade orogenic core, Sutlej valley, NW India: Tectonophysics, v. 477, p. 77-92.

Chen, Z., Liu, Y., Hodges, K. V., Burchfiel, B. C., Royden, L. H., and Deng, C., 1990, The Kangmar Dome; a metamorphic core complex in southern Xizang (Tibet): Science, v. 250, p. 1552-1556.

Connolly, J., 2009, The geodynamic equation of state: What and how: Geochemistry Geophysics Geosystems, v. 10, 19 p.

Cottle, J. M., Jessup, M. J., Newell, D. L., Horstwood, M. S. A., Noble, S. R., Parrish, R. R., Waters, D. J., and Searle, M. P., 2009a, Geochronology of granulitized eclogites from the Ama Drime Massif: implications for the tectonic evolution of the South Tibetan Himalaya: Tectonics, v. 28, p. 1-25.

Cottle, J.M., Searle, M.P., Horstwood, M.S.A., and Waters, D.J., 2009b, Timing of mid-crustal metamorphism, melting and deformation in the Mt. Everest region of southern Tibet revealed by U(-Th)-Pb geochronology: Journal of Geology, v. 117, p. 643-664.

Cottle, J.M., Horstwood, M.S.A., and Parrish, R.R., 2009c, A new approach to single shot laser ablation analysis and its application to in-situ geochronology: Journal of Analytical Atomic Spectrometry, v. 24, p. 1355-1363.

D'Lemos, R., Brown, M., and Strachan, R., 1992, Granite magma generation, ascent and emplacement within a transpressional orogen: Journal of the Geological Society [London], v. 149, p. 487-490.

de Segoyer, J., Guillot, S., and Dick, P., 2004, Exhumation of the ultrahigh-pressure Tso Morari unit in eastern Ladakh (NW Himalaya): A case study: Tectonics, v. 23, doi:10.1029/2002TC001492.

DeWolf, C., Beshaw, N., and O'Nion, R., 1993, A metamorphic history from micron-scale $^{207}Pb/^{206}Pb$ chronometry of Archean monazite: Earth and Planetary Science Letters, v. 120, p. 207-220.

Foster, G., Gibson, H., Parrish, R., Horstwood, M., Fraser, M., and Tindle, A., 2002, Textural, chemical and isotopic insights into the nature and behavior of metamorphic monazite: Chemical Geology, v. 191, p. 183-207.

Foster, G. L., Kinny, P., Vance, D., Prince, C., and Harris, N. B. W., 2000, The significance of monazite U-Th-Pb age data in metamorphic assemblages; a combined study of monazite and garnet chronometry: Earth and Planetary Science Letters, v. 181, p. 327-340.

Foster, G., Parrish, R., Horstwood, M., Chenery, S., Pyle, J., and Gibson, H., 2004, The generation of prograde P-T-t points and paths; a textural, compositional, and chronological study of metamorphic monazite: Earth and Planetary Science Letters, v. 228, p. 125-142.

Frank, W., Graseman, B., Guntli, P., and Miller, C., 1995, Geological map of the Kishtwar-Chambu-Kulu region (NW Himalayas, India): Jahrbuch der Geologischen Bundesanstalt, v. 138, p. 299-308.

Fuhrman, M., and Lindsley, D., 1988, Ternary-feldspar modeling and thermometry: American Mineralogist, v. 73, p. 201-215.

Grasemann, B., Fritz, H., and Vannay, J. C., 1999, Quantitative kinematic flow analysis from the Main Central Thrust Zone (NW-Himalaya, India): implications for a decelerating strain path and the extrusion of orogenic wedges" Journal of Structural Geology, v. 21, p. 837-853.

Grujic, D., Casey, M., Davidson, C., Hollister, L. S., Kundig, R., Pavlis, T., and Schmid, S., 1996, Ductile extrusion of the Higher Himalayan Crystalline in Bhutan: Evidence from quartz microfabrics: Tectonophysics, v. 260, p. 21-43.

Grujic, D., Hollister, L. S., and Parrish, R. R., 2002, Himalayan metamorphic sequence as an orogenic channel: insight from Bhutan: Earth and Planetary Science Letters, v. 198, p. 177-191.

Harris, N., and Massey, J., 1994, Decompression and anatexis of Himalayan metapelites: Tectonics, v. 13, p. 1537-1546.

Harrison, T. M., McKeegan, K.D., and LeFort, P., 1995, Detection of inherited monazite in the Manaslu leucogranite by $^{208}Pb/^{232}Th$ ion microprobe dating: Crystallization age and tectonic implications: Earth and Planetary Science Letters, v. 133, p. 271-282.

Hawkins, D., and Bowring, S., 1997, U-Pb systematic of monazite and xenotime: case studies from the Paleoproterozoic of the Grand Canyon, Arizona: Contributions to Mineralogy and Petrology, v. 127, p. 87-103.

Hintersberger, E., Thiede, R. C., and Strecker, M.R., 2011, The role of extension during brittle deformation within the NW Indian Himalaya: Tectonics, v. 30, doi:10.1029/2010TC002822.

Hintersberger, E., Thiede, R. C., Strecker, M. R., and Hacker, B., 2010, E-W extension in the NW Indian Himalaya: Geological Society of America Bulletin, v. 122, p. 1499-1515.

Hodges, K.V., 1998, The thermodynamics of Himalayan orogenesis, *in* Treloar, P.J., and O'Brien, P.J., eds., What drives metamorphism and metamorphic reactions?: Geological Society [London] Special Publication, v. 138, p. 7-22.
Hodges, K. V., 2000, Tectonics of the Himalaya and southern Tibet from two perspectives: Geological Society of America Bulletin, v. 112, p. 324-350.
Hodges, K., 2006, A synthesis of the channel flow-extrusion hypothesis as developed for the Himalayan-Tibetan orogenic system, *in* Law, R.D., Searle, M.P., and Godin, L., eds., Channel flow, ductile extrusion and exhumation in continental collision zones: Geological Society [London] Special Publication, v. 268, p. 71-90.
Holland, T., Baker, J., and Powell, R., 1998, Mixing properties and activity-composition relationships of chlorites in the system MgO-FeO-Al_2O_3-SiO_2-H_2O: European Journal of Mineralogy, v. 10, p. 395-406.
Holland, T. J. B., and Powell, R., 1998, An internally consistent thermodynamic data set for phases of petrological interest: Journal of Metamorphic Geology, v. 16, p. 309-343.
Hollister, L., and Crawford, M., 1986, Melt-enhanced deformation: A Major tectonic process: Geology, v. 14, p. 558-561.
Horstwood, M., Foster, G., Parrish, R., Noble, S., and Nowell, G., 2003, Common-Pb corrected in situ U-Pb accessory mineral geochronology by LA-MC-ICP-MS: Journal of Analytical Atomic Spectrometry, v. 18, p. 837-846.
Inger, S., and Harris, N. 1993, Geochemical constraints on leucogranite magmatism in the Langtang Valley, Nepal Himalaya: Journal of Petrology, v. 34, p. 345-368.
Jamieson, R., Beaumont, C., Nguyen, M., and Grujic, D., 2006, Provenance of the Greater Himalayan Sequence and associated rocks: Predictions of channel flow models, *in* Law, R.D., Searle, M.P., and Godin, L., eds., Channel flow, ductile extrusion and exhumation in continental collision zones: Geological Society [London] Special Publication, v. 268, p.165-182.
Jessup, M.J., and Cottle, J.M., 2010, Progression from South-Directed Extrusion to Orogen-Parallel Extension in the Southern Margin of the Tibetan Plateau, Mount Everest Region, Tibet: Journal of Geology, v. 118, p. 467-486.
Jessup, M. J., Newell, D. L., Cottle, J. M., Berger, A. L., and Spotila, J. A., 2008, Orogen-parallel extension and exhumation enhanced by focused denudation in Arun River gorge, Ama Drime Massif, Tibet-Nepal: Geology, v. 36, p. 587-590.
Kali, E., Leloup, P., Arnaud, N., Mahéo, G., Liu, D., Boutonnet, E., Van der Woerd, J., Liu, X., Liu-Zeng, J., and Halibing, L., 2010, Exhumation history of the deepest central Himalayan rocks, Ama Drime range: Key pressure-temperature-deformation-time constraints on orogenic models: Tectonics, v. 29, doi:10.1029/2009TC002551.
Kapp, P., and Guynn, J. H., 2004, Indian punch rifts Tibet: Geology, v. 32, p. 993-996.
Kellett, D. A., Grujic, D., and Erdmann, S., 2009, Miocene structural reorganization of the South Tibetan detachment, eastern Himalaya: Implications for continental collision: Lithosphere, v. 1, p. 259-281.
Kingsbury, J., Miller, C., Wooden, and Harrison, T.M., 1993, Monazite paragneiss and U-Pb systematic in rocks of the eastern Mojave Desert, California, U.S.A.: implications for thermochronometry: Chemical Geology, v. 10, p. 147-167.

Kohn, M. J., and Malloy, M. A., 2004, Formation of monazite via prograde metamorphic reactions among common silicates: implications for age determinations: Geochimica et Cosmochimica Acta, v. 68, p. 101-113.
Kohn, M. J., and Spear, F., 2000, Retrograde net transfer reaction insurance for pressure-temperature estimates: Geology, v. 28, p. 1127-1130.
Kruckenburg, S., Whitney, D., Teyssier, C., Fanning, C., and Dunlap, W., 2008, Paleocene-Eocene migmatite crystallization, extension, and exhumation in the hinterland of the northern Cordillera: Okanogan dome, Washington, USA: Geological Society of America Bulletin, v. 120, p. 912-929.
Lacassin, R., Valli, F., Arnaud, N., et al., 2004, Large-scale geometry, offset and kinematic evolution of the Karakoram fault, Tibet: Earth and Planetary Science Letters, v. 219, p. 255-269.
Langille, J., Jessup, M., Cottle, J., Newell, D., and Seward, G., 2010, Kinematics of the Ama Drime Detachment: Insights into orogen-parallel extension and exhumation of the Ama Drime Massif, Tibet-Nepal: Journal of Structural Geology, v. 32, p. 900-919.
Larson, K., Godin, L., Davis, W., and Davis, D., 2010, Out-of-sequence deformation and expansion of the Himalayan orogenic wedge: insights from the Changgo culmination, south central Tibet: Tectonics, v. 29, p. 1-30.
Lee, J., Hacker, B. R., and Wang, Y., 2004, Evolution of North Himalayan Gneiss Domes: Structural and metamorphic studies in Mabja Dome, southern Tibet: Journal of Structural Geology, v. 26, p. 2297-2316.
Lee, J., Hacker, B., Dinklage, W., Wang, Y., Gans, P., Calvert, A., Wan, J.L., Blythe, A., and McClelland, W., 2000, Evolution of the Kangmar Dome, southern Tibet: Structural, petrologic, and thermochronologic constraints: Tectonics, v. 19, p. 872-895.
Lee, J., Hager, C., Wallis, S., Stockli, D., Whitehouse, M., Aoya, M., and Wang, Y., 2011, Middle to late Miocene extremely rapid exhumation and thermal reequilibration in the Kung Co rift, southern Tibet: Tectonics, v. 30, p. 1-26.
Lee, J., and Whitehouse, M., 2007, Onset of mid-crustal extensional flow in southern Tibet: Evidence from U/Pb zircon ages: Geology, v. 35, p. 45-48.
Leech, M. L., 2008, Does the Karakoram fault interrupt mid-crustal channel flow in the western Himalaya?: Earth and Planetary Science Letters, v. 276, p. 314-322.
Ludwig K. R., 2000, Isoplot/Ex version 2.4. A Geochronological Toolkit for Microsoft Excel: Berkeley Geochronological Centre Special Publication, 55 p.
Mahan, K., Goncalves, P., Williams, M., and Jercinovic, M., 2006, Dating metamorphic reactions and fluid flow: applications to exhumation of high-P granulites in a crustal-scale shear zone, western Canadian Shield: Journal of Metamorphic Geology, v. 24, p. 193-217.
McFadden, R., Teyssier, C., Siddoway, C., Whitney, D., and Fanning, C., 2010, Oblique dilation, melt transfer, and gneiss dome emplacement: Geology, v. 38, p. 375-378.
Miller, C., Thöni, M., Frank, W., Grasemann, B., Klötzli, U., Guntli, P., and Draganits, E., 2001, The early Paleozoic magmatic event in the Northwest Himalaya, India: source, tectonic setting, and age of emplacement: Geologic Magazine, v. 138, p. 237-251.
Mitsuishi, M., Wallis, S., Aoya, M., Lee, J., and Wang, Y., 2012, E-W extension at 19 Ma in the Kung Co area, S. Tibet: Evidence for contemporaneous E-W and N-S extension in the Himalayan orogen: Earth and Planetary Science Letters, v. 325-326, p. 10-20.

Molnar, P., and Chen, W. P., 1983, Focal depths and fault plane solutions of earthquakes under the Tibetan Plateau: Journal of Geophysical Research, v. 88, p. 1180-1196.
Montel, J., 1993, A model for monazite/melt equilibrium and application to the generation of granitic magmas: Chemical Geology, v. 110, p. 127-146.
Murphy, M., and Burgess, P., 2006: Geometry, kinematics, and landscape characteristics of an active transtension zone, Karakoram fault system, southwest Tibet: Journal of Structural Geology, v. 28, p. 268-283.
Murphy, M. A., 2007, Isotopic characteristics of the Gurla Mandhata metamorphic core complex: Implications for the architecture of the Himalayan orogen: Geology, v. 35, p. 983-986.
Murphy, M. A., Saylor, J. E., and Ding, L., 2009, Late Miocene topographic inversion in southwest Tibet based on integrated paleoelevation reconstructions and structural history: Earth and Planetary Science Letters, v. 282, p. 1-9.
Murphy, M. A., Yin, A., Kapp, P., Harrison, T.M., Ding, L., and Guo, J., 2000, Southward propagation of the Karakoram fault system, southwest Tibet: Timing and magnitude of slip: Geology, v. 28, p. 451-454.
Murphy, M. A., Yin, A., Kapp, P., Harrison, T. M., Manning, C. E., Ryerson, F. J., Lin, D., and Jinghui, G., 2002, Structural evolution of the Gurla Mandhata detachment system, Southwest Tibet; implications for the eastward extent of the Karakoram fault system: Geological Society of America Bulletin, v. 114, p. 428-447.
Najman, Y., Appel, E., Boudagher-Fadel, M., Bown, P., Carter, A., Garzanti, E., Godin, L., Han, J., Liebke, U., Oliver, G., Parrish, R., and Vezzoli, G., 2010, Timing of India-Asia collision: Geological, biostratigraphic, and paleomagnetic constrains: Journal of Geophysical Research, v. 115, doi:10.1029/2010JB007673.
Ni, J., and Barazangi, M., 1985, Active tectonics of the western Tethyan Himalaya above the underthrusting Indian plate: The Upper Sutlej River basin as a pull-apart structure: Tectonophysics, v. 112, p. 277-295.
Norlander, B., Whitney, D., Teyssier, C., and Vanderhaeghe, O., 2002, Partial melting and decompression of the Thor-Odin dome, Shuswap metamorphic core complex, Canadian Cordillera: Lithos, v. 61, p. 103-125.
Paquette, J., Nédélec, A., and Moine, B., 1994, U-Pb, single zircon Pb-evaporation, and Sm-Nd study of a granulite domain in SE Madagascar: Journal of Geology, v. 102, p. 523-538.
Patino-Douce, A. and Harris, N., 1998, Experimental constraints on Himalayan anatexis: Journal of Petrology, v. 39, p. 689-710.
Phillips, R.J., Parrish, R.P., and Searle, M.P., 2004, Age constraints on ductile deformation and long-term slip-rates along the Karakoram fault zone, Ladakh: Earth and Planetary Science Letters, v. 226, p. 305-319.
Powell, R., and Holland, T., 1998, An internally-consistent thermodynamic dataset for phases of petrological interest: Journal of Metamorphic Geology, v. 16, p. 309-344.
Powell, R., and Holland, T., 1999, Relating formulations of the thermodynamics of mineral solid solutions: Activity modeling of pyroxenes, amphiboles, and micas: American Mineralogist, v. 84, p. 1-14.
Pyle, J., and Spear, F., 1999, Yttrium zoning in garnet: Coupling of major and accessory phases during metamorphic reactions: Geological Materials Research, v. 1, p. 1-49.

Pyle, J., Spear, F., Rudnick, R., and McDonough, 2001, Monazite-xenotime-garnet equilibrium in metapelites and a new monazite-garnet thermometer: Journal of Petrology, v. 42, p. 2083-2107.

Quigley, M., Liangjun, Y., Xiaohan, L., Wilson, C. J. L., Sandiford, M., and Phillips, D., 2006, $^{40}Ar/^{39}Ar$ thermochronology of the Kampa Dome, southern Tibet: Implications for tectonic evolution of the North Himalayan gneiss domes: Tectonophysics, v. 421, p. 269-297.

Ratschbacher, L., Frisch, G., Liu, G., and Chen, C., 1994, Distributed deformation in southern and western Tibet during and after the Indus-Asia collision: Journal of Geophysical Research, v. 99, p. 917-945.

Rey, P., Vanderhaeghe, O., and Teyssier, C., 2001, Gravitational collapse of the continental crust; definition, regimes and modes: Tectonophysics, v. 342, p. 435-449.

Royden, L.H., 1996, Coupling and decoupling of crust and mantle in convergent orogens: implications for strain partitioning in the crust: Journal of Geophysical Research, v. 101, p. 17679-17705.

Sanchez, V., Murphy, M., Dupré, W., Ding, L., and Zhang, R., 2010, Structural evolution of the Neogene Gar Basin, western Tibet: Implications for releasing bend development and drainange patterns: Geological Society of America Bulletin, v. 122, p. 926-945.

Saylor, J., DeCelles, P., Gehrels, G., Murphy, M., Zhang, R., and Kapp, P., 2010, Basin formation in the High Himalaya by arc-parallel extension and tectonic damming: Zhada basin, southwestern Tibet: Tectonics, v. 29, p. 1-24.

Schärer, U., 1984, The effect of initial ^{230}Th disequilibrium on young U-Pb ages: the Makalu case, Himalaya: Earth and Planetary Science Letters, v. 67, p. 191-204.

Searle, M. P., Law, R. D., and Jessup, M. J. 2006, Crustal structure, restoration and evolution of the Greater Himalaya in Nepal-South Tibet; implications for channel flow and ductile extrusion of the middle crust, *in* Law, R.D., Searle, M.P., and Godin, L., eds., Channel flow, ductile extrusion and exhumation in continental collision zones: Geological Society [London] Special Publication, v. 268, p. 355-378.

Searle, M. P., and Phillips, R.J., 2007, Relationships between right-lateral shear along the Karakoram fault and metamorphism, magmatism, exhumation and uplift: evidence from the K2-Gasherbrum-Pangong ranges, north Pakistan and Ladakh: Journal of Geological Society [London], v. 164, p. 439-450.

Searle, M., Windley, B., Coward, M., Cooper, D., Rex, A., Tingdong, L., Xuchang, X., Jan, M., Thakur, V., and Kumar, S., 1987, The closing of the Tethys and the tectonics of the Himalaya: Geological Society of America Bulletin, v. 98, p. 678-701.

Seydoux-Guillaume, A., Paquette, J., Wiedenbeck, M., Montel, J., and Heinrich, W., 2002, Experimental resetting of the U-Th-Pb systems in monazite: Chemical Geology, v. 191, p. 165-181.

Singh, S., Sinha, P., Jain, A. K., Singh, V. N., and Srivastava, L. S., 1975, Preliminary report on the January 19, 1975, Kinnaur earthquake in Himachal Pradesh: Earthquake Engineering Studies, v. 75, p. 1-32.

Spear, F., 1995, Metamorphic phase equilibria and pressure-temperature-time paths: Mineralogical Society of America, 799 p.

Spear, F., and Pyle, J., 2002, Apatite, monazite, and xenotime in metamorphic rocks: Reviews in Mineralogy and Geochemistry, v. 48, p. 293-335.

Spear, F., and Pyle, J., 2010, Theoretical modeling of monazite growth in a low-Ca metapelite: Chemical Geology, v. 273, p. 111-119.
Styron, R., Taylor, M., and Murphy, M., 2011, Oblique convergence, arc parallel extension, and the role of strike slip faulting in the High Himalaya: Geosphere, v. 7, p. 582-596.
Taylor, M., Yin, A., Ryerson, F., Kapp, P., and Ding, L., 2003, Conjugate strike-slip faulting along the Bangong-Nujiang suture zone accommodates coeval east-west extension and north-south shortening in the interior of the Tibetan Plateau: Tectonics, v. 22, p. 1-25.
Teyssier, C., and Whitney, D., 2002, Gneiss domes and orogeny: Geology, v. 30, p. 1139-1142.
Thiede, R. C., Arrowsmith, J. R., Bookhagen, B., McWilliams, M., Sobel, E. R., and Strecker, M. R., 2006, Dome formation and extension in the Tethyan Himalaya, Leo Pargil, northwest India: Geological Society of America Bulletin, v. 118, p. 635-650.
Valli, F., Arnaud, N., Leloup, P., Sobel, E., Mahéo, G., Lacassin, R., Guillot, S., Li, H., and Tapponnier, P., 2007, Twenty million years of continuous deformation along the Karakorum fault, western Tibet: A thermochronological analysis: Tectonics, v. 26, p. 1-26.
Vannay, J. C., and Grasemann, B., 2001, Himalayan inverted metamorphism and syn-convergence extension as a consequence of a general shear extrusion: Geological Magazine, v. 138, p. 253-276.
Vannay, J., Grasemann, B., Rahn, M., Frank, W., Carter, A., Baudraz, V., and Cosca, M., 2004, Miocene to Holocene exhumation of metamorphic crustal wedges in the NW Himalaya: Evidence for tectonic extrusion coupled with fluvial erosion: Tectonics, v. 23, p. 1-24.
White, R., Powell, R., Holland, T., and Worley, B., 2000, The effect of TiO_2 and Fe_2O_3 on metapelitic assemblages at greenschist and amphibolite facies conditions: mineral equilibria calculations in the system K_2O-FeO-MgO-Al_2O_3-SiO_2-H_2O-TiO_2-Fe_2O_3: Journal of Metamorphic Geology, v. 18, p. 497-511.
White, R., Powell, R., and Holland, T., 2001, Calculation of partial melting equilibria in the system Na_2O-CaO-K_2O-FeO-MgO-Al_2O_3-SiO_2-H_2O (NCKFMASH): Journal of Metamorphic Geology, v. 19, p. 139-153.
Whitney, D., Teyssier, C., Fayon, A., Hamilton, M., and Heizler, M., 2003, Tectonic controls on metamorphism, partial melting, and intrusion: timing and duration of regional metamorphism and magmatism in the Niğde Massif, Turkey: Tectonophysics, v. 376, p. 37-60.
Whitney, D., Teyssier, C., and Heizler, M., 2007, Gneiss domes, metamorphic core complexes, and wrench zones: Thermal and structural evolution of the Niğde Massif, central Anatolia: Tectonics, v. 26, doi:10.1029/2006TC002040.
Wiesmayr, G., and Grasemann, B., 2002, Eohimalayan fold and thrust belt: Implications for the geodynamic evolution of the NW-Himalaya (India): Tectonics, v. 21, p. 1058-1077.
Williams, M. L., and Jercinovic, M. J., 2002, Microprobe monazite geochronology: putting absolute time into microstructural analysis: Journal of Structural Geology, v. 24, p. 1013-1028.
Williams, M. L., Jercinovic, M. J., and Terry, M. P., 1999, Age mapping and dating of monazite on the electron microprobe: Deconvoluting multistage tectonic histories: Geology, v. 27, p. 1023-1026.

Wu, C., Nelson, K., Wortman, G., Samson, S., Yue, Y., Li, J., Kidd, W., and Edward, M., 1998, Yadong cross structure and south Tibetan detachment in the east central Himalaya (89°-90°E): Tectonics, v. 17, p. 28-45.

Zeitler, P., Koons, P., Bishop, M., Chamberlain, C., et al., 2001, Crustal reworking at Nanga Parbat, Pakistan: Metamorphic consequences of thermal-mechanical coupling facilitated by erosion: Tectonics, v. 20, p. 712-728.

Zhang, J., Ding, L., Zhong, D., and Zhou, Y., 2000, Orogen-parallel extension in Himalaya: Is it the indicator of collapse or the product in process of compressive uplift?: Chinese Science Bulletin, v. 45, p. 114-120.

Appendix 2.1

Compositional Maps of Metamorphic Monazite

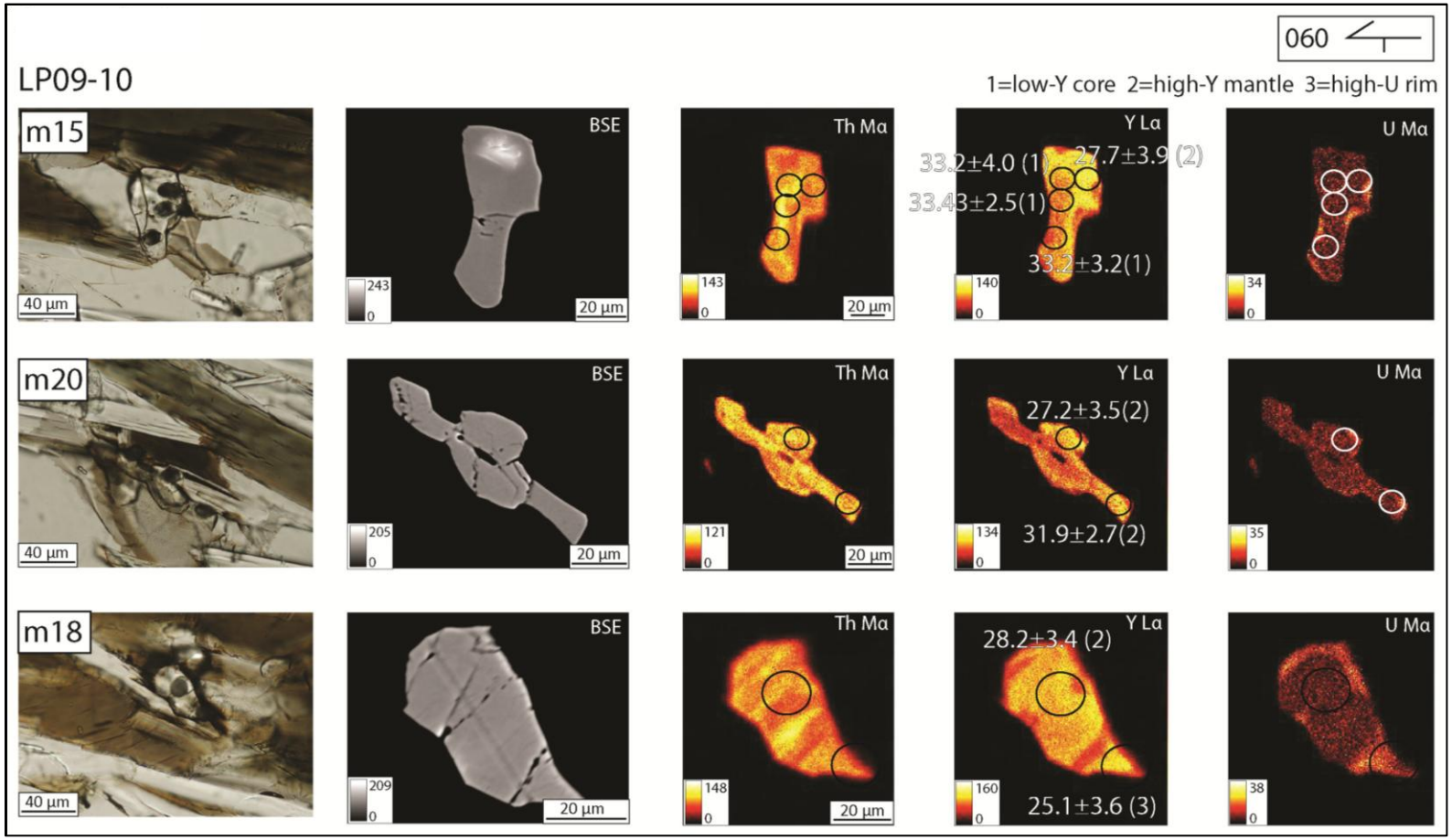

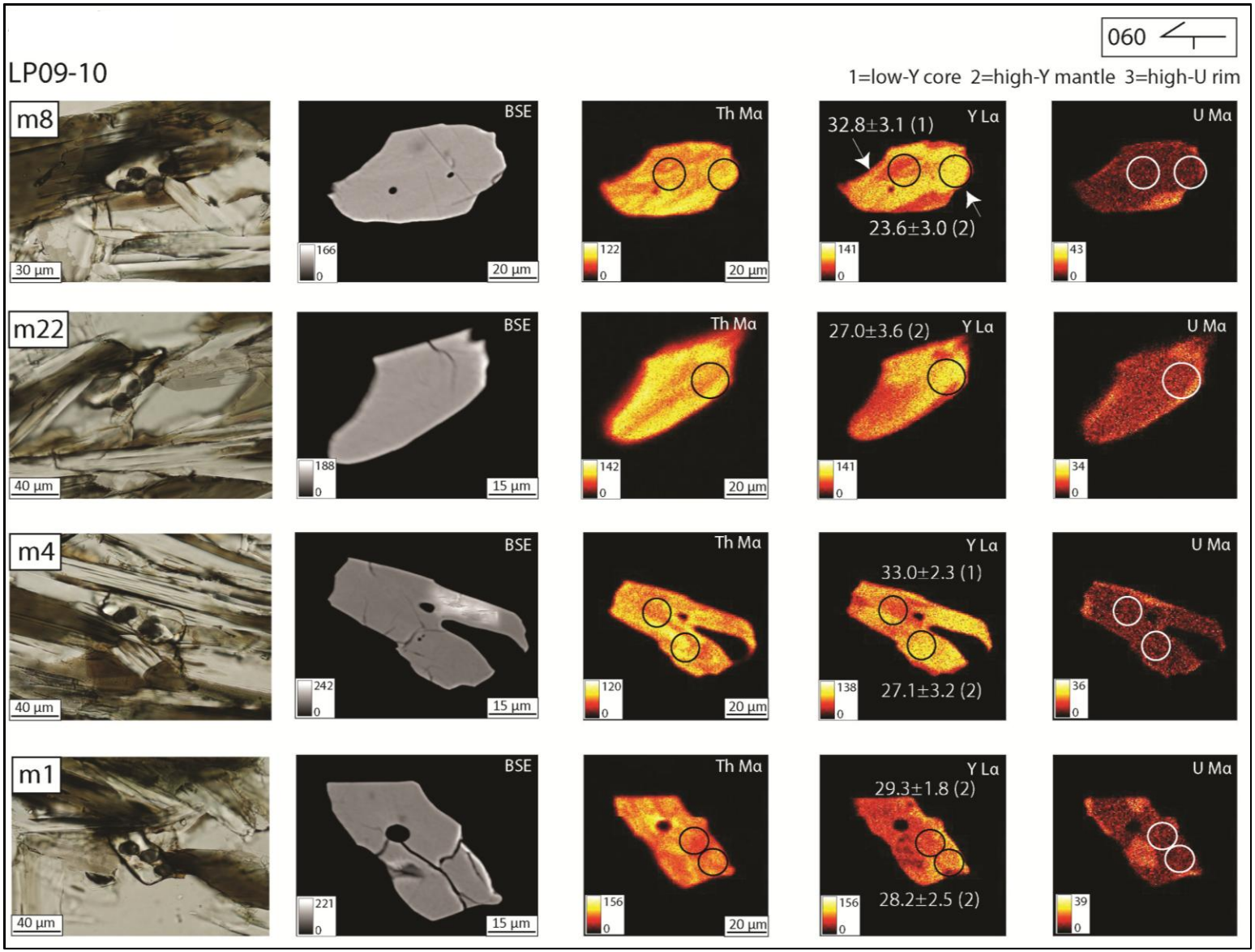
060
LP09-10
1=low-Y core 2=high-Y mantle 3=high-U rim
m8
BSE
Th Mα
32.8±3.1 (1)
Y Lα
23.6±3.0 (2)
U Mα
30 µm
20 µm
m22
27.0±3.6 (2)
40 µm
15 µm
m4
33.0±2.3 (1)
27.1±3.2 (2)
m1
29.3±1.8 (2)
28.2±2.5 (2)

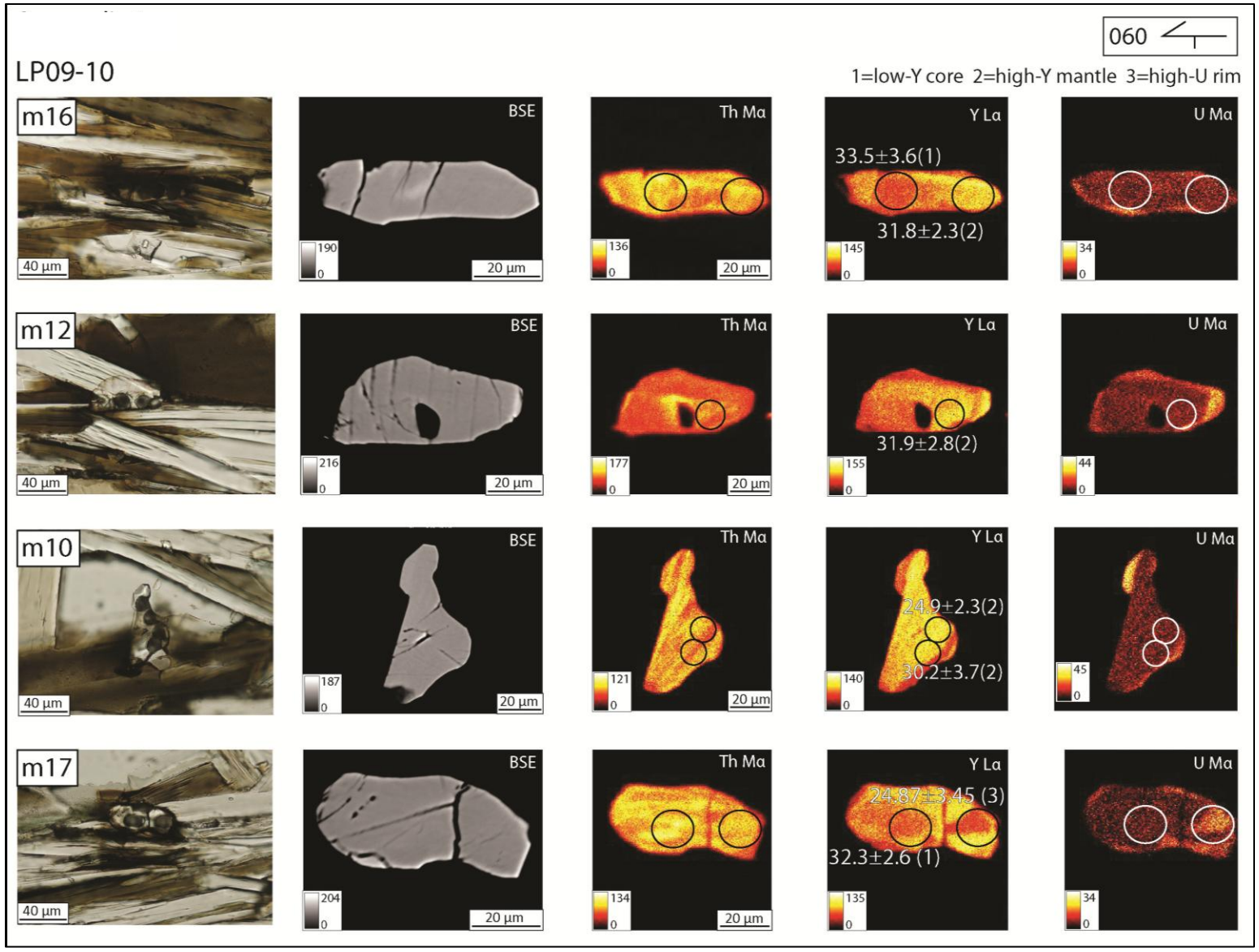
060
LP09-10
1=low-Y core 2=high-Y mantle 3=high-U rim
m16
BSE
Th Ma
Y La
U Ma
33.5±3.6(1)
31.8±2.3(2)
m12
31.9±2.8(2)
m10
24.9±2.3(2)
30.2±3.7(2)
m17
24.87±3.45 (3)
32.3±2.6 (1)
40 µm
20 µm

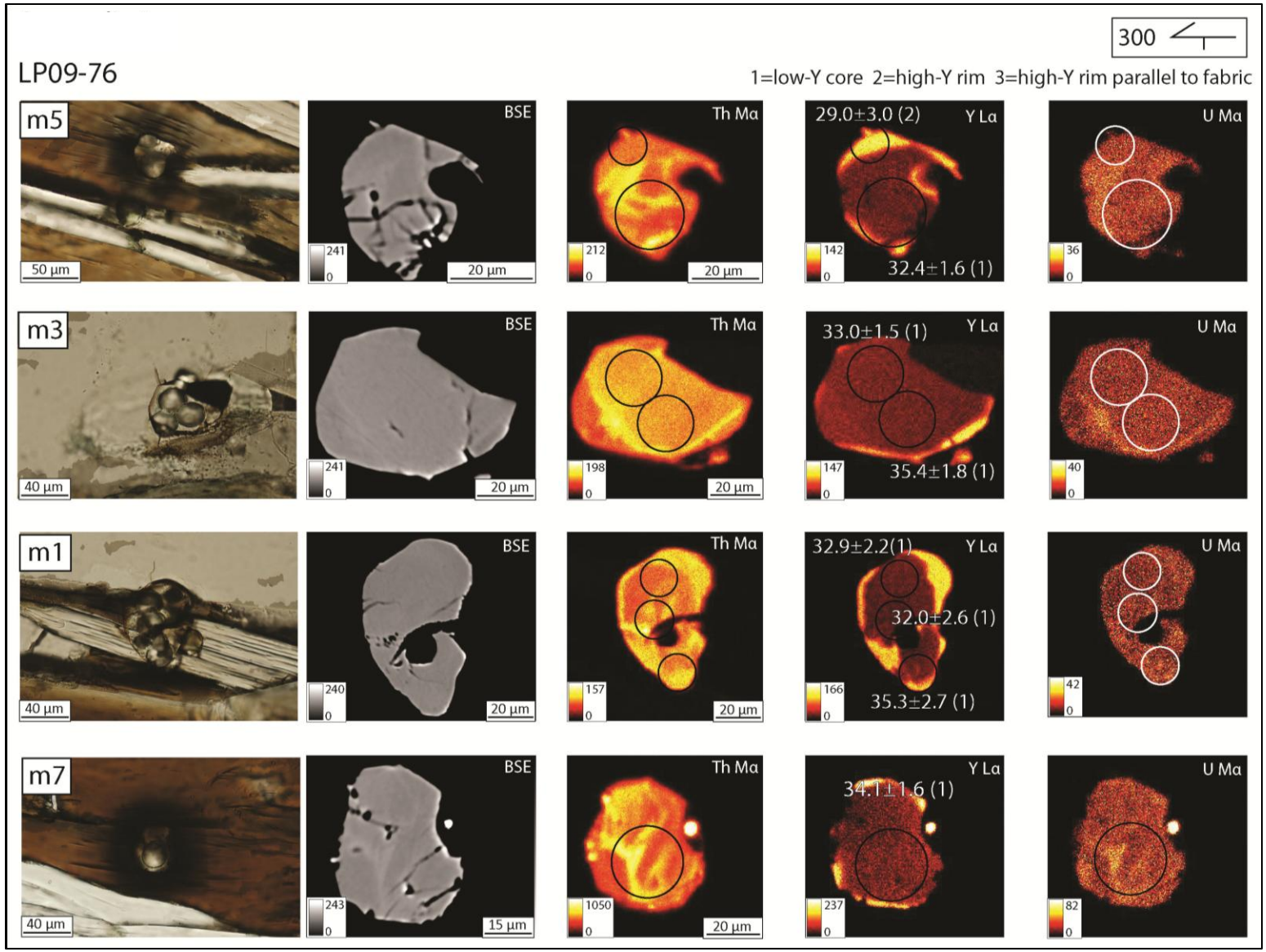
300
LP09-76
1=low-Y core 2=high-Y rim 3=high-Y rim parallel to fabric
m5
BSE
Th Mα
29.0±3.0 (2)
Y Lα
32.4±1.6 (1)
U Mα
50 µm
20 µm
m3
33.0±1.5 (1)
35.4±1.8 (1)
40 µm
m1
32.9±2.2(1)
32.0±2.6 (1)
35.3±2.7 (1)
m7
34.1±1.6 (1)
15 µm

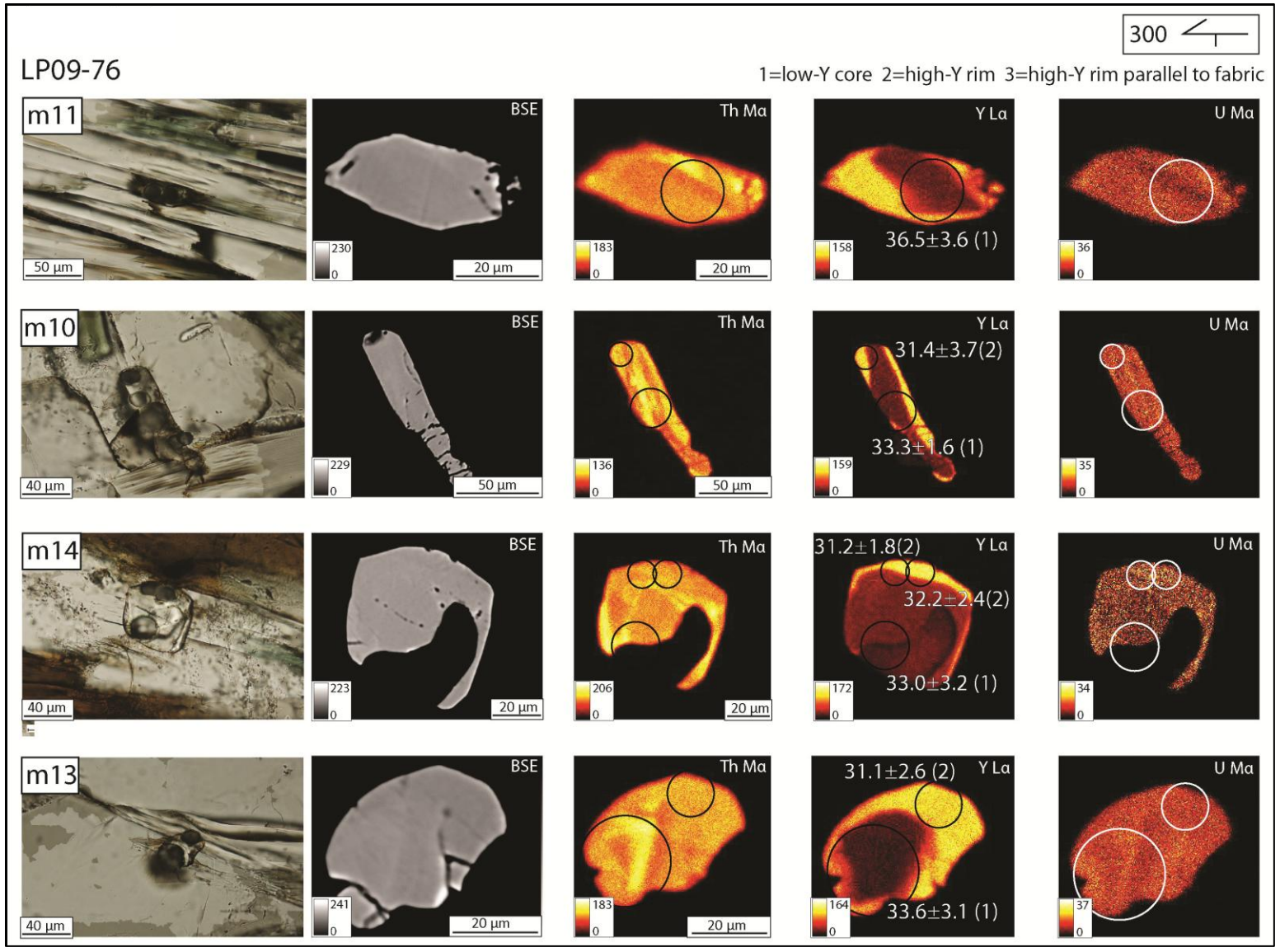
300
LP09-76
1=low-Y core 2=high-Y rim 3=high-Y rim parallel to fabric
m11
BSE
Th Mα
Y Lα
U Mα
36.5±3.6 (1)
50 µm
20 µm
m10
31.4±3.7(2)
33.3±1.6 (1)
40 µm
50 µm
m14
31.2±1.8(2)
32.2±2.4(2)
33.0±3.2 (1)
m13
31.1±2.6 (2)
33.6±3.1 (1)

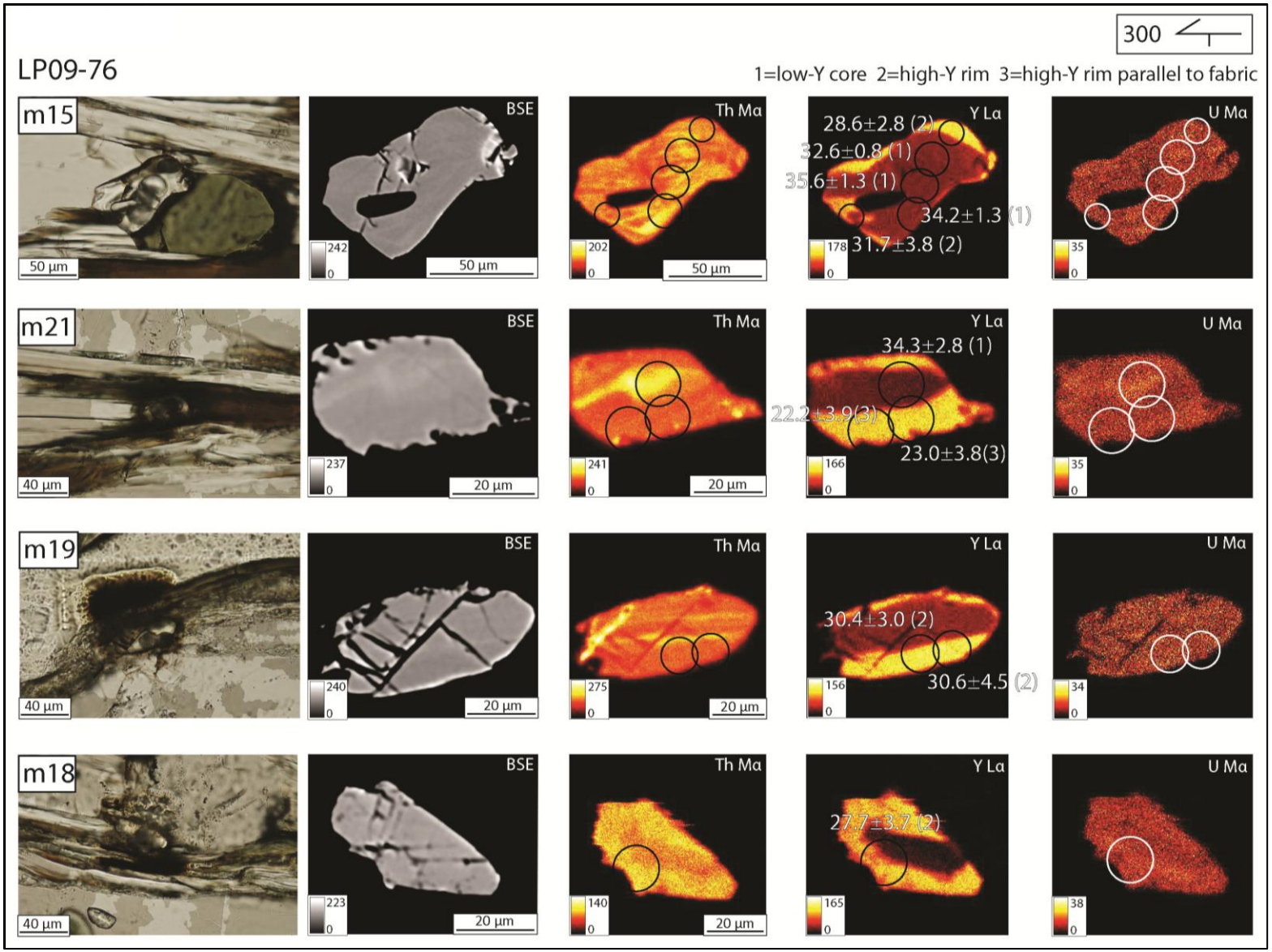
300
LP09-76
1=low-Y core 2=high-Y rim 3=high-Y rim parallel to fabric
m15
BSE
Th Mα
Y Lα
U Mα
28.6±2.8 (2)
32.6±0.8 (1)
35.6±1.3 (1)
34.2±1.3 (1)
31.7±3.8 (2)
50 µm
m21
34.3±2.8 (1)
22.2±3.9(3)
23.0±3.8(3)
40 µm
20 µm
m19
30.4±3.0 (2)
30.6±4.5 (2)
m18
27.7±3.7 (2)

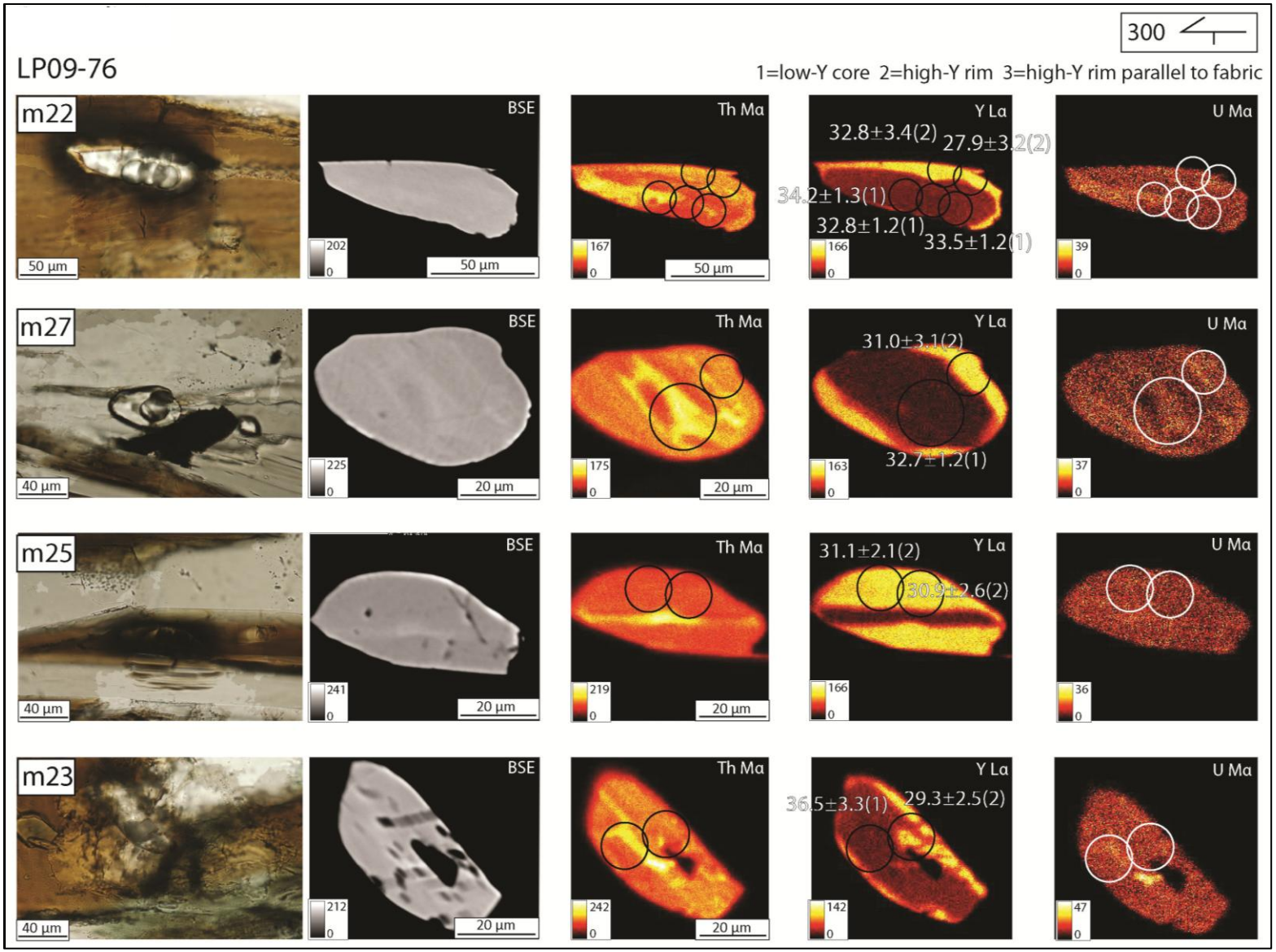
300
LP09-76
1=low-Y core 2=high-Y rim 3=high-Y rim parallel to fabric
m22
BSE
Th Ma
Y La
U Ma
32.8±3.4(2)
27.9±3.2(2)
34.2±1.3(1)
32.8±1.2(1)
33.5±1.2(1)
50 µm
m27
31.0±3.1(2)
32.7±1.2(1)
40 µm
20 µm
m25
31.1±2.1(2)
30.9±2.6(2)
m23
36.5±3.3(1)
29.3±2.5(2)

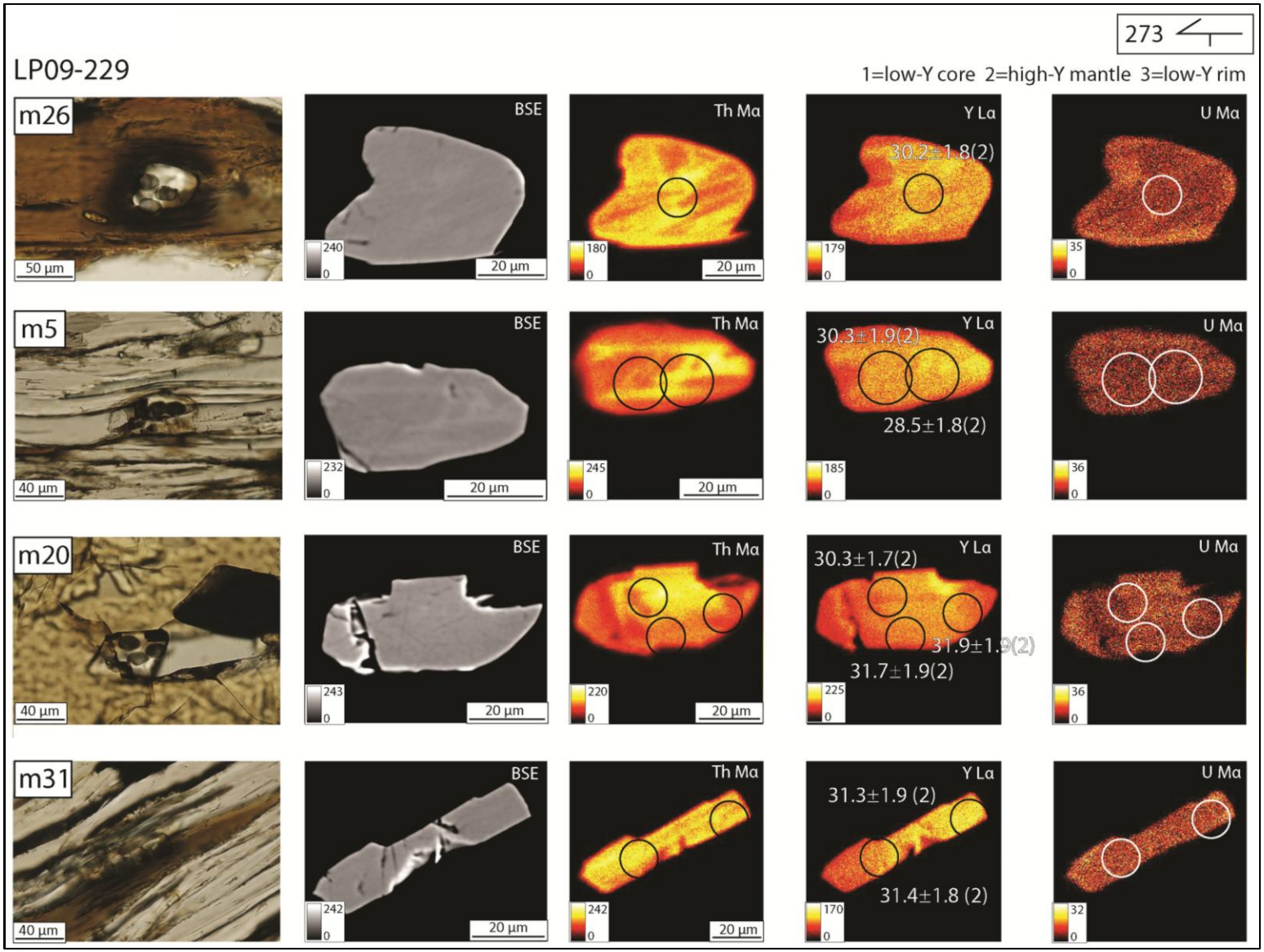
273
LP09-229
1=low-Y core 2=high-Y mantle 3=low-Y rim
m26
BSE
Th Mα
Y Lα
30.2±1.8(2)
U Mα
50 µm
20 µm
m5
30.3±1.9(2)
28.5±1.8(2)
40 µm
m20
30.3±1.7(2)
31.9±1.9(2)
31.7±1.9(2)
m31
31.3±1.9 (2)
31.4±1.8 (2)

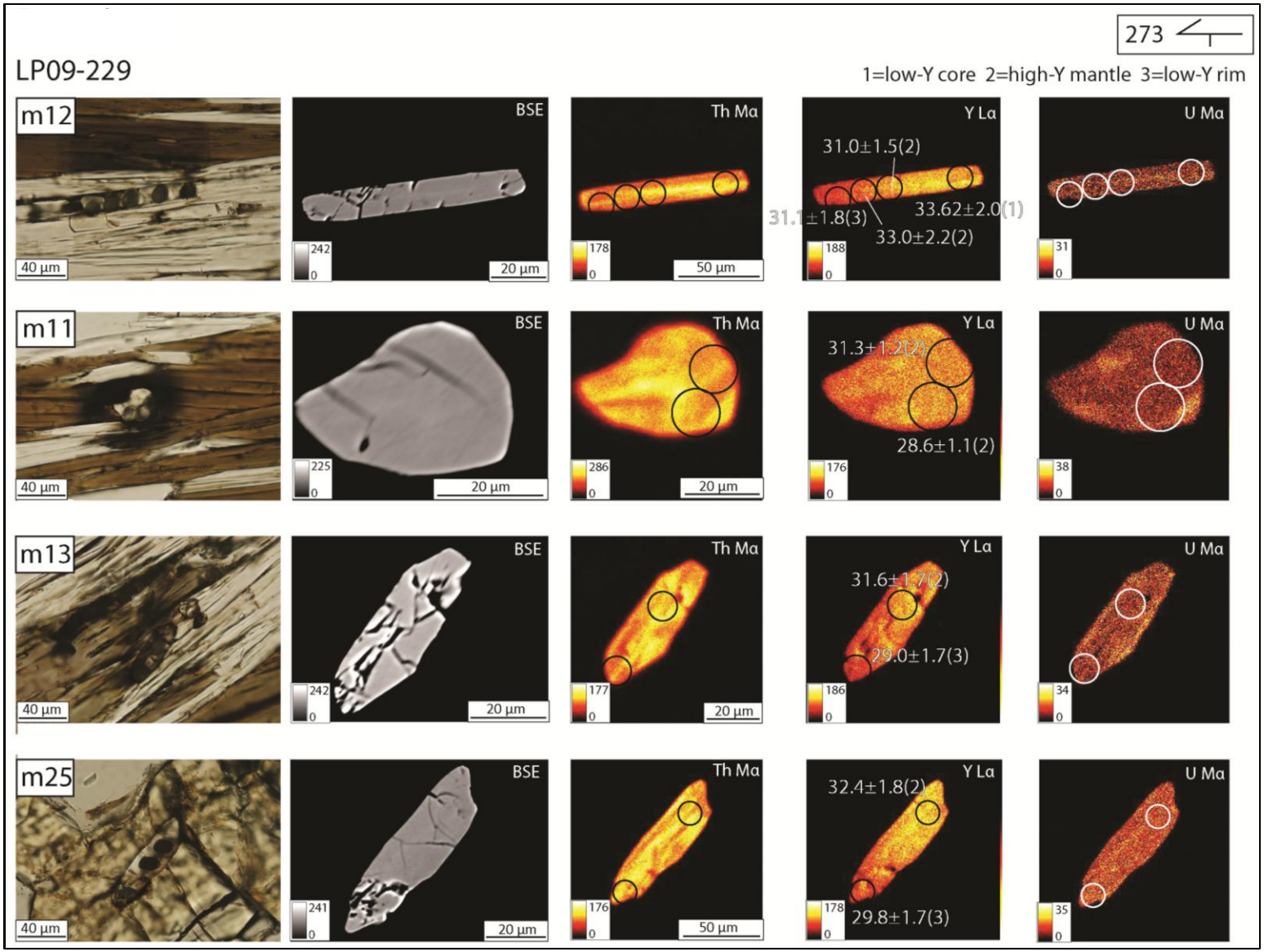
273
LP09-229
1=low-Y core 2=high-Y mantle 3=low-Y rim
m12
BSE
Th Ma
Y La
U Ma
31.0±1.5(2)
33.62±2.0(1)
31.1±1.8(3)
33.0±2.2(2)
m11
31.3±1.2(2)
28.6±1.1(2)
m13
31.6±1.7(2)
29.0±1.7(3)
m25
32.4±1.8(2)
29.8±1.7(3)
40 µm
20 µm
50 µm

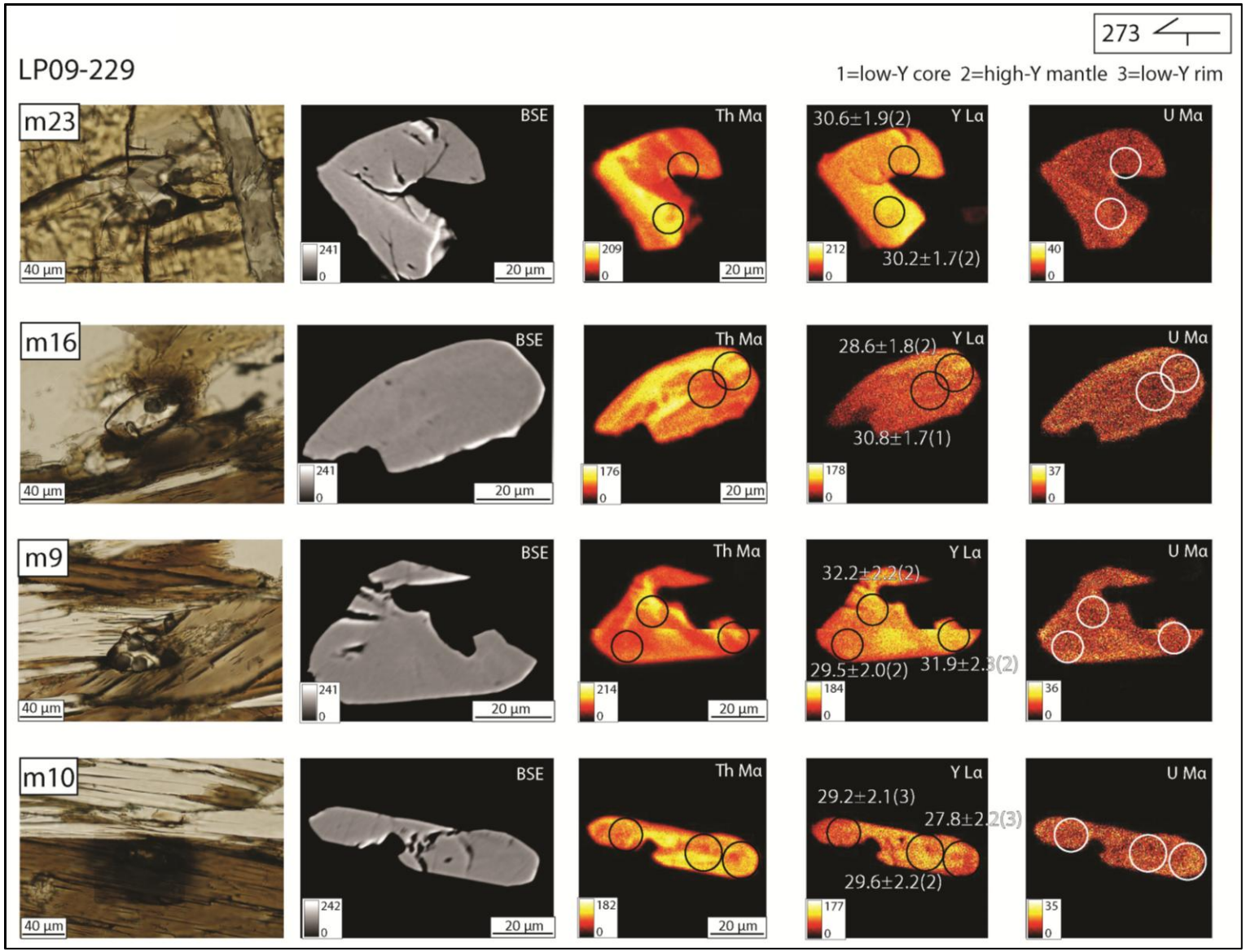
273
LP09-229
1=low-Y core 2=high-Y mantle 3=low-Y rim
m23
BSE
Th Mα
30.6±1.9(2)
Y Lα
U Mα
30.2±1.7(2)
m16
28.6±1.8(2)
30.8±1.7(1)
m9
32.2±2.2(2)
29.5±2.0(2)
31.9±2.3(2)
m10
29.2±2.1(3)
27.8±2.2(3)
29.6±2.2(2)
40 µm
20 µm

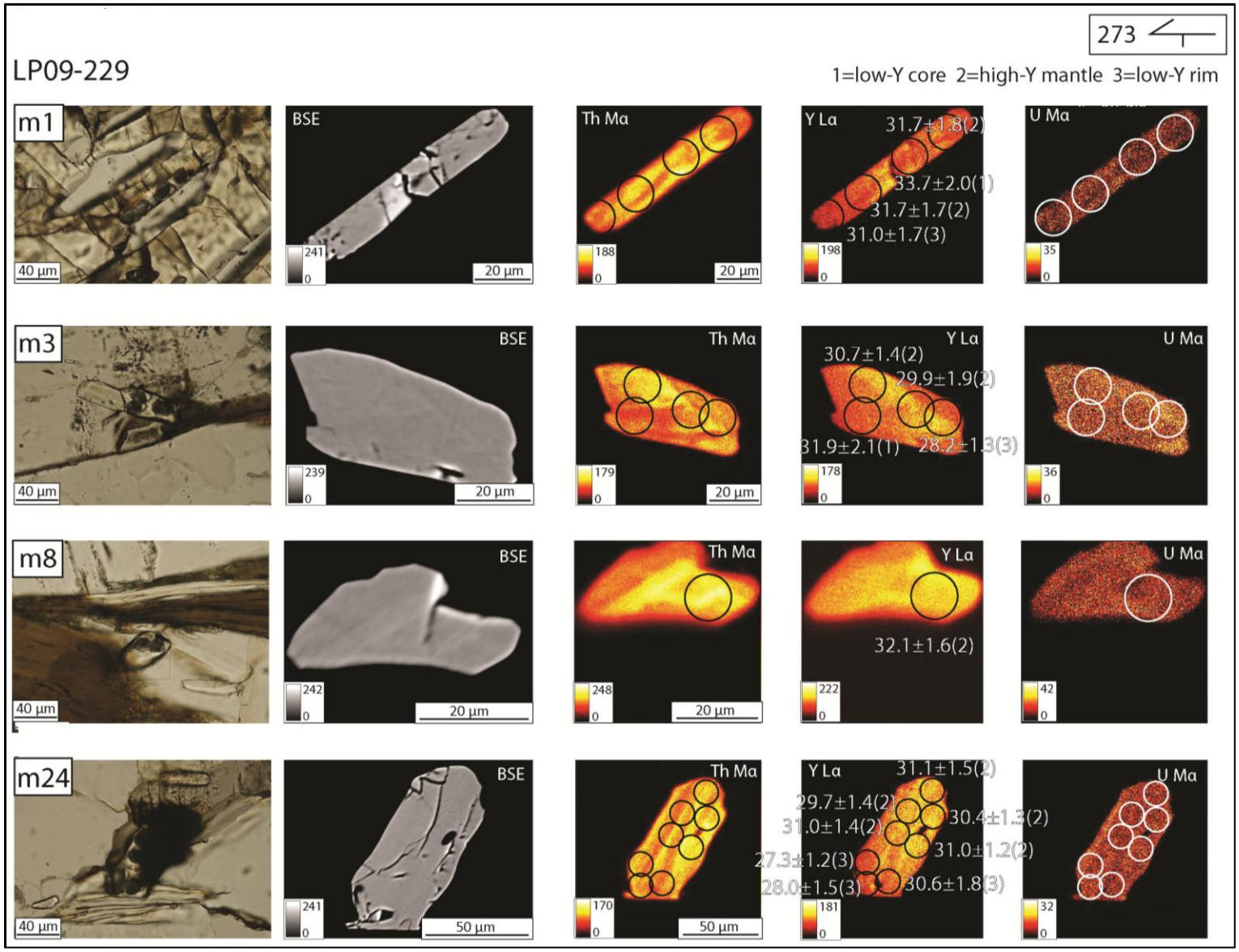
273
LP09-229
1=low-Y core 2=high-Y mantle 3=low-Y rim
m1
BSE
Th Mα
Y Lα
31.7±1.8(2)
33.7±2.0(1)
31.7±1.7(2)
31.0±1.7(3)
U Mα
m3
BSE
Th Mα
Y Lα
30.7±1.4(2)
29.9±1.9(2)
31.9±2.1(1)
28.2±1.3(3)
U Mα
m8
BSE
Th Mα
Y Lα
32.1±1.6(2)
U Mα
m24
BSE
Th Mα
Y Lα
31.1±1.5(2)
29.7±1.4(2)
31.0±1.4(2)
30.4±1.3(2)
27.3±1.2(3)
31.0±1.2(2)
28.0±1.5(3)
30.6±1.8(3)
U Mα
40 µm
20 µm
50 µm

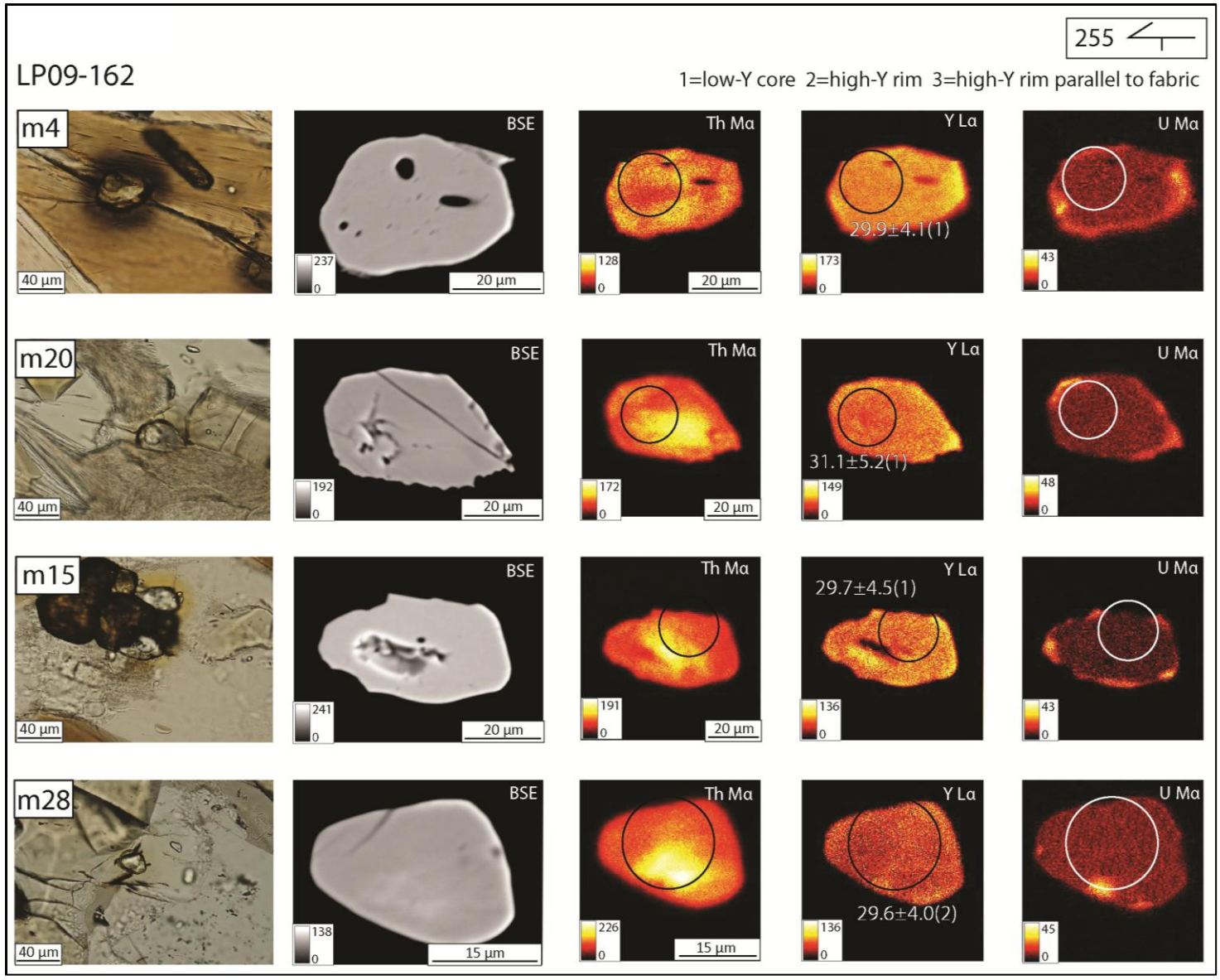
255
LP09-162
1=low-Y core 2=high-Y rim 3=high-Y rim parallel to fabric
m4
m20
m15
m28
BSE
Th Mα
Y Lα
U Mα
29.9±4.1(1)
31.1±5.2(1)
29.7±4.5(1)
29.6±4.0(2)
40 µm
20 µm
15 µm

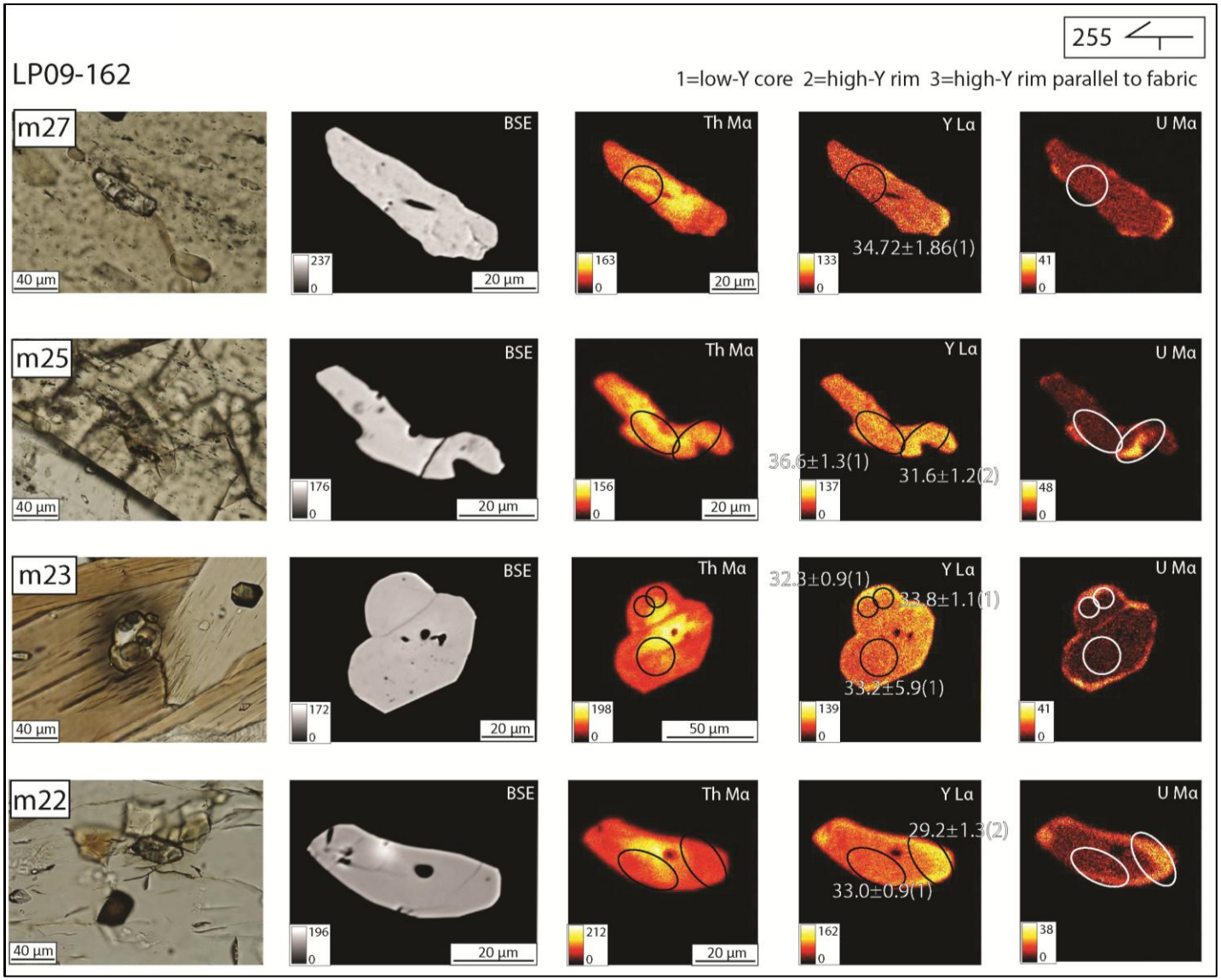
255
LP09-162
1=low-Y core 2=high-Y rim 3=high-Y rim parallel to fabric
m27
BSE
Th Mα
Y Lα
U Mα
34.72±1.86(1)
40 µm
20 µm
m25
36.6±1.3(1)
31.6±1.2(2)
m23
32.3±0.9(1)
33.8±1.1(1)
33.2±5.9(1)
50 µm
m22
29.2±1.3(2)
33.0±0.9(1)

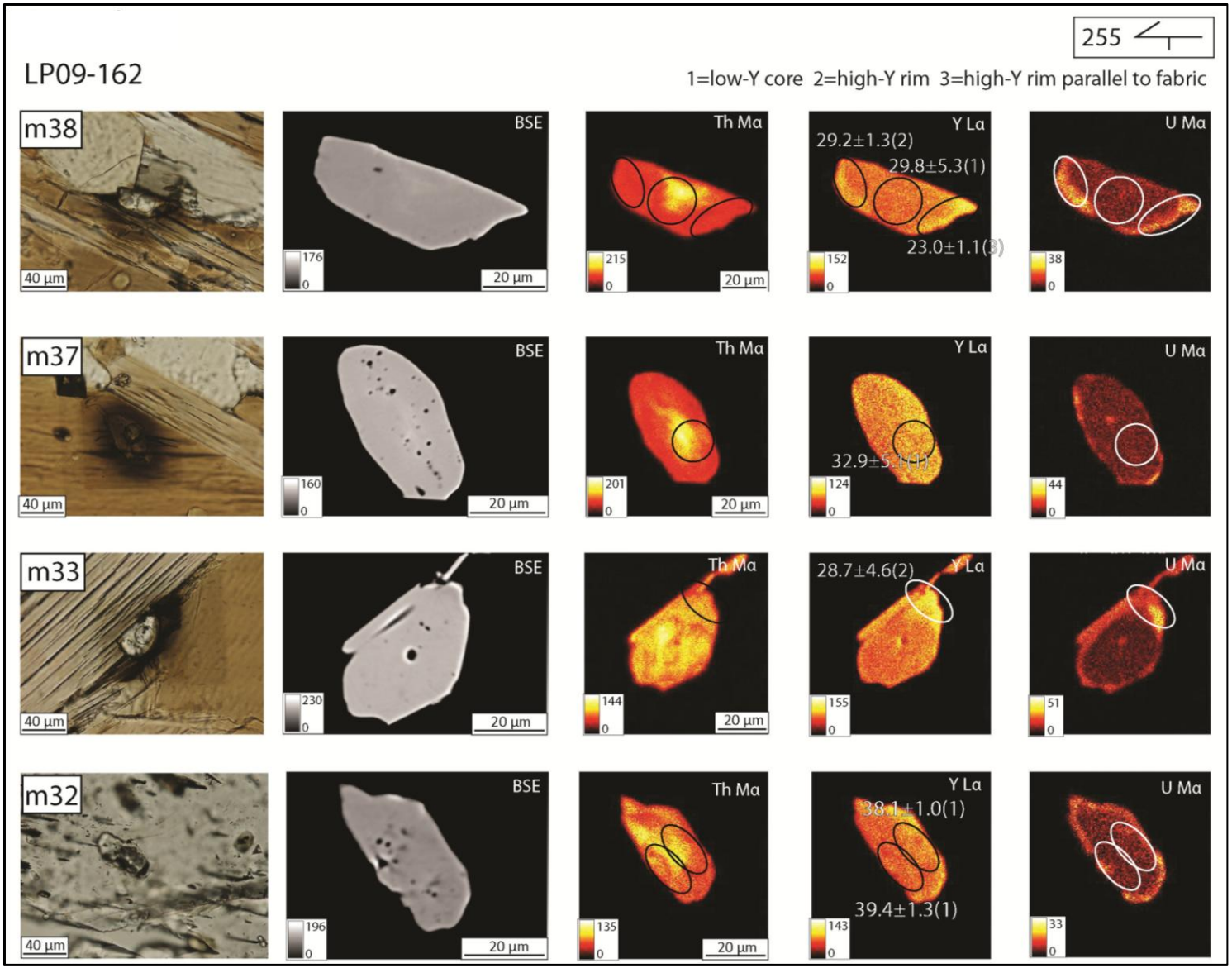
255
LP09-162
1=low-Y core 2=high-Y rim 3=high-Y rim parallel to fabric
m38
BSE
Th Mα
Y Lα
29.2±1.3(2)
29.8±5.3(1)
23.0±1.1(3)
U Mα
m37
32.9±5.1(1)
m33
28.7±4.6(2)
m32
38.1±1.0(1)
39.4±1.3(1)
40 µm
20 µm

Appendix 2.2

Appendix 2.2. U-Th-Pb Isotopic Data From Monazite Grains in Metamorphic Rocks.

Analysis	^{204}Pb cps	^{206}Pb cps	^{207}Pb cps	Uncorrected isotopic ratios				Uncorrected ages (Ma)		Location[a]
				^{206}Pb/^{238}U	1σ %	^{208}Pb/^{232}Th	1σ %	^{208}Pb/^{232}Th	2σ abs	
LP09-10										
Low-Y Cores										
m4a	27	17214	1268	0.0055	5.4	0.00163	3.5	33.0	2.3	mx
m8a	53	15322	1183	0.0047	5.1	0.00162	4.8	32.8	3.1	mx
m15a	21	16950	1217	0.0043	5.0	0.00164	4.8	33.2	3.2	mx
m15b	12	13920	1081	0.0059	5.0	0.00164	6.0	33.2	4.0	mx
m15c	20	16671	1191	0.0040	5.5	0.00166	3.7	33.4	2.5	mx
m16a	28	15586	1091	0.0043	4.8	0.00166	5.2	33.5	3.6	mx
m17a	33	16802	1333	0.0050	4.6	0.00160	4.0	32.3	2.6	mx
High-Y Mantles										
m1a	15	15730	1327	0.0050	5.7	0.00140	4.5	28.2	2.5	mx
m1b	27	16946	1221	0.0052	4.6	0.00145	3.1	29.3	1.8	mx
m4b	40	14933	1273	0.0047	5.2	0.00134	5.9	27.1	3.2	mx
m8b	86	19711	1999	0.0037	6.6	0.00117	6.3	23.6	3.0	mx
m10a	19	16190	1096	0.0040	4.2	0.00123	4.6	24.9	2.3	mx
m10b	20	15265	1066	0.0047	6.2	0.00150	6.1	30.2	3.7	mx
m12	13	23573	1710	0.0039	4.3	0.00158	4.4	31.9	2.8	mx
m15d	44	13981	1453	0.0036	6.8	0.00137	7.0	27.7	3.9	mx
m16b	28	15499	1105	0.0050	4.9	0.00158	3.6	31.8	2.3	mx
m18a	33	14958	1185	0.0042	5.4	0.00140	6.0	28.2	3.4	mx
m20a	33	17575	1363	0.0046	4.4	0.00135	6.4	27.2	3.5	mx
m20b	189	18588	2881	0.0049	7.0	0.00158	4.3	31.9	2.7	mx
m22	27	14872	1065	0.0036	6.0	0.00134	6.7	27.0	3.6	mx
High-U Rims										
m17b	39	14128	1199	0.0041	5.9	0.00123	7.0	24.8	3.5	mx
m18b	57	12750	1219	0.0041	5.8	0.00124	7.2	25.1	3.6	mx

Appendix 2.2. Continued.

Analysis	^{204}Pb cps	^{206}Pb cps	^{207}Pb cps	Uncorrected isotopic ratios				Uncorrected ages (Ma)		Location[a]
				^{206}Pb/^{238}U	1σ %	^{208}Pb/^{232}Th	1σ %	^{208}Pb/^{232}Th	2σ abs	
LP09-76										
Low-Y Cores										
m1a	68	57992	3715	0.0050	1.0	0.00175	3.8	35.3	2.7	mx
m1b	148	47980	4341	0.0048	0.9	0.00159	4.1	32.0	2.6	mx
m1c	87	56309	3978	0.0051	1.1	0.00163	3.4	32.9	2.2	mx
m3a	106	68688	4724	0.0050	0.9	0.00163	2.3	33.0	1.5	mx
m3b	100	67141	4683	0.0055	0.8	0.00175	2.5	35.4	1.8	mx
m5a	179	46983	4828	0.0052	1.2	0.00160	2.4	32.4	1.6	mx
m7	125	58361	4685	0.0052	0.9	0.00169	2.3	34.1	1.6	mx
m10a	127	65311	4834	0.0048	1.2	0.00165	2.4	33.3	1.6	mx
m11	39	33946	2286	0.0052	5.0	0.00181	4.9	36.5	3.6	mx
m13a	70	29770	2434	0.0053	1.4	0.00166	4.6	33.6	3.1	mx
m14a	149	35435	4095	0.0052	1.4	0.00164	4.9	33.0	3.2	mx
m15a	91	54191	3794	0.0051	2.6	0.00161	1.2	32.6	0.8	mx
m15b	49	49221	3504	0.0052	2.6	0.00177	1.8	35.6	1.3	mx
m15c	77	49190	3614	0.0049	2.6	0.00169	1.9	34.2	1.3	mx
m21a	71	39952	3167	0.0052	4.3	0.00170	4.1	34.3	2.8	mx
m22a	59	51450	3388	0.0052	2.6	0.00166	1.7	33.5	1.2	mx
m22b	67	52260	3702	0.0052	2.7	0.00162	1.8	32.8	1.2	mx
m22c	89	55026	4218	0.0053	2.7	0.00170	1.9	34.2	1.3	mx
m23a	73	29240	2290	0.0055	5.5	0.00181	4.5	36.5	3.3	mx
m27a	50	43594	3199	0.0056	2.6	0.00162	1.9	32.7	1.2	mx
High-Y Rims										
m5b	47	31597	2842	0.0052	5.0	0.00144	5.2	29.0	3.0	mx
m10b	51	38198	2724	0.0044	4.8	0.00156	5.9	31.4	3.7	mx
m13b	103	30825	3449	0.0044	6.2	0.00154	4.2	31.1	2.6	mx
m14b	82	36127	2877	0.0053	4.1	0.00154	3.0	31.2	1.8	mx
m14c	90	37000	2895	0.0046	4.7	0.00159	3.7	32.2	2.4	mx
m15d	90	32980	2618	0.0043	5.1	0.00142	4.8	28.6	2.8	mx
m15e	125	19788	2971	0.0047	5.1	0.00157	6.1	31.7	3.8	mx

Appendix 2.2. Continued.

Analysis	^{204}Pb	^{206}Pb	^{207}Pb	Uncorrected isotopic ratios				Uncorrected ages (Ma)		Location[a]
	cps	cps	cps	$^{206}Pb/^{238}U$	1σ %	$^{208}Pb/^{232}Th$	1σ %	$^{208}Pb/^{232}Th$	2σ abs	
m18	149	20918	3307	0.0051	4.1	0.00137	6.7	27.7	3.7	mx
m19a	53	36141	2813	0.0052	3.9	0.00150	5.0	30.4	3.0	mx
m19b	334	31022	6803	0.0061	5.3	0.00152	7.4	30.6	4.5	mx
m22e	119	34179	3099	0.0050	6.2	0.00162	5.2	32.8	3.4	mx
m22f	72	29537	2438	0.0047	4.7	0.00138	5.7	27.9	3.2	mx
m23b	116	27859	3272	0.0058	4.8	0.00145	4.3	29.3	2.5	mx
m25a	65	38093	2651	0.0041	3.8	0.00154	3.4	31.1	2.1	mx
m25b	55	35254	2610	0.0045	4.5	0.00153	4.3	30.9	2.6	mx
m27b	39	36659	2597	0.0045	4.3	0.00154	5.1	31.0	3.1	mx
High-Y Rims parallel to fabric										
m21b	71	20473	2218	0.0031	7.2	0.00114	8.3	23.0	3.8	mx
m21c	70	15967	1765	0.0042	6.4	0.00110	8.7	22.2	3.9	mx
LP09-229										
Low-Y Cores										
m1a	16	12876	624	0.0047	4.1	0.00167	3.0	33.7	2.0	st
m3a	0	11203	572	0.0048	2.6	0.00158	3.3	31.9	2.1	mx
m12a	5	7095	516	0.0043	5.4	0.00166	3.0	33.6	2.0	mx
m16a	5	12696	615	0.0054	4.2	0.00153	2.8	30.8	1.7	mx
High-Y Mantles										
m1b	11	11423	583	0.0051	4.0	0.00157	2.9	31.7	1.8	st
m1c	10	14271	691	0.0047	3.7	0.00157	2.7	31.7	1.7	st
m3b	0	11645	602	0.0052	2.7	0.00148	3.2	29.9	1.9	mx
m3c	1	12393	610	0.0050	4.7	0.00152	2.2	30.7	1.4	mx
m5a	12	14979	701	0.0048	4.1	0.00150	3.1	30.3	1.9	mx
m5b	8	14367	708	0.0044	3.9	0.00141	3.1	28.5	1.8	mx
m8	15	12891	640	0.0046	4.2	0.00159	2.5	32.1	1.6	mx
m9a	0	9133	519	0.0053	2.7	0.00159	3.4	32.2	2.2	mx
m9b	4	11298	575	0.0047	2.6	0.00146	3.4	29.5	2.0	mx
m9d	0	8617	463	0.0045	2.4	0.00158	3.5	31.9	2.3	mx
m10a	5	10746	542	0.0044	2.8	0.00146	3.8	29.6	2.2	mx

Appendix 2.2. Continued.

Analysis	^{204}Pb	^{206}Pb	^{207}Pb	Uncorrected isotopic ratios				Uncorrected ages (Ma)		Location[a]
	cps	cps	cps	^{206}Pb/^{238}U	1σ %	^{208}Pb/^{232}Th	1σ %	^{208}Pb/^{232}Th	2σ abs	
m11a	0	11506	581	0.0045	4.9	0.00155	1.9	31.3	1.2	mx
m11b	5	11479	586	0.0043	4.5	0.00142	2.0	28.6	1.1	mx
m12c	1	11700	543	0.0046	4.5	0.00154	2.3	31.0	1.5	mx
m12d	0	9463	524	0.0043	5.0	0.00164	3.4	33.0	2.2	mx
m13a	13	15502	816	0.0042	4.0	0.00157	2.8	31.6	1.7	mx
m16b	7	13158	663	0.0052	3.9	0.00142	3.2	28.6	1.8	mx
m20a	0	18199	966	0.0043	3.4	0.00150	2.8	30.3	1.7	st
m20b	0	14022	683	0.0049	3.7	0.00158	2.9	31.9	1.9	st
m20c	0	14336	700	0.0048	3.8	0.00157	3.1	31.7	1.9	st
m23a	0	17778	864	0.0052	3.6	0.00150	2.8	30.2	1.7	st
m23b	0	10056	523	0.0043	4.1	0.00152	3.1	30.6	1.9	st
m24a	6	11509	601	0.0049	5.1	0.00151	2.2	30.4	1.3	mx
m24b	0	12861	693	0.0044	4.6	0.00154	2.0	31.0	1.2	mx
m24c	0	12123	613	0.0049	4.8	0.00154	2.4	29.7	1.4	mx
m24d	6	11797	580	0.0054	4.6	0.00154	2.2	31.0	1.4	mx
m24e	10	12014	687	0.0044	4.6	0.00147	2.4	31.1	1.5	mx
m25a	14	13867	707	0.0047	3.9	0.00160	2.8	32.4	1.8	st
m26	6	14282	738	0.0043	4.2	0.00149	2.9	30.2	1.8	mx
m31a	0	11619	631	0.0046	4.1	0.00155	2.8	31.4	1.8	mx
m31b	10	7557	553	0.0051	4.3	0.00155	3.0	31.3	1.9	mx
Low-Y Rims										
m1d	3	12578	639	0.0040	4.1	0.00153	2.8	31.0	1.7	st
m3d	0	10607	566	0.0050	4.7	0.00139	2.3	28.2	1.3	mx
m10b	2	10258	520	0.0044	3.4	0.00145	3.5	29.2	2.1	mx
m10c	8	10753	585	0.0043	2.5	0.00138	3.9	27.8	2.2	mx
m12e	5	6782	465	0.0042	5.3	0.00154	2.9	31.1	1.8	mx
m13b	2	11342	618	0.0044	4.1	0.00143	2.9	29.0	1.7	mx
m24f	7	11764	580	0.0043	4.8	0.00139	2.6	28.0	1.5	mx
m24g	0	11840	650	0.0047	4.7	0.00135	2.3	27.3	1.2	mx
m24h	0	13655	647	0.0045	4.1	0.00151	2.9	30.6	1.8	mx
m25b	10	14776	714	0.0046	4.2	0.00148	2.8	29.8	1.7	st

Appendix 2.2. Continued.

Analysis	^{204}Pb cps	^{206}Pb cps	^{207}Pb cps	Uncorrected isotopic ratios ^{206}Pb/^{238}U	1σ %	^{208}Pb/^{232}Th	1σ %	Uncorrected ages (Ma) ^{208}Pb/^{232}Th	2σ abs	Location[a]
LP09-162										
Low-Y Cores										
m4	30	10759	673	0.0054	5.4	0.00148	6.7	29.9	4.1	mx
m15	8	9243	569	0.0060	5.6	0.00147	7.5	29.7	4.5	mx
m20	25	10861	667	0.0064	5.9	0.00154	8.3	31.1	5.2	mx
m22a	17	11171	747	0.0052	2.3	0.00164	1.4	33.0	0.9	mx
m23a	0	9277	610	0.0066	5.3	0.00165	7.4	33.2	5.9	mx
m23b	0	15502	918	0.0058	2.7	0.00167	1.6	33.8	1.1	mx
m23c	0	10725	619	0.0070	2.8	0.00160	1.5	32.3	0.9	mx
m25a	10	7514	457	0.0064	3.6	0.00181	1.8	36.6	1.3	st
m27	16	13758	924	0.0060	3.8	0.00172	2.7	34.7	1.9	st
m32a	46	8262	702	0.0062	2.4	0.00189	1.3	38.1	1.0	ky
m32b	17	4235	320	0.0054	2.4	0.00195	1.7	39.4	1.3	ky
m37a	24	8167	577	0.0063	4.7	0.00166	7.8	32.9	5.1	mx
m38a	12	8198	525	0.0057	4.9	0.00150	8.8	29.8	5.3	mx
High-Y Rims										
m33	5	7441	478	0.0058	6.4	0.00144	8.6	28.7	4.6	mx
m28	0	11596	707	0.0051	4.4	0.00147	6.8	29.6	4.0	st
m22b	23	13650	880	0.0042	2.5	0.00144	2.2	29.2	1.3	mx
m25b	13	11719	765	0.0046	3.6	0.00156	2.0	31.6	1.2	st
m38b	20	8434	632	0.0042	3.6	0.00145	2.2	29.2	1.3	mx
High-Y Rims parallel to fabric										
m38c	21	9527	713	0.0034	3.6	0.00114	2.4	23.0	1.1	mx

[a] st, staurolite inclusion; ky, kyanite inclusion; mx, matrix.

Appendix 2.3

Appendix. 2.3. U-Th-Pb Isotopic Data from Monazite Grains in Granites.

Uncorrected isotopic ratios				Uncorrected ages (Ma)	
$^{206}Pb/^{238}U$	2σ%	$^{208}Pb/^{232}Th$	2σ%	$^{208}Pb/^{232}Th$	2σ abs
LP09-157					
0.0033	1.2	0.00093	1.1	18.8	0.2
0.0032	1.6	0.00094	1.1	18.9	0.3
0.0031	1.6	0.00094	1.1	18.9	0.3
0.0033	1.5	0.00095	1.1	19.1	0.2
0.0034	1.5	0.00095	1.1	19.2	0.2
0.0033	1.8	0.00096	1.0	19.4	0.3
0.0034	1.5	0.00097	1.0	19.7	0.2
0.0035	1.6	0.00098	1.0	19.8	0.3
0.0034	1.5	0.00098	1.0	19.8	0.3
0.0033	1.6	0.00098	1.1	19.8	0.3
0.0033	1.5	0.00099	1.0	20.0	0.3
0.0034	1.6	0.00100	1.0	20.2	0.3
0.0035	1.4	0.00100	1.0	20.2	0.3
0.0034	1.6	0.00100	1.0	20.2	0.2
0.0034	1.5	0.00100	1.0	20.2	0.3
0.0036	1.4	0.00100	1.0	20.2	0.2
0.0034	1.6	0.00100	1.0	20.2	0.3
0.0035	1.4	0.00100	1.0	20.3	0.2
0.0035	1.6	0.00101	1.0	20.3	0.3
0.0034	1.5	0.00101	1.0	20.4	0.3
0.0034	1.6	0.00102	2.0	20.5	0.3
0.0035	1.7	0.00102	1.0	20.6	0.3
0.0035	1.6	0.00102	1.0	20.7	0.3
0.0033	1.5	0.00103	1.0	20.8	0.3
0.0033	1.5	0.00105	1.0	21.3	0.3
0.0035	1.4	0.00106	0.9	21.4	0.3
0.0035	1.1	0.00106	0.9	21.4	0.3
0.0034	1.2	0.00106	0.9	21.4	0.2
0.0035	1.6	0.00106	0.9	21.5	0.3
0.0034	1.5	0.00107	0.9	21.6	0.3
0.0035	1.6	0.00107	0.9	21.7	0.3
0.0035	1.1	0.00108	0.9	21.8	0.3
0.0035	1.6	0.00108	0.9	21.8	0.3
0.0035	1.1	0.00108	0.9	21.8	0.3
0.0035	1.1	0.00108	0.9	21.8	0.3
0.0035	1.4	0.00108	1.9	21.9	0.3
0.0036	1.6	0.00108	0.9	21.9	0.3
0.0035	1.1	0.00108	0.9	21.9	0.3
0.0035	1.1	0.00108	0.9	21.9	0.3

Appendix 2.3. Continued.

Uncorrected isotopic ratios				Uncorrected ages (Ma)	
$^{206}Pb/^{238}U$	2σ%	$^{206}Pb/^{238}U$	2σ%	$^{206}Pb/^{238}U$	2σ abs
0.0035	1.4	0.00109	0.9	21.9	0.3
0.0035	1.4	0.00109	0.9	22.1	0.3
0.0035	1.4	0.00110	0.9	22.2	0.3
0.0035	1.1	0.00110	0.9	22.3	0.3
0.0035	1.1	0.00111	0.9	22.4	0.2
0.0036	1.1	0.00112	0.9	22.6	0.3
0.0036	1.1	0.00112	1.8	22.7	0.3
0.0036	1.1	0.00113	0.9	22.9	0.3
0.0036	1.1	0.00114	0.9	23.1	0.3
LP09-158					
0.0029	1.4	0.00096	1.0	19.4	0.3
0.0032	0.9	0.00097	1.0	19.6	0.2
0.0031	1.3	0.00097	1.0	19.7	0.2
0.0032	1.4	0.00098	1.0	19.7	0.2
0.0031	1.3	0.00098	1.0	19.8	0.2
0.0030	1.3	0.00098	1.0	19.8	0.3
0.0032	1.4	0.00099	1.0	20.0	0.2
0.0032	0.9	0.00100	1.0	20.1	0.2
0.0032	1.4	0.00100	1.0	20.2	0.2
0.0032	1.3	0.00100	1.0	20.2	0.2
0.0032	1.4	0.00100	1.0	20.3	0.2
0.0031	1.3	0.00101	1.0	20.3	0.2
0.0033	1.4	0.00101	1.0	20.3	0.2
0.0031	1.3	0.00101	1.0	20.4	0.3
0.0032	1.4	0.00101	1.0	20.4	0.2
0.0032	1.3	0.00101	1.0	20.5	0.2
0.0031	1.4	0.00101	1.0	20.5	0.2
0.0032	0.9	0.00101	1.0	20.5	0.2
0.0032	1.3	0.00101	1.0	20.5	0.2
0.0031	1.3	0.00102	1.0	20.5	0.2
0.0032	0.9	0.00102	1.0	20.5	0.2
0.0031	1.3	0.00102	1.0	20.6	0.3
0.0033	1.2	0.00102	1.0	20.6	0.3
0.0031	1.3	0.00102	1.0	20.7	0.3
0.0032	1.3	0.00103	1.0	20.8	0.3
0.0032	1.4	0.00104	1.0	21.1	0.3
0.0033	1.2	0.00105	1.9	21.2	0.3
0.0032	1.4	0.00106	0.9	21.5	0.2
0.0032	1.3	0.00108	0.9	21.8	0.3
0.0032	1.4	0.00108	0.9	21.9	0.2
0.0034	1.5	0.00109	1.8	22.1	0.3
0.0034	1.2	0.00110	0.9	22.2	0.3
0.0034	1.2	0.00111	1.8	22.4	0.4

Appendix 2.3. Continued.

Uncorrected isotopic ratios				Uncorrected ages (Ma)	
$^{206}Pb/^{238}U$	2σ%	$^{206}Pb/^{238}U$	2σ%	$^{206}Pb/^{238}U$	2σ abs
LP09-166					
0.0030	1.3	0.00089	1.1	18.1	0.2
0.0030	1.0	0.00090	1.1	18.1	0.2
0.0030	1.3	0.00090	1.1	18.2	0.2
0.0030	1.3	0.00090	1.1	18.2	0.2
0.0030	1.0	0.00090	1.1	18.2	0.2
0.0030	1.0	0.00090	1.1	18.3	0.2
0.0029	1.0	0.00090	1.1	18.3	0.2
0.0030	1.3	0.00091	1.1	18.3	0.2
0.0030	1.3	0.00091	1.1	18.3	0.2
0.0030	1.0	0.00091	1.1	18.3	0.2
0.0029	1.0	0.00091	1.1	18.4	0.2
0.0030	1.3	0.00091	1.1	18.4	0.2
0.0030	1.0	0.00091	1.1	18.4	0.2
0.0029	1.0	0.00091	1.1	18.5	0.2
0.0029	1.0	0.00091	1.1	18.5	0.2
0.0030	1.0	0.00091	1.1	18.5	0.2
0.0030	1.3	0.00092	1.1	18.5	0.2
0.0030	1.3	0.00092	1.1	18.5	0.2
0.0029	1.4	0.00092	1.1	18.5	0.2
0.0030	1.3	0.00092	1.1	18.5	0.2
0.0030	1.3	0.00092	1.1	18.5	0.3
0.0030	1.3	0.00092	1.1	18.6	0.2
0.0029	1.4	0.00092	1.1	18.6	0.2
0.0029	1.4	0.00093	1.1	18.7	0.2
0.0030	1.0	0.00093	1.1	18.7	0.2
0.0030	1.0	0.00093	1.1	18.7	0.2
0.0030	1.3	0.00093	1.1	18.8	0.2
0.0030	1.3	0.00093	1.1	18.8	0.2
0.0029	1.0	0.00093	1.1	18.9	0.2
0.0030	1.3	0.00094	1.1	18.9	0.2
0.0030	1.3	0.00094	1.1	18.9	0.2
0.0031	1.0	0.00094	1.1	19.0	0.2
0.0030	1.3	0.00094	1.1	19.0	0.3
0.0030	1.3	0.00094	1.1	19.0	0.2
0.0030	1.3	0.00094	1.1	19.1	0.2
0.0030	1.3	0.00095	1.1	19.2	0.2
0.0030	1.3	0.00095	1.1	19.2	0.2
0.0032	0.9	0.00097	1.0	19.5	0.2
LP09-167					
0.0031	1.0	0.00091	1.1	18.4	0.2
0.0031	1.0	0.00091	1.1	18.4	0.2

Appendix 2.3. Continued.

Uncorrected isotopic ratios				Uncorrected ages (Ma)	
$^{206}Pb/^{238}U$	2σ%	$^{206}Pb/^{238}U$	2σ%	$^{206}Pb/^{238}U$	2σ abs
0.0030	1.0	0.00091	1.1	18.5	0.2
0.0031	1.0	0.00092	1.1	18.6	0.2
0.0032	1.3	0.00093	1.1	18.7	0.2
0.0032	1.3	0.00094	1.1	19.1	0.2
0.0033	0.9	0.00095	1.1	19.1	0.2
0.0033	1.2	0.00095	1.1	19.1	0.2
0.0032	1.6	0.00095	2.1	19.2	0.3
0.0033	1.2	0.00095	1.1	19.3	0.2
0.0033	0.9	0.00096	1.0	19.4	0.2
0.0033	1.2	0.00097	1.0	19.6	0.2
0.0035	2.3	0.00099	2.0	19.9	0.3
0.0033	0.9	0.00099	1.0	19.9	0.2
0.0033	0.9	0.00099	1.0	20.0	0.2
0.0034	0.9	0.00101	1.0	20.3	0.2
0.0034	1.2	0.00101	1.0	20.4	0.2
0.0033	1.2	0.00101	1.0	20.4	0.2
0.0034	1.2	0.00102	1.0	20.7	0.2
0.0033	1.2	0.00102	1.0	20.7	0.2
0.0034	0.9	0.00103	1.0	20.8	0.2
0.0034	0.9	0.00104	1.0	20.9	0.2
0.0034	0.9	0.00104	1.0	20.9	0.2
0.0034	1.2	0.00104	1.0	20.9	0.3
0.0033	0.9	0.00104	1.0	21.0	0.2
0.0034	1.2	0.00104	1.0	21.0	0.3
0.0034	1.2	0.00105	1.0	21.2	0.2
0.0035	0.9	0.00105	1.0	21.2	0.2
0.0035	1.1	0.00105	1.0	21.2	0.2
0.0035	0.9	0.00105	1.0	21.2	0.2
0.0034	0.9	0.00105	1.0	21.2	0.2
0.0034	0.9	0.00105	1.0	21.3	0.2
0.0035	0.9	0.00106	0.9	21.3	0.2
0.0034	0.9	0.00106	0.9	21.4	0.2
0.0035	0.9	0.00106	0.9	21.4	0.2
0.0034	0.9	0.00106	0.9	21.4	0.2
0.0035	0.9	0.00106	0.9	21.4	0.2
0.0034	0.9	0.00106	0.9	21.4	0.2
0.0036	1.1	0.00106	0.9	21.5	0.2
0.0035	1.1	0.00106	0.9	21.5	0.2
0.0034	1.2	0.00106	0.9	21.5	0.2
0.0035	0.9	0.00107	0.9	21.6	0.2
0.0034	0.9	0.00107	0.9	21.6	0.2
0.0034	0.9	0.00107	0.9	21.6	0.2
0.0034	0.9	0.00107	0.9	21.7	0.2

Appendix 2.3. Continued.

Uncorrected isotopic ratios				Uncorrected ages (Ma)	
$^{206}Pb/^{238}U$	2σ%	$^{206}Pb/^{238}U$	2σ%	$^{206}Pb/^{238}U$	2σ abs
0.0035	0.9	0.00107	0.9	21.7	0.2
0.0034	1.2	0.00108	0.9	21.7	0.2
0.0034	0.9	0.00108	0.9	21.8	0.2
0.0035	1.1	0.00108	0.9	21.8	0.2
0.0034	0.9	0.00108	0.9	21.9	0.2
0.0034	0.9	0.00108	0.9	21.9	0.2
0.0034	1.2	0.00109	0.9	21.9	0.2
0.0034	0.9	0.00109	0.9	21.9	0.2
0.0035	0.9	0.00109	0.9	22.0	0.2
0.0034	1.2	0.00109	0.9	22.0	0.2
0.0034	1.2	0.00109	0.9	22.0	0.2
0.0034	1.2	0.00109	0.9	22.0	0.2
0.0035	1.1	0.00109	0.9	22.1	0.2
0.0034	1.2	0.00109	0.9	22.1	0.2
0.0034	1.2	0.00110	0.9	22.2	0.2
0.0034	1.2	0.00110	0.9	22.2	0.2
0.0035	0.9	0.00111	0.9	22.3	0.2
0.0035	1.1	0.00111	0.9	22.4	0.3
0.0035	1.1	0.00111	0.9	22.4	0.3
0.0036	1.1	0.00111	0.9	22.5	0.2
0.0035	1.1	0.00112	0.9	22.7	0.3
0.0036	1.4	0.00113	0.9	22.8	0.3
0.0036	1.1	0.00118	0.8	23.8	0.2
0.0039	1.0	0.00122	0.8	24.7	0.2

CHAPTER III:
STRUCTURAL EVOLUTION OF THE LEO PARGIL DOME, NORTHWEST INDIA: IMPLICATIONS FOR THE TECTONICS OF THE WESTERN HIMALAYA

A version of this chapter is in preparation for publication by Jackie Langille:

My major contributions to this paper include: (1) field mapping and sample collection, (2) conducting the kinematic, vorticity, deformation temperature, and thermobarometry analyses that are included in the manuscript, (3) writing the manuscript, (4) creating the illustrations, and (5) preparing the manuscript for publication.

Abstract

Building of the Himalaya and Tibetan Plateau since the Eocene involved an interplay between crustal thickening and extension that continues today. Early mountain building was dominated by thrusting, crustal thickening, and exhumation of the high-grade core of the Himalaya. Since the Miocene, crustal deformation in the Himalaya and Tibetan Plateau has been accommodated by south-directed thrusting at the Himalayan front and by east-west extension within the Himalaya and Tibetan Plateau along normal and strike-slip faults. The northwest Indian Himalaya contains north-south oriented normal faults and northeast oriented normal-sense shear zones (i.e. shear zones that bound the Leo Pargil dome), southwest of the dextral Karakoram strike-slip fault system. West-directed extension on the normal-displacement Leo Pargil shear zone, bounding the southwest flank of the Leo Pargil dome began by 23 Ma, earlier than documented anywhere else in the Himalaya. Deformation temperatures and mean kinematic vorticity estimates (W_m) during ductile shearing on the Leo Pargil shear zone are integrated with pressure-temperature estimates during crustal thickening prior to initiation of the extension to evaluate the kinematic evolution of the Leo Pargil shear zone. Kinematic vorticity analysis of quartz fabrics in rocks within the Leo Pargil shear zone suggest that these rocks were thinned by up to 63% during west-directed shearing. Deformation temperatures of 400-500° C at the uppermost structural depths within the shear zone to >650° C at the deepest levels suggest that the rocks within the shear zone were exhumed from depths of up to >26 km by ~28-35 km of ductile displacement on the Leo Pargil shear zone, assuming a geothermal gradient of 25°C/km. These data combined with age constraints on the Leo Pargil shear zone and the Karakoram fault from other studies suggest that extensional exhumation in the western Himalaya on the shear zones bounding the Leo Pargil dome, southwest of the Karakoram fault system, could explained as being controlled by southward propagation of the dextral strike-slip Karakoram fault system.

Introduction

Continental collision between the Indian and Eurasian plates since the Eocene (e.g., Searle et al., 1987; Najman et al., 2010) resulted in the building of the largest mountain range on Earth, the Himalaya, and the Tibetan Plateau by a unique combination of north-south-directed crustal shortening and vertical thickening and east-west-directed extension. The arc-parallel Main Central thrust zone (MCTZ) and the South Tibetan detachment system (STDS) are major structures exposed across the Himalayan front that were active until the middle Miocene (e.g., Grujic et al., 1996; Grasemann et al., 1999; Vannay and Grasemann, 2001; Grujic et al., 2002; Vannay et al., 2004; Searle et al., 2006). The STDS was active as recent as ~11 Ma in the eastern Himalaya (Kellett et al., 2009). In the central Himalaya, displacement transitioned from the MCTZ and the STDS to orogen-parallel extension on normal faults that began at ~13 Ma (e.g., Jessup and Cottle, 2010; Kali et al., 2010).

Crustal extension parallel to the Himalayan front is a fundamental process that is ongoing in the Himalaya and Tibetan Plateau to accommodate active deformation. Modern day convergence is accommodated along the Main Frontal thrust, strike-slip faults within and bounding the Tibetan Plateau, and approximately north-south trending normal faults within the Himalaya and Tibetan Plateau (Fig. 3.1) (e.g., Jouanne et al., 2004; Styron et al., 2011). The present geodetic convergence rate between the Indian and Eurasian plates is ~35 mm/yr (e.g., Bilham et al., 1997; Bettinelli et al., 2006). ~20 mm/yr (Holocene slip-rate) is accommodated by north-south shortening along the Main Frontal thrust (e.g., Wesnousky et al., 1999; Lavé and Avouac, 2000). The remainder is accommodated by orogen-parallel extension along strike-slip faults within the Tibetan Plateau and by the north-south oriented normal faults in the Himalaya and Tibetan Plateau (Styron et al., 2011). >3 mm/yr is accommodated by normal faults across the Himalayan front and the southern Tibetan Plateau (Styron et al., 2011).

Crustal extension across the Himalaya and Tibetan Plateau is partitioned along left-lateral strike-slip faults throughout the northern Tibetan Plateau, on right-lateral strike slip faults throughout the southern Tibetan Plateau, and along normal faults and graben throughout the Himalayan front and the Tibetan Plateau (Fig. 3.1) (e.g., Taylor et al., 2003; Hintersberger et al.,

Figure 3.1. *(a) Active faults and suture zones in the Himalaya overlain on a digital elevation model (DEM) of the Himalaya and Tibetan Plateau. Faults modified after Taylor and Yin (2009). Numbers are ages (Ma) for normal or strike-slip fault initiation (Coleman and Hodges, 1995; Harrison et al., 1995; Murphy et al., 2000; Blisniuk et al., 2001; Murphy et al., 2002; de Sigoyer et al., 2004; Lacassin et al., 2004; Phillips et al., 2004; Phillips and Searle, 2007; Thiede et al., 2006; Valli et al., 2007; Kali et al., 2010; Lee et al., 2011; Leloup et al., 2011; Mitsuishi et al., 2012; Langille et al., in review). (b) Simplified geologic map of the western Himalaya with active structures in red (Vannay and Grasemann, 2001; Murphy et al., 2002; Thiede et al., 2006; Valli et al., 2007; Langille et al., in review). Focal mechanisms are included.*

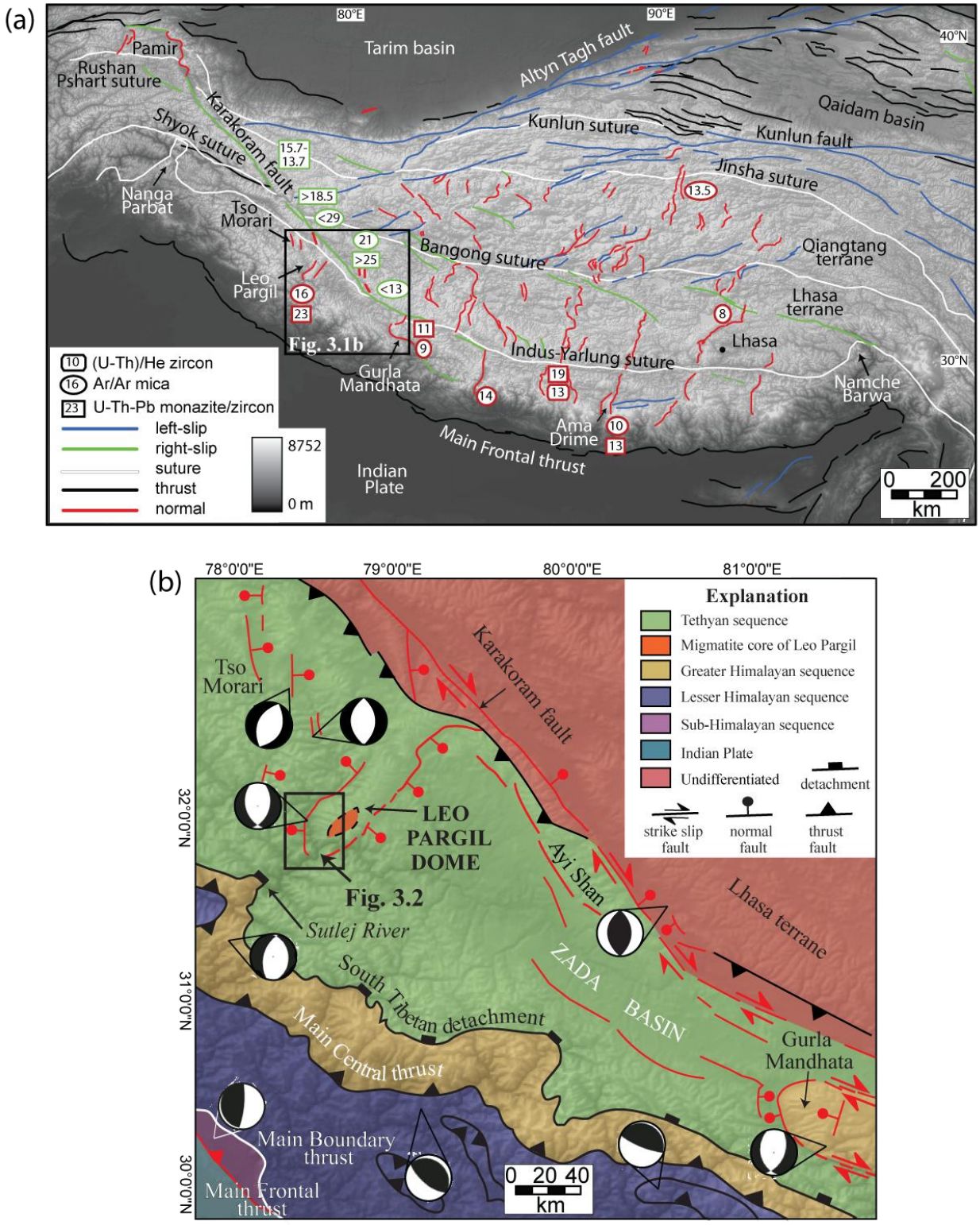
(a)
80°E
90°E
40°N
30°N
Tarim basin
Altyn Tagh fault
Pamir
Rushan
Pshart suture
Karakoram fault
Shyok suture
Kunlun suture
Kunlun fault
Qaidam basin
Jinsha suture
Nanga
Parbat
Tso
Morari
15.7-
13.7
>18.5
<29
13.5
21
>25
<13
Bangong suture
Qiangtang
terrane
Leo
Pargil
16
23
Fig. 3.1b
11
9
Lhasa
terrane
8
Lhasa
Indus-Yarlung suture
Gurla
Mandhata
19
13
14
Namche
Barwa
Ama
Drime
10
13
Main Frontal thrust
Indian
Plate
10 (U-Th)/He zircon
16 Ar/Ar mica
23 U-Th-Pb monazite/zircon
left-slip
right-slip
suture
thrust
normal
8752
0 m
0 200
km
(b)
78°0'0"E
79°0'0"E
80°0'0"E
81°0'0"E
32°0'0"N
31°0'0"N
30°0'0"N
Explanation
Tethyan sequence
Migmatite core of Leo Pargil
Greater Himalayan sequence
Lesser Himalayan sequence
Sub-Himalayan sequence
Indian Plate
Undifferentiated
detachment
strike slip fault
normal fault
thrust fault
Karakoram fault
Tso
Morari
LEO
PARGIL
DOME
Fig. 3.2
Ayi Shan
Lhasa terrane
Sutlej River
South Tibetan detachment
ZADA
BASIN
Main Central thrust
Gurla
Mandhata
Main Boundary
thrust
Main Frontal
thrust
0 20 40
km

2010; Hintersberger et al., 2011; Styron et al., 2011). These normal faults are roughly oriented north-south but can be separated into two sets: those that radiate from northwest to northeast from west to east throughout the Himalaya and Tibetan Plateau, and those that are oriented perpendicular to the orogenic front southwest of the Karakoram fault (Fig. 3.1) (e.g., the Leo Pargil shear zone, LPSZ).

Many models have been proposed to explain orogen-parallel extension in the Himalaya and Tibetan Plateau (e.g., Tapponnier et al., 1982; Nelson et al., 1996; McCaffrey and Nabelek, 1998; Kapp and Guynn, 2004; Hintersberger et al., 2010; Styron et al., 2011). Models that have been proposed include but are not limited to: (1) gravitational collapse of an overthickened crust (e.g., Molnar and Tapponnier, 1975; Mercier et al., 1987), (2) lateral flow of the mid-crust (Nelson et al., 1996), (3) oroclinal bending (e.g., Ratschbacher et al., 1994; Robinson et al., 2007), (4) oblique convergence (e.g., McCaffrey and Nabelek, 1998; Styron et al., 2011), (5) extrusion of the Tibetan Plateau as a rigid block via large strike-slip faults (e.g., Tapponnier et al., 1982), and (6) collisional stresses localized along the southern portion of the Himalayan arc (Kapp and Guynn, 2004).

East and west-directed normal faults and shear zones in the central Himalaya accommodate orogen-parallel extension (e.g., Ama Drime detachment, Dinggyê graben, Tingri graben, Thakkola graben) (e.g., Kapp & Guynn, 2004; Jessup et al., 2008; Jessup and Cottle, 2010; Lee et al., 2011). These normal faults and graben have been kinematically linked to strike-slip faults in the interior of the plateau (e.g., Armijo et al., 1986; Taylor et al., 2003; Kapp and Guynn, 2004; Jessup and Cottle, 2010). Similarly, in the western Himalaya young metamorphic domes (e.g., the Leo Pargil and the Gurla Mandhata domes) were exhumed along normal sense shear zones (Fig.3.1) (Murphy et al., 2002; Thiede et al., 2006; Langille et al., in review). The normal sense shear zones that bound these domes extend north into the Karakoram fault system (Murphy et al., 2000). The Gurla Mandhata detachment records late Miocene orogen-parallel extension that is kinematically linked to strike-slip fault displacement on the Karakoram fault system (e.g., Murphy et al., 2002). Orogen-parallel extension on the LPSZ that bounds the southwest side of the Leo Pargil dome (LPD) began >23 Ma (Langille et al., in review). Previous studies have suggested that extension on the LPSZ is kinematically linked to the Karakoram fault system (e.g., Ni and Barazangi, 1985; Thiede et al., 2006; Hintersberger et al., 2010; Hintersberger et al.,

2011) but this relationship remains poorly understood, due to a lack of kinematic constraints on the LPSZ and observations where the two systems intersect.

Structural data and rock samples were collected from throughout the dome and the hanging wall of the LPSZ to constrain the kinematic evolution of the LPSZ and to understand the role of orogen-parallel extension in the western Himalaya. Thin sections of select deformed samples from the LPSZ were analyzed using quartz and feldspar recrystallization textures, kinematic vorticity, and pressure-temperature methods. These methods constrain the temperatures at which the samples were deformed, the kinematics during deformation, and the temperatures and pressures that were recorded in the rocks during prograde metamorphism.

Regional Geology

In the southern Sutlej valley, the Main Boundary thrust and Main Frontal thrust are present in the footwall of the MCTZ (e.g., Vannay and Grasemann, 2001). To the north, the Greater Himalayan sequence (GHS) is exposed between the MCTZ and the STDS (locally termed the Sangla detachment) (Fig. 3.1) (e.g., Vannay and Grasemann, 2001). The GHS is composed of Neoproterozoic to Cambrian rocks that record metamorphism and anatexis in the Miocene, during exhumation along the MCTZ and STDS (e.g., Law et al., 2004; Jessup et al., 2006; Searle et al., 2006). The Lesser Himalayan sequence underlies the GHS, structurally beneath the MCTZ (Fig. 3.1b). The Tethyan Sedimentary sequence (TSS) structurally overlies the GHS. The base of the TSS, above the Sangla detachment in the northern Sutlej valley, is comprised of the Lower Proterozoic to Cambrian metasediments of the Haimanta Group (e.g., Frank et al., 1995; Vannay and Grasemann, 2001; Wiesmayr and Grasemann, 2002; Chambers et al., 2009). The base of the Haimanta Group is intruded by the 488 Ma Akpa (also termed ‘Kinnaur Kailas’) granite (e.g., Miller et al., 2001).

North from the Akpa granite, metamorphic grade decreases up-section in the north-dipping Haimanta Group from the kyanite-isograd exposed structurally above the Akpa granite to the biotite-isograd approximately 6 km up-section (Chambers et al., 2009). The Haimanta Group at the staurolite-isograd (Fig. 3.2), just south of the dome, reached peak conditions of ~600° C and 7 kbar during Barrovian metamorphism (Chambers et al., 2009; Jessup et al., in prep; Langille et

al., in review). The Haimanta Group transitions to south-dipping at the southern end of the LPD (Fig. 3.2). Chambers et al. (2009) demonstrated that prograde metamorphism in the Haimanta Group in the Sutlej valley began at >34 Ma with peak burial at 30 Ma and garnet growth ending by 28 Ma. Staurolite and kyanite growth ceased at ~30 Ma (Langille et al., in review). The Haimanta Group in the Sutlej valley contains upright sedimentary bedding that is deformed by recumbent folds. The top of the Haimanta Group is separated from the overlying Ordovician to Jurassic sedimentary rocks of the TSS associated with the former Indian passive margin (e.g., Shian, Pin, and Muth Formations) by an unconformity (Wiesmayr & Grasemann, 2002).

The arc-perpendicular normal faults and shear zones that bound the Leo Pargil and Gurla Mandhata domes (Murphy et al., 2002; Langille et al., in review) extend north to the dextral Karakoram fault system (Fig. 3.1b). From northwest, the Karakoram fault extends from the Pamirs to the southeast where it links to the Gurla Mandhata detachment. A portion of the strain at the southern extent of the Karakoram fault is interpreted to continue along the Indus-Yarlung suture (Lacassin et al., 2004) (Fig. 3.1a). Ages for the onset of the Karakoram fault system and the total amount of displacement are widely debated. Phillips et al. (2004) interpret ages from mylonitic and undeformed leucogranites in Ladakh, northwest of Tso Morari, to suggest that the Karakoram here initiated between 15.7-13.7 Ma. An age from synkinematic granite near Tso Morari (Fig. 3.1a) suggests that the Karakoram here initiated at >18.5 Ma (Leloup et al., 2011). 29 Ma age rocks near Tso Morari are deformed by the Karakoram fault suggesting that here the fault initiated at <29 Ma (de Sigoyer et al., 2004). U-Th-Pb ages from mylonitic granites in the Ayi Shan, east of the LPD, (Fig. 3.1a) interpreted to be synkinematic range from 25-21 Ma suggesting that the Karakoram here initiated at >25 Ma (Lacassin et al., 2004). Near the Gurla Mandhata dome, the southern end of the Karakoram fault overprints the South Kailas thrust which was active at 13 Ma, suggesting that here the Karakoram is younger than 13 Ma (Murphy et al., 2000) (Fig. 3.1a). The discrepancy between initiation ages using variably deformed leucogranites (i.e. 15.7-13.7 Ma versus >25 Ma) stems from differing interpretations that the variably deformed leucogranites analyzed are either prekinematic or synkinematic leucogranites (Lacassin et al., 2004; Phillips et al., 2004; Searle and Phillips, 2007; Valli et al., 2007). Based on younging of ages toward the southeast along the southern segment of the Karakoram

Figure 3.2. *Geologic map of the southern end of the Leo Pargil dome from Langille et al. (in review). Main foliation and stretching lineation data presented for each of the domains. See Figure 3.1b for location. Refer to Langille et al. (in review) for cross sections. n, number of data points; grt, garnet; st; staurolite; ky, kyanite; sil, sillimanite; crd, cordierite.*

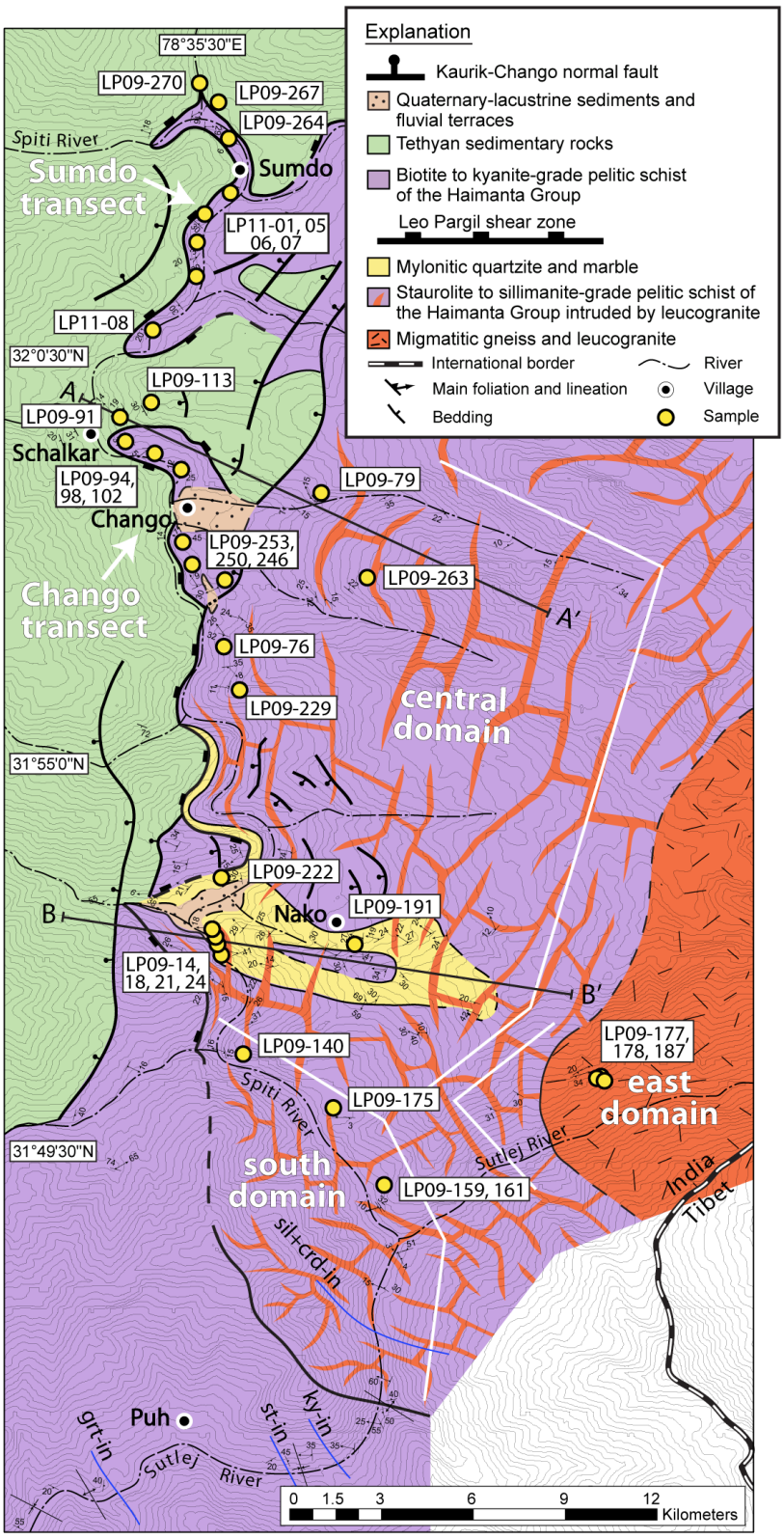
Explanation
Kaurik-Chango normal fault
Quaternary-lacustrine sediments and fluvial terraces
Tethyan sedimentary rocks
Biotite to kyanite-grade pelitic schist of the Haimanta Group
Leo Pargil shear zone
Mylonitic quartzite and marble
Staurolite to sillimanite-grade pelitic schist of the Haimanta Group intruded by leucogranite
Migmatitic gneiss and leucogranite
International border
River
Main foliation and lineation
Village
Bedding
Sample
78°35'30"E
32°0'30"N
31°55'0"N
31°49'30"N
Spiti River
Sumdo
Sumdo transect
Schalkar
Chango
Chango transect
Nako
Puh
Sutlej River
India
Tibet
central domain
south domain
east domain
LP09-270
LP09-267
LP09-264
LP11-01, 05 06, 07
LP11-08
LP09-113
LP09-91
LP09-94, 98, 102
LP09-253, 250, 246
LP09-79
LP09-263
LP09-76
LP09-229
LP09-222
LP09-191
LP09-14, 18, 21, 24
LP09-140
LP09-175
LP09-159, 161
LP09-177, 178, 187
A
A′
B
B′
sil+crd-in
ky-in
st-in
grt-in
0 1.5 3 6 9 12 Kilometers
Contour Interval 100 m

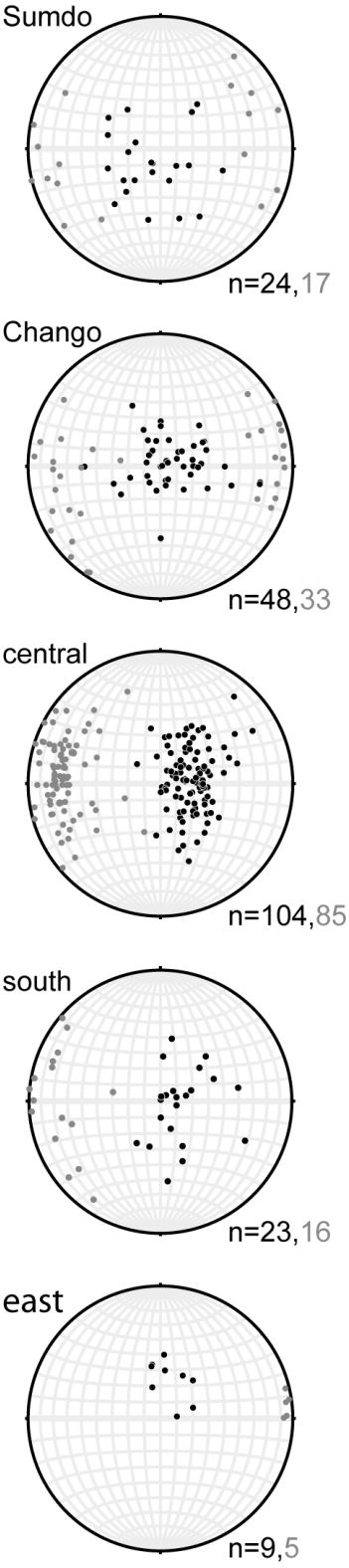
Sumdo
n=24,17
Chango
n=48,33
central
n=104,85
south
n=23,16
east
n=9,5
foliation
stretching lineation

fault, Murphy et al. (2000) suggests that the Karakoram fault developed as a southward propagating system.

The amount of offset accommodated along the Karakoram fault has been interpreted from recent studies of the correlation of offset suture zones, lithologic units, and the Indus River (Searle et al., 1998; Phillips et al., 2004; Lacassin et al., 2004; Searle and Phillips, 2007; Robinson, 2009). Maximum offsets of ≥400 km have been documented by correlation of the Bangong-Nujiang and Rushan-Pshart sutures (Lacassin et al., 2004). Searle and Phillips (2007) suggest that the Bangong-Nujiang suture correlates to the Shyok suture rather than the Rushan-Pshart suture, suggesting ~120 km of offset rather than ≥400 km (Fig. 3.1a). The Karakoram fault has offset the 18 Ma Baltoro granite in Ladakh by a maximum of 150 km suggesting a slip-rate of 8.4 mm/yr since 18 Ma on this segment of the Karakoram (Searle et al., 1998; Phillips et al., 2004; Searle and Phillips, 2007). Offset of the Aghil formation, just north of the Baltoro granite, suggests 149-167 km of displacement along the Karakoram fault (Robinson, 2009). Assuming initiation of the Karakoram fault at ~15 Ma (e.g., Phillips et al., 2004) or ~23 Ma (Lacassin et al., 2004), displacement of 149-167 km suggests a slip-rate of either ~11 mm/yr or ~7 mm/yr, respectively (Robinson, 2007). The Indus River in Ladakh has been dextrally offset by 120 km. Lacassin et al. (2004) suggest that this offset began at 12 Ma yielding a long-term slip-rate of 10 mm/yr, similar to estimates using the offset Baltoro granite or the Aghil formation. The Gurla Mandhata detachment at the southern extent of the Karakoram fault exhumed rocks by up to 66 km of displacement (Murphy et al., 2000). Assuming all this slip was transferred from the Karakoram fault, a dip of 22° for the detachment (Murphy et al., 2000) suggests that the Karakoram fault here accommodated ~61 km of horizontal displacement (Murphy et al., 2000).

Geodetic slip-rates for the northwest Himalaya suggest a modern slip-rate of ~10 mm/yr on the Karakoram (Banerjee and Bürgmann, 2002; Chevalier et al., 2005). The Holocene slip-rate determined from offset Quaternary glacial landforms along the Karakoram fault in the Ladakh region in India is ~4 mm/yr (Brown et al., 2002). Geodetic slip-rates on the Indus-Yarlung suture, at the southernmost end of the Karakoram suggest a modern rate of <1 cm/yr (Styron et al., 2011). Hintersberger et al. (2010) suggests that in the western Himalaya, the southern segment of the Karakoram fault only accommodates a portion of the modern east-west

displacement from within the Tibetan Plateau. The remainder of the deformation from the Tibetan Plateau is transferred south of the Karakoram fault to a system of north-south trending brittle normal faults, including the brittle faults on the southwest flank of the LPD (Fig. 3.1b) (Hintersberger et al., 2010; Hintersberger et al., 2011).

Geology of the Leo Pargil Dome

The LPD in northwest India is defined on the west flank by the northeast-trending normal-sense LPSZ and brittle faults that extend northeast into the right-lateral Karakoram fault system and are interpreted to accommodate orogen-parallel extension (Figs. 3.1 and 3.2) (Ni and Barazangi, 1985; Zhang et al., 2000; Thiede et al., 2006; Hintersberger et al., 2010). On the southwest flank of the dome, the LPSZ is a dominantly west-dipping zone that accommodated normal-displacement (Figs. 3.2 and 3.3a) (Thiede et al., 2006). The southwest flank of the dome is composed of amphibolite-facies metamorphic rocks that are intruded by several generations of leucogranite (Fig. 3.3b). Toward the core, the rocks transition to gneiss and migmatite (Fig. 3.2). The rocks within the dome and the core are overprinted by distributed top-down-to-the-west shearing of the LPSZ (Fig. 3.3). Migmatites in the core record a transition to top-down-to-the-east shear sense. The Kaurik-Chango brittle normal fault on the west side of the dome offsets the LPSZ (Fig. 3.2) (Thiede et al., 2006). The dome extends northeast to the Ayi Shan that is bound to the north by the Karakoram fault system (Valli et al., 2007; Sanchez et al., 2010) (Fig. 3.1). The northeast-striking, southeast- dipping Qusum detachment fault (Zhang et al., 2000) separates the southeastern margin of the dome from the Zada basin (Murphy et al., 2009; Saylor et al., 2010).

The amphibolite-facies rocks on the southwest side of the dome belong to the Haimanta Group and record peak Barrovian metamorphism at ~30 Ma at ~600° C and ~7-8 kbar (Langille et al., in review), overlapping with estimates from the Haimanta Group south of the dome (Chambers et al., 2009; Jessup et al., in prep). Based on the structure and lithology, the migmatite in the core of the dome presumably belongs to the GHS but this needs to be further evaluated. Barrovian metamorphism in the Haimanta Group rocks within the LPD is overprinted

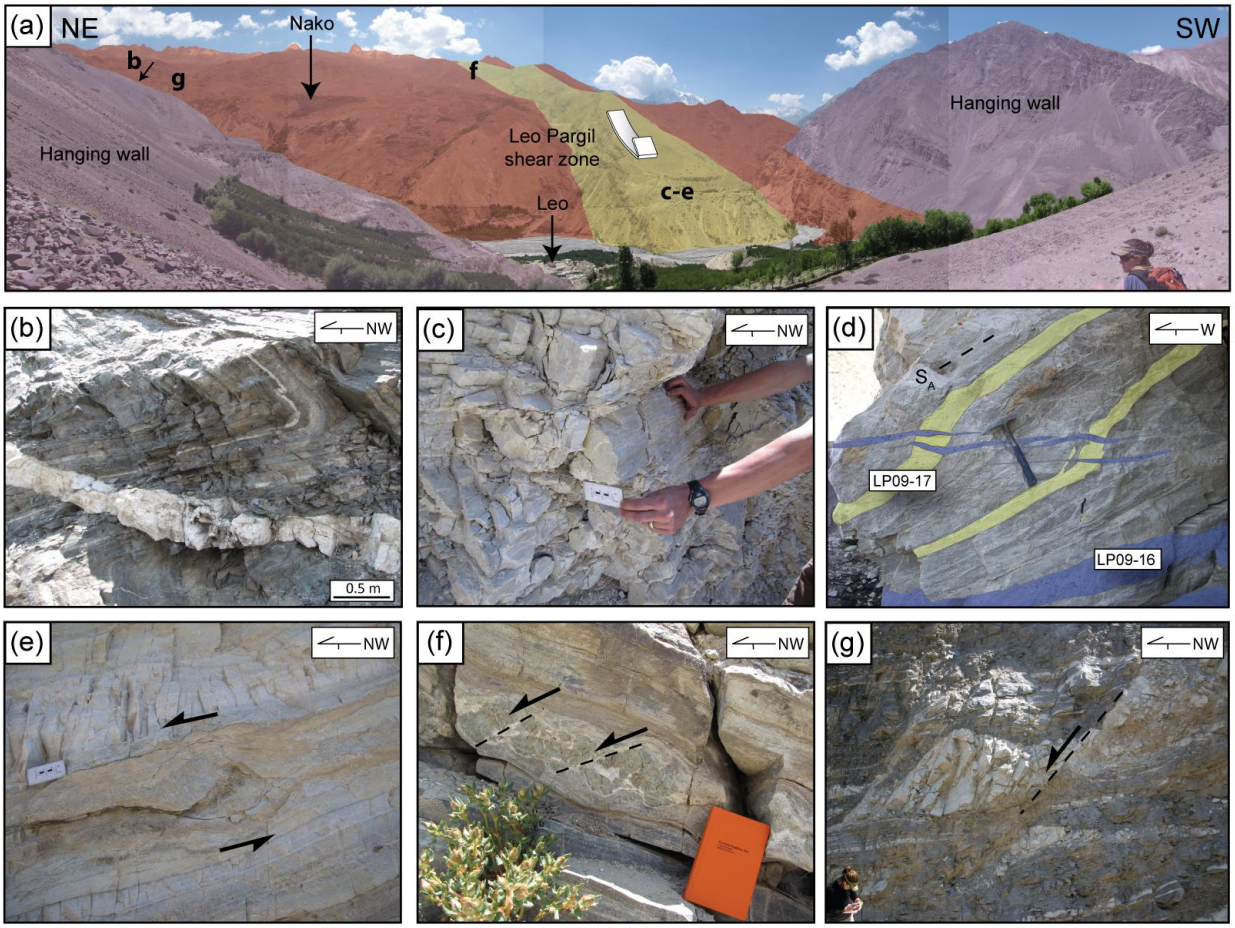

Figure 3.3. *Field photographs from the Leo Pargil dome. (a) A portion of the Leo Pargil shear zone (LPSZ; yellow and red) viewed toward the east. Red corresponds to the Haimanta Group intruded by leucogranite within the dome. Other colors correspond to Figure 3.2. (b) Deformed and undeformed leucogranites within the LPSZ. (c through e) Mylonitic quartzite and marble (yellow unit). (c) L-tectonite fabric. (d) LP09-16 is an undeformed leucogranite and LP09-17 is deformed. (e and f) Sheared marble within the quartzite demonstrates top-down-to-the-west shear sense. (g) Sheared leucogranite suggests top-down-to-the-west shear sense.*

by decompression and top-down-to-the-west shearing of the LPSZ that began by 23 Ma (Langille et al., in review). A quartzite and marble unit exposed within the LPSZ with deformed and undeformed leucogranites contains a strong foliation and stretching lineation, with an outcrop of quartzite with L-tectonite fabrics suggesting heterogeneous strain distribution in this portion of the shear zone (Fig. 3.3c and d). Macroscopic shear sense indicators record top-down-to-the-west to northwest shear sense (Fig. 3.3e through g). Initiation of extension on the LPSZ

was followed by leucogranite generation in the migmatite core that was emplaced into schist and older leucogranites at structurally higher levels from 23 to 18 Ma (Fig. 3.3b and d) (Langille et al., in review).

The dome is separated into five domains: the Chango and Sumdo transects and the south, central, and east domains (Fig. 3.2). The Chango and Sumdo transects include the Haimanta Group rocks that are within the uppermost structural positions of the LPSZ, in the hanging wall of the Kaurik-Chango normal fault near the villages of Chango and Sumdo (Fig. 3.2). Haimanta Group rocks within the LPSZ in the Chango and Sumdo transects are folded and define a gentle anticline (Fig. 3.2). The rocks within these transects were folded following the development of a stretching lineation, which now dip toward the east or west (Fig. 3.2). Microscopic shear sense indicators including strain shadows on porphyroclasts, shear bands, and mica fish are consistent with top-down-to-the-west shear sense (Fig. 3.4a and b; Table 3.1). In the hanging wall of the LPSZ within the Chango transect (green, Fig. 3.2), rocks transition from low-temperature metamorphic rocks with a weak fabric (Table 3.1) to undeformed, unmetamorphosed sedimentary rocks. The rocks in the hanging wall of the LPSZ in the Sumdo transect transition to low-temperature metasedimentary rocks with a weak lineation and foliation that record weakly developed top-to-the-east shearing (Table 3.1).

Rocks within the south and central domains dominantly contain a west dipping foliation that defines the LPSZ. These rocks dominantly contain a top-down-to-the-west stretching lineation (Fig. 3.2) and macroscopic shear sense indicators suggest top-down-to-the-west shear sense (Fig. 3.3e through g). Microscopic shear sense indicators such as strain shadows on rigid porphyroclasts, quartz oblique fabrics, and shear bands suggest top-down-to-the-west shear sense (Fig. 3.4c through e; Table 3.1). Rocks within the east domain are the structurally deepest rocks in the dome and contain an east-directed stretching lineation (Fig. 3.2). Macroscopic shear bands in migmatitic gneiss suggest a transition to top-down-to-the-east shear sense (Langille et al., in review). Microscopic shear sense indicators including shear bands and strain shadows on garnet porphyroclasts are consistent with an east-directed shear sense (Fig. 3.4f; Table 3.1).

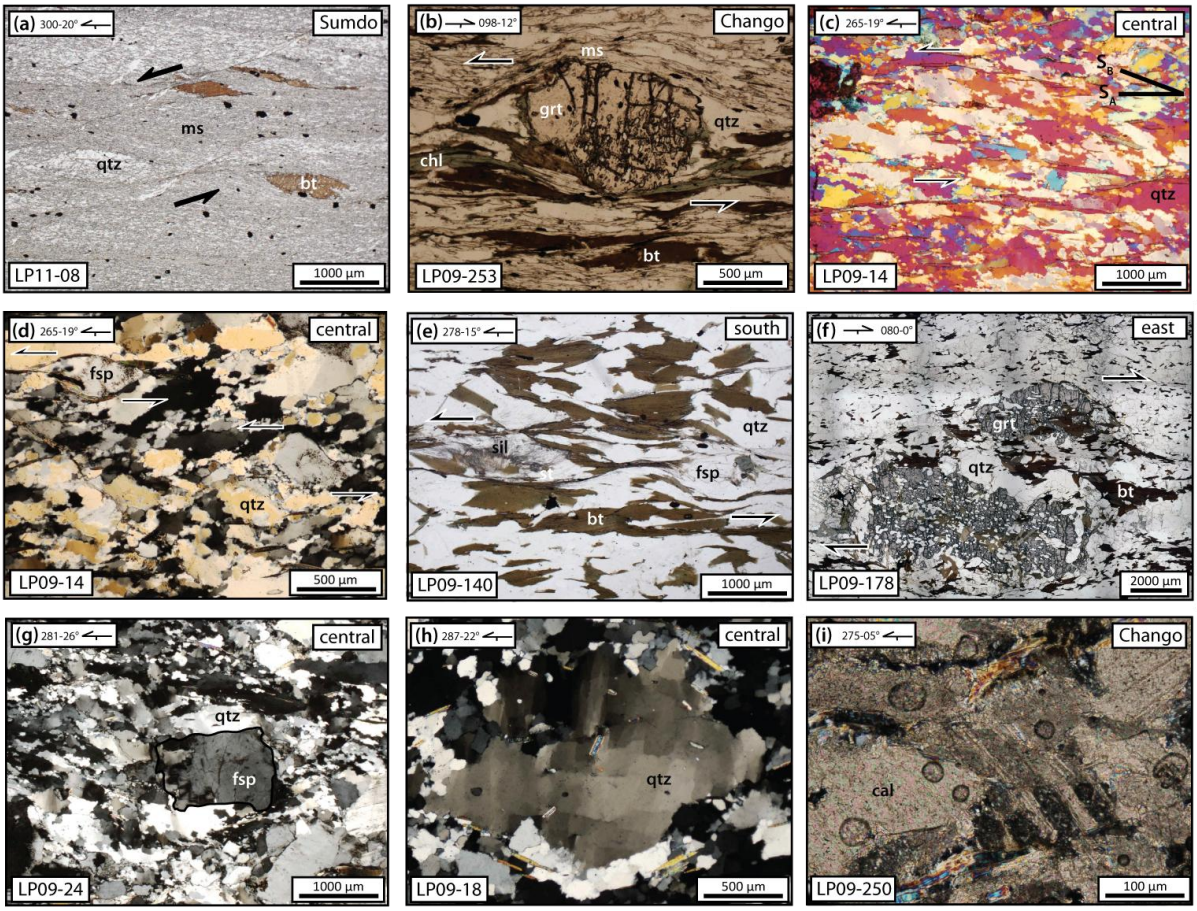

Figure 3.4. *Photomicrographs of samples from the Leo Pargil dome. (a) Biotite (bt) fish and shear bands indicating top-down-to-the-northwest shear sense. qtz, quartz; ms, muscovite. (b) Strain shadow on garnet porphyroclast suggesting top-down-to-the-west shear sense. chl, chlorite. (c) Oblique quartz fabric exhibiting grains that preserve grain boundary migration recrystallization (GBM) suggesting top-down-to-the-west shear sense at temperatures of >500° C. (d) Quartz recording GBM and deformed feldspars (fsp) suggesting top-down-to-the-west shear sense and temperatures of >500° C. (e) Rotated feldspar and sillimanite suggest top-down-to-the-west shear sense. (f) Strain shadow on garnet clasts indicate east-directed shear. (g)Quartz exhibiting GBM and a feldspar grain (outlined in black for clarity) with sub-grain rotation recrystallization suggesting temperatures of >600° C. (h) Checker board extinction in quartz indicating >650° C. (i) Type IV calcite (cal) twins surrounded by other calcite grains that have been completely recrystallized at temperatures of >300° C.*

Table 3.1. Summary of Kinematic and Deformation Temperature Data.

Sample	Rock type	Shear Sense	Shear Sense Indicators	W_m	% pure shear	R_{xz}	% down-dip extension	% shortening[a]	Deformation Temperature (° C)	Temperature Indicator
Sumdo transect										
LP09-274	phyllite	top-60	mica fish, shear bands	—	—	—	—	—	<280	rigid quartz
LP09-270	phyllite	top-093	mica fish, shear bands	—	—	—	—	—	~280	onset of BLG in quartz
LP09-267	calc-silicate	—	—	—	—	—	—	—	200-300	type II calcite twins
LP11-08	schist	top-300	mica fish, shear bands	—	—	—	—	—	400-500	quartz SGR
LP09-264	schist	top-230	shear bands	—	—	—	—	—	400-450	quartz SGR, rigid feldspar
LP11-01	schist	top-200	shear bands	—	—	—	—	—	400-500	quartz SGR
LP11-07	schist	top-250	strain shadows	—	—	—	—	—	400-450	quartz SGR, rigid feldspar
LP11-05	schist	top-220	mica fish	—	—	—	—	—	400-450	quartz SGR, rigid feldspar
LP11-06	schist	top-255	strain shadows	—	—	—	—	—	400-450	quartz SGR, rigid feldspar
Chango transect										
LP09-113	limestone	—	—	—	—	—	—	—	—	—
LP09-91	marble	—	—	—	—	—	—	—	200-300	type II calcite twins
LP09-94	schist	top-260	shear bands	—	—	—	—	—	400-500	quartz SGR
LP09-102	schist	top-270	shear bands	—	—	—	—	—	400-450	quartz SGR[c], rigid feldspar
LP09-98	schist	top-225	shear bands	—	—	—	—	—	400-450	quartz SGR[c], rigid feldspar
LP09-253	schist	top-278	shear bands, strain shadows	—	—	—	—	—	400-450	quartz SGR[c], rigid feldspar
LP09-250	calc-silicate	top-275	shear bands	—	—	—	—	—	400-500	quartz SGR[c], calcite recrystallized
LP09-246	schist	top-250	mica fish	—	—	—	—	—	400-500	quartz SGR[c]

Table 3.1. Continued.

Sample	Rock type	Shear Sense	Shear Sense Indicators	W_m	% pure shear	R_{xz}	% down-dip extension	% shortening[a]	Deformation Temperature (° C)	Temperature Indicator
central domain										
LP09-191[b]	quartzite	top-286	oblique fabric, mica fish, LPO	0.83-0.98	36-11	11-30	66-118	40-54	500-650	quartz GBM, prism <a>
LP09-222[b]	leucogranite	top-210	oblique fabric, strain shadows, LPO	0.90-0.98	28-11	15-30	66-108	40-52	>650	quartz checker board extinction, prism [c]
LP09-24[b]	leucogranite	top-281	oblique fabric, tails, mica fish, LPO	0.74-0.93	42-22	14-30	137-168	58-63	600-650	quartz GBM, feldspar SGR, prism <a>
LP09-21[b]	quartzite	top-268	oblique fabric, mica fish	—	—	—	—	—	500-650	quartz GBM, prism <a>
LP09-18	quartzite	top-287	oblique fabric, mica fish	—	—	—	—	—	>650	quartz checker board extinction
LP09-14[b]	quartzite	top-265	oblique fabric, strain shadows, mica fish, LPO	0.84-0.97	35-12	5-11	43-64	30-38	600-650, 663 ± 30	quartz GBM, feldspar SGR, opening angle
LP09-76	schist	top-300	shear bands, strain shadows	—	—	—	—	—	500-650	quartz GBM
LP09-229	schist	top-273	shear bands, strain shadows	—	—	—	—	—	500-650	quartz GBM
LP09-79	schist	top-290	shear bands, strain shadows	—	—	—	—	—	500-650	quartz GBM
LP09-263	schist	top-270	shear bands	—	—	—	—	—	500-650	quartz GBM
south domain										
LP09-140	schist	top-287	shear bands, strain shadows	—	—	—	—	—	600-650	quartz GBM, feldspar SGR
LP09-175	schist	top-270	tails	—	—	—	—	—	600-650	quartz GBM, feldspar SGR
LP09-159	schist	top-230	shear bands, strain shadows	—	—	—	—	—	500-650	quartz GBM

Table 3.1. Continued.

Sample	Rock type	Shear Sense	Shear Sense Indicators	W_m	% pure shear	R_{xz}	% down-dip extension	% shortening[a]	Deformation Temperature (° C)	Temperature Indicator
LP09-161	schist	top-260	strain shadows	—	—	—	—	—	600-650	quartz GBM, feldspar SGR
east domain										
LP09-177	gneiss	top-081	shear bands	—	—	—	—	—	500-650	quartz GBM
LP09-178	gneiss	top-080	shear bands, strain shadows	—	—	—	—	—	500-650	quartz GBM
LP09-187	gneiss	top-075	strain shadows	—	—	—	—	—	>650	quartz checker board extinction, myrmekite

Note: SGR, subgrain rotation; GBM, grain boundary migration. Sample locations are in the Appendix 3.1.
[s]Shortening is normal to the down-dip direction.
[b]Analyzed with electron backscattered diffraction (EBSD).
[c]SGR in quartz is overprinted by BLG.

Temperatures and Kinematics during Deformation

Methodology for Estimating Deformation Temperatures

Deformation temperatures during top-down-to-the-west shearing were estimated using (1) recrystallized quartz and feldspar microstructures (Hirth and Tullis, 1992; Fitz Gerald and Stünitz, 1993; Stipp et al., 2002a; Stipp et al., 2002b), (2) quartz slip systems determined from quartz lattice preferred orientation (LPO) patterns (e.g., Mainprice et al., 1986), (3) the opening angle of quartz [c] axis LPO patterns (Kruhl, 1998; Law et al., 2004), and (4) calcite twins (e.g., Weber et al., 2001; Ferrill et al., 2004). These temperatures were used to constrain the depth in the crust in which deformation occurred, from which the amount of exhumation on the LPSZ can be estimated.

Quartz exhibits bulging recrystallization (BLG) at temperatures of 280-400° C, sub-grain rotation recrystallization (SGR) at temperatures of 400-500° C, and grain boundary migration recrystallization (GBM) at temperatures >500° C (Fig. 3.4c, d, and g) (Stipp et al., 2002a; Stipp et al., 2002b). At temperatures of >650° C, quartz begins to develop checker board extinction (Fig. 3.4h). At temperatures of <450° C, where quartz experiences BLG recrystallization, feldspar is rigid and deforms by brittle fracturing (Pryer, 1993). Dislocation glide (Fig. 3.4b) and BLG recrystallization is possible in feldspars at 450-600° C (Pryer, 1993). BLG and SGR recrystallization can occur in feldspar at temperatures of >600° C (Fig. 3.4g) (Tullis and Yund, 1991).

Deformation temperatures can also be inferred from the slip systems that accommodated recrystallization during deformation within quartz grains. The slip systems are determined from the LPOs of the quartz grains within a sample, viewed in the plane perpendicular to foliation and parallel to lineation (XZ section). The LPOs, when plotted on a stereonet, yield maxima indicative of the slip systems (Fig. 3.5) (e.g., Lister and Hobbs, 1980; Law, 1990). Quartz LPOs were obtained using electron backscattered diffraction patterns collected using an FEI Quanta 400 FEG scanning electron microscope coupled with a HKL Nordlys 2 EBSD camera at the University of California, Santa Barbara. CHANNEL 5 HKL software was used to index the diffraction patterns with Hough resolution of 80, detecting 7-8 bands with standard divergence and a quartz structure file containing 60 reflectors.

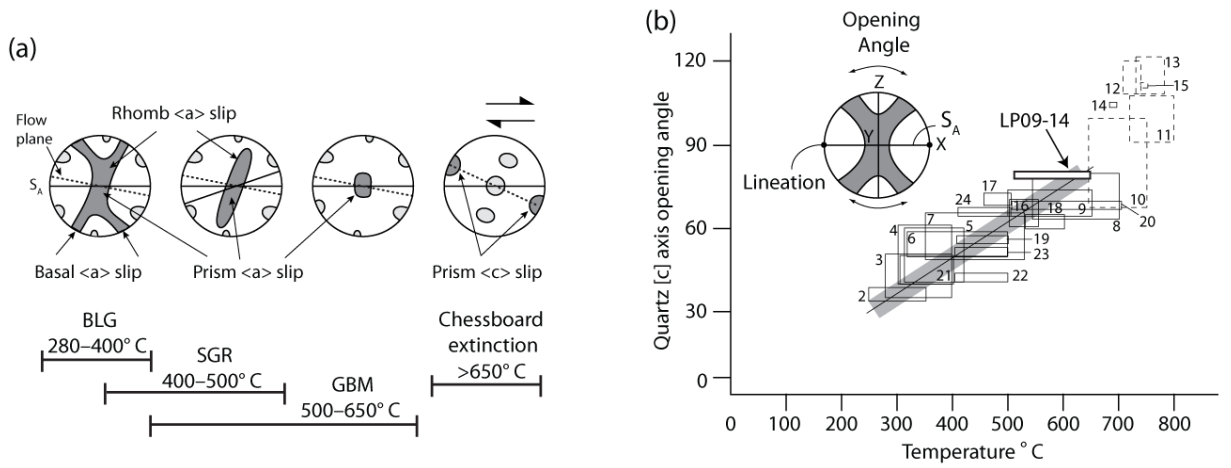

Figure 3.5. *(a) Quartz lattice-preferred orientation (LPO) patterns and slip systems expected for plane strain non-coaxial deformation with increasing temperature (modified from Passchier and Trouw, 2005; Langille et al., 2010a). (b) Correlation between opening angle and temperature. Dashed boxes represent data from quartz with prism [c] slip. Boxes 1-15: Kruhl, 1998; 16: Law et al., 1992; 17: Nyman et al., 1995; 18: Okudaira et al., 1995; 19-20: Langille et al., 2010b; 21-24: Langille et al., 2010a. Opening angle from this study included, plotted against temperatures inferred from quartz and feldspar textures. Modified from Law et al. (2004).*

While basal <a>, prism <a>, and rhomb <a> slip can occur at a range of temperatures, basal <a> slip is dominant at temperatures of 280-400° C, prism <a> and rhomb <a> are dominant at temperatures of 400-500° C, and prism <a> is dominant at 500-650° C. At temperatures of >650° C, prism [c] becomes dominant (e.g., Lister and Dornsiepen, 1982; Mainprice et al., 1986; Kruhl, 1998) (Fig. 3.5a). LPO patterns that exhibit basal <a>, prism <a>, and rhomb <a> slip often contain a crossed girdle pattern (Fig. 3.5). The opening angle is defined as the angle between the girdles (Kruhl, 1998). Experimental studies (e.g., Tullis et al., 1973; Lister et al., 1978; Lister and Hobbs, 1980; Lister and Dornsiepen, 1982; Wenk et al., 1989) indicate that the opening angle of quartz [c] axis LPOs increases with increasing deformation temperature (Fig. 3.5b) so the opening angle can be used to calculate the deformation temperature (e.g., Kruhl, 1998). Previous studies attributed an error of ± 50° C to the temperature estimate using this method, based on the standard deviation of the data from temperatures of 280° C to >650° C (e.g., Kruhl, 1998). However, the linear relationship between opening angle and temperature changes at conditions of >650° C, when prism [c] slip begins to develop in quartz (Fig. 3.5b). Recalculating the standard deviation of the data from temperatures between

280° C to 650° C yields an error of ± 30° C. Other factors such as strain rate also play a role in the development of the opening angle (Tullis et al., 1973). However, the compiled data (Fig. 3.5b) are from samples of varying deformation state with varying measurement error and the correlation between temperature and opening angle is still expressed, implying that the effect of factors other than temperature are within error of the temperature estimate.

In addition to quartz and feldspar, calcite twins can be indicative of deformation temperatures. Type I twins are characterized by thin lines that develop at temperatures of <200° C (e.g., Weber et al., 2001; Ferrill et al., 2004). At temperature of 200-300° C, wide bands (type II twins) develop in calcite during dislocation glide (e.g., Weber et al., 2001; Ferrill et al., 2004). With increasing temperature the calcite twins begin to obtain curvature (type III) and become patchy (type IV) with the onset of dynamic recrystallization (Fig. 3.4i). Complete dynamic recrystallization occurs at >300° C (e.g., Weber et al., 2001; Ferrill et al., 2004).

Results

Metamorphosed and deformed Haimanta Group rocks within the LPSZ in the Chango and Sumdo transects transition into weakly to undeformed, low-temperature metasedimentary rocks in the hanging wall of the LPSZ (Fig. 3.2). The rocks within the LPSZ in these transects (Fig. 3.2) contain quartz that exhibits sub-grain rotation and feldspar that remained rigid suggesting temperatures of 400-450° C (Table 3.1). The quartz in some of the samples is overprinted by BLG recrystallization indicating continued recrystallization during exhumation through 280-400° C (Table 3.1). LP09-250 contains calcite that has been completely dynamically recrystallized indicating temperatures of >300° C, overlapping with temperatures recorded by the quartz and feldspar (Table 3.1). The metasedimentary rocks in the hanging wall of the LPSZ, with decreasing structural depth above the LPSZ transition from containing quartz that records the onset of BLG recrystallization, to samples with type II calcite twins, to samples with quartz that have not been recrystallized (Fig. 3.2; Table 3.1).

Deformed metamorphic rocks in the south and central domain within the dome contain quartz grains that exhibit GBM and feldspar grains that record SGR suggesting temperatures of 500-650° C (Table 3.1). Checker board extinction of quartz occurs in some samples indicating temperatures of >650° C. Quartz LPO patterns from samples in the central domain dominantly

exhibit prism <a> to prism [c] slip suggesting temperatures of 500-650° C and >650° C, respectively (Fig. 3.6; Table 3.1). The LPO pattern of sample (LP09-14) forms a girdle and the opening angle of the girdle suggests temperatures of 663 ± 30° C (Fig. 3.6; Table 3.1).

Samples from the eastern transect are migmatitic gneiss that are located structurally in the core of the dome. These samples contain myrmekite and quartz grains that record GBM and/or checker board extinction. These textures suggest temperatures of 500° C to >650° C (Table 3.1).

Methodology for Estimating Vorticity and Results

Vorticity analyses were conducted to quantify the relative contribution of pure shear (flattening) and simple shear (shearing with no flattening) during ductile deformation which yields insights into the amount of down-dip extension and thinning normal to extension that occurred during exhumation along the LPSZ. A contribution of pure shear suggests crustal thinning (assuming plane strain) of the deformed material and higher strain and extrusion rates relative to simple shear (Law et al., 2004). Kinematic vorticity number (W_k) is a measure of the contributions of pure ($W_k = 0$) and simple ($W_k = 1$) shear during steady-state deformation. Pure and simple shear components are equal when $W_k = 0.71$ (Tikoff and Fossen, 1995; Law et al., 2004). The vorticity in naturally deformed rocks can have spatial and temporal variations which are accounted for by using a time-averaged estimate to calculate the bulk vorticity, known as the mean kinematic vorticity number (W_m) (e.g., Fossen and Tikoff, 1997, 1998; Jiang, 1998). A steady-state deformation history is assumed. W_m methods require that deformation progressed during plane strain conditions. However, a small deviation from plane strain may cause only a small error (Tikoff and Fossen, 1995) that is within the error associated with conducting vorticity methods. To avoid this small error, these methods were not applied to samples that exhibited L-tectonite fabrics (constriction, Fig. 3.3c). Furthermore, quartz LPO data for samples in which these methods were applied suggest plane strain conditions (Figs. 3.5a and 3.6). The quartz grain shape foliation technique was applied (Fig. 3.7) (Wallis, 1995) to thin sections cut perpendicular to the foliation and parallel to the lineation (XZ section) to estimate W_m. Quartz grains that recrystallize during deformation are stretched parallel to the instantaneous stretching axis (ISA) (Wallis, 1995). During deformation, quartz rotates to a maximum angle relative to the flow

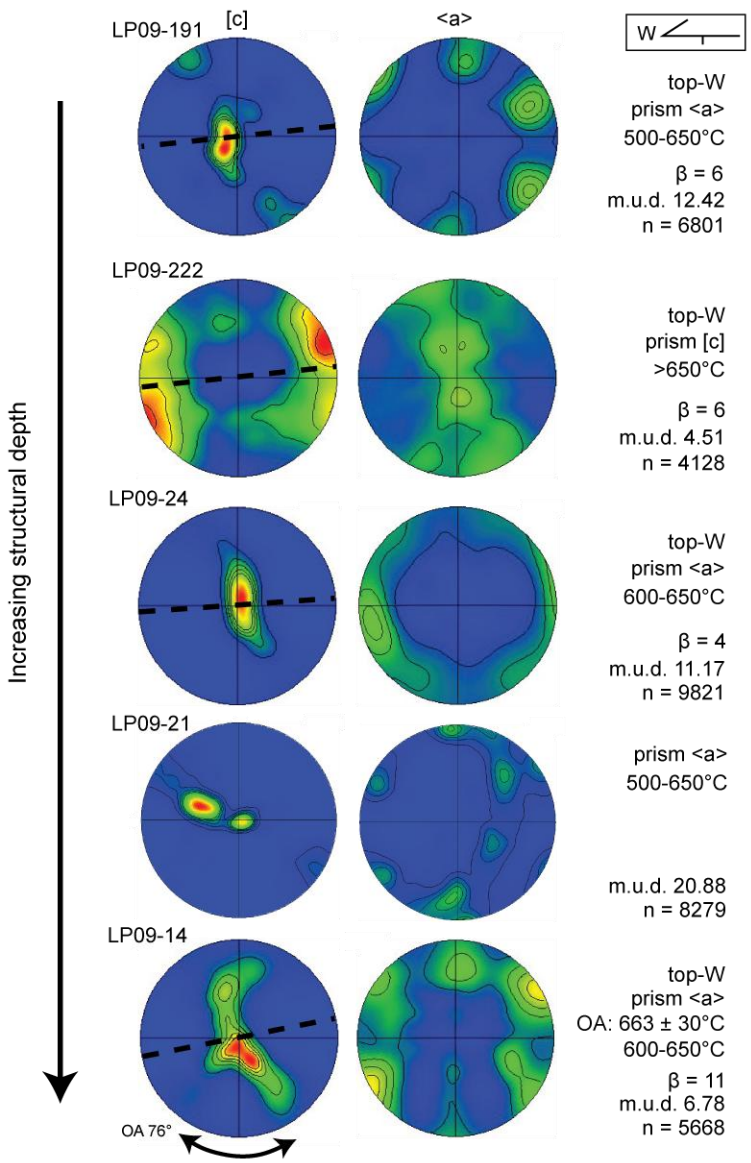

Figure 3.6. *Quartz lattice-preferred orientation (LPO) patterns for deformed quartzite and leucogranite samples from the quartzite unit in the central domain. Dashed line represents the flow plane. Interpreted shear sense, dominant slip system, and temperatures determined from quartz and feldspar textures are included. m.u.d. mean uniform distribution; n = number of points; OA, opening angle. See Figure 3.7 for definition of β.*

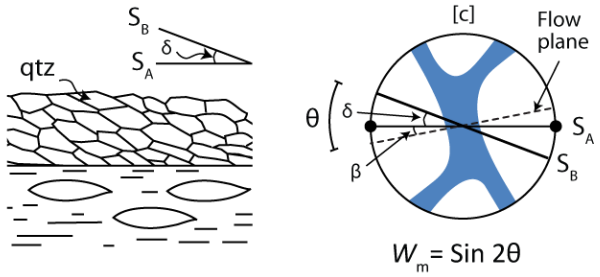

Figure 3.7. *Diagram depicting the aspects used in estimation of vorticity (W_m) from an oblique fabric defined by quartz. Modified from Xypolias (2009).*

plane, which approximates the ISA (Fig. 3.7) (Wallis, 1995). θ is the angle between the oblique grain shape fabric (S_B) (Fig. 3.4c) and the flow plane (Figs. 3.5, 3.6, and 3.7). The flow plane is defined as the perpendicular to the [c] axis girdle of the quartz LPO where β is the angle between the flow plane and the main foliation (S_A) (Fig. 3.7) (Law, 1990; Wallis, 1995). The angle between the oblique grain shape fabric (S_B) and the flow plane is related to W_m by the equation:

$$W_m = \sin 2\theta = \sin [2(\delta+\beta)] \quad (1)$$

where δ is the angle between the quartz oblique grain shape fabric (S_B) and S_A (Fig. 3.7) (Wallis, 1995).

The long axis of the quartz grains from four samples were measured from high-resolution mosaic image of the thin sections and the flow planes were measured from the quartz LPO patterns. To accurately define the ISA, θ was measured on >100 quartz grains per sample. Application of the grain shape foliation technique requires a well-developed quartz LPO and oblique grain shape fabric to accurately define both the flow plane and the ISA, and thus θ (Wallis, 1995; Xypolias and Koukouvelas, 2001; Xypolias, 2009, 2010). I suggest that θ at the peak of the histogram represents the angle to which the bulk of the quartz grains rotated to, which best represents the angle of the ISA. To merge this with the Wallis (1995) method for approximating the ISA, a range in θ defined as where the frequency of θ on the histogram reaches its highest value to where it declines to a maximum measured angle is used (methods utilized in Langille et al., 2010a).

Uncertainties in vorticity values estimated using this technique can be attributed to: (1) heterogeneity of the matrix material, (2) the presence of porphyroclasts, and (3) folding—which

may all deflect or influence the orientation and/or development of the quartz fabric. To limit possible inaccuracies, measurements were made from quartz fabrics that were unaffected by these interferences.

Quartz grains in four quartzite and quartz rich leucogranite samples from the quartzite unit in the central domain (Fig. 3.2) contained well developed oblique fabrics. LPO patterns from these samples exhibit well developed maxima from which the flow plane could be determined (Fig. 3.6), making these prime samples for W_m analysis using the quartz grain shape foliation technique. These methods yielded W_m estimates of 0.74 to 0.98 (42 to 11% pure shear) (Fig. 3.8; Table 3.1).

Thermobarometry

Methodology and Results

Estimates of the P-T conditions at peak temperatures during metamorphism were obtained to evaluate the transition from crustal thickening to exhumation on the LPSZ. Chemical data for thermobarometric estimates were obtained on a Cameca SX-100 electron microprobe at the University of Tennessee. X-ray maps using wavelength-dispersive spectrometery of Mg, Mn, and Ca along with quantitative line transects were conducted across garnet porphyroblasts at 15 kV, 30 nA, 30 ms, and a 6 μm spot size to characterize compositional zonation. Point analyses at 15 kV, 20 nA, and a spot size of 1μm were conducted on biotite, plagioclase, and muscovite to assess compositional heterogeneities of each phase throughout the sample. Plagioclase was analyzed at 10 kV. Natural and synthetic compounds were used for standards and were checked prior to and following the analyses. Elemental abundances <300 ppm are considered below the detection limit for all elements except for Y which is ~400 ppm.

Mn content in garnet decreases from core to rim, indicative of prograde zonation (Fig. 3.9). Garnet contains a thin (5-10 μm) rim with an increase in Mn as a result of retrograde net transfer reactions (Kohn and Spear, 2000). Compositions obtained from biotite, muscovite, and plagioclase varied little and were averaged for the P-T estimate (Table 3.2). These data were combined with the garnet near-rim composition with the lowest Mn value (Fig. 3.9; Table 3.2).

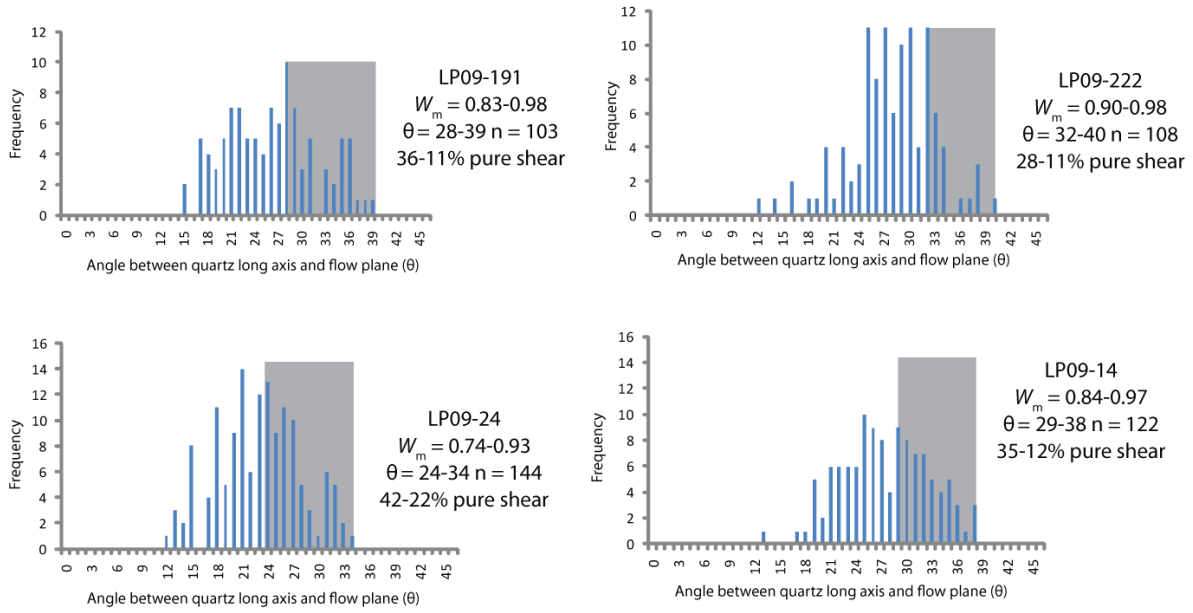

Figure 3.8. *Histograms of quartz grain orientation data and W_m estimates. Refer to Figure 3.6 for the angle between the flow plane and the main foliation (β).*

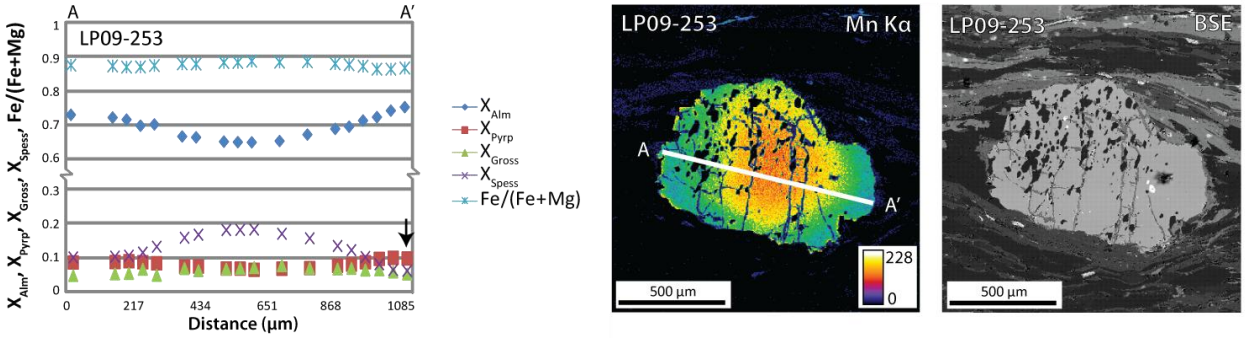

Figure 3.9. *Compositional data from the garnet used for the pressure-temperature estimate. Arrow points to the rim composition used.*

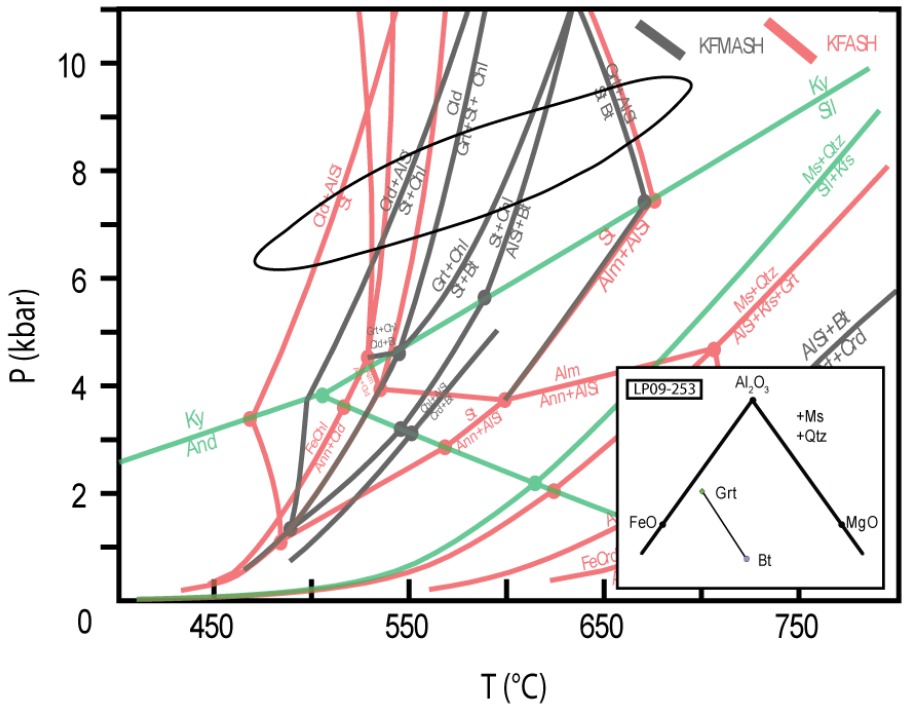

Figure 3.10. *Pressure-temperature estimate overlain on a petrogenetic grid from Holland and Powell (1998). Inset shows AFM diagram of the assemblage projected from muscovite.*

Table 3.2. Compositional Data (in wt. %) for Near-Garnet-Rim Thermobarometric Analyses.

	Garnet near rim	Biotite	Plagioclase	Muscovite
LP09-253		(18)	(21)	(12)
SiO_2	37.16	35.62	65.87	46.35
TiO_2	0.01	1.64	0	0.32
Al_2O_3	21.04	18.35	21.73	34.90
FeO	34.00	19.20	0.11	2.21
MnO	3.21	0.14	0	0.01
MgO	2.72	9.80	0	0.62
CaO	2.21	0.01	2.51	0.01
Na_2O	0.05	0.20	9.54	1.07
K_2O	0	9.14	0.08	9.09
∑	100.40	98.10	99.84	98.58
Si	2.99	5.48	2.89	6.20
Ti	0.00	0.19	0	0.03
Al	2.00	3.33	1.12	5.50
Fe	2.29	2.47	0.00	0.25
Mn	0.22	0.02	0	0.00
Mg	0.33	2.25	0	0.13
Ca	0.19	0.00	0.12	0.00

Table 3.2. Continued.

Na	0.01	0.06	0.81	0.28
K	0	1.80	0.01	1.55
∑	8.03	19.59	4.95	17.94

Note: Numbers in parenthesis represent the number of data points averaged.
Analyses of 0 indicate that the composition was not analyzed.

P-T estimates at peak temperatures were calculated from the chemical data using THERMOCALC v. 3.33 in the average P-T mode (Powell et al., 1998). Calculations were made using the updated Holland & Powell (1998) data set (tc-ds55.txt). Activity coefficients for each phase were calculated using the AX software. No endmembers were excluded. These methods yield 570 ± 105° C and 8.0 ± 1.8 kbar (cor = 0.84 and fit = 0.19) (Fig. 3.10).

Discussion

Evolution of the Leo Pargil Shear Zone

Rocks within the LPSZ in the Sumdo and Chango transects record west-directed shearing from temperatures of 400-500° C to 280-400° C. These rocks are overlain by low-grade (<300° C; Table 3.1) metasedimentary to sedimentary rocks in the hanging wall of the LPSZ that do not record west-directed shearing, rather those in the Sumdo transect record top-to-the-east shearing immediately structurally above the LPSZ (green, Fig. 3.2; Table 3.1). East-directed shearing in these rocks are interpreted as a record of deformation that is not associated with dome formation.

Samples from the central and south domains all record temperatures during west-directed deformation of 500° C to >650° C, deeper structural depths than the rocks exposed in the Chango and Sumdo transects. The rocks in the quartzite/marble unit in the central domain experienced 42 to 11% pure shear during deformation indicating that simple shear dominated but a component of thinning occurred during deformation in this portion of the shear zone. The strain ratio (R_{xz}) can be calculated from this data using the following equation which utilizes the angular relationships between the quartz oblique grain shape fabrics and quartz [c] axis fabrics (e.g., Xypolias, 2009):

$$R_{xz} = \frac{1-\tan\theta*\tan\beta}{\tan^2\beta+ \tan\theta*\tan\beta} \quad (2)$$

where

$$\tan\theta = \cot[2(\beta + \delta)] \quad (3)$$

β is the angle between the flow plane and S_A as measured from the quartz [c] axis fabric and δ is the angle between the quartz oblique fabric (S_B) and the main foliation (S_A) (Fig. 3.7). This equation was applied to samples LP09-191, LP09-222, LP09-24, and LP09-14, all within the quartzite and marble unit (yellow, Fig. 3.2), and yielded R_{xz} values from 5 to 30 (Table 3.1).

The percent down-dip extension and shortening normal to down-dip was calculated from the shortening value (S) using the following equation (Wallis et al., 1993):

$$S = \{0.5(1 - W_m^2)^{0.5}[(R_{xz} + R_{xz}^{-1} + \frac{2(1+W_m^2)}{(1-W_m^2)})^{0.5} + (R_{xz} + R_{xz}^{-1} - 2)^{0.5}]\}^{-1} \quad (4)$$

This yielded 43 to 168% down-dip extension and 30 to 63% shortening normal to extension (Table 3.1). The large range in R_{xz} and S for each sample is attributed to the large range in W_m values from each sample, calculated from the range of θ from the peak of the histogram to the maximum value (Fig. 3.8). The range of R_{xz} and S from sample to sample suggests that strain was partitioned heterogeneously throughout the quartzite/marble unit in this portion of the LPSZ, potentially due to heterogeneities in rheology between the quartzite, marble, and leucogranite lithologies. Some of the quartzite in this section record L-tectonite fabrics associated with constriction rather than plane strain (Fig. 3.3c), further demonstrating the heterogeneous strain distribution in this portion of the shear zone.

Samples from the east domain contain quartz and feldspar textures recording similar deformation temperatures as those recorded in the central and south domains (500° C to >650° C), although textures indicating >650° C are more abundant (Table 3.1). The shear sense transitions from west-directed in the central and southern domains to east-directed in the east domain (Fig. 3.4f; Table 3.1). The high temperatures in the core of the dome, within the east domain, are a record of the deepest structural depths within the dome (>26 km, assuming a geothermal gradient of 25° C/km). The central and south domains are at shallower structural

positions. The similar high temperature in these domains is attributed to thermal influx from injection of leucogranite that followed initiation of deformation (23-18 Ma; Langille et al., in review). The deformation temperatures from within the central and south domains (500° C to >650° C) overlap with metamorphic temperatures for the south domain during decompression (~600° C) related to the onset of exhumation along the LPSZ and subsequent intrusion of leucogranite (Langille et al., in review). This supports decompression concurrently with west-directed deformation on the LPSZ and the onset of leucogranite injection.

The rocks at the uppermost structural positions within the LPSZ in the Chango and Sumdo transects are not intruded by leucogranite, so the temperatures of deformation (400-500° C overprinted by 280-400° C) correspond to the depth where deformation occurred (20-16 km through 16-11 km, assuming 25° C/km). Barrovian metamorphism, that predates initiation of the LPSZ (Barrovian ending at ~30 Ma, LPSZ beginning by 23 Ma; Langille et al., in review), in the Chango transect occurred at ~570° C (Table 3.1) (~23 km depth at peak temperatures). This suggests that rocks in the Chango transect were vertically exhumed from a maximum 23 km depth by deformation on the LPSZ following Barrovian metamorphism, with the rocks recording top-down-to-the-west deformation from 20-11 km depth. The remaining 11 km of vertical exhumation occurred at temperatures of <280° C via processes such as erosion and brittle normal displacement on the Kaurik-Chango normal fault system. Assuming an average dip of 25° for the LPSZ (from the footwall of the Kaurik-Chango normal fault) (Fig. 3.2),~28 km of ductile displacement exhumed these rocks from 23 km to 11 km depth following peak metamorphism. The brittle Kaurik-Chango normal fault system offsets the ductile LPSZ. The angle of these brittle faults and the amount of erosion is unconstrained so the amount of offset via brittle faulting was not calculated. Rocks now exposed in the central and south domains record peak Barrovian metamorphism at ~592° C (24 km depth) and ~630° C (25 km), respectively (Langille et al., in review). Assuming ductile top-down-to-the-west deformation exhumed these rocks from these depths to 11 km (280° C, end of ductile displacement), ~29 km and ~34 km of ductile top-down-to-the-west displacement occurred in the central and southern domains respectively. Peak metamorphic temperatures are not documented for the rocks in the east domain, in the migmatite core of the dome, but top-down-to-the-west deformation occurred at >650° C (>26 km depth) in

these rocks. This suggests that >35 km of ductile displacement exhumed these rocks from >26 km depth to 11 km depth.

Initial depths of >26 km in the migmatitic core, immediately structurally underlying the base of the Haimanta Group, and 23 km depth at the uppermost structural positions of the Haimanta Group in the Sumdo and Chango transects suggests that the Haimanta Group now exposed in the LPD was initially >3 km thick. R_{xz} data suggest that 30 to 63% shortening parallel to down-dip extension occurred in the quartzite/marble unit within the LPSZ. Assuming that the rocks within the LPSZ outside of the quartzite/marble unit experienced similar strain ratios, the rocks within the dome were thinned from an initial thickness of >3 km to between >2.1 km (30% shortening) and >1.1 km (63% shortening).

Implications for Orogen-Parallel Extension and the Tectonics in the Western Himalaya

Kapp and Guynn (2004) show that most of the normal faults throughout the Himalaya and Tibetan Plateau are oriented in a radial pattern fanning from a northwest strike to a northeast strike from west to east (Fig. 3.1a). The axis of symmetry bisects the Himalayan arc at the southernmost arc of the Himalaya, subparallel to the present day convergence vector. Elastic modeling shows that collisional stresses localized along the southern part of the Himalayan arc can result in the orientation of normal faults observed and continued insertion of Indian crust into Tibet allows persistent extension and elevation increase of the Tibetan Plateau (Kapp and Guynn, 2004). This model predicts the northwest to northeast radial orientation of normal faults and graben from west to east across the Himalaya and Tibetan Plateau. However, a second set of normal faults exist southwest of the Karakoram fault that are oriented perpendicular to the Himalayan front (e.g., faults bounding the Leo Pargil domes). This model does not explain the role of strike-slip faults and this second set of normal faults. This could suggest that a different process controls strike-slip fault development and normal faults southwest of the Karakoram fault, such as the LPSZ.

Hintersberger et al. (2010) suggests that the Tibetan Plateau north of the Karakoram fault has an modern eastward extension direction that results in east-west extension accommodated along active north-south oriented brittle normal faults in the northwest Indian Himalaya, including faults that bound the west flank of the LPD. This suggests that modern displacement is

transferred to the south from the Tibetan Plateau, across the Karakoram fault system. This interpretation assumes the Karakoram fault only accommodates a small portion of modern displacement transferred from the Tibetan Plateau. Geodetic slip-rates support that the southern portion of the Karakoram fault has a low modern slip-rate, <1 cm/yr on the Indus-Yarlung suture at the southernmost end of the Karakoram (Styron et al., 2011) but the long-term and modern rates for the northern portion of the Karakoram are ~10 mm/yr (e.g., Banerjee and Bürgmann, 2002; Lacassin et al., 2004; Phillips et al., 2004; Chevalier et al., 2005), suggesting that the northern portion of the fault has and still does accommodate deformation. This model does not explain the northeast trend of the LPD, initiation of the LPSZ at >23 Ma, or the variation in ages and slip-rates along the Karakoram fault in the western Himalaya.

Data presented here combined with age constraints for the LPSZ from Langille et al. (in review) suggest that top-down-to-the-west displacement on the LPSZ began at >23 Ma at depths of >26 km in the crust. Soon after, these rocks were ductiley exhumed ~28-35 km along the LPSZ. Based on these data along with existing age constraints for the Karakoram fault (Fig. 3.1a), three working models for extension in the western Himalaya can be proposed (Kapp and Guynn, 2004; Hintersberger et al., 2010).

Model 1: The western initiation of the Karakoram fault occurred at >23 Ma (overlapping with older initiation ages for the Karakoram fault; e.g., Lacassin et al., 2004). By 23 Ma, the Karakoram fault had propagated south and terminated at the present day intersection location with the LPD. This termination induced a northwest-southeast extensional pull-apart regime in which the northeast oriented LPSZ initiated by 23 Ma (Fig. 3.11a). This occurred during a time of active deformation on the STDS and MCTZ to the south. This was followed by southward propagation of the Karakoram fault (Murphy et al., 2000) which extended this stress regime to the southeast, initiating the development of the Gurla Mandhata detachment at its termination at ~11 Ma (Murphy et al., 2000) (Fig. 3.11a), in a similar manner to the LPD. Apatite fission track data from the LPD show a drop in exhumation rates at 10 Ma, when brittle faulting began on the north-south oriented normal faults on the southwest flank of the LPD (Thiede et al., 2006). Hintersberger et al. (2010) suggests that the modern day slip-rate on the Karakoram fault is low so the extensional stress regime resulting in the north-south oriented normal faults is dominated by eastward extension transferred from the Tibetan Plateau, suggesting that the slip-rate on the

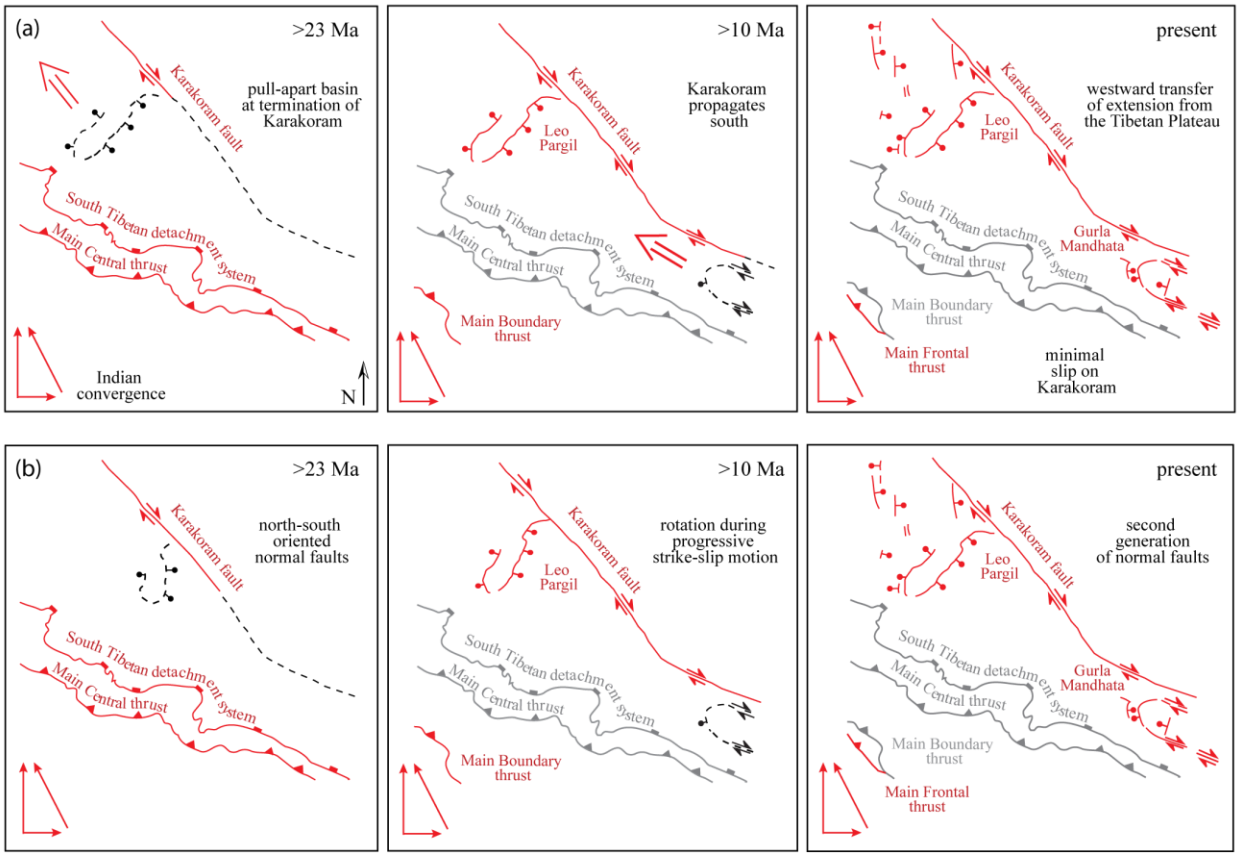

Figure 3.11. *Schematic diagrams depicting two models for the temporal evolution of the western Himalaya. Dashed black lines represent incipient faults, red are active faults, and grey are inactive faults. See text for discussion.*

Karakoram fault here would have decreased by ~10 Ma. This resulted in the formation of north trending brittle faults in the western Himalaya, including those on the southwest flank of the LPD (Fig. 3.11) (Kapp and Guynn, 2004; Hintersberger et al., 2010).

This model predicts that: (1) the LPSZ records northwest-directed extension by 23 Ma, (2) it predates initiation of the Gurla Mandhata detachment (11 Ma), (3) both the LPSZ and Gurla Mandhata predate initiation of the north-south oriented normal faults, (4) slip on the Karakoram fault in this region would be active between 23 and 11 Ma and would essentially cease by ~10 Ma, (5) slip-rates on the Karakoram fault between 23 and 11 Ma would decrease to the south as slip was transferred to the faults bounding the LPSZ and Gurla Mandhata, and (6) displacement on the north-south oriented brittle structures is transferred from north of the Karakoram fault.

Model 2: This model builds off the previous model where the Karakoram fault propagates southward, but invokes rotation of normal faults during dextral displacement on the Karakoram (Fig. 3.11b). At 23 Ma, the southern termination of the Karakoram fault was located somewhere between the LPD and the Gurla Mandhata. The LPSZ initiated at 45° to the Karakoram fault (north-south oriented) during dextral movement at ~23 Ma. With progressive dextral displacement, the LPSZ was rotated toward the northeast and younger normal-faults developed at 45° to the Karakoram fault (the north-south oriented faults). These younger faults have yet to be rotated with progressive dextral-displacement on the Karakoram.

Predictions for this model include: (1) the LPSZ would initially record west-directed shear sense beginning at 23 Ma that was later rotated to top-down-to-the-northwest, assuming no ductile overprinting occurred, (2) the LPD would record a larger degree of rotation than the younger Gurla Mandhata dome (11 Ma), (3) the youngest faults would be north-south oriented, and (4) the amount of total displacement and slip-rates on the Karakoram fault would decrease to the south as slip is transferred to the normal faults.

Model 3: A third model for the kinematics in the western Himalaya is that the Karakoram fault was not the kinematic driver for the initial onset of west-directed shearing along the LPSZ. In this model, the onset of west-directed extension in this portion of the Himalaya may have begun prior to initiation of the Karakoram fault and was initially decoupled from strike-slip faulting. In this model, the LPSZ initiated perpendicular to the orogenic front (northeast-trending). Initiation of the LPSZ was followed by initiation of the Karakoram fault (overlapping with younger ages for initiation of the Karakoram fault; e.g., Phillips et al., 2004; Searle et al., 2007). Approximately north-south oriented normal faults develop either due to transfer of slip from the Karakoram fault or slip is transferred across the Karakoram from within the Tibetan Plateau. In this model the northeast oriented LPSZ would initiate during northwest directed shearing parallel to the orogenic front.

Kinematics on the western flank of the dome, where the shear zone is oriented northeast is unconstrained. On the southwest flank where the shear zone changes strike, the LPSZ records dominantly top-down-to-the-west shear (Fig. 3.2). If the dome rotated according to model 2, the southern flank would have initially recorded top-down-to-the-southwest shear sense. Because of the lack of data to the north within the shear zone, the degree of rotation of the LPD relative to

the Gurla Mandhata dome cannot be addressed. The shear sense orientation for the southwest portion of the dome does not distinguish between any of the models.

Geodetic slip-rates for the northwest Himalaya suggest a modern slip-rate of ~10 mm/yr on the Karakoram (Banerjee and Bürgmann, 2002; Chevalier et al., 2005). The Holocene slip-rate determined from offset Quaternary glacial landforms along the Karakoram fault in the Ladakh region in India is ~4 mm/yr (Brown et al., 2002). This rate may be lower because here the Karakoram fault splays into several strands and this rate may not accommodate the entire slip history along the fault. Geodetic slip-rates on the Indus-Yarlung suture, at the southernmost end of the Karakoram suggest a modern rate of <1 cm/yr (Styron et al., 2011). This suggests that while dextral displacement southeast of the Gurla Mandhata is low, the Karakoram fault is still actively transferring displacement and the slip-rate decreases to the south The decrease in slip-rates toward the south could be due to transfer of slip to normal faults. These indicate that the Karakoram is actively accommodating displacement from within the Tibetan Plateau, in contrast to model 1. Data from this study suggests that ~28-35 km of ductile down-dip displacement occurred on the LPSZ. An average dip of 25° for the shear zone implies 25-32 km of horizontal displacement occurred. Murphy et al. (2002) document 66 to 35 km of down-dip displacement on the 22° dipping Gurla Mandhata detachment, suggesting 61 to 33 km of horizontal displacement. If all of this displacement was transferred from the Karakoram fault system, this suggests a minimum total horizontal slip of 93 to 86 km on the Karakoram fault. This estimate does not factor in exhumation on the east side of the LPD, brittle exhumation of the southwest flank of the LPD, or east-west extension to the northwest of the dome which are all unconstrained. However, it does suggest that the amount of extension on these normal faults may be compatible with total displacement estimates calculated from the offset of the Indus River, Baltoro granites, and Aghil formation (120-167 km; Lacassin et al., 2004; Phillips et al., 2004; Searle and Phillips, 2007; Robinson, 2009)–compatible with models that the LPSZ initiated by transfer of displacement from the Karakoram fault.

Conclusions

Data from the shear zone on the southwest flank of the LPD suggests that the rocks now exposed in the dome were thinned by up to 63% and exhumed from depths of up to >26 km by ~28-35 km of ductile displacement on the LPSZ. The LPSZ developed as a widely-distributed zone that penetrated most of the Haimanta Group and potentially the upper portion of the GHS. Our data incorporated with other data from this portion of the Himalaya suggests that extensional exhumation in the western Himalaya on north to northeast oriented normal faults (including those that bound the Leo Pargil and Gurla Mandhata domes), southwest of the Karakoram fault system, may have been controlled by southward propagation of the dextral Karakoram fault system that initiated at >23 Ma. Assuming that slip is transferred from the Karakoram fault system to the northeast and north-trending normal faults, displacement estimates from the Leo Pargil shear zone and Gurla Mandhata detachment suggest a minimum of 93 to 86 km of slip on the Karakoram fault system.

References

Armijo, R., Tapponnier, P., Mercier, J. L., and Han, T.L., 1986, Quaternary extension in southern Tibet: Field observations and tectonic implications: Journal of Geophysical Research, v. 91, p. 13803-13872.

Banerjee, P., and Bürgmann, R., 2002, Convergence across the northwest Himalaya from GPS measurements: Geophysical Research Letters, v. 29, p. 30-34.

Bettinelli, P., Avouac, J.-P., Flouzat, M., Jouanne, F., Bollinger, L., Willis, P., and Chitrakar, G., 2006, Plate Motion of India and Interseismic Strain in the Nepal Himalaya from GPS and DORIS Measurements: Journal of Geodesy, v. 80, no. 8, p. 567-589.

Bilham, R., Larson, K. M., Freymueller, J. T., Jouanne, F., Le Fort, P., Leturmy, P., Mugnier, J. L., Gamond, J. F., Glot, J. P., Martinod, J., Chaudury, N. L., Chitrakar, G. R., Gautam, U. P., Koirala, B. P., Pandey, M. R., Ranabhat, R., Sapkota, S. N., Shrestha, P. L., Thakuri, M. C., Timilsina, U. R., Tiwari, D. R., Vidal, G., Vigny, C., Galy, A., and de Voogd, B., 1997, GPS measurements of present-day convergence across the Nepal Himalaya: Nature, v. 386, p. 61-64.

Blisniuk, P. M., Hacker, B. R., Glodny, J., Ratschbacher, L., Bi, S., Wu, Z., McWilliams, M. O., and Calvert, A., 2001, Normal faulting in central Tibet since at least 13.5 Myr ago: Nature, v. 412, no. 6847, p. 628-632.

Brown, E. T., Bendick, R., Bourlès, D. L., Gaur, V., Molnar, P., Raisbeck, G. M., and Yiou, F., 2002, Slip-rates of the Karakorum fault, Ladakh, India, determined using cosmic ray exposure dating of debris flows and moraines: Journal of Geophysical Research, v. 107, no. B9, p. 2192.

Chambers, J. A., Caddick, M., Argles, T. W., Horstwood, M. S. A., Sherlock, S., Harris, N. B. W., Parrish, R. R., and Ahmad, T., 2009, Empirical constraints on extrusion mechanisms from the upper margin of an exhumed high-grade orogenic core, Sutlej valley, NW India: Tectonophysics, v. 477, p. 77-92.

Chevalier, M. L., Ryerson, F. J., Tapponier, P., Finkel, R. C., Van Der Woerd, J., Haibing, L., and Qing, L., 2005, Slip-rate measurements on the Karakoram fault may imply secular variations in fault motion: Science, v., 307, p. 411-414.

Coleman, M., and Hodges, K. V., 1995, Evidence for Tibetan Plateau uplift before 14 Myr ago from a new minimum age for east-west extension: Nature, v. 374, no. 6517, p. 49-52.

de Sigoyer, J., Guillot, S., and Dick, P., 2004, Exhumation of the ultrahigh-pressure Tso Morari unit in eastern Ladakh (NW Himalaya): A case study: Tectonics, v. 23, no. 3, p. TC3003-TC3003.

Ferrill, D. A., Morris, A. P., Evans, M. A., Burkhard, M., Groshong Jr, R. H., and Onasch, C. M., 2004, Calcite twin morphology: a low-temperature deformation geothermometer: Journal of Structural Geology, v. 26, no. 8, p. 1521-1529.

Fitz Gerald, J., and Stünitz, H., 1993, Deformation of granitoids at low metamorphic grades. I: Reactions and grain size reduction: Tectonophysics, v. 221, p. 269-297.

Fossen, H., and Tikoff, B., 1997, Forward modeling of non-steady state deformations and the 'minimum strain path': Journal of Structural Geology, v. 19, p. 987-996.

Fossen, H., and Tikoff, B., 1998, Forward modeling of non-steady-state deformations and the 'minimum strain path': Reply: Journal of Structural Geology, v. 20, p. 979-981.

Frank, W., Grasemann, B., Guntli, P., and Miller, C., 1995, Geological map of the Kishtwar-Chambu-Kulu region (NW Himalayas, India): Jahrbuch der Geologischen Bundesanstalt, v. 138, p. 299-308.
Grasemann, B., Fritz, H., and Vannay, J. C., 1999, Quantitative kinematic flow analysis from the Main Central Thrust Zone (NW-Himalaya, India): implications for a decelerating strain path and the extrusion of orogenic wedges: Journal of Structural Geology, v. 21, no. 7, p. 837-853.
Grujic, D., Casey, M., Davidson, C., Hollister, L. S., Kundig, R., Pavlis, T., and Schmid, S., 1996, Ductile extrusion of the Higher Himalayan Crystalline in Bhutan: Evidence from quartz microfabrics: Tectonophysics, v. 260, no. 1-3, p. 21-43.
Grujic, D., Hollister, L. S., and Parrish, R. R., 2002, Himalayan metamorphic sequence as an orogenic channel: insight from Bhutan: Earth and Planetary Science Letters, v. 198, no. 1-2, p. 177-191.
Harrison, T. M., Copeland, P., Kidd, W. S. F., and Lovera, O. M., 1995, Activation of the Nyainqentanghla Shear Zone: Implications for uplift of the southern Tibetan Plateau: Tectonics, v. 14, no. 3, p. 658-676.
Hintersberger, E., Thiede, R. C., and Strecker, M. R., 2011, The role of extension during brittle deformation within the NW Indian Himalaya: Tectonics, v. 30, no. 3, p. TC3012.
Hintersberger, E., Thiede, R. C., Strecker, M. R., and Hacker, B. R., 2010, East-west extension in the NW Indian Himalaya: Geological Society of America Bulletin, v. 122, no. 9-10, p. 1499-1515.
Hirth, G., and Tullis, J., 1992, Dislocation creep regimes in quartz aggregates: Journal of Structural Geology, v. 14, no. 2, p. 145-159.
Holland, T. J. B., and Powell, R., 1998, An internally consistent thermodynamic data set for phases of petrological interest: Journal of Metamorphic Geology, v. 16, no. 3, p. 309-343.
Jessup, M., Langille, J., and Ahmad, T., in prep, Crustal anisotropies and strain localization during exhumation of mid-crustal rocks in convergent orogens: insights from the Himalaya, NW India: Geological Society [London].
Jessup, M. J., and Cottle, J. M., 2010, Progression from South-Directed Extrusion to Orogen-Parallel Extension in the Southern Margin of the Tibetan Plateau, Mount Everest Region, Tibet: Journal of Geology, v. 118, no. 5, p. 467-486.
Jessup, M. J., Law, R. D., Searle, M. P., and Hubbard, M. S., 2006, Structural evolution and vorticity of flow during extrusion and exhumation of the Greater Himalayan Slab, Mount Everest Massif, Tibet/ Nepal; implications for orogen-scale flow partitioning, *in* Law, R. D., Searle, M. P., and Godin, L., eds., Channel flow, ductile extrusion and exhumation in continental collision zones: Geological Society [London] Special Publications, v. 268, p. 379-413.
Jiang, D., 1998, Forward modeling of non-steady-state deformations and the 'minimum strain path': Discussion: Journal of Structural Geology, v. 20, p. 975-977.
Jouanne, F., Mugnier, J. L., Gamond, J. F., Fort, P. L., Pandey, M. R., Bollinger, L., Flouzat, M., and Avouac, J. P., 2004, Current shortening across the Himalayas of Nepal: Geophysical Journal International, v. 157, no. 1, p. 1-14.
Kali, E., Leloup, P. H., Arnaud, N., Mahéo, G., Liu, D., Boutonnet, E., Van der Woerd, J., Liu, X., Liu-Zeng, J., and Li, H., 2010, Exhumation history of the deepest central Himalayan

rocks, Ama Drime range: Key pressure-temperature-deformation-time constraints on orogenic models: Tectonics, v. 29, no. 2, p. TC2014.
Kapp, P., and Guynn, J. H., 2004, Indian punch rifts Tibet: Geology, v. 32, no. 11, p. 993-996.
Kellett, D. A., Grujic, D., and Erdmann, S., 2009, Miocene structural reorganization of the South Tibetan detachment, eastern Himalaya: Implications for continental collision: Lithosphere, v. 1, no. 5, p. 259-281.
Kohn, M. J., and Spear, F., 2000, Retrograde net transfer reaction insurance for pressure-temperature estimates: Geology, v. 28, p. 1127-1130.
Kruhl, J. H., 1998, Reply: Prism- and basal-plane parallel subgrain boundaries in quartz: a microstructural geothermometer: Journal of Metamorphic Geology, v. 16, p. 142-146.
Lacassin, R., Valli, F., Arnaud, N., Leloup, P. H., Paquette, J. L., Haibing, L., Tapponnier, P., Chevalier, M. L., Guillot, S., Maheo, G., and Xu, Z. Q., 2004, Large-scale geometry, offset and kinematic evolution of the Karakorum fault, Tibet: Earth and Planetary Science Letters, v. 219, p. 255-269.
Langille, J., Jessup, M., Cottle, J., Lederer, G., and Ahmad, T., in review, Timing of metamorphism, melting, and exhumation of the Leo Pargil dome, northwest India: Journal of Metamorphic Geology.
Langille, J., Jessup, M., Cottle, J., Newell, D., and Seward, G., 2010a, Kinematics of the Ama Drime Detachment: Insights into orogen-parallel extension and exhumation of the Ama Drime Massif, Tibet-Nepal: Journal of Structural Geology, v. 32, p. 900-919.
Langille, J., Lee, J., Hacker, B., and Seward, G., 2010b, Middle crustal ductile deformation patterns in southern Tibet: insights from vorticity studies in Mabja Dome: Journal of Structural Geology, v. 32, p. 70-85.
Lavé, J., and Avouac, J. P., 2000, Active folding of fluvial terraces across the Siwaliks Hills, Himalayas of central Nepal: Journal of Geophysical Research, v. 105, no. B3, p. 5735-5770.
Law, R. D., 1990, Crystallographic fabrics: a selective review of their applications to research in structural geology: Geological Society [London] Special Publications, v. 54, no. 1, p. 335-352.
Law, R. D., Morgan, S. S., Casey, M., Sylvester, C. M., and Nyman, M., 1992, The Papoose Flat pluton of eastern California: a re-assesment of its emplacement history in the light of new microstructural and crystallographic fabric observations: Transactions of the Royal Society of Edinburgh: Earth Sciences, v. 83, p. 361-375.
Law, R. D., Searle, M. P., and Simpson, R. L., 2004, Strain, deformation temperatures and vorticity of flow at the top of the Greater Himalayan Slab, Everest Massif, Tibet: Journal of the Geological Society, v. 161, p. 305-320.
Lee, J., Hager, C., Wallis, S. R., Stockli, D. F., Whitehouse, M. J., Aoya, M., and Wang, Y., 2011, Middle to late Miocene extremely rapid exhumation and thermal reequilibration in the Kung Co rift, southern Tibet: Tectonics, v. 30, no. 2, p. TC2007.
Leloup, P., Boutonnet, E., Davis, W., and Hattori, K., 2011, Long-lasting intracontinental strike-slip faulting: new evidence from the Karakoram shear zone in the Himalayas: Terra Nova, v. 23, p. 92-99.
Lister, G. S., and Dornsiepen, U. F., 1982, Fabric transitions in the Saxony granulite terrain: Journal of Structural Geology, v. 4, no. 1, p. 81-92.

Lister, G. S., and Hobbs, B. E., 1980, The similation of fabric development during plastic deformation and its application to quartzite: the influence of deformation history: Journal of Structural Geology, v. 2, no. 355-370, p. 355.
Lister, G. S., Paterson, M. S., and Hobbs, B. E., 1978, The simulation of fabric development in plastic deformation and its application to quartzite: The model: Tectonophysics, v. 45, p. 107-158.
Mainprice, D., Bouchez, J.L., Blumenfeld, P., and Tubia, J. M., 1986, Dominant c slip in naturally deformed quartz: Implications for dramatic plastic softening at high temperature: Geology, v. 14, no. 10, p. 819-822.
McCaffrey, R., and Nabelek, J., 1998, Role of oblique convergence in the active deformation of the Himalayas and southern Tibet plateau: Geology, v. 26, no. 8, p. 691-694.
Mercier, J.L., Armijo, R., Tapponnier, P., Carey-Gailhardis, E., and Lin, H. T., 1987, Change from Late Tertiary compression to Quaternary extension in southern Tibet during the India-Asia Collision: Tectonics, v. 6, no. 3, p. 275-304.
Miller, C., Thoni, M., Frank, W., Grasemann, B., Klotzli, U., Guntli, P., and Draganits, E., 2001, The early Palaeozoic magmatic event in the Northwest Himalaya, India: source, tectonic setting and age of emplacement: Geological Magazine, v. 138, no. 3, p. 237-251.
Mitsuishi, M., Wallis, S., Aoya, M., Lee, J., and Wang, Y., 2012, E-W extension at 19 Ma in the Kung Co area, S. Tibet: Evidence for contemporaneous E-W and N-S extension in the Himalayan orogen: Earth and Planetary Science Letters, v. 325-326, p. 10-20.
Molnar, P., and Tapponnier, P., 1975, Cenozoic Tectonics of Asia: Effects of a Continental Collision: Science, v. 189, no. 4201, p. 419-426.
Murphy, M. A., Saylor, J. E., and Ding, L., 2009, Late Miocene topographic inversion in southwest Tibet based on integrated paleoelevation reconstructions and structural history: Earth and Planetary Science Letters, v. 282, p. 1-9.
Murphy, M. A., Yin, A., Kapp, P., Harrison, T. M., Lin, D., and Jinghui, G., 2000, Southward propagation of the Karakoram fault system, southwest Tibet: Timing and magnitude of slip: Geology, v. 28, no. 5, p. 451-454.
Murphy, M. A., Yin, A., Kapp, P., Harrison, T. M., Manning, C. E., Ryerson, F. J., Lin, D., and Jinghui, G., 2002, Structural evolution of the Gurla Mandhata detachment system, Southwest Tibet; implications for the eastward extent of the Karakoram fault system: Geological Society of America Bulletin, v. 114, no. 4, p. 428-447.
Najman, Y., Appel, E., Boudagher-Fadel, M., Bown, P., Carter, A., Garzanti, E., Godin, L., Han, J., Liebke, U., Oliver, G., Parrish, R., and Vezzoli, G., 2010, Timing of India-Asia collision: Geological, biostratigraphic, and palaeomagnetic constraints: Journal of Geophysical Research, v. 115, no. B12, p. B12416.
Nelson, K. D., Zhao, W., Brown, L. D., Kuo, J., Che, J., Liu, X., Klemperer, S. L., Makovsky, Y., Meissner, R., Mechie, J., Kind, R., Wenzel, F., Ni, J., Nabelek, J., Chen, L., Tan, H., Wei, W., Jones, A. G., Booker, J., Unsworth, B., Kidd, W. S. F., Hauck, M., Alsdorf, D., Ross, A., Cogan, M., Wu, C., Sandvol, E. A., and Edwards, M. A., 1996, Partially molten middle crust beneath southern Tibet; synthesis of Project INDEPTH results: Science, v. 274, no. 5293, p. 1684-1688.
Ni, J., and Barazangi, M., 1985, Active tectonics of the western Tethyan Himalaya above the underthrusting Indian Plate; the upper Sutlej River basin as a pull-apart structure, *in*

Kobayashi, Kazuo; Sacks, I Selwyn, eds., Structures and processes in subduction zones: Tectonophysics, v. 112, no. 1-4, p. 277-295.
Nyman, M. W., Law, R. D., and Morgan, S. S., 1995, Conditions of contact metamorphism, Papoose Flat Pluton, eastern California, USA: implications for cooling and strain histories: Journal of Metamorphic Geology, v. 13, p. 627-643.
Okudaira, T., Takeshita, T., Hara, I., and Ando, J., 1995, A new estimate of the conditions for transition from basal <a> to prism [c] slip in naturally deformed quartz: Tectonophysics, v. 250, no. 1-3, p. 31-46.
Passchier, C. W., and Trouw, R. J., 2005, Microtectonics: Berlin, Springer.
Phillips, R.J., Parrish, R.P., and Searle, M.P., 2004, Age constraints on ductile deformation and long-term slip-rates along the Karakoram fault zone, Ladakh: Earth and Planetary Science Letters, v. 226, p. 305-319.
Powell, R., Holland, T., and Worley, B., 1998, Calculating phase diagrams involving solid solutions via non-linear equations, with examples using THERMOCALC: Journal of Metamorphic Geology, v. 16, no. 4, p. 577-588.
Pryer, L. L., 1993, Microstructures in feldspars from a major crustal thrust zone: The Grenville Front, Ontario, Canada: Journal of Structural Geology, v. 15, no. 1, p. 21-36.
Ratschbacher, A., Frisch, W., Liu, G., and Chen, C., 1994, Distributed deformation in southern and western Tibet during and after the India-Asia collision: Washington, DC, ETATS-UNIS, American Geophysical Union.
Robinson, A. C., 2009, Geologic offsets across the northern Karakoram fault: Implications for its role and terrane correlations in the western Himalayan-Tibetan orogen: Earth and Planetary Science Letters, v. 279, p. 123-130.
Robinson, A. C., Yin, A., Manning, C. E., Harrison, T. M., Zhang, S.H., and Wang, X.F., 2007, Cenozoic evolution of the eastern Pamir: Implications for strain-accommodation mechanisms at the western end of the Himalayan-Tibetan orogen: Geological Society of America Bulletin, v. 119, no. 7-8, p. 882-896.
Sanchez, V. I., Murphy, M. A., Dupré, W. R., Ding, L., and Zhang, R., 2010, Structural evolution of the Neogene Gar Basin, western Tibet: Implications for releasing bend development and drainage patterns: Geological Society of America Bulletin, v. 122, p. 926-945.
Saylor, J., DeCelles, P., Gehrels, G., Murphy, M., Zhang, R., and Kapp, P., 2010, Basin formation in the High Himalaya by arc-parallel extension and tectonic damming: Zhada basin, southwestern Tibet: Tectonics, v. 29, no. 1, p. TC1004.
Searle, M. P., Law, R. D., and Jessup, M. J., 2006, Crustal structure, restoration and evolution of the Greater Himalaya in Nepal-South Tibet; implications for channel flow and ductile extrusion of the middle crust, *in* Law, R. D., Searle, M. P., and Godin, L., eds., Channel flow, ductile extrusion and exhumation in continental collision zones: Geological Society [London] Special Publications, v. 268, p. 355-378.
Searle, M. P., and Phillips, R.J., 2007, Relationships between right-lateral shear along the Karakoram fault and metamorphism, magmatism, exhumation and uplift: evidence from the K2-Gasherbrum-Pangong ranges, north Pakistan and Ladakh: Journal of Geological Society [London], v. 164, p. 439-450.

Searle, M.P., Weinberg, R.F., and Dunlap, W.J., 1998, Transpressional tectonics along the Karakoram fault zone, northern Ladakh: constraints on Tibetan extrusion: Geological Society [London] Special Publications, v. 135, p. 307-326.

Searle, M. P., Windley, B. F., Coward, M. P., Cooper, D. J. W., Rex, A. J., Rex, D., Tingdong, L., Xuchang, X., Jan, M. Q., Thakur, V. C., and Kumar, S., 1987, The closing of Tethys and the tectonics of the Himalaya: Geological Society of America Bulletin, v. 98, p. 678-701.

Stipp, M., Stunitz, H., Heilbronner, R., and Schmid, S., 2002a, Dynamic recrystallization of quartz: correlation between natural and experimental conditions, *in* De Meer, S., Drury, M. R., De Bresser, J. H. P., and Pennock, G. M., eds., Deformation Mechanisms, Rheology and Tectonics: Current Status and Future Perspectives: Geological Society [London] Special Publications, v. 200, p. 171-190.

Stipp, M., Stünitz, H., Heilbronner, R., and Schmid, S. M., 2002b, The eastern Tonale fault zone: a 'natural laboratory' for crystal plastic deformation of quartz over a temperature range from 250 to 700 °C: Journal of Structural Geology, v. 24, no. 12, p. 1861-1884.

Styron, R. H., Taylor, M. H., and Murphy, M. A., 2011, Oblique convergence, arc-parallel extension, and the role of strike-slip faulting in the High Himalaya: Geosphere, v. 7, no. 2, p. 582-596.

Tapponnier, P., Peltzer, G., Le Dain, A. Y., Armijo, R., and Cobbold, P., 1982, Propagating extrusion tectonics in Asia: New insights from simple experiments with plasticine: Geology, v. 10, no. 12, p. 611-616.

Taylor, M., and Yin, A., 2009, Active structures of the Himalayan-Tibetan orogen and their relationships to earthquake distribution, contemporary strain field, and Cenozoic volcanism: Geosphere, v. 5, no. 3, p. 199-214.

Taylor, M., Yin, A., Ryerson, F., Kapp, P., and Ding, L., 2003, Conjugate strike slip faulting along the Bangong-Nujiang suture zone accommodates coeval east-west extension and north-south shortening in the interior of the Tibetan Plateau: Tectonics, v. 22, doi:10.1029/2002TC001361.

Thiede, R. C., Arrowsmith, J. R., Bookhagen, B., McWilliams, M., Sobel, E. R., and Strecker, M. R., 2006, Dome formation and extension in the Tethyan Himalaya, Leo Pargil, northwest India: Geological Society of America Bulletin, v. 118, p. 635-650.

Tikoff, B., and Fossen, H., 1995, The limitations of three-dimensional kinematic vorticity analysis: Journal of Structural Geology, v. 17, no. 12, p. 1771-1784.

Tullis, J., Christie, J. M., and Griggs, D. T., 1973, Microstructures and Preferred Orientations of Experimentally Deformed Quartzites: Geological Society of America Bulletin, v. 84, no. 1, p. 297-314.

Tullis, J., and Yund, R. A., 1991, Diffusion creep in feldspar aggregates: experimental evidence: Journal of Structural Geology, v. 13, no. 9, p. 987-1000.

Valli, F., Arnaud, N., Leloup, P. H., Sobel, E. R., Mahéo, G., Lacassin, R., Guillot, S., Li, H., Tapponnier, P., and Xu, Z., 2007, Twenty million years of continuous deformation along the Karakorum fault, western Tibet: A thermochronological analysis: Tectonics, v. 26, no. 4, p. TC4004.

Vannay, J. C., and Grasemann, B., 2001, Himalayan inverted metamorphism and syn-convergence extension as a consequence of a general shear extrusion: Geological Magazine, v. 138, no. 3, p. 253-276.
Vannay, J. C., Grasemann, B., Rahn, M., Frank, W., Carter, A., Baudraz, V., and Cosca, M., 2004, Miocene to Holocene exhumation of metamorphic crustal wedges in the NW Himalaya: Evidence for tectonic extrusion coupled to fluvial erosion: Tectonics, v. 23, no. 1, p. TC1014-TC1014.
Wallis, S. R., 1995, Vorticity analysis and recognition of ductile extension in the Sanbagawa belt, SW Japan: Journal of Structural Geology, v. 17, p. 1077-1093.
Wallis, S. R., Platt, J. P., and Knott, S. D., 1993, Recognition of syn-convergence extension in accretionary wedges with examples from the Calabrian Arc and the Eastern Alps: American Journal of Science, v. 293, p. 463-495.
Weber, J. C., Ferrill, D. A., and Roden-Tice, M. K., 2001, Calcite and quartz microstructural geothermometry of low-grade metasedimentary rocks, Northern Range, Trinidad: Journal of Structural Geology, v. 23, no. 1, p. 93-112.
Wenk, H. R., Canova, G., Molinari, A., and Kocks, U. F., 1989, Viscoplastic Modeling of Texture Development in Quartzite: Journal of Geophysical Research, v. 94, no. B12, p. 17895-17906.
Wesnousky, S. G., Kumar, S., Mohindra, R., and Thakur, V. C., 1999, Uplift and convergence along the Himalayan Frontal Thrust of India: Tectonics, v. 18, no. 6, p. 967-976.
Wiesmayr, G., and Grasemann, B., 2002, Eohimalayan fold and thrust belt: Implications for the geodynamic evolution of the NW-Himalaya (India): Tectonics, v. 21, no. 6, p. 1058-1058.
Xypolias, P., 2009, Some new aspects of kinematic vorticity analysis in naturally deformed quartzites: Journal of Structural Geology, v. 31, no. 1, p. 3-10.
Xypolias, P., 2010, Vorticity analysis in shear zones: A review of methods and applications: Journal of Structural Geology, v. 32, no. 12, p. 2072-2092.
Xypolias, P., and Koukouvelas, I. K., 2001, Kinematic vorticity and strain patterns associated with ductile extrusion in the Chelmos shear zone (External Hellenides, Greece): Tectonophysics, v. 338, p. 59-77.
Zhang, J., Ding, L., Zhong, D., and Zhou, Y., 2000, Orogen-parallel extension in Himalaya: Is it the indicator of collapse or the product in process of compressive uplift?: Chinese Science Bulletin, v. 45, no. 2, p. 114-120.

Appendix 3.1

Appendix 3.1. Sample Locations.

Sample	Latitude	Longitude	Sample	Latitude	Longitude
LP09-274	32.0683°	78.5932°	LP09-191	31.8735°	78.6303°
LP09-270	32.0675°	78.5974°	LP09-222	31.8943°	78.6013°
LP09-267	32.0649°	78.6029°	LP09-24	31.8741°	78.6024°
LP11-08	32.0207°	78.5852°	LP09-21	31.8634°	78.5980°
LP09-264	32.0600°	78.6058°	LP09-18	31.8622°	78.6062°
LP11-01	32.0505°	78.6034°	LP09-14	31.8736°	78.6043°
LP11-07	32.0380°	78.5943°	LP09-76	31.9462°	78.6023°
LP11-05	32.0434°	78.5965°	LP09-229	31.9349°	78.6027°
LP11-06	32.0417°	78.5932°	LP09-79	31.9772°	78.6220°
LP09-113	31.9954°	78.5761°	LP09-263	31.9587°	78.6298°
LP09-91	31.9950°	78.5740°	LP09-140	31.8495°	78.6019°
LP09-94	31.9930°	78.5753°	LP09-175	31.8337°	78.6322°
LP09-102	31.9844°	78.5928°	LP09-159	31.8069°	78.6332°
LP09-98	31.9909°	78.5809°	LP09-161	31.8069°	78.6332°
LP09-253	31.9650°	78.5924°	LP09-177	31.8432°	78.6829°
LP09-250	31.9610°	78.5946°	LP09-178	31.8432°	78.6829°
LP09-246	31.9582°	78.6018°	LP09-187	31.8432°	78.6830°

CONCLUSION

East-west directed extension on normal faults and shear zones occur across the Himalayan front and the Tibetan Plateau, including the faults that bound the Ama Drime Massif and Leo Pargil dome. Field mapping and sample collection combined with kinematic, microstructural, thermobarometric, and geochronologic methods on samples from the Ama Drime detachment and Leo Pargil shear zone constrain the metamorphic conditions recorded in the samples, the kinematics of deformation during shearing, the amount of exhumation, and the timing of metamorphism and shear zone initiation. These data demonstrate the extension on these normal-sense shear zones in the Himalaya is deeply rooted and exhumed rocks from mid-crustal depths (~24 to >26 km). A regional kinematic setting that favored extension combined with a ductile mid-crust led to strain partitioning and shear zone initiation, reactivation of older fault systems, and decompression-driven melting in the Leo Pargil dome. Approximately north-south oriented extensional systems across the Himalayan front are kinematically linked to strike-slip faults within the Tibetan Plateau that accommodate eastward displacement of the Tibetan Plateau, some of which initiated during a time of active north-directed extension along the South Tibetan detachment system. In the western Himalaya, oblique collision potentially controlled the development of strike-slip faults that transfer displacement to the normal-sense faults and shear zones that accommodate orogen-parallel extension.

VITA

Jackie Langille was born in Phoenix, Arizona and raised in Pocatello, Idaho. She attended Idaho State University and earned a Bachelor of Science degree in geology with a minor in geotechnologies in 2006. While at Idaho State, she worked as a Geographic Information Systems and Remote Sensing Technician for the Bureau of Land Management in collaboration with Idaho State University. She left Idaho to attend Central Washington University in Ellensburg, Washington where she earned a Master of Science degree in geology in 2008. Her thesis was titled "Middle Crustal Ductile Deformation Patterns in Southern Tibet: Insights from Vorticity Studies in Mabja Dome" conducted under Dr. Jeffrey Lee. After completion of her Masters degree, she began work toward a Doctor of Philosophy degree in geology at the University of Tennessee, Knoxville with a concentration on constraining extensional exhumation in the Himalaya. Following completion of this degree, she will begin a position at the University of North Carolina–Asheville as an Assistant Professor.